LOCALIZED AND CELLULAR BUCKLING IN STIFFENED PLATES

A thesis submitted to Imperial College London for the degree of Doctor of Philosophy

by
Maryam Farsi

Department of Civil and Environmental Engineering,
Imperial College of Science, Technology and Medicine
London SW7 2AZ, United Kingdom
June 2014

Declaration:

I confirm that this thesis is my own work and that any material from published or unpublished work from others is appropriately referenced.

Abstract

Nonlinear buckling behaviour of a thin-walled simply-supported stiffened panel that has uniformly spaced longitudinal stiffeners is studied. The structure is made from a linear elastic, isotropic and homogeneous material. The panel is subjected to pure compression applied at the centroid of whole cross-section. In such structures, the nonlinear interaction can occur between a global (Euler) buckling and local plate (*i.e.* the stiffener or the main plate) buckling modes. The interactive buckling behaviour is usually more unstable than when the modes are triggered individually. This can lead to a significant reduction of the load-carrying capacity. The current work focuses on the case where the stiffening is only on one side of the main plate.

An analytical model of a perfect thin-walled stiffened plate is formulated based on variational principles by minimizing the total potential energy. The equations of equilibrium are then solved numerically using the continuation and bifurcation software AUTO to determine the post-buckling behaviour. Cellular buckling (or *snaking*) is revealed analytically in such a component arising from nonlinear local–global interactive buckling, perhaps for the first time. In addition, the effect of varying the rigidity at the main plate–stiffener junction is studied; a rapid erosion of the cellular buckling response is revealed by increasing the joint rigidity.

The initial model is then developed by including more degrees of freedom within the stiffened panel and the introduction of global and local imperfections. The results

from the analytical model are validated by the finite element (FE) method using the commercial software Abaqus as well as by comparing against some experimental results taken from the literature.

To obtain a greater understanding of the drivers of the structural behaviour, parametric studies are conducted for a variety of different plate and stiffener geometries as well as an investigation into the heightened sensitivity to geometric imperfections. The worst forms of local imperfection are identified in terms of the initial amplitude, number of waves and the degree of localization. The imperfection sensitivity and the parametric studies are conducted for two limiting cases, where the main plate–stiffener joint is assumed to be fully pinned or fully rigid. A framework for establishing the zone where structural designers need to consider mode interaction carefully is presented.

Acknowledgements

I am indebted to all the great people who have helped and directed me during my doctoral studies and those whose support made this thesis possible.

First and foremost, I would like to express my deepest gratitude to my PhD supervisor, Dr M. Ahmer Wadee, for his outstanding guidance, encouragement and patience. His dedication together with his professionalism and expertise, have been beyond doubt inspiring and motivating, especially through the hardest stages of the work. I learned a lot from Dr Wadee and it has been an honour for me to be his PhD student. This thesis would have never been possible without his support.

I would like to thank the Civil and Environmental Engineering Department and the library staff at Imperial College for providing facilities, support and assistance. I would also like to thank all my colleagues, especially Li Bai, Elizabeth Liu and Chi Hui whom I shared my problems with and they always offered me so much help during my PhD research. I am grateful to all my friends, who had righteous understanding of my study situation and honestly backed me with my PhD study path.

A special thanks to my husband, Danial. He was truly encouraging, patient and supportive from the initial steps right through to its final stages. His love and sacrifices made the past three years, less stressful especially during the difficult times.

Acknowledgements

Finally, I would like to express my deepest gratefulness to my loving family, my brother and my little sister. Words cannot express how indebted I am for all of the support and sacrifices that they have made on my behalf. I would like to express my warm gratitude to my father and to dedicate this thesis to him.

Contents

List of Figures

List of Tables

Nomenclature

Coordinates, Stress, Strains, Loads and Energy

x	Transverse direction along panel breadth
y	Transverse direction along stiffener depth
z	Longitudinal direction
$N_x,\ N_y,\ N_{xy}$	In-plane forces in directions x, y, xy respectively
$\sigma_x,\ \sigma_y,\ \sigma_z$	Direct stress in directions x, y, z respectively
$\tau_{xy},\ \tau_{yz},\ \tau_{zx}$	Shear stress in planes xy, yz, zx respectively
$\varepsilon_x,\ \varepsilon_y$	Direct strain in directions x and y respectively
ε_{zt}	Direct strain in z direction for top stiffeners
ε_{zb}	Direct strain in z direction for bottom stiffeners
ε_{zp}	Direct strain in z direction for plate
$\gamma_{xy},\ \gamma_{xz}$	Shear strain in planes xy and xz respectively
γ_{yzt}	Shear strain in plane yz for top stiffeners
γ_{yzb}	Shear strain in plane yz for bottom stiffeners
V	Total potential energy
$\mathcal{L}$	Lagrangian
χ	Bending curvature
U	Total strain energy
U_{bo}	Strain energy of global bending

U_{bl}	Strain energy of local bending
U_m	Strain energy stored in the membrane of the stiffener
U_d	Strain energy stored in the membrane of the stiffener due to direct strains
U_s	Strain energy stored in the membrane of the stiffener due to shear strains
U_{sp}	Strain energy stored in rotational spring
M	Bending moment
P	External load
P^{C}	Critical buckling load
P_o^{C}	Global buckling load
P_l^{C}	Local buckling load
p	Normalized load (P/P_o^{C})
P_E	Euler load
P^{M}	Maxwell load
P_U	Ultimate load
p_u	Normalized ultimate load
σ_Y	Yield stress
σ^{C}	Critical buckling stress
σ_o^{C}	Global buckling stress
σ_{ls}^{C}	Local buckling stresses of the stiffeners
σ_{lp}^{C}	Local buckling stresses of the plate
k_p	Plate buckling coefficient
Φ	Airy stress function
C	Critical bifurcation point
S	Secondary bifurcation point
T	First snap-back point
$\mathcal{E}$	Total end-shortening

Geometric properties

L	Stiffened plate length
b	Distance between adjacent stiffeners
h_1	Height of top stiffener
h_2	Height of bottom stiffener
t_s	Thickness of stiffeners
t_p	Thickness of main plate
c_p	Stiffness of rotational spring at the stiffener to main plate junction
I_p	Second moment of area of the main plate
A	Total cross-section area
r	Radius of gyration
λ_o, λ_l	Global and stiffener local slendernesses respectively
$\bar{\lambda}_o, \bar{\lambda}_l$	Normalized global and stiffener local slendernesses respectively

Material Properties

E	Young's modulus
ν	Poisson's ratio
D_s	Flexural rigidity of stiffener
D_p	Flexural rigidity of main plate
G	Shear modulus

Displacements and generalized coordinates

$W(z)$	Sway component of global buckling
$\theta(z)$	Tilt component of global buckling
q_s	Amplitude of sway component
q_t	Amplitude of tilt component
q_s^{S}	q_s at secondary bifurcation point
q_s^{T}	q_s at first limit point after S
q_s^{D}	Limiting global amplitude q_s
$w_s(y,z)$	Local out-of-plane displacement of stiffeners
$w_p(x,z)$	Local out-of-plane displacement of main plate
$w_{\max}^{\mathrm{D}}$	Limiting local amplitude $w_{\max}$
$u(y,z)$	Local in-plane displacement
Δ	Pure squash displacement
λ_p	Out-of-plane displacement ratio of the main plate to the stiffener
Λ	Wavelength of $w(z)$
χ	Bending curvature

Imperfections

$W_0(z)$	Initial out of straightness of global mode
q_{s0}	Initial amplitude of sway component
$\theta_0(z)$	Initial rotation of a plane section of global mode
q_{t0}	Initial amplitude of tilt component
$w_{s0}(y,z)$	Imperfect local out-of-plane displacement of stiffener
$w_{p0}(x,z)$	Imperfect local out-of-plane displacement of main plate

A_0	Amplitude of local imperfection
α	Degree of localization of local imperfection
$\beta\pi/L$	Wave number of local imperfection
η	Offset of peak imperfect displacement
$\mathcal{E}_0$	Initial end-shortening of imperfection
χ_0	Initial curvature

Chapter 1

Introduction

A thin-walled structure comprises thin plates that are joined along their edges. In such a structure, the plate thickness is small compared to other dimensions such as the width and the length. Thin plated steel structures are made from light gauge steelwork and may be stabilized in one direction by stiffeners. Such structures are used extensively in various structural applications including industrial and residential buildings, offshore structures (Ghavami & Khedmati, 2006), box girder bridges (Murray, 1973; Choi *et al.*, 2009), ship hulls (Grondin *et al.*, 1999; Sheikh *et al.*, 2002), aircraft skins (Butler *et al.*, 2000; Loughlan, 2004) and particularly where a high strength to weight ratio is important and desirable. Thin-walled plated structures are also utilized extensively in sub-surface structures such as tanks, pipes and culverts (Carrera *et al.*, 2012).

There are a number of reasons to give special consideration to thin-walled structures in terms of their analysis and design. Such structures are susceptible to local buckling as well as global (Euler) buckling. These structures buckle locally if the in-plane stresses reach the critical values for the individual elements. If this happens, the geometry of the structural cross-section can change significantly, in contrast to global buckling

where the cross-section is relatively unchanged. Therefore, thin-walled structures must be designed against both local and global buckling modes of instability.

Theory and experiments show that under certain circumstances, these two modes of instability may interact and when this happens the actual collapse load can be decreased to below the critical value of the individual buckling loads (Murray, 1984). This type of instability can be highly unstable, with recent studies highlighting the interaction of buckling modes leading to localization (Hunt & Wadee, 1998; Woods & Champneys, 1999; Wadee & Gardner, 2012; Wadee & Bai, 2014). In particular, Murray (1973), discussed the failure of design codes to take into account that stiffened plates should have a higher safety factor; he presented a large number of variables that influence collapse and attempted to define quantitatively the important interdependencies based on analytical techniques and experimental evidence. Although, in more recent years, efforts have been made to include such effects in the design procedures, a fundamental understanding and an analytical predictability is only just emerging from the aforementioned recent studies. The aim of the current work is to make additional contributions specifically for stiffened plates.

1.1 Structural stability

In an engineering structure, failure can occur due to material failure, structural instability or a combination of the two. The former type relates to the strength of the material, whereas the latter is particularly due to geometric nonlinearities, *e.g.* buckling.

The load at which a structure becomes unstable, known as the "critical load" P^{C}, depends primarily on structural geometric properties, especially the so-called slenderness of an element or structure. This latter quantity tends to be independent

of the material strength. The deformed configuration introduces nonlinearities that amplify the stresses in the structure (sometimes known as the $P-\delta$ effect). In the case of thin-walled structures, the $P-\delta$ effect can be significant, leading to modal interactions between the global and local buckling modes that, in turn, can lead to localization, which is well known to promote undesirable features such as effective negative stiffnesses, gross sensitivity to initial defects and perhaps even dynamic snap-back behaviour (Wadee, 2007).

1.2 Interactive buckling

Since thin-walled structures can suffer from local buckling as well as global buckling along the length, the interaction between these two modes gives a possibility for a third mode of structural instability, namely interactive buckling. The nonlinear interaction of local and global buckling instabilities is found in some common structures such as thin-walled I-beams (Wadee & Gardner, 2012), I-section struts (Wadee & Bai, 2014), sandwich structures (Hunt & Wadee, 1998), built-up columns (Thompson & Hunt, 1973) and corrugated or stiffened plates (Thompson & Hunt, 1984; Pignataro *et al.*, 2000). In addition, for compression members built up from thin plates, a design in which buckling of the whole structure and local buckling of the plate elements occur simultaneously was often accepted as the optimum design (Tvergaard, 1973b), owing to the simple notion of maximizing the critical loads, see Figure 1.1. However, since the development of nonlinear structural stability theory, from the 1960s, this notion is seen as a naive and potentially dangerous viewpoint.

In the case where the global mode of buckling is critical, the corresponding amplitude of buckling can grow until deflections become sufficiently large to induce a secondary instability, where the local buckling mode is induced and begins to interact with the existing global mode. Periodic Rayleigh–Ritz analysis, assuming symmetric

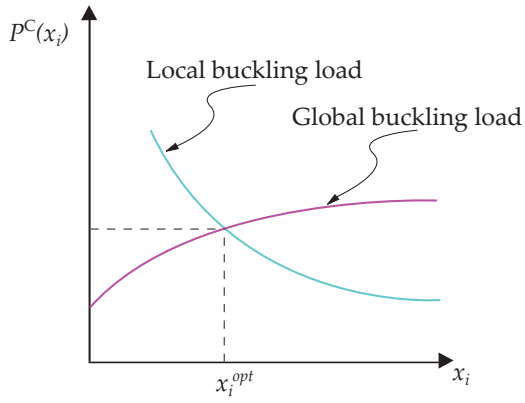

Figure 1.1: The optimum design curve for a perfect stiffened plate: x_i is a geometric dimension. The quantity x_i^{opt} has been termed the "naive optimum" in the literature (Koiter & Pignataro, 1976).

and asymmetric local modes, has been used to study this type of interactive buckling phenomenon in sandwich structures (Hunt *et al.*, 1988), with an extension for orthotropic cores (Da Silva & Hunt, 1990). The approach used Timoshenko beam theory in which shear strain becomes important. The use of a shear deformable bending theory has allowed an analytical and later a variational approach to be applied to such vulnerable structures. Indeed, Hunt and Wadee (1998) studied the interactive buckling behaviour using the variational approach and were the first to provide an analytical model that demonstrated localization from local–global mode interaction in the elastic range. Later, they demonstrated that orthotropic core materials exacerbate the behaviour (Wadee & Hunt, 1998) and by changing the core constitutive model they showed that so-called "cellular buckling" could be triggered (Hunt *et al.*, 2000). Similarly, in a more recent study, Wadee and Gardner (2012), investigated the interaction of flange local buckling and lateral torsional buckling in a thin-walled I-beam subjected to uniform moment and discovered cellular buckling there also.

The latter work gave the idea that cellular buckling may be inherently linked to the response of thin-walled structures. One of the most well known examples of global and

local mode interaction is in the study of stringer-stiffened plates (Koiter & Pignataro, 1976; Ronalds, 1989; Butler *et al.*, 2000). The current work, presents a series of analytical developments that predict and demonstrate the occurrence of behaviour such as localization and cellular buckling in such structures.

1.3 Research outline

Although the behaviour of metallic stiffened plates has been studied over the past decades, it is apparent that some of the stability aspects in terms of interactive buckling and localization are still not well understood in such structures. In 1970, the West Gate Melbourne bridge collapsed by compression buckling of the top flange. The 112 m steel box girder span was in the simply supported condition when the failure occurred. Similarly in 1971, the Koblenz bridge collapse, was associated with instability of thin plating in compression, this time due to a detailing error (Smith, 1976). In this thesis, the buckling and post-buckling behaviour of a thin-walled simply-supported plated panel with uniformly spaced longitudinal stiffeners (or stringers), as shown in Figure 1.2, is studied using a series of analytical models based on variational principles and nonlinear stability theory. A linear elastic system is assumed throughout and this section outlines the sequence in which the models and results are presented.

1.3.1 Aims and objectives

In this research work, a series of analytical models based on total potential energy principles, has been developed. A combination of discrete and continuum mechanics approaches with a first order shear deformable bending theory have been key to modelling the response. The analytical models have led to systems of nonlinear differential equations that describe the interactive buckling behaviour. The primary goal of the

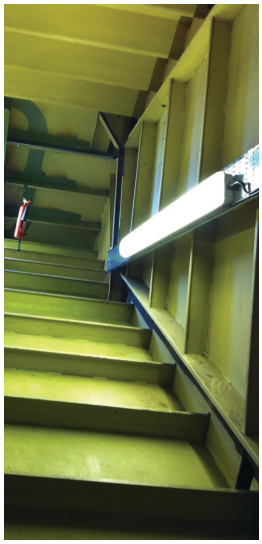

Figure 1.2: A practical example of a stiffened plate. Photograph of the inside of the Humber Bridge (UK) box-girder. (Taken by the author).

research is to investigate the phenomenon of local–global modal interactions in the buckling behaviour of a stringer-stiffened panel. This phenomenon has been found in analogous structural components such as sandwich structures (Hunt & Wadee, 1998), in I-section beams (Wadee & Gardner, 2012), in I-section columns (Wadee & Bai, 2014) and is well known to be a potentially dangerous form of instability.

The interaction can occur between the global buckling of the stiffened plate and the local buckling of the stiffener as well as the main plate between the stiffeners. Analytical models are formulated such that a more rigorous theoretical understanding can be achieved. The corresponding analytical results are validated through numerical modelling from the finite element (FE) method and from published experiments. The validation shows that the equilibrium states described by the analytical model can be reproduced, in terms of the combination of the load with local and global deformations. Finally, the effects of changing the geometry of the individual elements of the stiffened plate and the introduction of imperfections are investigated.

1.3.2 Methodology

An analytical approach has been favoured currently with variational principles playing a pivotal role, in conjunction with the principle of minimum potential energy. The expression for the total potential energy V comprises the gained potential energy from internal deformations, so-called strain energy U, and the work-done by the external loads $P\mathcal{E}$, where:

$$V = U - P\mathcal{E}. \tag{1.1}$$

The corresponding equations of equilibrium that are obtained by minimizing V, using the calculus of variations, are then solved numerically by the continuation and bifurcation software Auto (Doedel & Oldeman, 2011), which is adept at solving nonlinear problems with instabilities. Moreover, the commercial software, Abaqus (2011) is utilized to simulate the stiffened plate using the finite element (FE) method. The results from the analytical model are compared to the FE model for validation; there are also a couple of relevant experimental results that are used for comparison purposes (Fok *et al.*, 1976).

1.3.3 Thesis layout

The thesis comprises six further chapters:

Chapter 2 outlines the research problem in detail and contains a review of the literature. It focuses on large deflection theory for thin-walled structures, elastic analysis of axially loaded stiffened plates, instability modes, approximate methods of analysis, and relevant research works detailing previous analytical, numerical and experimental research; some of which have already been mentioned.

Chapter 3 details an analytical model formulation based on variational principles

for a perfect thin-walled stiffened panel subjected to axial compression. The developed equations are then solved numerically by the continuation and bifurcation software Auto-07p (Doedel & Oldeman, 2011). The interaction phenomenon is between global (Euler) buckling of whole stiffened plate and local buckling of the stiffener leading to localized buckling in the stiffener. Detailed numerical results are presented for an assumed plate geometry. It is worth noting that a rotational spring at the main plate–stiffener junction represents a relative rigidity of the joint. By varying the rotational stiffness parameter, investigations are conducted for a series of cases ranging from a pinned to essentially a rigid joint between the stiffener and the main plate.

Chapter 4 presents a detailed extension of the analytical model formulated in Chapter 3. The global buckling mode is considered to interact with local buckling of the stiffener and the main plate. An initial imperfection, in terms of an out-of-straightness of the global stiffened plate, is considered as well as initial out-of-plane imperfections of the stiffeners and the main plate. The total potential energy is again developed. Moreover, a link between the main plate deflection and the stiffener deflection is established by assuming that the joint between the two elements is connected by a rotational spring, which potentially allows the model to be compared against actual experiments. The corresponding differential equations are again solved numerically using Auto-07p and numerical results are presented.

The results for the imperfect case from the analytical model are then compared to the FE model formulated in Abaqus in Chapter 5. Moreover, the analytical and the FE models are compared against existing physical experimental results by Fok *et al* (1976). Comparisons show excellent correlations for both cases.

A parametric study, to determine the effects of varying global and local slendernesses, is presented in Chapter 6. The variation in the global and the local slenderness is

achieved by varying the strut length and the height of the stiffener respectively for different boundary conditions at the main plate–stiffener junction. Furthermore, imperfection sensitivity is studied by varying the imperfect amplitude of global buckling of the strut as well as the initial local displacement of the stiffeners and the main plate. The parametric regions for structural designers to avoid, are highlighted for the examples presented.

Chapter 7 closes the thesis by presenting the conclusions and suggesting where further work may be conducted to advance the current modelling work. It summarizes the implications of the results. In addition, a preliminary formulation on the modelling of lipped stiffened plates is outlined as a possible extension to the research presented.

Chapter 2

Literature review

The study of thin-walled structures is focused around the behaviour of the individual plate elements that comprise the components. The first mathematical study of thin plates was probably conducted by Euler, who presented a free vibration analysis of such structures in 1776 (Webster & Plimpton, 1955). A decade later, various modes of free vibration were discovered by a German physicist named Chladni. In 1795, Johann Bernoulli, the Swiss mathematician, attempted to justify Chladni's findings and Bernoulli's solution became known as the now well-known "Euler–Bernoulli bending theory". In 1813, Germain, a French mathematician, developed a plate differential equation by adding shear terms; subsequently, Lagrange, improved the equation by adding more terms, thus presenting the general plate differential equation for the first time (Ventsel & Krauthammer, 2001).

Cauchy and Poisson formulated the plate bending problem based on general equations of the "theory of elasticity". In 1829, Poisson developed the Germain–Lagrange plate differential equation as the solution for a plate under static loading where the plate flexural rigidity D, a measure of the plate bending stiffness, was considered as a constant term. The first satisfactory concept for the theory of plate bending is associated

with Navier, the French engineer and physicist (Forray, 1968), who considered a simply supported rectangular plate with thickness t as a function of flexural rigidity D. An asymptotically exact method for calculating the deflections, stresses and strains was investigated for uniformly loaded plates by introducing the loading as a double Fourier series. Kirchhoff published an important thesis on the theory of thin plates in 1850; later, in 1888, Love presented what become known as the Kirchhoff–Love theory for plates (Bazant & Cedolin, 1991). The solution for rectangular plates, with two opposite edges as simply-supported and the other two supports being arbitrary, was successfully solved by Levy in the late 19th century by proposing a single Fourier series solution.

Extensive studies in the area of plate bending theory and its various applications were also made by Timoshenko (1915), Galerkin (1933), Woinowsky-Krieger (1959), Hencky (1921), Huber (1929), von Kármán, *et al* (1932) and Nadai and Föppl (Ventsel & Krauthammer, 2001). In addition, the behaviour of thin-walled structures has been investigated by a large number of researchers since the 1930s (Cox, 1934). In this chapter, after a brief overview of the elements of the theory of bending, a review of some of the relevant literature associated with the stability analysis of elastic thin-walled plated structures is presented. Moreover, the development of the theory of general linear and nonlinear buckling is examined, followed by a survey of the key phenomenological features of the nonlinear buckling of plated structures, mode interaction, localized and cellular buckling, all of which are relevant in the current study.

2.1 Plate bending

In the theory of bending, structures that are sufficiently slender are considered. A structure is slender when the ratio of the length to the cross-section dimensions is

sufficiently large, for practical purposes usually over approximately a ratio of 10:1 (Bazant & Cedolin, 1991). For such slender members, the Kirchhoff–Love theory of bending represents a very good approximation to the exact solution according to three-dimensional elasticity. Deformation of such structures gives stresses through the structure that are assumed to be constant over time. Such systems are referred to as "quasi-static" as inertial effects can be neglected (Wadee, 1998). The fundamental assumptions of the linear, elastic, small-deflection theory of bending for thin plates are summarized below (Ventsel & Krauthammer, 2001):

1. The plate material is elastic, isotropic and homogeneous.
2. The plate is initially flat.
3. The deflection of the mid-plane is small compared to the thickness of the plate.
4. The straight lines, initially normal to the mid-plane before bending, remain straight and normal to the mid-plane during deformation.
5. The stress, normal to the mid-plane, is small compared to the other stress components.
6. The mid-plane remains unstrained after bending since the displacements of the plate are small.

2.1.1 Linearized (small deflection) plate theory

Small deflection theory was first suggested by Bernoulli in 1705 and systematically developed by Navier in 1826. The Euler–Bernoulli beam theory (often termed engineer's beam theory) is based on the following fundamental hypothesis: (*i*) during deflection, the plane normal to the mid-section of the beam remains plane and normal to the deflected centroidal axis of the beam; (*ii*) the transverse normal stresses are negligible; see Figure 2.1(a). Timoshenko (1921) improved upon the Euler–Bernoulli theory by adding the effect of shear, whereby, the normal plane section rotates by an

amount θ, which is not equal to $\mathrm{d}W/\mathrm{d}z$, as shown in Figure 2.1(b). The expression

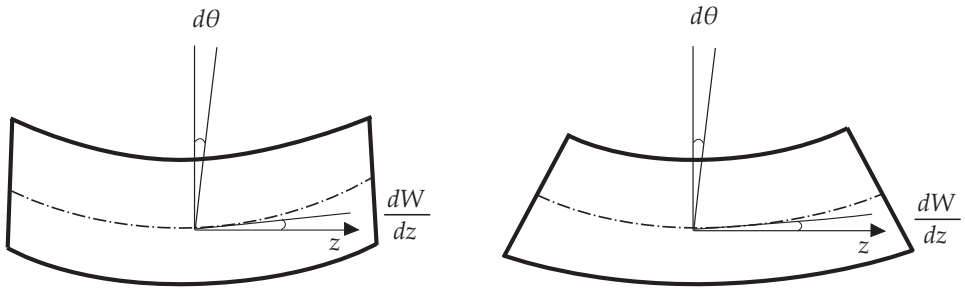

(a) $\mathrm{d}\theta = \frac{\mathrm{d}W}{\mathrm{d}z}$ (b) $\mathrm{d}\theta \neq \frac{\mathrm{d}W}{\mathrm{d}z}$

Figure 2.1: Outline of two theories of beam bending; (a) Euler–Bernoulli beam theory, (b) Timoshenko beam theory: the dot-dashed lines represent the neutral axis of bending and W is the global deflection.

for the bending moment is given by:

$$M = -\int_A \sigma y \, \mathrm{d}A, \tag{2.1}$$

where A is the cross-section area of the beam and σ is the bending stress. Since the definition of the second moment of area of the cross section $I = \int y^2 \, \mathrm{d}A$, the bending moment about the neutral axis can be expressed as:

$$M = \frac{EI}{\rho} = \frac{\sigma I}{y}, \tag{2.2}$$

where E is the Young's modulus, y is the perpendicular distance from the neutral axis and ρ is the radius of curvature. By using the small rotation definition of curvature, the Euler–Bernoulli equation for the quasi-static bending of slender, isotropic, homogeneous beams under uniform bending is given thus:

$$-EI\frac{\mathrm{d}^2}{\mathrm{d}z^2}W(z) = M(z). \tag{2.3}$$

For thin-walled plated structures, there are several theories of bending that attempt to describe the deformation and stress distributions. The two most well-known are:

the Kirchhoff–Love theory of plates (also termed classical plate theory), which is an extension of Euler–Bernoulli beam theory for thin-walled structures, and the Mindlin–Reissner plate theory (also termed the first-order shear deformation theory of plates). The fundamental assumptions of Kirchhoff–Love theory are: (i) straight lines normal to the mid-surface remain straight and normal to the mid-surface after deformation; (ii) the thickness of the plate does not change during the deformation. However, in Mindlin–Reissner theory the special assumption is that normals to the mid-surface remain straight and inextensible but are not necessarily normal to the mid-surface after deformation; hence it is the plate bending equivalent to the Timoshenko beam theory.

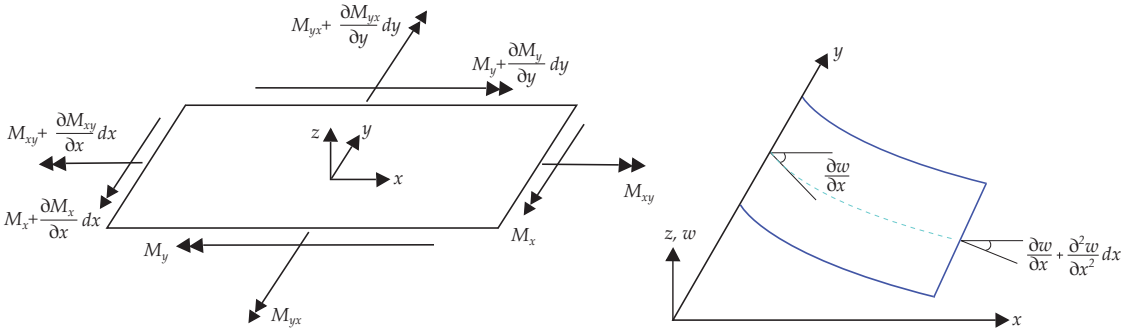

Figure 2.2: (a) Bending (M_i) and twisting (M_{ij}) moments of Kirchhoff–Love plates, (b) differential element under cylindrical bending about the y axis for plate bending.

Consider an element of a thin rectangular homogeneous and isotropic plate of thickness t with Young's modulus E and Poisson's ratio ν, under the bending and twisting moments as shown in Figure 2.2(a). According to the definition for the stresses and the strains in the x and y directions of the plate, taking moments about the neutral axis give the following expressions for the bending moments M_x and M_y (per unit

length) in the x and y directions respectively, thus:

$$M_x = \int_t \sigma_x z \, \mathrm{d}z = -D\left(\frac{\partial^2 w}{\partial x^2} + \nu \frac{\partial^2 w}{\partial y^2}\right),$$
$$M_y = \int_t \sigma_y z \, \mathrm{d}z = -D\left(\frac{\partial^2 w}{\partial y^2} + \nu \frac{\partial^2 w}{\partial x^2}\right), \tag{2.4}$$

where D is the flexural rigidity of a plate, which corresponds to the quantity EI in beams, and is defined as:

$$D = \frac{Et^3}{12(1-\nu^2)}. \tag{2.5}$$

Since the condition of plane stress is assumed (*i.e.* $\sigma_z = \tau_{xy} = \tau_{yz} = 0$), the expressions of the twisting moments (per unit length) M_{xy} and M_{xy} are thus:

$$M_{xy} = M_{yx} = \int_t \tau_{xy} z \, \mathrm{d}z = D(1-\nu)\frac{\partial^2 w}{\partial x \partial y}. \tag{2.6}$$

2.1.2 Approximate methods of analysis

A large amount of research work was conducted to find a solution for the equation of equilibrium for plates (Marguerre, 1937; Coan, 1951; Yamaki, 1959). An analytically exact solution for plate bending problems with small deflections using classic methods was proposed by both Navier and Levy. The problems were limited to relatively simple plate geometries, load configurations, and boundary conditions. The simplest differential equation for a plate, based on small deflections, was derived by Lagrange in 1811 and then was developed by Navier in 1820. In 1883, Saint Venant modified both equations by considering more loading terms, as expressed in Equation (2.7):

$$\frac{\partial^4 w}{\partial x^4} + \frac{2\partial^4 w}{\partial x^2 \partial y^2} + \frac{\partial^4 w}{\partial y^4} = \frac{1}{D}\left[q + N_x \frac{\partial^2 w}{\partial x^2} + N_y \frac{\partial^2 w}{\partial y^2} + 2N_{xy}\frac{\partial^2 w}{\partial x \partial y}\right], \tag{2.7}$$

where q, N_x, N_y and N_{xy} are forces denoting lateral (q), axial (N_x, N_y) and shear (N_{xy}) external loading; note that q is a pressure and N_x, N_y and N_{xy} are forces per unit length. Therefore, for more complicated loading and boundary conditions (Rhodes & Harvey, 1971a; Rhodes & Harvey, 1971b), the classical analysis methods become

increasingly difficult or even impossible to use. Hence, in such cases, approximate methods are the only approaches that can be realistically employed for the solution of practically important plate bending problems.

In this section, approximate methods, which are widely used for plate and shell bending analysis, are discussed. These approximate methods are divided into two groups: indirect and direct (Ventsel & Krauthammer, 2001). Indirect methods are used to obtain numerical values of unknown functions by, primarily, discretization of the governing differential equation of the corresponding boundary value problem. Well-known indirect methods include the *Finite difference* method, the *Boundary collocation* method, the *Boundary element* method and *Galerkin's* method. Direct methods, however, are based on the variational principles for determining numerical fields of unknown functions (*i.e.* deflections, internal forces and moments). Two well-known direct methods are the *Finite element* method and the *Ritz* (Energy) method.

Ritz (Energy) method

The energy method is based on the principle of minimum total potential energy V. The total potential energy V is the summation of strain energy U and the work done $P\Delta$. Note that the work done is negative, because the compressive stresses caused by the load P act in the opposite direction to the movement and therefore causes a loss in V:

$$V = U + (-P\Delta). \tag{2.8}$$

To determine the equilibrium state, the first variation of total potential energy δV must vanish for any small changes, hence:

$$\delta V = \delta U + \delta(-P\Delta) = 0. \tag{2.9}$$

The strain energy due to bending U in the x and y directions, $\mathrm{d}U_x$ and $\mathrm{d}U_y$ respec-

tively, for the linear elastic case, are given by:

$$\begin{aligned} \mathrm{d}U_x &= \frac{1}{2} M_x \,\mathrm{d}y \left(-\frac{\partial^2 w}{\partial x^2} \right), \\ \mathrm{d}U_y &= \frac{1}{2} M_y \,\mathrm{d}x \left(-\frac{\partial^2 w}{\partial y^2} \right). \end{aligned} \tag{2.10}$$

The component of strain energy due to the twisting moment M_{xy} is:

$$\mathrm{d}U_{xy} = \frac{1}{2} M_{xy} \,\mathrm{d}y \left(\frac{\partial^2 w}{\partial x \partial y} \,\mathrm{d}x \right). \tag{2.11}$$

By substituting the bending and twisting moments from Equations (2.4) and (2.6) and integrating over the volume of the plate, the total strain energy stored in bending is derived thus:

$$U = \frac{D}{2} \int_A \left\{ \left(\frac{\partial^2 w}{\partial x^2} + \frac{\partial^2 w}{\partial y^2} \right)^2 - 2(1-\nu) \left[\frac{\partial^2 w}{\partial x^2} \frac{\partial^2 w}{\partial y^2} - \left(\frac{\partial^2 w}{\partial x \partial y} \right)^2 \right] \right\} \mathrm{d}A, \tag{2.12}$$

where D is the flexural rigidity of the plate as before and A is the total cross-sectional area. The work done $P\Delta$ for a general plate problem where lateral loads q and shear stresses τ_{xy} are possible, can be expressed as:

$$P\Delta = \int_A \left\{ wq + \frac{t}{2} \left[\sigma_x \left(\frac{\partial w}{\partial x} \right)^2 + \sigma_y \left(\frac{\partial w}{\partial y} \right)^2 + 2\tau_{xy} \left(\frac{\partial w}{\partial x} \right) \left(\frac{\partial w}{\partial y} \right) \right] \right\} \mathrm{d}A. \tag{2.13}$$

The Ritz method then introduces a trial function for w and uses minimization techniques to determine approximate equilibrium states.

Galerkin's method

Galerkin's method is an alternative to the Ritz method. In this method, an approximate shape function w is substituted into the original equilibrium equation derived in Equation (2.7) rather that the total potential energy V. Therefore, since w is not precisely accurate, an error is introduced when using this method (Bulson, 1970). The method minimizes the error in a similar way to the Ritz method.

Finite difference method

The finite difference method is particularly useful for plates with mixed boundary conditions or varying flexural rigidity. This method is an approximate numerical procedure which is based on the use of an approximate expression for the deflection derivatives, that appear in the governing differential equation (Bulson, 1970). The technique is to subdivide the plate, longitudinally and transversely into a grid system, where the mesh size is the distance between adjacent grid lines, δx and δy respectively. The first derivative is the slope at each point, which can be given as the difference between adjacent deflections divided by the distance between them. The higher derivatives can be defined in a similar way. Substitution into Equation (2.7) gives the difference equation valid at each point in terms of the deflections at the surrounding points. This can be applied to each point of the grid, resulting in a system of linear equations that can be solved computationally with considerable speed.

Finite element method

The finite element (FE) method has become widely used in recent years for finding solutions for plate buckling problems (Crisfield, 1997). In this method, the plate is divided into a number of elements joined only at specific nodes with shape functions defining the relations between the nodes. Therefore, continuity and equilibrium are established at these nodes (Bulson, 1970). Hence, there is no need to formulate the governing partial differential equation formally. The advantage of the finite element method is that it produces a matrix formulation for deflections as well as loading and boundary conditions. This makes it suitable for use when programming by computer and the results obtained from the FE method are commonly validated against experimental data (Becque, 2008; Becque & Rasmussen, 2009a; Becque & Rasmussen,

2009b).

2.1.3 Nonlinear (large deflection) plate theory

Kirchhoff's linear plate bending theory, is valid only for small deflections (*i.e.* $w \lesssim 0.2t$) (Ventsel & Krauthammer, 2001), where t is the thickness of the plate. The linear theory ignores the straining of the middle surface of the plate and the corresponding in-plane stresses are also neglected. Therefore, the applied load is only carried by the bending action of the plates. However, if the magnitude of the lateral deflections increases, the plate deflection is accompanied by significant stretching of the middle surface, so-called "membrane" action. Therefore, in large deflection theory, a load is carried by the combined mechanism of bending and membrane action. A classic approach to the evaluation of the post-buckling behaviour of plates, based on large deflection theory, was devised by von Kármán in 1910 (Timoshenko & Woinowsky-Krieger, 1959). In this regard, the Airy stress function $\Phi(x, y)$ is introduced to define the in-plane stresses in the system as follows:

$$N_x = t\frac{\partial^2 \Phi}{\partial y^2}, \qquad N_y = t\frac{\partial^2 \Phi}{\partial x^2}, \qquad N_{xy} = -t\frac{\partial^2 \Phi}{\partial x \partial y}. \tag{2.14}$$

The corresponding critical buckling load P^{C} and stresses σ^{C} can be evaluated from exact methods, as well as the approximate methods for more complicated conditions, as previously described. Given that an elastic flat plate can carry stresses higher than σ^C due to the stretching of the mid-surface that is inherent in bending in two orthogonal directions, the behaviour of a plate should be considered after the critical bifurcation point, *i.e.* the so-called post-buckling response, where nonlinearities need to be considered.

2.1.4 Approximate methods for the post-buckling response

Approximate methods for nonlinear plate buckling problems focus on obtaining an alternative form of the governing differential equation. In this regard, the nonlinear version equation of equilibrium, Equation (2.7), can be formulated using the *Energy* method, the *Effective width* method, and the *Dynamic* method (Ventsel & Krauthammer, 2001). More recently approximate methods for post-buckling response problems have included such as the *Finite strip* method and *Generalized beam theory*. Some of the more common approximate methods are outlined briefly below.

Energy method

The Energy method can be used to determine the behaviour beyond the bifurcation point in the large deflection plate problems. To consider large deflections, the strain energy component due to stretching of the mid-surface, the so-called 'membrane energy' U_m is added to the original total strain energy U; this can be calculated from the expression below given a plane stress assumption:

$$\begin{aligned} U_m &= \frac{t}{2}\int_A \left[\sigma_x\varepsilon_x + \sigma_y\varepsilon_y + \tau_{xy}\gamma_{xy}\right] \, \mathrm{d}A, \\ &= \frac{t}{2}\int_A \left[E(\varepsilon_x^2 + \varepsilon_y^2) + G\gamma_{xy}^2\right] \, \mathrm{d}A, \end{aligned} \tag{2.15}$$

in which σ_x, σ_y, τ_{xy} represent the stresses in the middle surface of the plate due to the in-plane forces. The total direct strains in the x and y directions, ε_x and ε_y respectively and the shear strain within the xy plane, γ_{xy}, for an element on the middle surface are given by:

$$\begin{aligned} \varepsilon_x &= \frac{\partial u}{\partial x} + \frac{1}{2}\left(\frac{\partial w}{\partial y}\right)^2, \\ \varepsilon_y &= \frac{\partial u}{\partial y} + \frac{1}{2}\left(\frac{\partial w}{\partial x}\right)^2, \\ \gamma_{xy} &= \frac{\partial u}{\partial y} + \frac{\partial v}{\partial x} + \frac{\partial w}{\partial x}\frac{\partial w}{\partial y}, \end{aligned} \tag{2.16}$$

where, u and v are the in-plane deflections in the x and y directions respectively and w is the out-of-plane deflection of the plate as before. The key terms in Equation (2.16) are each of the final terms, these are known as the von Kármán strain components. The aforementioned Ritz method could then be used to calculate the post-buckling equilibrium states.

Effective width

An early analysis of the actual post-buckling behaviour of axially loaded plates was conducted by von Kármán *et al.* (1932). They suggested a simplified approach to obtain an estimate for the ultimate load carried by the buckled plate, based on experimental observations. Consequently, they introduced the notion that the ultimate buckling load of the plate P_u is carried exclusively by two strips of equal width, the so-called *effective width*, located along the unloaded edges and therefore, the reduced but positive post-buckling stiffness could be determined. This method was further developed by Cox (1934) and Marguerre (1937) for different boundary conditions.

Consider a rectangular simply-supported plate subjected to compressive stresses in one direction, Figure 2.3(a). Before the plate buckles, the compressive stresses are uniformly distributed across the width b. However, after buckling (*i.e.* beyond the critical bifurcation point) the distribution of stresses along the loaded edges becomes progressively nonlinear, see Figure 2.3(b). Therefore, the stress distributions have a minimum value at the centre, and a maximum at the vicinity of the plate edges. A typical compressive stress distribution along the plate cross section is shown in Figure 2.3(c). Since the distribution of the compressive stresses depends on the boundary conditions, for a uniform compressive stress, the stress distribution at both sides in the vicinity of the plate edges are equal (*i.e.* $b_{e1} = b_{e2} = b_e/2$), as shown in Figure 2.3(d).

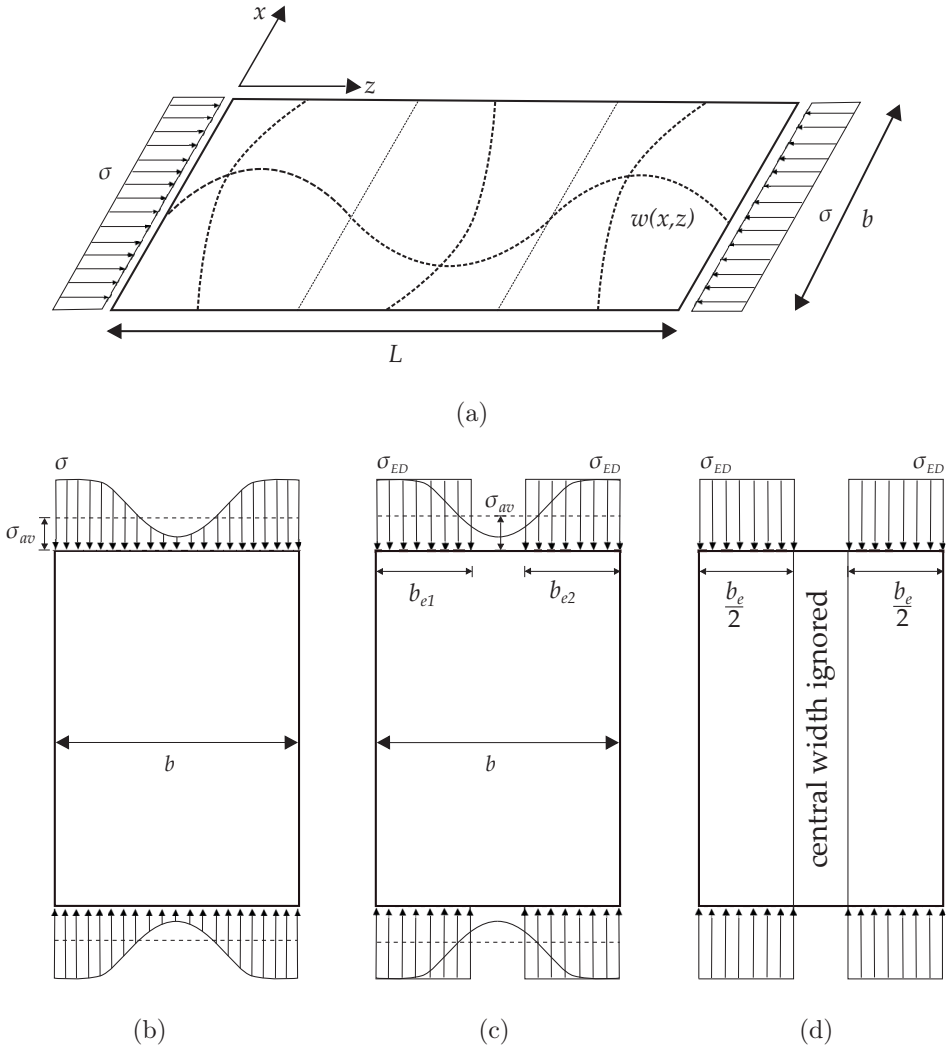

Figure 2.3: Effective width approximation for the plate post-buckling stiffness; (a) axially loaded and simply-supported rectangular plate with width b, length L and thickness t; (b) ultimate stress distribution σ along the loaded edge; (c) a uniform edge stress σ_{ED} distribution at both sides in the vicinity of the plate edge (*i.e.* b_{e1} and b_{e2}); (d) effective width concept where the central region is ignored. Note that σ_{av} is the average ultimate stress.

The effective width method can also be applied for stiffened plates with longitudinal stiffeners, assuming the buckling stress distribution in the stiffener is the same as in an effective portion of the plate (Ventsel & Krauthammer, 2001). Note that the effective width in this case, is obtained by multiplying a slenderness reduction factor $\bar{\lambda}_p$ by the actual width of the plate b (EN1993, 2001). The effective width method is still the preferred method of design in order to consider the effects of local buckling in the buckling behaviour of thin walled, steel plated structures. In the Eurocode for steel design (EN1993, 2001), the effective width is obtained for thin-walled plane elements with and without stiffeners.

Finite Strip Method and Generalized Beam Theory

One of the more recent post-buckling analysis methods presented in the literature is the finite strip method which forms the basis of the Direct Strength Method (DSM) devised by Schafer and Peköz (1999). The finite strip method is often known as a semi-analytical technique, which works for prismatic thin-walled structural elements. This method differs from the finite element method in such a way that the structural element is only divided into a number of longitudinal strips, not transversely (Graves Smith & Sridharan, 1978). The behaviour of each strip is then determined using energy principles. A large number of numerical studies have been conducted to investigate the buckling behaviour in various types of structural components, using the finite strip method (Plank & Wittrick, 1974; Hancock, 1978; Sridharan & Peng, 1989).

Hancock (1981) used the finite strip method to study the local, distortional and flexural-torsional buckling of I-beams, bent about their major axes. Graphs of buckling load were presented for I-beams with different cross-sections about their major axis. Hancock's model has been found to provide a good prediction for the type of

critical mode for I-beams with different lengths and cross-sectional dimensions, as well as with lateral and torsional restraints. The distortional buckling behaviour in lipped thin-walled sections has been investigated by Schafer (2002) also using the finite strip method. Later, he provided a review of the development of this method for cold-formed steel member design (Schafer, 2008).

Another well-known method of analysis for buckling instability problems is the so-called Generalized Beam Theory (GBT) which is an extension to conventional engineering beam theory (e.g. Euler–Bernoulli beam theory). It allows cross-section distortion to be considered in the equation of equilibrium. GBT was first presented by Schardt (1994). He continued the development of the basic theory at the Technical University of Darmstadt for almost three decades (Gell & Thompsson, 2013). Later, this method was developed by Davies *et al.* (1994). This method is valid for prismatic, open cross-sections and is capable of computing the contributions of each deformation mode relative to the global displacement field (Davies *et al.*, 1994). The cross-section and member lengths are analysed separately, with each possible mode of deformation analysed in turn as separate degrees of freedom, which reduces computation time. The explicit DSM and GBT based software applications are few, but a couple of examples are CUFSM (2010) and GBTUL (2011).

2.2 Nonlinear buckling of stiffened plates

The essential characteristic of buckling is that the load at which it occurs depends primarily on the elastic modulus E and the cross-section properties, and it is almost independent of the material strength. Stiffened panels have been widely used as primary structural components for many structural systems subjected to compressive stresses, and are vulnerable to different types of buckling phenomena. In the stability analysis of stiffened plates, two basic types of buckling mode may be considered. One

possible mode is a global buckling mode of the entire stiffened plate, a second one is the local buckling of the stiffener or the main plate. Therefore, four largely recognized forms of structural failure have been found in stiffened plates (Murray, 1973; Bonello *et al.*, 1993): (*i*) main plate induced global buckling; (*ii*) stiffener induced global buckling; (*iii*) local buckling of the stiffener or the main plate and finally (*iv*) stiffener tripping, which is associated with the plastic collapse of the stiffeners in a localized mechanism.

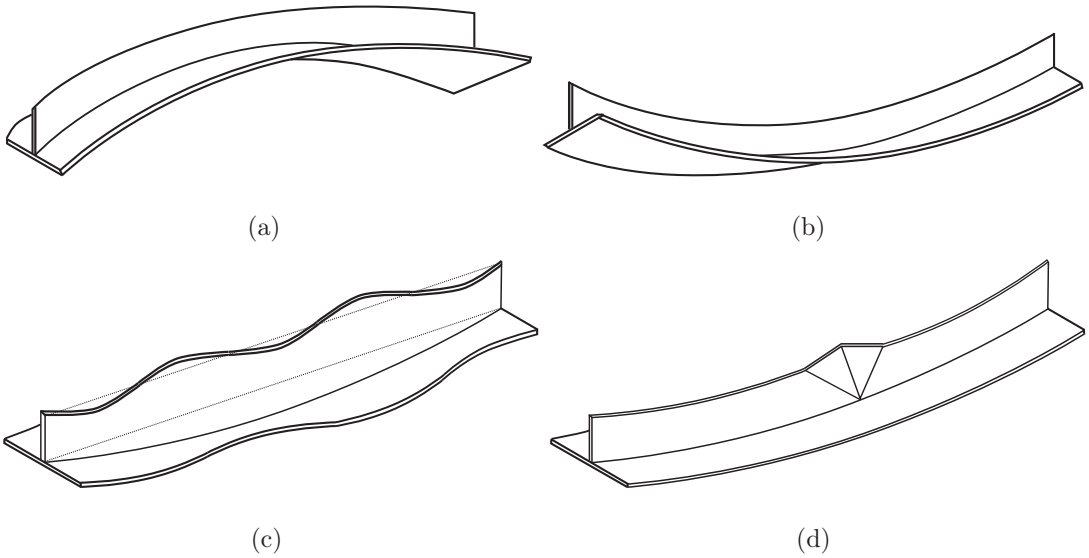

Figure 2.4: Buckling modes of the stiffened plates; global buckling mode due to the (a) stiffener, (b) main plate; (c) local buckling in the stiffener and the main plate; (d) stiffener tripping.

Global buckling is often referred to as 'Euler buckling' and is characterized by simultaneous buckling of the stiffener and the main plate acting as one in single curvature. This mode of instability is shown in Figure 2.4(a–b). Plate buckling is characterized by buckling of the stiffener, possibly as well as with the main plate between the stiffeners, which results in the load redistribution from the main plate into the stiffeners. This mode of instability is illustrated in Figure 2.4(c). Stiffener tripping, is the rota-

tion of the stiffener about the main plate–stiffener junction followed by the formation of a plastic mechanism; this mode of failure is illustrated in Figure 2.4(d). Failure by tripping can be more catastrophic than failure by local buckling of the plate (*i.e.* stiffeners or main plates), because it is associated with sudden plastic collapse in conjunction with instability (Butler *et al.*, 2000). Therefore, generous safety margins exist against collapse triggered by yielding or tripping (Danielson *et al.*, 1990).

A more economical design could potentially be obtained if local and global buckling occur simultaneously at approximately the same stress level (Koiter, 1963). This, however, is known to trigger the phenomenon known as interactive buckling and is explained in more detail in Section §2.3. Later, Koiter and Pignataro (1976) presented that the potential energy expression depends on the ratio of critical stresses for global and local buckling ($\lambda_E = \sigma_E/\sigma_l$), where σ_E and σ_l are the global buckling and local buckling critical stresses respectively. They also investigated that this energy depends on one additional parameter that depends only on the cross-section properties. The effect of magnitude and direction of applied uniform bending on the axial capacity of stiffened plates, was also investigated by Bonello *et al* (1993). They compared two alternative design approaches, namely an interaction equation and a method based on the Perry–Robertson design equation (Trahair *et al.*, 2008) compared with experimental results for continuous stiffened plates under combined axial compression and lateral pressure. In terms of design approaches, it is found that, the interaction equation is more conservative than the Perry method.

2.2.1 Global buckling

Given that stiffened plates may buckle globally or locally, each of these types of mode are now introduced in detail. The stability analysis of plates in terms of global deflection, is qualitatively similar to the stability analysis of a strut (Timoshenko &

Gere, 1961). The concept of stability of an elastic structure at which the equilibrium bifurcates, was introduced by Euler (1744). He also provided the solution of the critical load P^{C} for columns with different boundary conditions and restraints. In fact, the full nonlinear problem of an axially-loaded pin-ended thin strut, as represented in Figure 2.5(a) was solved by Euler completely.

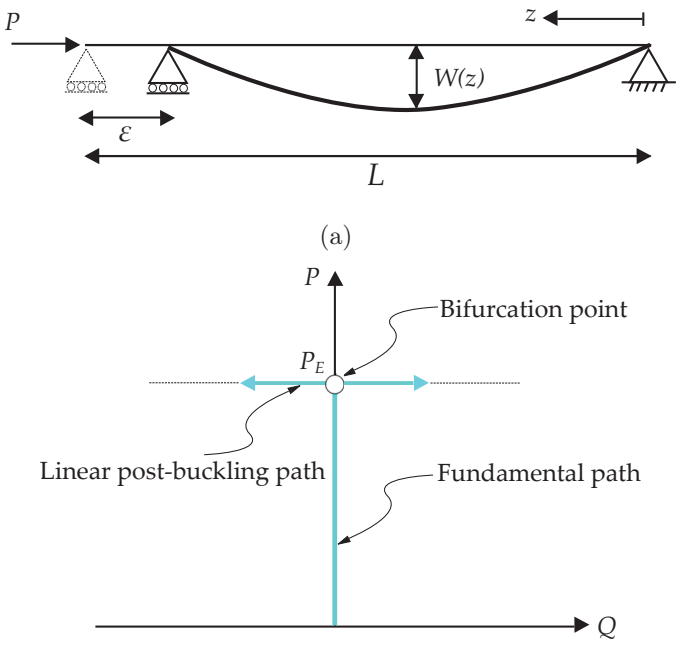

Figure 2.5: (a) Strut with flexural rigidity EI; (b) neutral equilibrium at Euler critical load P_E (small deflection assumption). The quantity Q represents the amplitude of W, the buckling deflection profile.

If a conservative load P is applied and buckling begins to occur, the bending moment in the deflected column is $M = PW$, where W is the out-of plane deflection. By substituting the expression for bending moment into Equation (2.3), the governing equation becomes:

$$EI\frac{\mathrm{d}^2W}{\mathrm{d}z^2} + PW = 0, \tag{2.17}$$

where EI is the flexural rigidity of the strut. This is a linear second order ordinary

differential equation. According to the boundary conditions for a pin-ended strut (*i.e.* $W = 0$ at $x = 0,L$), this equation has a trivial solution $W = 0$, but non-trivial solutions exist and are defined as the linear eigenvalue solution:

$$W_n(z) = Q \sin \frac{n\pi z}{L}, \quad P_n = \frac{n^2 \pi^2 EI}{L^2}, \tag{2.18}$$

where n is an integer and Q is the amplitude of the lateral deflection. The lowest critical load is associated with $n = 1$, the first eigenvalue, denoted as the well-known *Euler load* $P^{\mathrm{C}} = P_E$ and is given by:

$$P_E = \frac{\pi^2 EI}{L^2}. \tag{2.19}$$

The Euler load P_E represents the buckling load only for perfect elastic columns in a static and conservative system. The fundamental equilibrium path for lateral deflection W is equal to zero. However, once the load reaches the critical value P_E, the solution $W = 0$ loses stability and the strut has an equal probability to exhibit positive or negative lateral displacement. This is shown by the load–deflection relationship sketch in Figure 2.5(b), which shows the relationship when small deflections are assumed.

As mentioned earlier, linear theory is not valid during structural failure and therefore the behaviour of the structure is nonlinear due to material (plasticity or large strains) or geometric (large deflections or buckling) effects. The profile of the load-deflection relationship after buckling is called post-buckling response. A general theory of the initial post-buckling behaviour in bifurcation problems was devised and presented by Koiter (1945) in his famous PhD thesis. The governing differential equations of equilibrium were derived from minimizing a continuous nonlinear potential energy functional V that was formulated over a domain S:

$$V = \int_S \mathcal{L} \, \mathrm{d}S, \tag{2.20}$$

where $\mathcal{L}$ is similar to the Lagrangian function from dynamical systems theory (Fox, 1987; Hunt & Wadee, 1991). For equilibrium, the total potential energy V must be

stationary and so the first variation of the total potential energy δV must be zero. Koiter (1945) proved that: (i) the equilibrium at the critical state is *stable* if the load P for the adjacent post-buckling equilibrium states is higher than the bifurcation load P^{C} and (ii) the equilibrium at the critical state of the perfect structure is *unstable* if there exist adjacent post-buckling equilibrium states for which the load P is lower than the critical load at the bifurcation point. This is shown in Figure 2.6. Thompson

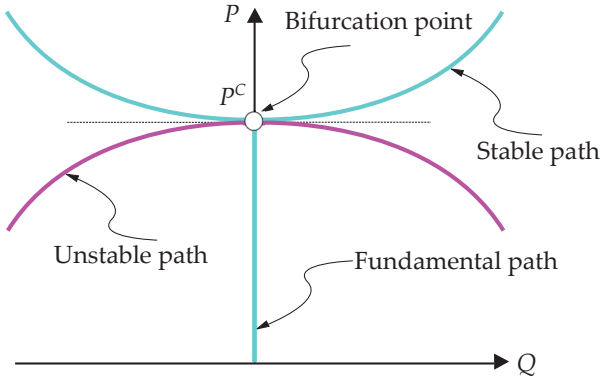

Figure 2.6: Stable and unstable post-buckling equilibrium paths (load–deflection relations). The graph shows the applied load P versus the modal amplitude Q; plates are inherently stable, but shell structures tend to be unstable after buckling.

and Hunt, with parallel work from Sewell, developed Koiter's study by applying the total potential energy principles to a discretized system. This led to the development of a systematic perturbation method for post-buckling analysis (Thompson & Hunt, 1973; Sewell, 1965). Therefore, the total potential energy V can be expressed in terms of a system of discrete coordinates or modal amplitudes Q_i as:

$$V = V(Q_1, Q_2, ..., Q_i, ..., Q_n), \tag{2.21}$$

and then two axioms linking V to the equilibrium states and their stability could be established:

Axiom 1. A stationary value of the total potential energy with respect to the generalized coordinates is necessary and sufficient for the equilibrium of the system.

Axiom 2. A complete relative minimum of the total potential energy with respect to the generalized coordinates is necessary and sufficient for the stability of an equilibrium state.

To determine the equilibrium state for a static system, the first derivative of V with respect to the generalized coordinates Q_i must be zero, and thus:

$$V_i = \frac{\partial V}{\partial Q_i} = 0, \tag{2.22}$$

then, to examine the stability of an equilibrium state, the second derivative of V with respect to the generalized coordinates Q_i must be calculated as below:

$$\mathbf{V}_{ij} = \frac{\partial^2 V}{\partial Q_i \partial Q_j}, \tag{2.23}$$

the equilibrium state being *stable* when the Hessian matrix $\mathbf{V}_{ij}$ is positive-definite, otherwise, the equilibrium state is *unstable*. The matrix becoming singular indicates that the equilibrium state is *critical*, which defines a bifurcation point that triggers a change in the equilibrium configuration and triggers the post-buckling response.

2.2.2 Local buckling

Local buckling of individual plates and within stiffened plates can either be within the main plate buckling or the stiffener buckling. Returning to an axially loaded rectangular plate shown in Figure 2.3(a). By considering the deflected shape for a long, thin plate, the deflection function can be expressed as:

$$w(x, z) = A \sin \frac{m\pi z}{L} \sin \frac{\pi x}{b}, \tag{2.24}$$

therefore, the corresponding strain energy U, Equation (2.12) and the work-done $P\Delta$, Equation (2.13), are given as:

$$\begin{aligned} U &= \frac{D}{2}\int_0^L\int_0^b \left\{\left(\frac{\partial^2 w}{\partial z^2}+\frac{\partial^2 w}{\partial x^2}\right)^2 - 2(1-\nu)\left[\frac{\partial^2 w}{\partial z^2}\frac{\partial^2 w}{\partial x^2}-\left(\frac{\partial^2 w}{\partial z \partial x}\right)^2\right]\right\} \mathrm{d}x\,\mathrm{d}z, \\ &= \frac{D\pi^4 Lb}{8}A^2\left(\frac{m^2}{L^2}+\frac{1}{b^2}\right)^2, \\ P\Delta &= \frac{t}{2}\int_0^L\int_0^b \sigma_z\left(\frac{\partial w}{\partial z}\right)^2 \mathrm{d}x\,\mathrm{d}z, \\ &= \frac{\sigma_z t m^2\pi^2 b}{8L}A^2. \end{aligned} \tag{2.25}$$

According to the definition for the total potential energy V and applying the aforementioned axioms, the critical stress σ^{C} is given by the following expression:

$$\sigma_l^{\mathrm{C}} = \frac{k_p \pi^2 E}{12(1-\nu^2)}\left(\frac{t}{b}\right)^2 \tag{2.26}$$

where the coefficient k_p is related to the number of half sine waves along the plate and is given by:

$$k_p = \left(\frac{m}{\phi}+\frac{\phi}{m}\right)^2, \qquad \phi = L/b. \tag{2.27}$$

The well-known k_p versus ϕ curves for different values of m, can be plotted as shown in Figure 2.7. This shows that long plates buckle in squares with $k_p \to 4$ for the case of a simply supported long plate under uniaxial compression (Bulson, 1970). Moreover, wide plates buckle with only one half sine wave along the length.

2.2.3 Initial imperfections and residual stresses

Since the nonlinear post-buckling behaviour of compression members is affected by geometric nonlinearities, an extensive literature exists regarding actual measurements of the magnitude and distribution of the initial imperfections and residual stresses (Paik *et al.*, 1999; Grondin *et al.*, 1999; Sheikh *et al.*, 2002). Initial imperfections and the residual stresses can arise from the manufacturing and welding processes, as well

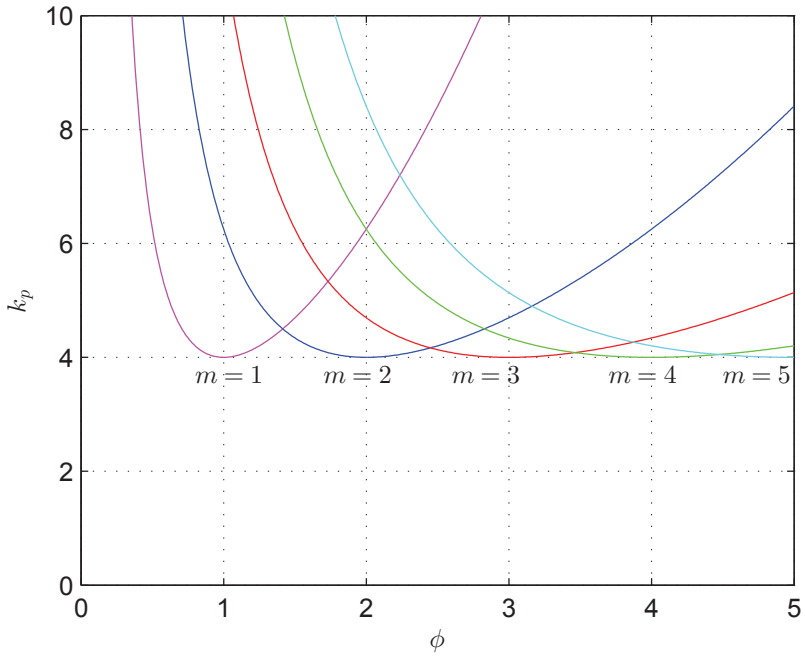

Figure 2.7: Buckling load coefficient k_p against the plate aspect ratio ϕ for a uniaxially-loaded simply supported plates.

as from damage or corrosion. A general statistical distribution was introduced for the magnitude of the imperfection parameter by Thompson (1967). In that work, asymptotic relationships were derived for the distribution of bifurcation loads. Small-scale experiments on the elastic buckling of stiffened plates were also presented by Thompson (1976); the nonlinear interaction between global and local modes of buckling was examined, considering both global and local imperfections. Koiter (1976) showed that, among the different bifurcations, the structures exhibiting asymmetric bifurcations have much higher imperfection sensitivity than the unstable symmetric ones. However, for an axially loaded plate in the elastic stable post-buckling range, the plate is relatively insensitive to initial imperfections and any imperfection sensitivity of the plate is usually associated with yielding (Wadee, 2000).

Thompson and Lewis (1972), calculated optimal designs of idealized columns with

equally imperfect flanges and no column imperfections. They proposed that the imperfection sensitivity is fundamentally more severe for smaller deflections rather than larger deflections (Thompson & Lewis, 1972; Koiter & Pignataro, 1976). In addition, based on the Koiter's general theory of elastic stability, (Koiter, 1963; Tvergaard, 1973a), it can be shown that a wide integrally stiffened panel under compression is particularly imperfection-sensitive when buckling of the panel as a wide Euler column and local buckling of the plate between the stiffeners, occur at the same critical stress. Moreover, interaction between global (Euler) buckling and local buckling suggests that failure would tend to localize into the centre (Hunt & Wadee, 1998). Regarding this issue, amplitude modulation is a key feature of the interactive buckling mode and finite element formulations for such structures have been presented (Sridharan & Zeggane, 2001).

2.3 Mode interaction

It is commonly found in practice that structural components may exhibit more than one buckling mode during the loading history. A very important aspect of stability of stiffened plates, which is beyond the scope of thin-walled beam theory, is the nonlinear interaction of local and global buckling. However, the design criterion of triggering both modes simultaneously is questionable, as was first pointed out by Koiter (1969) on the basis that local buckling may promote global failure and vice versa.

Although the behaviour of the individual buckling modes might be well understood, when these buckling modes are triggered in combination, the behaviour of the system is normally much more complex than when they are triggered individually (Budiansky, 1976). A major step towards a general theory for nonlinear interaction buckling problems where one mode destabilizes another, is associated with Supple (1967). The research work presented an elastic system with two degrees of freedom that

exhibited symmetric bifurcations; equilibrium equations were derived for uncoupled and coupled modes based on total potential energy principles. The total potential energy V was a function of the load P and the deflection Q_i, thus:

$$V = V(Q_i, P), \tag{2.28}$$

where $i = 1, 2$. A perturbation scheme allowed the development of the equilibrium equations for the doubly symmetric system, in a truncated form of a power series:

$$\begin{aligned} V_{11}Q_1 + \frac{1}{3!}(V_{1111}Q_1^3 + 3V_{1122}Q_1Q_2^2) + \delta P V'_{11}Q_1 = 0, \\ V_{11}Q_2 + \frac{1}{3!}(V_{2222}Q_2^3 + 3V_{1122}Q_2Q_1^2) + \delta P V'_{22}Q_2 = 0, \end{aligned} \tag{2.29}$$

where a subscript i on V denotes partial differentiation of V with respect to the corresponding generalized coordinate Q_i; a prime on V denotes partial differentiation of V with respect to P and δP is the incremental change in P from a known state $P = P_0$. For uncoupled modes ($Q_1 = 0$ or $Q_2 = 0$), Equation (2.29) simplified and it was found that the system would exhibit a stable or unstable symmetric bifurcation when $V_{iiii} > 0$ and $V_{iiii} < 0$ respectively. For coupled modes, a relationship between Q_1 and Q_2 was obtained on eliminating δP from Equation (2.29), thus:

$$XQ_1^2 + YQ_2^2 = -6V'_{11}V'_{22}\Delta P, \tag{2.30}$$

where ΔP is the difference between the two critical values of P with X and Y being coefficients given by the following expressions:

$$\begin{aligned} X &= V'_{22}V_{1111} - 3V'_{11}V_{1122}, \\ Y &= V'_{22}V_{1122} - 3V'_{11}V_{2222}. \end{aligned} \tag{2.31}$$

It was found that the behaviour of the interacting modes is predominantly controlled by the coefficients X and Y, where each can be positive or negative. Supple (1967) summarized the solutions for various conditions of X, Y and ΔP. In general, for $\Delta P \neq 0$, there are two types of solutions, represented by an ellipse and a hyperbola in the Q_1Q_2 plane, as shown in Figure 2.8. The post-buckling stability for different

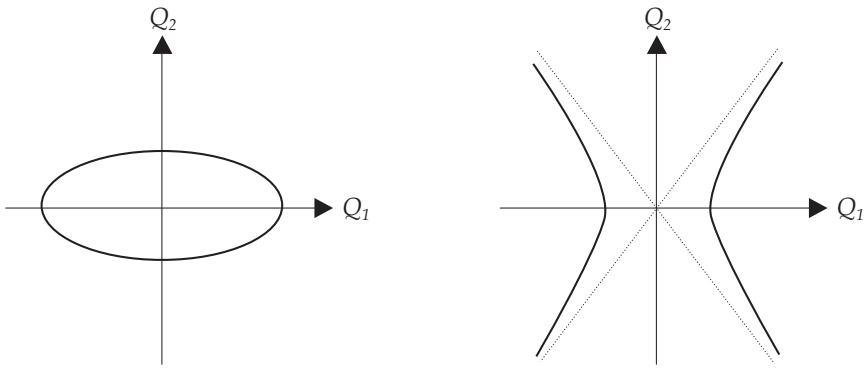

(a) Elliptic (b) Hyperbolic

Figure 2.8: Major forms of coupled solutions relating generalized coordinates in the post-buckling range.

conditions of X, Y and ΔP was summarized into four theorems. The work highlighted an important feature such that the post-buckling behaviour from the coupled instabilities can be unstable, even if individual modes exhibit a stable symmetric bifurcation. Parallel work was conducted by Chilver (1967) with the focus being on both symmetric and asymmetric systems.

Various types of structural components that exhibit interactive buckling have been studied analytically (Lundquist & Stowell, 1942a; Lundquist & Stowell, 1942b; van der Neut, 1968; Croll & Walker, 1972; van der Neut, 1974; Koiter & Pignataro, 1976; Goltermann & Møllmann, 1989; Møllmann & Goltermann, 1989; Hunt & Wadee, 1998; Butler *et al.*, 2000). Williams and Wittrick (1971), produced numerical results by matrix analysis, for buckling under uniform longitudinal compression of panels with unflanged and flanged integral stiffeners and with Z-section stiffeners. Cylindrical shells (Hutchinson & Koiter, 1970; Hunt *et al.*, 1986) are perhaps the most efficient load carriers, particularly in compression. They can exhibit the nonlinear interaction between different buckling modes, leading to the classic localized diamond buckling mode pattern (Lord *et al.*, 1997; Yamaki, 1984). In addition, plated structures are also susceptible to interactive buckling, such as I-section columns and beams (Han-

cock, 1981; Menken *et al.*, 1991; Wadee & Gardner, 2012), sandwich panels (Allen, 1969; Wadee & Hunt, 1998; Wadee *et al.*, 2010) as shown in Figure 2.9, and stiffened plates (Murray, 1973; van der Neut, 1976; Tvergaard & Needleman, 1976; Koiter & Pignataro, 1976), where mode interaction often leads to localized buckling (Champneys *et al.*, 1999).

Perhaps the most classic piece of work on the interactive buckling of columns is associated with van der Neut (1969). He studied the interaction of local and global (Euler) buckling of an idealized thin-walled compression member, which comprised two load carrying flanges with width b, thickness h and length L, and a web with depth $2c$ that was laterally rigid and had no longitudinal stiffness, as shown in Figure 2.10. In the study, a perfect column and an imperfect one with an initial local deformation in the flanges, as well as one with an initial out-of-straightness were investigated. The stiffness reduction factor η was expressed as:

$$\eta = \frac{\mathrm{d}(P/P_l)}{\mathrm{d}(\varepsilon/\varepsilon_l)} \tag{2.32}$$

where P and ε were the applied compressive force and the direct strain within the flanges respectively. Note that the subscript l referred to the local buckling mode. For a specific value of the flange width b and thickness h, the investigation examined the impact of the column length L on the critical buckling mode and the stability of the corresponding critical state, as is summarized in Table 2.1. The results in Table 2.1 are also illustrated by the classic van der Neut curves, as shown in Figure 2.10(b). Note that K is the applied compression on the entire strut (as distinct from P) with K_E and K_l being the Euler load and the local buckling critical load respectively.

The nonlinear interaction between global and local buckling modes is also found commonly in sandwich structures (Hunt *et al.*, 1988; Hunt & Wadee, 1998; Wadee, 1999). Such structures usually consist of two stiff face plates separated by a relatively soft core material. In sandwich structures, for global buckling, the effect of shearing in the core can be accounted for by decomposing the global half sine wave mode derived

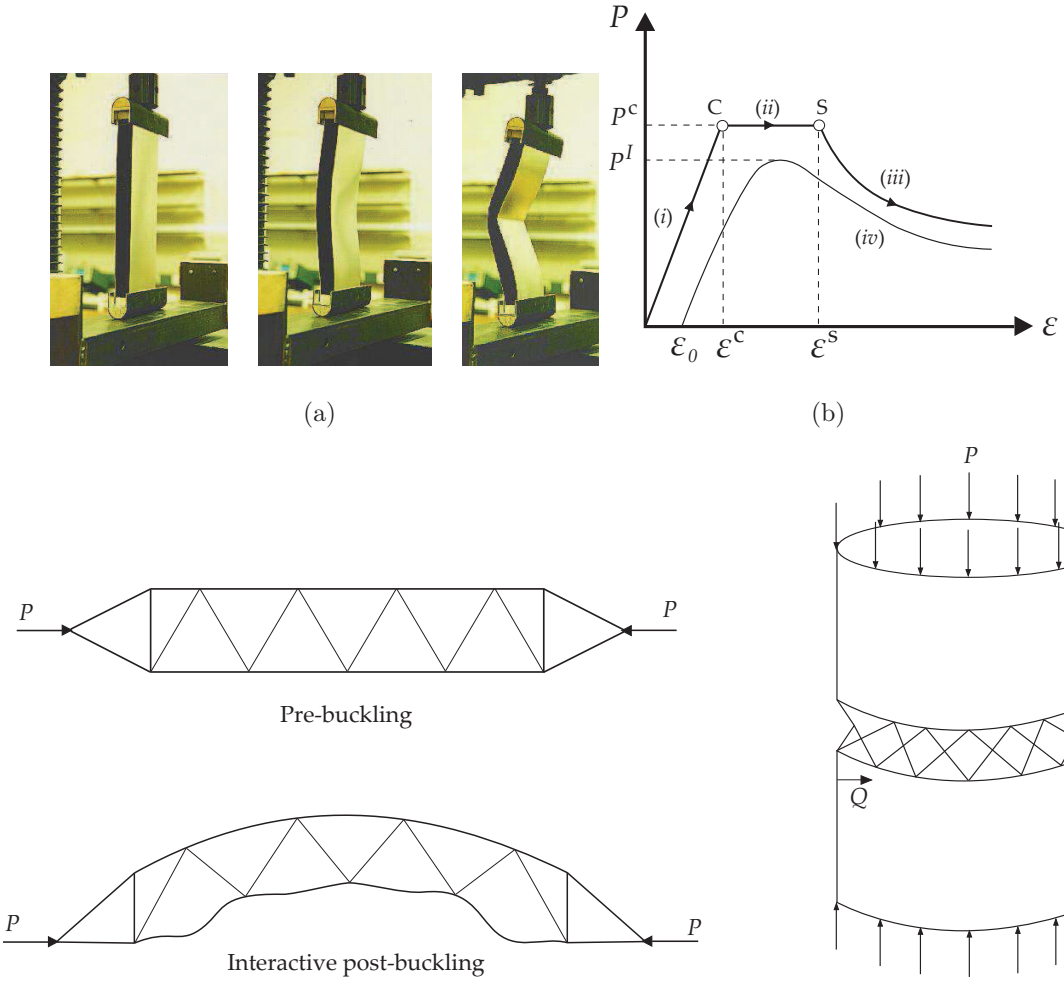

Figure 2.9: Examples of structural components exihibiting interactive buckling; (a) photographs of an experimental specimen of a sandwich strut under axial compression (Wadee, 1999). From left to right: pre-buckling followed by global buckling and subsequent interaction between global and local buckling modes leading to localization; (b) equilibrium diagram for sandwich panels: (*i*) fundamental path; (*ii*) critical path of global buckling triggered at critical bifurcation C; (*iii*) secondary path of interactive buckling triggered at secondary bifurcation S; (*iv*) typical imperfect path with limit load P^{I}; (c) a reticulated or compound column with initial configuration and the possible interactive buckling mode combining global and local modes; (d) a cylindrical shell with the localized buckling pattern.

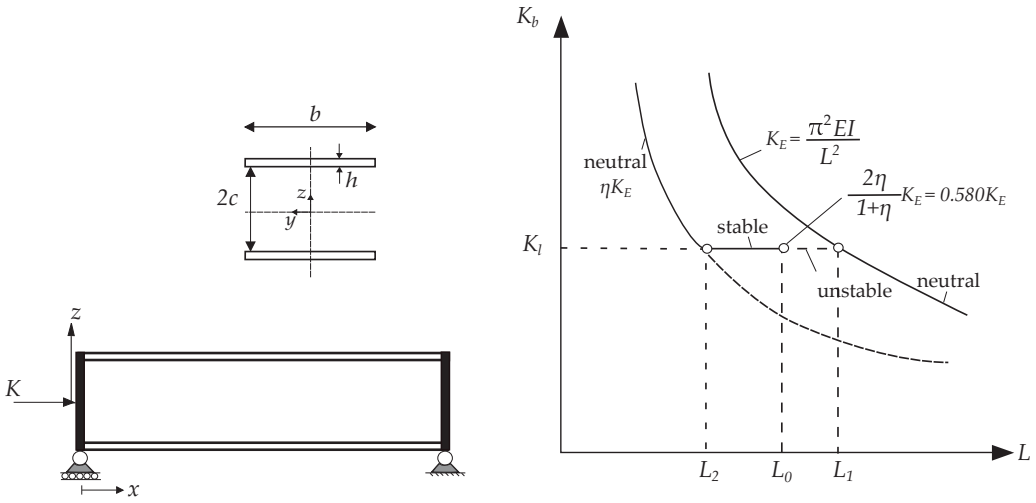

(a)

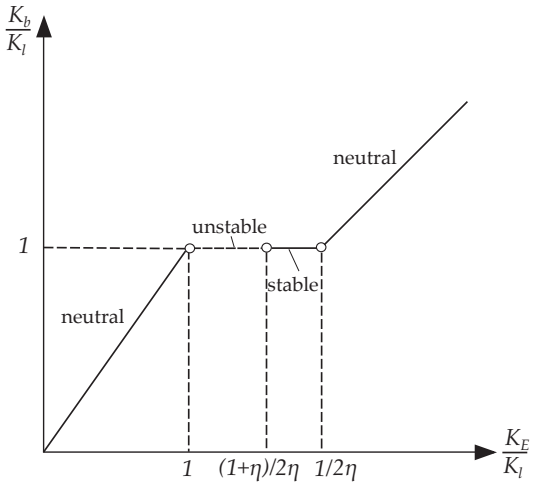

(b)

Figure 2.10: The van der Neut (1969) column: (a) column cross-section and buckling load K_b versus length L, (b) normalized column buckling load K_b/K_l versus K_E/K_l, showing the post-buckling characteristics.

Category	Column Length	Critical mode	Post-buckling characteristics
1	$L \geq L_1$	Euler buckling	Neutral (approx)
2	$L \leq L_2$	Local buckling	Neutral (approx)
3	$L_2 \leq L \leq L_0$	Local buckling	Stable
4	$L_0 \leq L \leq L_1$	Local buckling	Unstable

Table 2.1: Critical buckling modes and post-buckling characteristics for the column length constraints in categories 1–4, Length $L = L_1$ is the case where the local buckling load and Euler buckling load are equal; $L_2 = \eta^{1/2} L_1$; $L_0 = (2\eta/(1+\eta))^{1/2} L_1$.

from Euler buckling with two generalized coordinates so-called 'sway' and 'tilt', as shown in Figure 2.11. Based on linear theory, the sway component $W(x)$ and the tilt

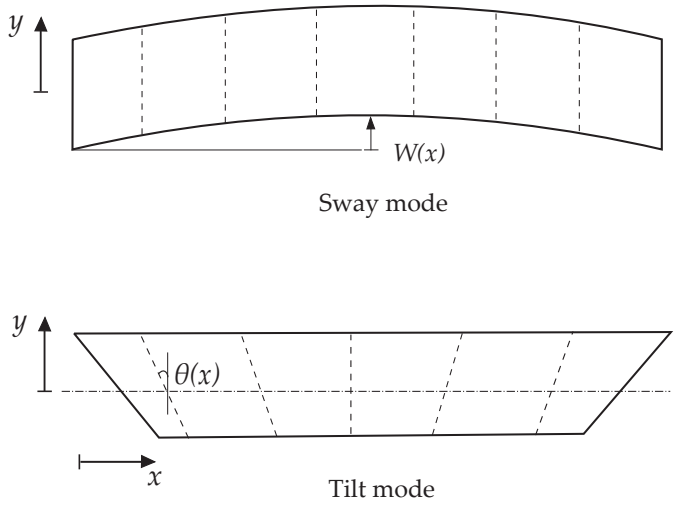

Figure 2.11: Decomposed modes for global buckling of a sandwich panel.

component $\theta(x)$ can be expressed by (Hunt *et al.*, 1988):

$$\begin{aligned} W(x) &= q_s L \sin \frac{\pi x}{L}, \\ \theta(x) &= q_t \pi \cos \frac{\pi x}{L}. \end{aligned} \tag{2.33}$$

In addition, for local buckling, two modal contributions named 'snake' and 'hourglass' can be considered, as shown in Figure 2.12. The local mode in sandwich structures is a

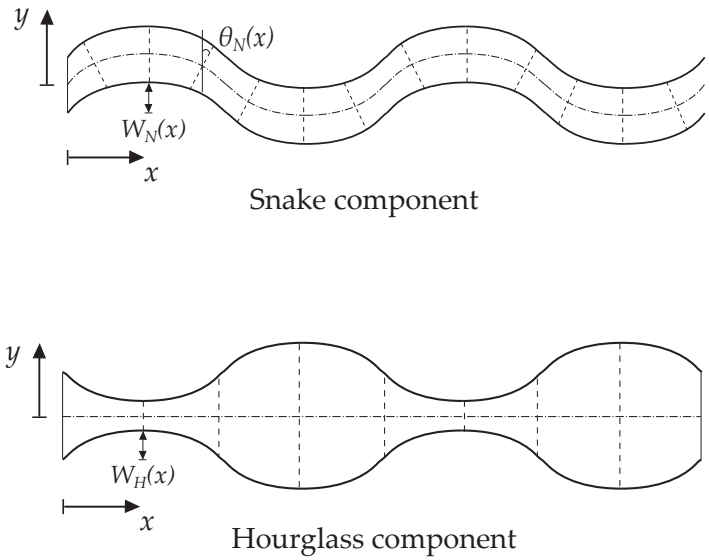

Figure 2.12: Decomposed modes for local buckling of a sandwich panel.

linear combination of snake (antisymmetric) and hourglass (symmetric) modes with an associated wave number $i\pi x/L$; these two modes originated in Goodier (1946). The lateral displacement W and the rotation of the plane section θ for the snake (N) and hourglass (H) modes are thus:

$$\begin{aligned} W_N(x) &= a_1 \frac{L}{i} \sin \frac{i\pi x}{L}, \\ \theta_N(x) &= a_2 \pi \cos \frac{i\pi x}{L}, \\ W_H(x) &= a_3 \frac{L}{i} \sin \frac{i\pi x}{L}, \end{aligned} \tag{2.34}$$

where L is the panel length, and x is the longitudinal axis. Note that a_1 is the amplitude of snake component, a_2 is the amplitude of tilt component of local snake and a_3 is the amplitude of the hourglass component. Since, one face remains predominantly straight, and the other face buckles periodically, $a_1 = a_3$ (Wadee, 1998). Hunt and Wadee (1998) studied the interactive buckling behaviour in an axially loaded sandwich panel using a variational formulation. The approach also followed Timoshenko beam theory since shear strain was found to be essential for the nonlinear interaction between the global and the local buckling modes and buckle pattern localization was

predicted for the first time.

The interactive buckling behaviour of stiffened panels was studied considering the global (Euler) and local buckling modes of the stiffener (van der Neut, 1969; Murray, 1973; Koiter & Pignataro, 1976; Sridharan & Peng, 1989). Mode interaction in unsymmetrical panel structures (*i.e.* a T-section stiffened plate) was investigated by van der Neut (1976). It was suggested that in such panels, the plate side is more affected by local buckling than the stiffener side. This effect is exaggeratedly represented in a model where the stiffeners do not participate in local buckling. Therefore, it was indicated that the sensitivity to imperfections of the model was restricted to a geometric parameter R, where $R = K_E/K_l$ and is ratio of the Euler and the local buckling loads. He proposed that this structure is strongly imperfection-sensitive in the case of coincident loads of global and local buckling. In a parallel study, Tvergaard and Needleman (1976), investigated the mode interaction and imperfection-sensitivity numerically and focused on similar features. Sridharan and Peng (1989; 1991), presented a theoretical formulation for an analytical model to study the nonlinear interaction of the local and global instabilities of axially compressed stiffened plates and they compared the results of their investigation with those given by Koiter and Pignataro (1976), and Tvergaard, (1973a). More recently with the advent of modern computational facilities, the post-buckling phenomena for isotropic stiffened panels with compression loading have been investigated using the FE method by Lillico *et al* (2003). The model has been incorporated within the strip program,Vipasa, with the constraint and optimization software, Viconopt, to design multi-bay stiffened panels (Durban *et al.*, 2001).

Very recently, Wadee and Gardner (2012) have studied the interaction of flange local buckling and lateral torsional buckling in a thin-walled I-beam subjected to uniform moment. A similarly variational approach was adopted as for the sandwich problem. The equilibrium paths after the secondary bifurcation point showed the behaviour

known as 'cellular buckling' (Hunt *et al.*, 2000) or 'snaking' (Burke & Knobloch, 2007). This is the phenomenon where the equilibrium after the secondary bifurcation undergoes a sequence of destabilizing and restabilizing processes, which is signified by a sequence of limit points (sometimes snap-backs) on the equilibrium paths, as sketched in Figure 2.13. Referring to the buckling modes, this phenomenon reflects

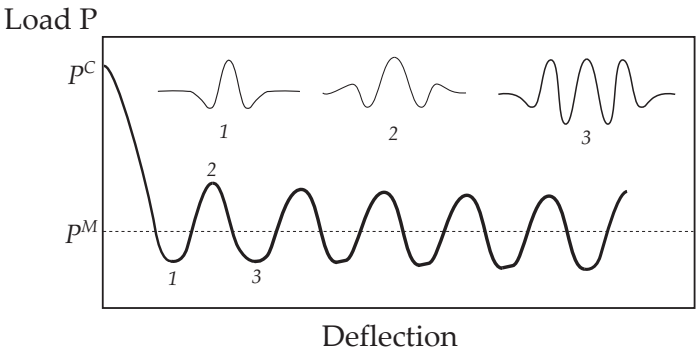

Figure 2.13: A example of cellular buckling or snaking in the equilibrium path of a structural system; P^{C} is the critical buckling load and P^{M} is the Maxwell load.

the progressively spreading waves in the structure, which was initially localized at mid-span, as found in the work on sandwich struts. Such a phenomenon has been also captured in cylindrical shell buckling (Hunt *et al.*, 1999; Hunt *et al.*, 2003) and in the sandwich problem for certain core material nonlinearities (Hunt *et al.*, 2000). These systems are usually associated with the Maxwell load P^{M}, where the load oscillates about a fixed load P^{M} as the deflection progresses, as shown in Figure 2.13, and is associated with the eventual periodic profile of the post-buckling mode emerging (Budd *et al.*, 2001). Structural systems exhibiting localization, cellular buckling, or snaking, exhibit what is normally considered to be dynamical systems behaviour involving homoclinic and heteroclinic orbits in phase space (Woods & Champneys, 1999; van der Heijden *et al.*, 2002; Chapman & Kozyreff, 2009; Taylor & Dawes, 2010), as sketched in Figure 2.14.

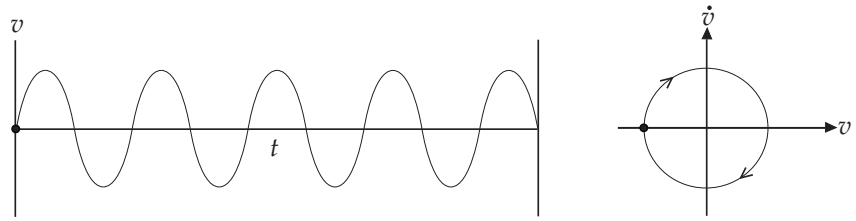

(a) Periodic orbit

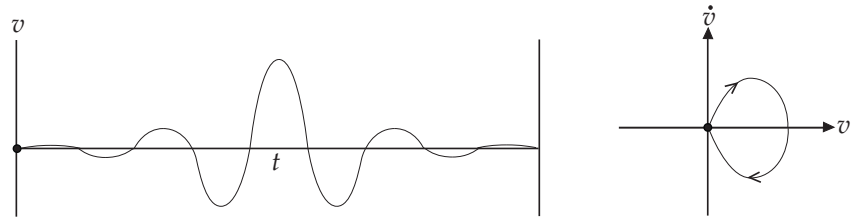

(b) Homoclinic orbit

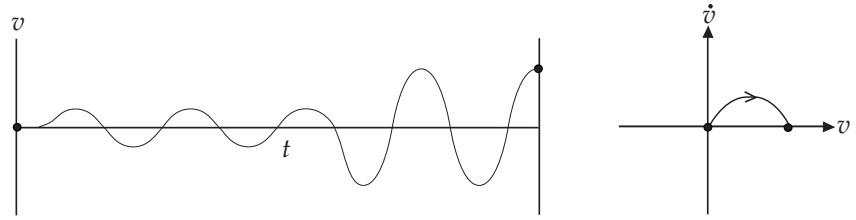

(c) Heteroclinic orbit

Figure 2.14: Examples of different kinds of orbits in nonlinear dynamical systems, where v and t represent displacement and time respectively. Dots represent the derivative of v with respect to t. Such solutions can also appear in nonlinear static systems in terms of deflections and slopes. (a) Periodic orbits are found in stable post-buckling systems such as compressed plates; (b) homoclinic orbits are found in systems exhibiting localization; (c) heteroclinic orbits are found in systems exhibiting cellular buckling.

2.4 Numerical continuation with Auto

If the equations of equilibrium of a structure presented as a system of ordinary differential equations (ODEs) that are accompanied by a number of boundary conditions, the system is known as a boundary-value problem (Seydel, 1994). Theoretically, buckling is caused by a bifurcation in the solution of the equations of equilibrium and post-buckling is defined as what happens after buckling has occurred. Mathematically, the post-buckling state describes the nonlinear behaviour of the system. There is specific software available to solve the equations of such systems such as: MatCont (Dhooge *et al.*, 2003), COCO (Dankowicz *et al.*, 2011) and Auto-07p (Doedel & Oldeman, 2011). These are collectively known as numerical continuation software. Auto-07p is a member of a particular class of such software which is capable of solving ODEs subjected to boundary and integral conditions and is used extensively in the current study. The accuracy of Auto has been tested in the past by related studies on nonlinear buckling phenomena and has been shown to be excellent (Lord *et al.*, 1997; Hunt & Wadee, 1998; Wadee & Hunt, 1998; Woods & Champneys, 1999; Hunt *et al.*, 1999; Hunt *et al.*, 2000; Wadee & Gardner, 2012; Wadee & Bai, 2014). It can also perform limited bifurcation analyses for algebraic systems and partial differential equations (PDEs). Moreover, Auto-07p allows the user to vary the input parameters and assess the evolution of obtained solutions on a parametric path. In other words, the user is able to assess the equations for a range of values, rather than just for a single value, which is the case for non-continuation solvers of ODEs. A number of branching or bifurcation points may also exist in solving the differential equations of equilibrium. Auto-07p has the ability to detect different types of bifurcating solutions on the evolution path. When solving ordinary differential equations with bifurcating branches, the process of 'branch switching' means to evaluate one solution that emerges on a new branch from a bifurcation point. This 'first solution' on the emanating branch then serves as the starting point for subsequent tracing of the

entire branch. Auto-07p and the other numerical continuation software mentioned earlier are able to capture and switch between different bifurcating branches, while generic non-continuation ODE solvers are usually unable to identify different branches in the first place. In addition, compared to other ODE continuation solvers, Auto-07p is computationally inexpensive to run. In contrast, MatCont and COCO are integrated in Matlab (2010) and are both accessible through their Matlab GUIs but are commensurately slower since they rely on the Matlab interpreter.

2.5 Numerical studies with Abaqus

Performing the structural analysis within the commercial FE code Abaqus (2011), eigenvalue analysis is used to predict the buckling loads and the corresponding buckling shapes (eigenmodes). The buckling load is generally used as a parameter in determining the post-buckling strength of members. From the static FE viewpoint, the eigenmode is used for describing the imperfection shape when the maximum amplitude of the imperfection is known but the distribution is not. Superposing multiple buckling shapes may be used as the initial geometric imperfection to analyse various mixed or interaction modes (Saito & Wadee, 2009). Another method is to use a stochastic process to generate signals randomly for the geometric imperfection shape. In addition, residual stresses can be also modelled as initial stress conditions where the variations of the residual stress through the thickness are given explicitly along the sections in the longitudinal direction of the member (Sarawit *et al.*, 2003). Although, to represent a true strength, it is desirable that the worst imperfection component is analysed so that safe designs can be established.

After buckling occurs, nonlinear analysis is required to investigate the load–deflection behaviour. When the loads are applied by means of prescribed displacements, and no snap-back behaviour occurs, an incremental method (where proportional loads or

displacements are applied) can be utilized. Numerical methods are inevitably employed to construct the equilibrium paths (load–displacement diagram). Incremental methods are the most widely used to determine a successive equilibrium state along the equilibrium path using an iterative procedure for a nonlinear system. The successive state can correspond to an increment of loading P or to an increment of displacement Δ, the corresponding methods respectively termed load control and displacement control incremental methods (see Figure 2.15). In the load control in-

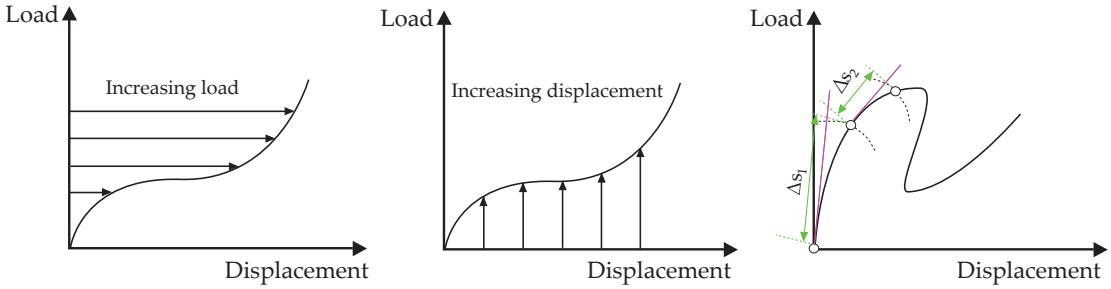

(a) (b) (c)

Figure 2.15: Numerical incremental techniques to find the nonlinear equilibrium path (load–displacement path): (a) Load control/Dead loading; (b) Displacement control/Rigid loading; (c) Arc-length method/modified Riks methods. Note that Δs_1 and Δs_2 are the arbitrary arclengths.

cremental method, Figure 2.15(a), equilibrium states are sought for various levels of loading. The load control method, however, cannot be applied to traverse past a limit point (where $\mathrm{d}P/\mathrm{d}\Delta = 0$) on an equilibrium path, even if the incremental step is reduced considerably. An alternative method, which deals with the limit point case, is based on finding successive equilibrium states corresponding to prescribed values of a displacement parameter; this method is referred to as the displacement control incremental method, Figure 2.15(b). Starting from a known equilibrium state, an unknown equilibrium state is sought for an increment in a displacement parameter; this usually stabilizes the structure unless there is snap-back present (where $\mathrm{d}\Delta/\mathrm{d}P = 0$). In other cases, the modified Riks method (an arclength method where

both loads and displacement are varied), Figure 2.15(c), can be used in order to be able to detect and go beyond limit points (Riks, 1972). The latter two approaches are effective in obtaining nonlinear static equilibrium states during the unstable phase of the response. In addition, for all methods, geometric imperfections must also be introduced to obtain some response in the buckling mode before the critical load is reached. Since Abaqus has been used extensively for studying nonlinear buckling problems successfully (Gardner & Nethercot, 2004a; Gardner & Nethercot, 2004b; Becque & Rasmussen, 2009b; Wadee *et al.*, 2010), it is used extensively in the current work, particularly for validation studies.

2.6 Experimental studies

Over the past decades a large number of experimental works have been published on the elastic behaviour of stiffened plates with small scale models. However, full-scale experimental studies of stiffened plated structures are relatively scarce. The physical tests by Murray (1973), Tulk and Walker (1976), Ghavami (1994) and Pan and Louca (1999) are some of the studies regarding the buckling behaviour of stiffened plates subjected to compression or bending. The more likely mode of failure in these experimental studies were stiffener tripping or, initially, plate buckling. However, an experimental study of a thin-walled stiffened plate conducted by Fok *et al.* (1976) focused on the case where global buckling was critical. The study investigated the effect of local elastic buckling of the stiffener outstands on the global behaviour of the stiffened plate. A simplified mathematical model was also developed, based on the post-buckling analysis of the stiffener. The imperfection sensitivity arising from the interaction of the global and the local buckling modes was also studied. Two specific small-scale tests with different lengths were presented. They also found that while the interaction occurs, the load in the equilibrium path in the post-buckling

stage reduces rapidly where the rate of unloading depended on the ratio of the local critical load P_l^{C} to the Euler (global buckling) load P_E. Moreover, the effect of a local imperfection in the stiffeners on the behaviour of the main plate was also investigated by the same authors (Fok *et al.*, 1977).

Grondin *et al.* (1999) conducted large-scale tests on twelve identical single stiffened steel plate specimens that were 2000 mm long, under axial compression and combined compression and lateral loads. The physical tests examined the behaviour of the struts for three different conditions of restraint at the unloaded longitudinal edge: fully restrained, free-end and the model with varying discrete restraints along the edge. Initial imperfections and the residual stresses were also considered in the physical experiments.

2.7 Concluding remarks

In the current study, a series of increasingly sophisticated models are presented that account for interactive buckling in axially-loaded stiffened panels including the possibility of localized and cellular buckling. The models build on existing interactive buckling work by developing a variational model based on elasticity theory to simulate the interaction between a global Euler-type mode and a local mode of buckling. Particular attention has been given to panels that exhibit highly unstable post-buckling behaviour. The models will be validated by FE models devised in Abaqus and compared against appropriate physical experiments found in the literature.

The present chapter has reviewed some of the most important research works that are relevant to the current research study. The development of plate theory was followed by a brief outline of the relevant linear and nonlinear buckling theories. Some classic works on the nonlinear interaction of different buckling modes in different

structural components, were reviewed. The more relevant approximate methods were also covered as was an outline of the numerical methods relevant to the study in the subsequent chapters. Finally, some experimental studies were highlighted, in particular, the experimental study by Fok *et al* (1976), the results from which will be compared against in Chapter 5.

Chapter 3

Cellular buckling in a perfect stiffened plate

The classic problem of a plated panel comprising a uniform flat plate stiffened by several evenly spaced blade-type longitudinal stiffeners under axial compression, made from a linear elastic material, is now studied. Under this type of loading, wide panels with many stiffeners can be divided into several struts, each with a single stiffener. These individual struts are primarily susceptible to a global (or overall) mode of instability namely Euler buckling, where flexure about the axis parallel to the main plate occurs once the theoretical global buckling load is reached. However, when the individual plate elements of the strut cross-section, namely the main plate and the stiffener, are relatively thin or slender, elastic local buckling of these may also occur; if this happens in combination with the global instability, the resulting behaviour is usually far more unstable than when the modes are triggered individually (Chilver, 1967; van der Neut, 1968; Thompson & Supple, 1973; Koiter & Pignataro, 1976; Thompson & Hunt, 1984).

The development of a variational model is presented that accounts for the interaction

between the global Euler buckling mode and the local buckling mode of the stiffener, such that the perfect elastic post-buckling response can be evaluated. At this stage, it is assumed that local buckling of the main plate does not occur. A system of nonlinear ordinary differential equations subject to integral constraints is derived and solved using the numerical continuation package Auto-07p (Doedel & Oldeman, 2011). It is indeed found that the system is highly unstable when interactive buckling is triggered; snap-backs in the response show a sequence of destabilization and restabilization that gives a progressive spreading of the initial localized buckling mode.

This latter type of response has become known in the literature as *cellular buckling* (Hunt *et al.*, 2000) or *snaking* (Burke & Knobloch, 2007) and it is shown to appear naturally in the current numerical results. This effect is particularly strong where the rotational restraint provided at the joint between the main plate and the stiffener is negligible. As far as the author is aware, this is the first time this phenomenon has been found analytically in stiffened plates undergoing Euler and local buckling simultaneously. Similar behaviour has been discovered in various other mechanical systems such as in the post-buckling of cylindrical shells (Hunt *et al.*, 2003) and the sequential folding of geological layers (Wadee & Edmunds, 2005). More recently it has also been found in the lateral buckling of thin-walled beams (Wadee & Gardner, 2012) and the flexural buckling of thin-walled columns (Wadee & Bai, 2014) both with characteristic I-sections. Moreover, cellular buckling has been captured in physical tests for some closely related structures that suffer from local–global mode interaction (Becque & Rasmussen, 2009a; Wadee & Gardner, 2012); it is revealed by the buckling elements exhibiting a continuously varying deformation wavelength. However, by increasing the rotational stiffness of the aforementioned joint, the snap-backs that characterize cellular buckling, can be moderated and the equilibrium path then shows an initially smoother response with the snap-backs appearing later in the interactive buckling process.

3.1 Analytical Model

Consider a thin-walled simply-supported plated panel that has uniformly spaced stiffeners above and below the main plate, as shown in Figure 3.1, with the associated coordinate system, where the panel length is L and the spacing between the stiffeners is b. The panel is made from a linear elastic, homogeneous and isotropic material with Young's modulus E, Poisson's ratio ν and shear modulus $G = E/[2(1+\nu)]$.

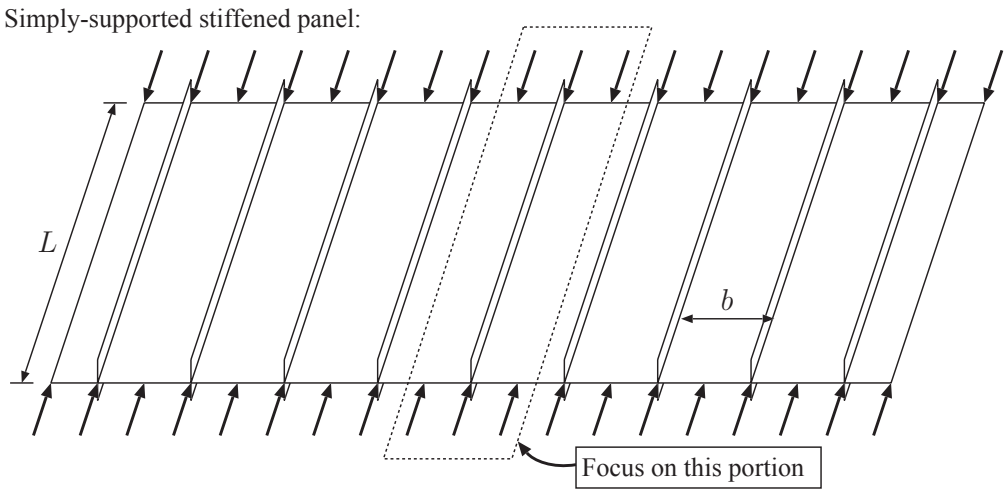

Figure 3.1: Simply-supported stiffened panel of length L.

According to Figure 2.7 for wide plates, the aspect ratio $\phi \to 0$ and therefore the local critical stresses calculated from Equation (2.26) reduces to the following equation which shows that the buckling of a wide plate is governed by the plate length only and not the width:

$$\sigma^{\mathrm{C}} = \frac{\pi^2 E}{12(1-\nu^2)(L/t)^2}. \tag{3.1}$$

A portion of the panel that is representative of its entirety can therefore be isolated as a strut, as shown in Figure 3.1, since the transverse bending curvature of the panel during buckling would be relatively small, particularly if $L \ll n_s b$, where n_s is the

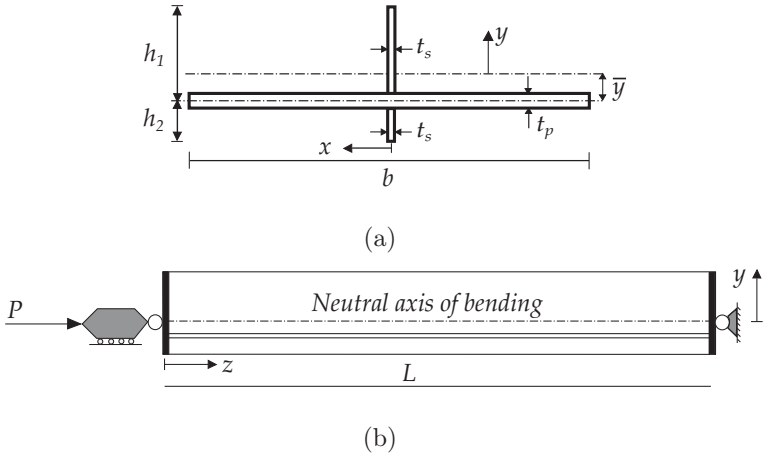

Figure 3.2: (a) Cross-section and (b) elevation of the representative panel portion compressed by a force P applied to the centroid.

number of stiffeners in the panel. The main plate (width b and thickness t_p) has upper and lower stiffeners (heights h_1 and h_2 respectively with equal thickness t_s) connected to it, as shown in Figure 3.2(a). The strut is loaded by an axial force P that is applied to the centroid of the cross-section, shown in Figure 3.2(b). Although the model is formulated for the general case with stiffeners on both sides of the main plate, the numerical results focus on the practically significant case where the stiffeners are only connected to one side of the panel, *i.e.* where $h_2 = t_p/2$.

3.1.1 Modal descriptions

In the current work, the geometries are chosen such that global buckling about the x-axis is the first instability mode encountered by the strut, before any local buckling in the main plate or stiffener occurs. The formulation for global buckling is based on small deflection assumptions, since it is well known that it has an approximately flat (or weakly stable) post-buckling response (Thompson & Hunt, 1973). The study is primarily concerned with global buckling forcing the stiffener to buckle locally shortly after or even simultaneously. It has been shown in several works (Hunt & Wadee,

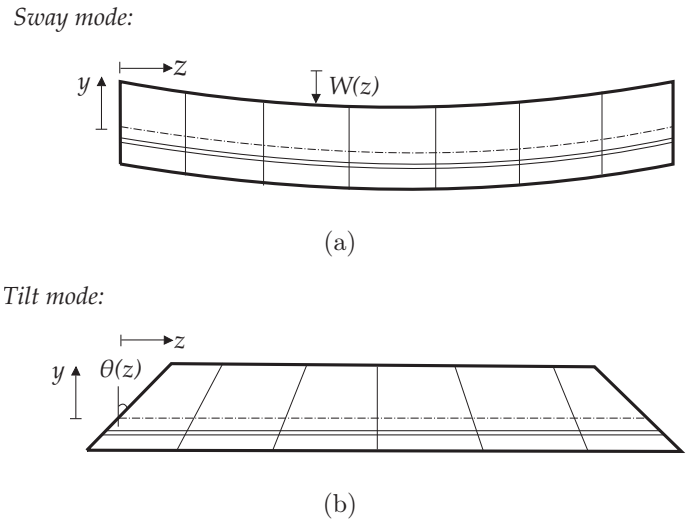

Figure 3.3: (a) Sway and (b) tilt components of the strong axis global buckling mode.

1998; Wadee *et al.*, 2010; Wadee & Gardner, 2012; Wadee & Bai, 2014) that shear strains need to be included to model the local–global mode interaction analytically. For thin-walled components, rather than, for instance, soft core materials used in sandwich structures (Wadee *et al.*, 2010), Timoshenko beam theory gives sufficiently accurate results (Wadee & Gardner, 2012). This can be applied to global flexural buckling within the framework of two degrees of freedom, known as "sway" and "tilt" in the literature (Hunt *et al.*, 1988; Hunt & Wadee, 1998). These are associated with functions describing the global lateral displacement W and the angle of inclination θ respectively defining the appropriate kinematics, as shown in Figure 3.3(a–b). From linear theory, it can be shown that $W(z)$ and $\theta(z)$ can be represented by the following expressions:

$$W(z) = -q_s L \sin\frac{\pi z}{L}, \qquad \theta(z) = q_t \pi \cos\frac{\pi z}{L}, \tag{3.2}$$

where the signs of q_s and q_t in $W(z)$ and $\theta(z)$ are representative of a "right-hand" coordinate system. The quantities q_s and q_t are the generalized coordinates of the sway and tilt components of global buckling respectively. The corresponding shear strain γ_{yz} during bending is given by the following expression:

$$\gamma_{yz} = \frac{\mathrm{d}W}{\mathrm{d}z} + \theta = -\left(q_s - q_t\right)\pi \cos\frac{\pi z}{L}, \tag{3.3}$$

of course if standard Euler–Bernoulli bending were used, then γ_{yz} would be zero and q_s would be equal to q_t. The initial global buckling displacement puts the stiffener into extra compression and it therefore becomes vulnerable to local buckling. The direction of global buckling is therefore crucially important; if the stiffener goes into extra compression and buckles locally, it can lead to catastrophic failure of the panel (Butler *et al.*, 2000), where excessive deflection can lead to a plastic collapse mechanism within the stiffener, leading to the so-called *tripping* phenomenon (Ronalds, 1989). Figure 3.4 shows this mode of failure. Plastic hinges occur at the outstand of the stiffener primarily due to the local buckles, causing overstressing of the extreme fibres.

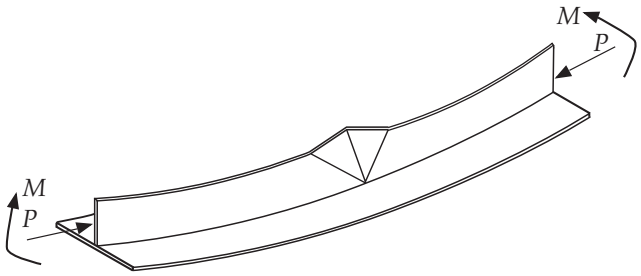

Figure 3.4: Plastic mechanism; "tripping" mode in a stiffener.

The stiffener is taken to be a flat plate (blade-type) throughout the current study. The local kinematics of the stiffener require careful consideration. A linear distribution in y for the local in-plane displacement $u(y, z)$ is assumed owing to the application of Timoshenko beam theory. The tips of the stiffeners have free edges but a rotational spring with stiffness c_p is included to model the resistance to rotation about the z-axis that the joint provides between the stiffeners and the main plate. Hence, if $c_p = 0$, the stiffeners are effectively pinned with the main plate. In the generic case ($c_p > 0$), however, the assumed out-of-plane displacement along the width of the stiffener $w_s(y, z)$ can be approximated by a function that is a summation of

trigonometric and polynomial terms. Figure 3.5 shows the form of the functions w

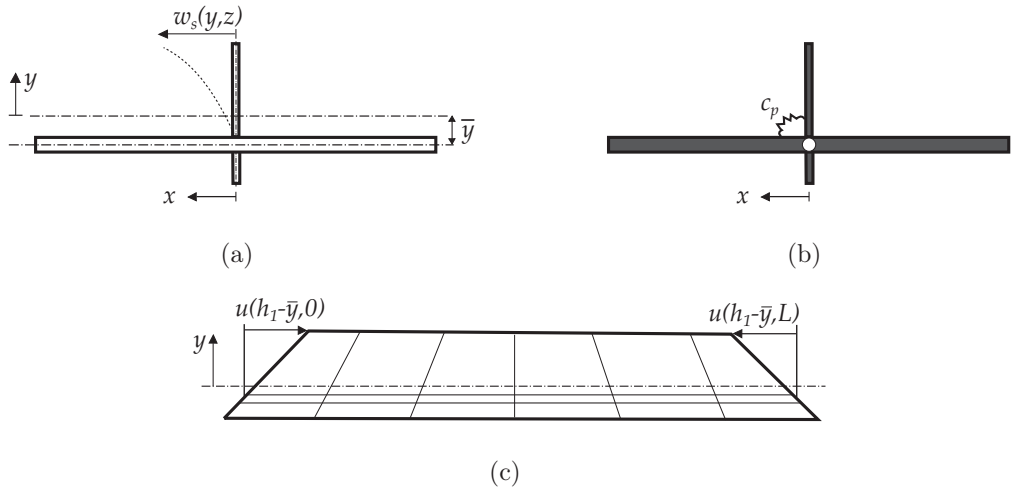

Figure 3.5: (a) Local out-of-plane displacement $w_s(y, z)$; (b) a pinned connection with an additional rotational spring of stiffness c_p to model joint fixity; (c) the local in-plane displacement $u(y, z)$.

and u with the algebraic expressions being given thus:

$$u(y,z) = Y(y)u(z), \quad w_s(y,z) = f(y)w(z), \tag{3.4}$$

where $Y(y) = (y + \bar{y})/h_1$ and

$$f(y) = B_0 + B_1 Y + B_2 Y^2 + B_3 Y^3 + B_4 \sin(\pi Y), \tag{3.5}$$

with B_0, B_1, B_2, B_3 and B_4 being constants evaluated by solving for the appropriate boundary conditions of the stiffener. The choice of shape reflects the possibility of the slope at the junction between the main plate and the stiffener being small in the less compressed zone of the stiffener. For $y = -\bar{y}$, at the junction between stiffener and the main plate, the conditions are:

$$w_s(-\bar{y},z) = 0, \quad D_s \frac{\partial^2}{\partial y^2} w_s(-\bar{y},z) = c_p \frac{\partial}{\partial y} w_s(-\bar{y},z), \tag{3.6}$$

and for $y = h_1 - \bar{y}$, the free-end, the conditions are:

$$D_s \frac{\partial^2}{\partial y^2} w_s(h_1 - \bar{y},z) = 0, \quad D_s \frac{\partial^3}{\partial y^3} w_s(h_1 - \bar{y},z) = 0, \tag{3.7}$$

where $\bar{y}$ is the location of the neutral-axis of bending measured from the centre line of the main plate, which is calculated using the standard method by equating the first moments of area:

$$\begin{aligned} A\bar{y} &= \sum_{m=1}^{n_s} A_m \bar{y}_m \\ \Rightarrow \qquad \bar{y} &= \frac{t_s \left[h_1^2 - h_2^2\right]}{2\left[(b - t_s)\, t_p + (h_1 + h_2)\, t_s\right]}. \end{aligned} \tag{3.8}$$

In this case, A is the cross-section area of one portion of the stiffened plate, which in total is divided into n_s elements. By applying the boundary conditions, the function for the deflected shape of the stiffener $w_s(y, z)$ is found to be:

$$w_s(y, z) = \left\{ Y - S_4 \frac{\pi^3}{6} \left[2Y - 3Y^2 + Y^3 - \frac{6}{\pi^3} \sin(\pi Y) \right] \right\} w(z), \tag{3.9}$$

where:

$$S_4 = \left\{ \pi \left[(D_s \pi^2)/(c_p h_1) + \pi^2/3 - 1 \right] \right\}^{-1}. \tag{3.10}$$

3.1.2 Total Potential Energy

The governing equations of equilibrium are derived from variational principles by minimizing the total potential energy V of the system. The total potential energy comprises the contributions of global and local strain energies of bending, U_{bo} and U_{bl} respectively, the strain energy stored in the "membrane" of the stiffener U_m arising from axial and shear stresses, and the work done by the external load $P\mathcal{E}$. The global bending energy accounts for the main plate and is hence given by the standard expression (Thompson & Hunt, 1973):

$$U_{bo} = \frac{1}{2} E I_p \int_0^L \ddot{W}^2 \, \mathrm{d}z = \frac{1}{2} E I_p \int_0^L q_s^2 \frac{\pi^4}{L^2} \sin^2 \frac{\pi z}{L} \, \mathrm{d}z, \tag{3.11}$$

where dots represent differentiation with respect to z and $I_p = (b - t_s)t_p^3/12 + (b - t_s)t_p\bar{y}^2$ is the second moment of area of the main plate about the global x-axis. The local bending energy U_{bl}, accounting for the stiffener only, is given by the standard expression (Allen & Bulson, 1980), thus:

$$\begin{aligned} U_{bl} &= \frac{D_s}{2}\int_0^L \int_{-\bar{y}}^{h_1-\bar{y}} \left\{ \left[\frac{\partial^2 w_s}{\partial z^2} + \frac{\partial^2 w_s}{\partial y^2}\right]^2 - 2\,(1-\nu)\left[\frac{\partial^2 w_s}{\partial z^2}\frac{\partial^2 w_s}{\partial y^2} - \left(\frac{\partial^2 w_s}{\partial z \partial y}\right)^2\right]\right\} \mathrm{d}y\,\mathrm{d}z, \\ &= \frac{D_s}{2}\int_0^L \left[\{f^2\}_y \ddot{w}^2 + \{f''^2\}_y w^2 + 2\nu\{ff''\}_y w\ddot{w} + 2(1-\nu)\{f'^2\}_y \dot{w}^2\right] \mathrm{d}z, \end{aligned} \tag{3.12}$$

where primes denote differentiation with respect to y, D_s is the plate flexural rigidity given by $Et_s^3/[12(1-\nu^2)]$ and the terms in braces, such as $\{F(y)\}_y$ are definite integrals thus:

$$\{F(y)\}_y = \int_{-\bar{y}}^{h_1-\bar{y}} F(y)\,\mathrm{d}y. \tag{3.13}$$

Here, $F(y)$ is an example function that is integrated with respect to y for the depth of the buckling stiffener. The compressive side of the panel only contributes to the local bending energy once global buckling occurs. The membrane energy U_m is derived from considering direct strains (ε) and shear strains (γ) in the stiffener. The longitudinal strain ε_z has to be modelled separately for the top and the bottom stiffener. Note that the tilt component of the in-plane displacement from the global mode is given by $u_t = y\theta$; hence:

$$\varepsilon_{z,\mathrm{global}} = \frac{\partial u_t}{\partial z} = -yq_t\frac{\pi^2}{L}\sin\frac{\pi z}{L}. \tag{3.14}$$

The local mode contribution is based on von Kármán plate theory (Bulson, 1970). A purely in-plane compressive strain Δ is also included. Assuming that b is much larger than both t_p and t_s, the value of $\bar{y}$ is relatively small. The direct strain for the main plate is given by: $\varepsilon_{zp} = -\Delta$. The combined expressions for the direct strains for the top and bottom stiffeners ε_{zt} and ε_{zb} respectively, including local and global

buckling, are:

$$\begin{aligned}\varepsilon_{zt} &= -y\ q_t\frac{\pi^2}{L}\sin\frac{\pi z}{L} - \Delta + \frac{\partial u}{\partial z} + \frac{1}{2}\left(\frac{\partial w_s}{\partial z}\right)^2, \\ &= -y\ q_t\frac{\pi^2}{L}\sin\frac{\pi z}{L} - \Delta + Y\dot{u} + \frac{1}{2}\{f^2\}_y\dot{w}^2, \\ \varepsilon_{zb} &= -y\ q_t\frac{\pi^2}{L}\sin\frac{\pi z}{L} - \Delta.\end{aligned} \tag{3.15}$$

This assumes of course that only the upper stiffener is susceptible to local buckling. The complete expression for the membrane strain energy U_m is given by:

$$\begin{aligned}U_m &= U_d + U_s \\ &= \frac{1}{2}\int_0^L \int_{-t_s/2}^{t_s/2}\left[\int_{-\bar{y}}^{h_1-\bar{y}}\left(E\varepsilon_{zt}^2 + G\gamma_{yzt}^2\right)\mathrm{d}y + \int_{-(h_2+\bar{y})}^{-\bar{y}}\left(E\varepsilon_{zb}^2 + G\gamma_{yzb}^2\right)\mathrm{d}y\right]\mathrm{d}x\,\mathrm{d}z,\end{aligned} \tag{3.16}$$

where U_d is the contribution from direct strains, which is given by the terms multiplied by the Young's modulus E; whereas U_s, the contribution arising from the shear strains, is given by the terms multiplied by the shear modulus G. The transverse component of the strain ε_y is neglected since it has been shown that it has no effect on the post-buckling stiffness of a long plate with three simply-supported edges and one free edge (Koiter & Pignataro, 1976). The total direct strain energy U_d is therefore:

$$\begin{aligned}U_d = \frac{1}{2}Et_s\int_0^L \Bigg\{ &\frac{1}{3}\left[(h_1-\bar{y})^3 + (h_2+\bar{y})^3\right]q_t^2\frac{\pi^4}{L^2}\sin^2\frac{\pi z}{L} + \Delta^2\left(h_1+h_2\right) \\ &+ \left[(h_1-\bar{y})^2 - (h_2+\bar{y})^2\right]\Delta q_t\frac{\pi^2}{L}\sin\frac{\pi z}{L} \\ &+ h_1\left[\frac{1}{3}\dot{u}^2 + \frac{1}{4h_1}\{f^4\}_y\dot{w}^4 + \left\{\frac{Yf^2}{h_1}\right\}_y\dot{u}\dot{w}^2\right] \\ &- q_t\frac{h_1\pi^2}{L}\sin\frac{\pi z}{L}\left[\left(\frac{2}{3}h_1 - \bar{y}\right)\dot{u} + \frac{1}{h_1}\{yf^2\}_y\dot{w}^2\right] \\ &- h_1\Delta\left[\dot{u} + \frac{1}{h_1}\{f^2\}_y\dot{w}^2\right] + \left(\frac{t_p}{t_s}\right)(b-t_s)\Delta^2\Bigg\}\,\mathrm{d}z.\end{aligned} \tag{3.17}$$

The shear strain energy U_s requires the shear strain γ_{yz}, which is also modelled separately for the compression and the tension side of the stiffeners. The general

expression for the shear strain γ_{yzi} in the stiffeners is thus:

$$\gamma_{yzi} = \frac{\mathrm{d}W}{\mathrm{d}z} + \theta + \frac{\partial u}{\partial y} + \frac{\partial w_s}{\partial z}\frac{\partial w_s}{\partial y}, \tag{3.18}$$

and the expressions for the top and bottom stiffeners are given respectively:

$$\begin{aligned} \gamma_{yzt} &= -\left(q_s - q_t\right)\pi \cos\frac{\pi z}{L} + \frac{u}{h_1} + \left\{ff'\right\}_y (w\dot{w}), \\ \gamma_{yzb} &= -\left(q_s - q_t\right)\pi \cos\frac{\pi z}{L}. \end{aligned} \tag{3.19}$$

The expression for U_s is therefore:

$$\begin{aligned} U_s = \frac{1}{2}Gt_s \int_0^L \Bigg\{ & \left(q_s - q_t\right)^2 \pi^2 \cos^2\frac{\pi z}{L}\left(h_1 + h_2\right) \\ & + \frac{1}{h_1}\left[u^2 + h_1\left\{\left(ff'\right)^2\right\}_y (w\dot{w})^2 + 2\left\{ff'\right\}_y (uw\dot{w})\right] \\ & - \left(q_s - q_t\right)\left[2u + 2\left\{ff'\right\}_y (w\dot{w})\right]\pi \cos\frac{\pi z}{L}\Bigg\}\,\mathrm{d}z. \end{aligned} \tag{3.20}$$

The strain energy stored in the rotational spring connecting the stiffeners to the main plate is:

$$U_{sp} = \frac{1}{2}c_p \int_0^L \left\{\frac{\partial}{\partial y} w_s(-\bar{y}, z)\right\}^2 \mathrm{d}z = \frac{1}{2}c_p \int_0^L \left[f'^2(-\bar{y})\right]\, w^2\,\mathrm{d}z, \tag{3.21}$$

where $F(-\bar{y})$ means that the example function F is evaluated at $y = -\bar{y}$. The final component to be identified is the work done by the axial load P, which is given by:

$$P\mathcal{E} = \frac{P}{2}\int_0^L \left[2\Delta + q_s^2\pi^2 \cos^2\frac{\pi z}{L} - 2\left(\frac{h_2 + \bar{y}}{h_1 + h_2}\right)\dot{u}\right]\mathrm{d}z, \tag{3.22}$$

where the end-shortening $\mathcal{E}$ comprises components from pure squash and sway from global buckling combined with the local buckling of the stiffener respectively. The total potential energy V is given by the summation of all the strain energy terms minus the work done, thus:

$$V = U_{bo} + U_{bl} + U_m + U_{sp} - P\mathcal{E}. \tag{3.23}$$

3.1.3 Variational Formulation

The governing equilibrium equations are obtained by performing the calculus of variations on the total potential energy V following a well established procedure that has been detailed in Hunt and Wadee (1998). The integrand of the total potential energy V can be expressed as the Lagrangian ($\mathcal{L}$) of the form:

$$V = \int_0^L \mathcal{L}\left(\ddot{w}, \dot{w}, w, \dot{u}, u, z\right) \mathrm{d}z. \tag{3.24}$$

The first variation of V is given by:

$$\delta V = \int_0^L \left[\frac{\partial \mathcal{L}}{\partial \ddot{w}}\delta\ddot{w} + \frac{\partial \mathcal{L}}{\partial \dot{w}}\delta\dot{w} + \frac{\partial \mathcal{L}}{\partial w}\delta w + \frac{\partial \mathcal{L}}{\partial \dot{u}}\delta\dot{u} + \frac{\partial \mathcal{L}}{\partial u}\delta u\right] \mathrm{d}z; \tag{3.25}$$

to determine the equilibrium states, V must be stationary, hence the first variation δV must vanish for any small change in w and u. Since, $\delta\ddot{w} = \mathrm{d}(\delta\dot{w})/\,\mathrm{d}z$, $\delta\dot{w} = \mathrm{d}(\delta w)/\,\mathrm{d}z$ and similarly $\delta\dot{u} = \mathrm{d}(\delta u)/\,\mathrm{d}z$, integration by parts allows δV to be expressed in terms of δw and δu only. This process develops the Euler–Lagrange equations for w and u; these comprise a fourth-order and a second-order nonlinear differential equation for w and u respectively. Differentiating the Lagrangian $\mathcal{L}$ partially with respect to the corresponding parameters gives the following expression for δV:

$$
\begin{aligned}
\delta V = \int_0^L & \left\{ D_s \left[\{f^2\}_y \ddot{w} + \nu \{f f''\}_y w \right] \right\} \delta \ddot{w} \\
& + \left\{ D_s \left[2\,(1-\nu)\,\{f'^2\}_y \dot{w} \right] + \frac{1}{2} E t_s \left[\{f^4\}_y \dot{w}^3 + 2\{Y f^2\}_y \dot{w}\dot{u} - 2\Delta \{f^2\}_y \dot{w} \right. \right. \\
& \left. - q_t \frac{\pi^2}{L} \sin\left(\frac{\pi z}{L}\right) \right] + G t_s \left[\{(f f')^2\}_y w^2 \dot{w} + \frac{1}{h_1} \{f f'\}_y w u \right. \\
& \left. \left. - (q_s - q_t)\,\pi \cos\left(\frac{\pi z}{L}\right) \{f f'\}_y w \right\} \delta \dot{w} \right. \\
& + \left\{ D_s \left[\{f''^2\}_y w + \nu \{f f''\}_y \ddot{w} \right] + G t_s \left[\{(f f')^2\}_y w \dot{w}^2 + \frac{1}{h_1} \{f f'\}_y \dot{w} u \right. \right. \\
& \left. \left. - (q_s - q_t)\,\pi \cos\left(\frac{\pi z}{L}\right) \{f f'\}_y \dot{w} \right] + c_p f'(-\bar{y})^2 w \right\} \delta w \\
& + \left\{ \frac{1}{2} E t_s h_1 \left[\frac{2}{3} \dot{u} - \Delta - q_t \frac{\pi^2}{L} \sin\left(\frac{\pi z}{L}\right) (2h_1/3 - \bar{y}) \right] - \frac{h_2 + \bar{y}}{h_1 + h_2} P \right\} \delta \dot{u} \\
& + \left\{ G t_s \left[\frac{1}{h_1} u + \frac{1}{h_1} \{f f'\}_y w \dot{w} - (q_s - q_t)\,\pi \cos\left(\frac{\pi z}{L}\right) \right] \right\} \delta u \, \mathrm{d}z.
\end{aligned}
\tag{3.26}
$$

Integrating by parts with respect to z, gives the following expression for δV:

$$
\begin{aligned}
\delta V = & \left\{ D_s \left[\{f^2\}_y \ddot{w} + \nu \{ff''\}_y w \right] \right\}_0^L \delta\dot{w} \\
& - \left\{ D_s \left[\{f^2\}_y \ddot{\dot{w}} + \nu \{ff''\}_y \dot{w} + 2(1-\nu)\{f'^2\}_y \dot{w} \right] \right. \\
& \quad + \frac{1}{2} E t_s \left[\{f^4\}_y \dot{w}^3 + 2\{Yf^2\}_y \dot{w}\dot{u} - 2\Delta \{f^2\}_y \dot{w} - q_t \frac{\pi^2}{L} \sin\left(\frac{\pi z}{L}\right) \right] \\
& \quad \left. + G t_s \left[\{(ff')^2\}_y w^2 \dot{w} + \frac{1}{h_1} \{ff'\}_y w u - (q_s - q_t)\pi \cos\left(\frac{\pi z}{L}\right) \{ff'\}_y w \right] \right\}_0^L \delta w \\
& + \left\{ \frac{1}{2} E t_s h_1 \left[\frac{2}{3}\dot{u} - \Delta - q_t \frac{\pi^2}{L} \sin\left(\frac{\pi z}{L}\right)(2h_1/3 - \bar{y}) \right] - \frac{h_2 + \bar{y}}{h_1 + h_2} P \right\}_0^L \delta u \\
& + \int_0^L \left\{ D_s \left[\{f^2\}_y \ddot{\ddot{w}} + 2\nu \{ff''\}_y \ddot{w} - 2(1-\nu)\{f'^2\}_y \ddot{w} + \{f''^2\}_y w \right] \right. \\
& \quad - \frac{1}{2} E t_s \left[\{f^4\}_y (3\dot{w}^2 \ddot{w}) + 2\{Yf^2\}_y (\ddot{w}\dot{u} + \dot{w}\ddot{u}) - 2\Delta \{f^2\}_y \ddot{w} - q_t \frac{\pi^3}{L^2} \cos\left(\frac{\pi z}{L}\right) \right] \\
& \quad - G t_s \left[\{(ff')^2\}_y (w\dot{w}^2 + w^2 \ddot{w}) + \frac{1}{h_1} \{ff'\}_y w\dot{u} \right. \\
& \quad \left. \left. + (q_s - q_t) \frac{\pi^2}{L} \{ff'\}_y \sin\left(\frac{\pi z}{L}\right) w \right] + c_p f'(-\bar{y})^2 w \right\} \delta w \, \mathrm{d}z \\
& + \int_0^L \left\{ \frac{1}{2} E t_s h_1 \left[-\frac{2}{3}\ddot{u} + q_t \frac{\pi^3}{L^2} \cos\left(\frac{\pi z}{L}\right)(2h_1/3 - \bar{y}) \right] \right. \\
& \quad \left. - G t_s \left[\frac{1}{h_1} u + \frac{1}{h_1} \{ff'\}_y w\dot{w} - (q_s - q_t)\pi \cos\left(\frac{\pi z}{L}\right) \right] \right\} \delta u \, \mathrm{d}z.
\end{aligned}
\tag{3.27}
$$

The variables are now rescaled with respect to the non-dimensional spatial coordinate $\tilde{z}$, defined as $\tilde{z} = 2z/L$. Similarly, non-dimensional out-of-plane and in-plane displacements $\tilde{w}$ and $\tilde{u}$ are defined with the scalings $2w/L$ and $2u/L$ respectively. Note that the scalings exploit symmetry about the midspan and the equations are hence solved for half the strut length; this assumption has been shown to be acceptable for cases where global buckling is critical (Wadee, 2000) as well as for the cases where local buckling is critical and L is much larger than the local buckling wavelength. The non-dimensional differential equations are thus:

$$
\begin{aligned}
&\ddot{\tilde{w}} + \frac{L^2}{2\{f^2\}_y}\left[\nu\{ff''\}_y - (1-\nu)\{f'^2\}_y\right]\ \ddot{\tilde{w}} + \tilde{k}\tilde{w} - \tilde{D}\left[\frac{\{f^4\}_y}{\{f^2\}_y}\left(3\tilde{\dot{w}}^2\ddot{\tilde{w}}\right)\right.\\
&\left.+\frac{\{2Yf^2\}_y}{\{f^2\}_y}\left(\tilde{\ddot{u}}\tilde{\dot{w}} + \tilde{\dot{w}}\tilde{\ddot{u}}\right) - 2\Delta\ddot{\tilde{w}} - 2\ q_t\frac{\pi^2}{L}\frac{\{yf^2\}_y}{\{f^2\}_y}\left(\sin\frac{\pi\tilde{z}}{2}\ddot{\tilde{w}} + \frac{\pi}{2}\cos\frac{\pi\tilde{z}}{2}\tilde{\dot{w}}\right)\right]\\
&- \frac{\tilde{G}L^2\tilde{w}}{2\{f^2\}_y}\left[\left\{(ff')^2\right\}_y\left(\tilde{\dot{w}}^2 + \tilde{w}\tilde{\ddot{w}}\right) + \frac{1}{h_1}\{ff'\}_y\tilde{\dot{u}} + (q_s - q_t)\pi^2\{ff'\}_y\sin\frac{\pi\tilde{z}}{2}\right] = 0,
\end{aligned}
\tag{3.28}
$$

$$
\begin{aligned}
&\tilde{\ddot{u}} - \frac{3}{4}\frac{\tilde{G}}{\tilde{D}}\psi\left\{\psi\left[\tilde{u} + \{ff'\}_y\left(\tilde{w}\tilde{\dot{w}}\right)\right] - 2\pi\left(q_s - q_t\right)\cos\frac{\pi\tilde{z}}{2}\right\} - \left\{\frac{3Y}{h_1}f^2\right\}_y\left(\tilde{\dot{w}}\tilde{\dot{w}}\right)\\
&+\frac{1}{2}\ q_t\pi^3\left(\psi - \frac{3\bar{y}}{2L}\right)\cos\frac{\pi\tilde{z}}{2} = 0,
\end{aligned}
\tag{3.29}
$$

where the rescaled quantities are:

$$
\tilde{D} = Et_sL^2/8D_s, \quad \tilde{G} = Gt_sL^2/8D_s, \quad \tilde{k} = \frac{L^4}{16\{f^2\}_y}\left[\left\{f''^2\right\}_y + c_pf'^2(-\bar{y})/D_s\right],
\tag{3.30}
$$

with $\psi = L/h_1$ and $f'^2(-\bar{y})$ is as described previously. Equilibrium also requires the minimization of the total potential energy with respect to the generalized coordinates Δ, q_s and q_t leading to the three integral equations in nondimensional form:

$$
\begin{aligned}
\frac{\partial V}{\partial\Delta} &= \Delta\left[1 + \frac{h_2}{h_1} + \frac{t_p(b-t_s)}{t_s}\right] - \frac{P}{Et_sh_1} + q_t\frac{\pi}{h_1L}\left[(h_1 - \bar{y})^2 - (h_2 + \bar{y})^2\right]\\
&\quad - \frac{1}{4}\int_0^2\left[\tilde{\dot{u}} + \frac{1}{h_1}\left\{f^2\right\}_y\left(\tilde{\dot{w}}^2\right)\right]\mathrm{d}\tilde{z} = 0,\\
\frac{\partial V}{\partial q_s} &= \pi^2q_s + \tilde{s}\left(q_s - q_t\right) - \frac{PL^2}{EI_p}q_s - \frac{\tilde{s}\tilde{\phi}}{2\pi}\int_0^2\cos\frac{\pi\tilde{z}}{2}\left[\tilde{u} + \{ff'\}_y\left(\tilde{w}\tilde{\dot{w}}\right)\right]\mathrm{d}\tilde{z} = 0,\\
\frac{\partial V}{\partial q_t} &= \pi^2q_t + \tilde{\Gamma}_3\Delta - \tilde{t}\left(q_s - q_t\right) - \frac{1}{2}\int_0^2\left\{\sin\frac{\pi\tilde{z}}{2}\left[\tilde{\Gamma}_1\tilde{\ddot{u}} + \tilde{\Gamma}_2\left(\tilde{\dot{w}}^2\right)\right]\right.\\
&\quad \left.- \frac{\tilde{t}\tilde{\phi}}{\pi}\cos\frac{\pi\tilde{z}}{L}\left[\tilde{u} + \{ff'\}_y\left(\tilde{w}\tilde{\dot{w}}\right)\right]\right\}\mathrm{d}\tilde{z} = 0,
\end{aligned}
\tag{3.31}
$$

where the rescaled quantities are:

$$\begin{aligned}
\tilde{\Gamma_1} &= \frac{Lh_1\left(2h_1-3\bar{y}\right)}{\left(h_1-\bar{y}\right)^3+\left(h_2+\bar{y}\right)^3}, & \tilde{\Gamma_2} &= \frac{3L\left\{yf^2\right\}_y}{\left(h_1-\bar{y}\right)^3+\left(h_2+\bar{y}\right)^3},\\
\tilde{\Gamma_3} &= \frac{6L\left[\left(h_1-\bar{y}\right)^2-\left(h_2+\bar{y}\right)^2\right]}{\pi\left[\left(h_1-\bar{y}\right)^3+\left(h_2+\bar{y}\right)^3\right]}, & \tilde{\phi} &= \frac{L}{h_1+h_2},\\
\tilde{s} &= \frac{Gt_s(h_1+h_2)L^2}{EI_p}, & \tilde{t} &= \frac{3GL^2(h_1+h_2)}{E\left[\left(h_1-\bar{y}\right)^3+\left(h_2+\bar{y}\right)^3\right]}.
\end{aligned} \tag{3.32}$$

Since the strut is an integral member, the relationships in Equation (3.31) provide a mathematical link between q_s and q_t before any interactive buckling occurs, *i.e.* when $w = u = 0$. The boundary conditions for $\tilde{w}$ and $\tilde{u}$ and their derivatives are for simply-supported conditions at $\tilde{z} = 0$ and for symmetry conditions at $\tilde{z} = 1$:

$$\tilde{w}(0) = \tilde{\ddot{w}}(0) = \tilde{\ddot{w}}(1) = \tilde{\ddot{w}}(1) = \tilde{u}(1) = 0, \tag{3.33}$$

with a further condition from matching the in-plane strain:

$$\frac{1}{3}\tilde{\ddot{u}}(0) + \frac{1}{2}\left\{\frac{Y}{h_1}f^2\right\}_y \tilde{\dot{w}}^2(0) - \frac{1}{2}\Delta + \frac{P}{Et_sh_1}\left(\frac{h_2+\bar{y}}{h_1+h_2}\right) = 0. \tag{3.34}$$

This final condition is derived from the term outside the integral and multiplied by δu in the expression for δV in Equation (3.27). It is also worth noting that the terms in braces in Equations (3.28)–(3.34) are integrated with respect to the original definition of y.

Linear eigenvalue analysis for the perfect strut ($q_{s0} = q_{t0} = A_0 = 0$) is conducted to determine the critical load for global buckling P_o^{C}. By considering the Hessian matrix $\mathbf{V}_{ij}$, thus:

$$\mathbf{V}_{ij} = \begin{bmatrix} \frac{\partial^2 V}{\partial q_s^2} & \frac{\partial^2 V}{\partial q_s \partial q_t} \\ \frac{\partial^2 V}{\partial q_t \partial q_s} & \frac{\partial^2 V}{\partial q_t^2} \end{bmatrix} \tag{3.35}$$

at the critical load, with the pre-buckling condition $q_s = q_t = w = u = 0$, the matrix is singular. Hence, the critical load for global buckling is:

$$P_o^{\mathrm{C}} = \frac{\pi^2 EI_p}{L^2}\left[1 + \frac{\tilde{s}}{\pi^2+\tilde{t}}\right]. \tag{3.36}$$

If the limit $G \to \infty$ is taken, a primary assumption in Euler–Bernoulli bending theory, P_o^{C} reduces to the expected classical Euler column buckling load for the properties of the stiffened plate considered.

3.2 Numerical results

The full system of equilibrium equations are difficult to solve analytically. The continuation and bifurcation software Auto-07p (Doedel & Oldeman, 2011) is thus used; it has been shown in previous works (Hunt & Wadee, 1998; Wadee & Gardner, 2012) to be an ideal tool to solve the equations for this kind of mechanical system. The solver is adept at locating bifurcation points and tracing branching paths as model parameters are varied. Numerical examples, representing the perfect behaviour of the strut, are shown in this section for the cases where global buckling is critical. In the current chapter, a fixed set of cross-section and material properties are chosen and are given in Table 3.1 (see Figure 3.2(a)).

Column length L	5000 mm
Plate breadth b	120 mm
Plate thickness t_p	2.4 mm
Stiffener depth(top) h_1	38 mm
Stiffener depth(bottom) h_2	1.2 mm
Stiffener thickness t_s	1.2 mm
Young's modulus E	210 kN/mm^2
Poisson's ratio ν	0.3

Table 3.1: Cross-section and material properties of an example stiffened plate used in the numerical study.

The global critical load P_o^{C} can be calculated using Equation (3.36), whereas the local

buckling critical stress σ_l^{C} can be evaluated using the well-known formula in Equation (2.26), where the coefficient k_p depends on the plate boundary conditions; limiting values being $k_p = 0.426$ and $k_p = 1.247$ for a long stiffener connected to the main plate with one edge free and the edge defining the junction between the stiffener and the main plate being taken to be pinned and fixed respectively (Bulson, 1970). For the panel geometry selected, Table 3.2 shows that global buckling is critical and that the stiffener could be next, to buckle locally since the local buckling stress of the main plate is much higher than that of the stiffener.

	σ_o^{C} (N/mm^2)	$\sigma_{l,s}^{\mathrm{C}}$ (N/mm^2)	$\sigma_{l,p}^{\mathrm{C}}$ (N/mm^2)	Critical mode
Pinned junction	4.89	80.22	309.85	Global
Fixed junction	4.89	236.02	539.91	Global

Table 3.2: Theoretical values of the global and local critical buckling stresses (σ_o^{C} and σ_l^{C}) respectively; subscripts "p" and "s" refer to the main plate and the stiffener respectively. The expression for $\sigma_o^{\mathrm{C}} = P_o^{\mathrm{C}}/A$, where A is the cross-sectional area of the strut.

3.2.1 Solution strategy

The current study comprises an analysis of a system of nonlinear non-autonomous ordinary differential equations (ODEs) subject to boundary conditions and integral constraints. To solve such equations, Auto computes families of equilibrium solutions and computes the stability of those solutions along these families (Doedel & Oldeman, 2011). The solver can also locate folds, branch points and bifurcations to tori along families of periodic solutions. Branch switching is possible at bifurcation points. This latter feature is important in the current investigation since the expected cellular behaviour comprises a secondary bifurcation followed by a sequence of limit points in the post-buckling range. The software package can also identify more complex critical points such as Hopf bifurcations, and period doubling bifurcations, which shows its

versatility in solving nonlinear problems, although some of these features are not particularly relevant to the current problem.

To solve the governing equations, the principal parameters used in the numerical continuation procedure in Auto-07p were interchangeable although generally q_s was varied for computing the equilibrium paths for the distinct buckling modes. However, the load P was used as the principal continuation parameter for computing the interactive buckling paths. Since the critical load was obtained analytically from Equation (3.36), the post-buckling path was generated from P_o^{C} and many bifurcation points were detected on the weakly stable post-buckling path. Initially, using a continuation method, the lowest value of q_s was determined at the location of the secondary bifurcation point S called q_s^{S}. Subsequently, the second run started from S using the branch switching function, after which the full equilibrium path was obtained with a sequence of snap-backs (in small values of c_p) when the interaction between the global and the local modes occurred. Figure 3.6(a) shows the procedure diagrammatically.

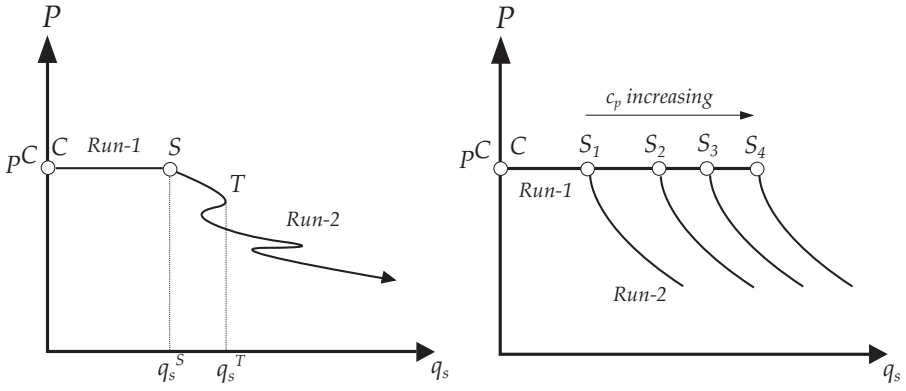

(a) (b)

Figure 3.6: (a) Diagrammatic representation of the sequence for computing the equilibrium paths for the perfect case; (b) shows the perfect case for different values of c_p with the corresponding secondary bifurcation points S_i as c_p is increased.

Moreover, the graph in Figure 3.6(b) shows the perfect case for different values of c_p with the corresponding secondary bifurcation points as c_p is increased. Figure 3.7

also presents a flowchart for the procedure for both perfect and imperfect cases when

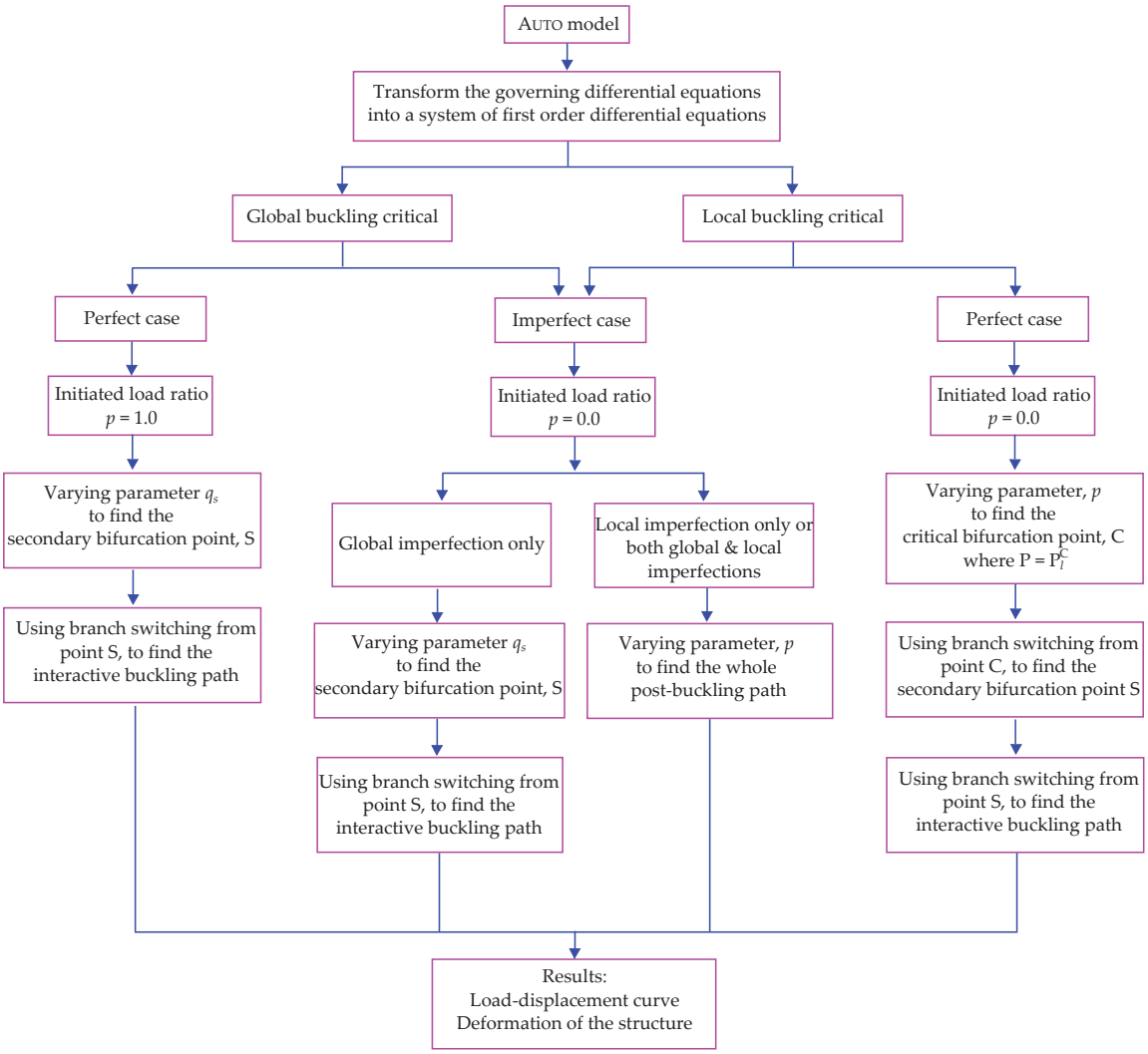

Figure 3.7: Numerical continuation procedure in Auto-07p to find the equilibrium paths for perfect and imperfect cases when the global or local buckling mode is critical.

the global or local buckling mode is critical.

Beyond this point, a new equilibrium path describing local–global interactive buckling was found. Typically, this reduced the load P with w and u becoming non-trivial as the interaction advanced. On the interactive buckling path, a progressive sequence of destabilization and restabilization, exhibited as a series of snap-backs in the equi-

librium paths was observed – the signature of cellular buckling (Hunt *et al.*, 2000; Wadee & Edmunds, 2005; Wadee & Gardner, 2012; Wadee & Bai, 2014). In Figure 3.6, the first such snap-back is labelled as T with $q_s = q_s^{\mathrm{T}}$ and the existence of it marks the beginning of the rapid spreading of the buckling profile from being initially localized to being eventually completely periodic.

3.2.2 Results and discussion

In the current section, the numerical results from the analytical solutions are presented. Initially the stiffness of the rotational spring c_p is set to be zero which defines a fully-pinned connection between the main plate and the stiffener. Later, by increasing c_p, semi-rigid and fully rigid connections are considered.

For the example being considered, Figure 3.8 shows equilibrium plots of the normalized axial load $p = P/P_o^{\mathrm{C}}$ versus (a) the generalized coordinates of the sway component q_s and (b) the maximum out-of-plane normalized deflection of the buckled stiffener ($w_{\max}/t_s$). The graphs in Figure 3.9(a) show the relative amplitudes of the global and local buckling modes and the graph in (b) plots the relationship between the sway q_s and tilt q_t components of the global buckling mode, which are almost equal; this indicates that the shear strain is small but, importantly, not zero. The second, fourth, sixth and the eighth cells are labelled as C_2, C_4, C_6 and C_8 respectively, which are generated from the initial buckling point C labelled in the corresponding graphs. Figure 3.10 illustrates the corresponding progression of the numerical solutions for the local buckling functions w and u for the secondary bifurcation S and the cells C_2 to C_8. One of the most distinctive features of the equilibrium path for pinned (*i.e.* $c_p = 0$ Nmm/mm) and semi-rigid (*i.e.* c_p less than 1000 Nmm/mm) cases, as shown in Figures 3.8 and 3.9, is the sequence of snap-backs that effectively separates the equilibrium path into 10 individual parts (or cells) in total, as shown.

Each path or cell corresponds to the formation of a new local buckling displacement peak or trough. Figure 3.11 shows a selection of 3-dimensional representations of the deflected stiffened plate at a specific state on paths C_2, C_4, C_6 and C_8. The results for this example clearly show cellular buckling with the spiky features in the graphs shown in Figures 3.8 and 3.9. Moreover, the buckling patterns, as seen in Figure 3.11, clearly show an initially localized buckle gradually spreading outwards from the panel midspan with more peaks and troughs. The maximum out-of-plane displacement $w_{\max}$ approaches a value of 1.65 mm, which is of the order of t_s (1.2 mm) and shows that the local stiffener deflections are large, thereby justifying the incorporation of von Kármán plate theory within the model (Timoshenko & Woinowsky-Krieger, 1959).

In the literature (Hunt *et al.*, 2000; Wadee & Edmunds, 2005) the Maxwell load (P^{M}) is calculated for snaking problems, which represents a realistic lower bound strength for the system. Presently, however, it is more complex to determine such a quantity because the system axial load P does not oscillate about a fixed load P^{M} as the deformation increases. This is primarily owing to the fact that, unlike systems that exhibit cellular buckling, such as cylindrical shells and confined layered structures (Hunt *et al.*, 2000), there are two effective loading sources as the mode interaction takes hold: the axial load P, which generally decreases and the sinusoidally varying (in z) tilt generalized coordinate q_t, which represents the axial component of the global buckling mode that generally increases. The notion of determining the "body force", discussed in Hunt and Wadee (1998), could be used as way to calculate the Maxwell load, but this has been left for future work.

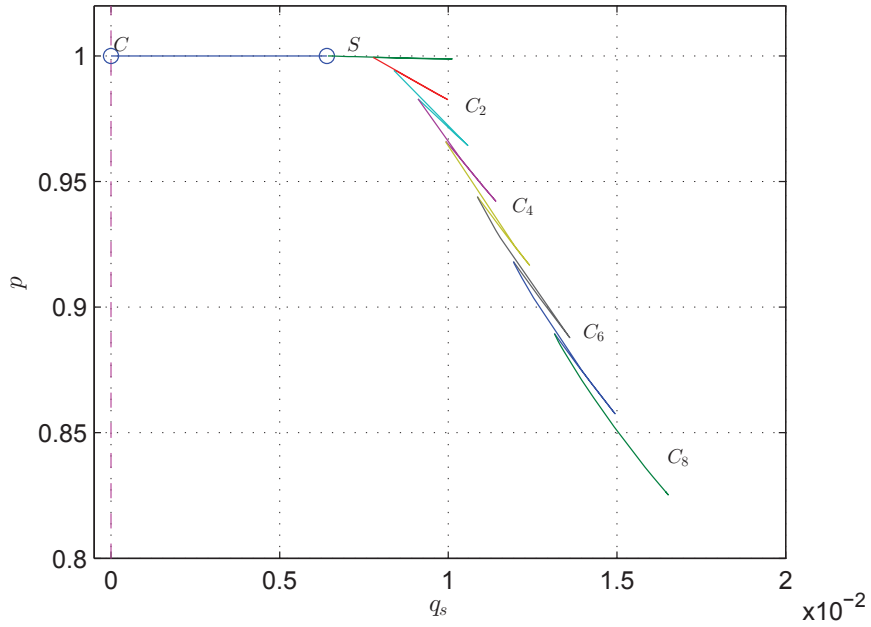

(a)

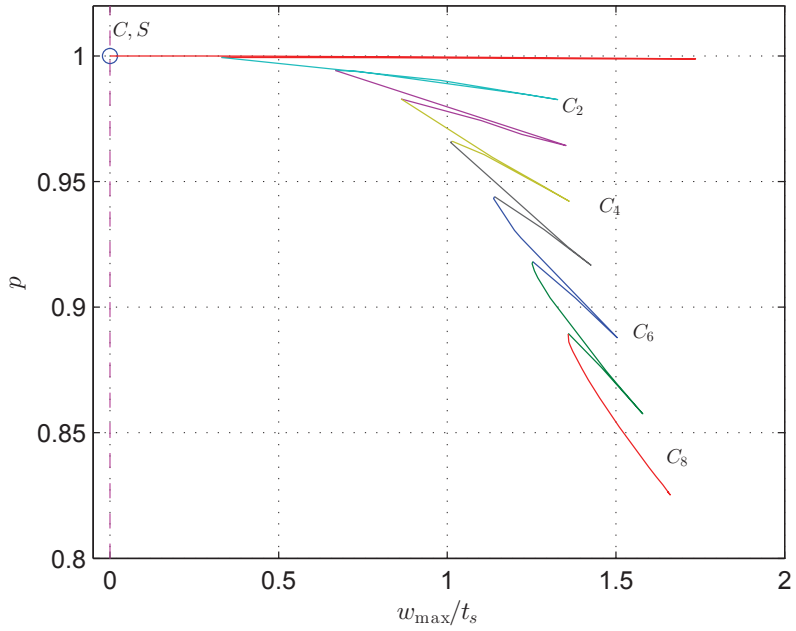

(b)

Figure 3.8: Numerical equilibrium paths with $c_p = 0$ Nmm/mm: normalized force ratio p $(= P/P_o^{\mathrm{C}})$ versus (a) the sway amplitude q_s and (b) the normalized maximum out-of-plane deflection of the stiffener $w_{\max}/t_s$.

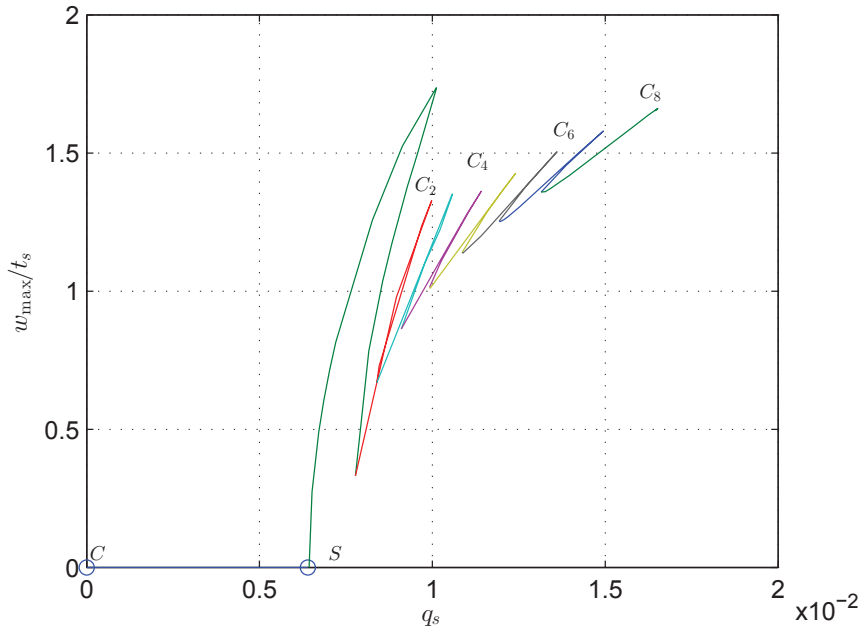

(a)

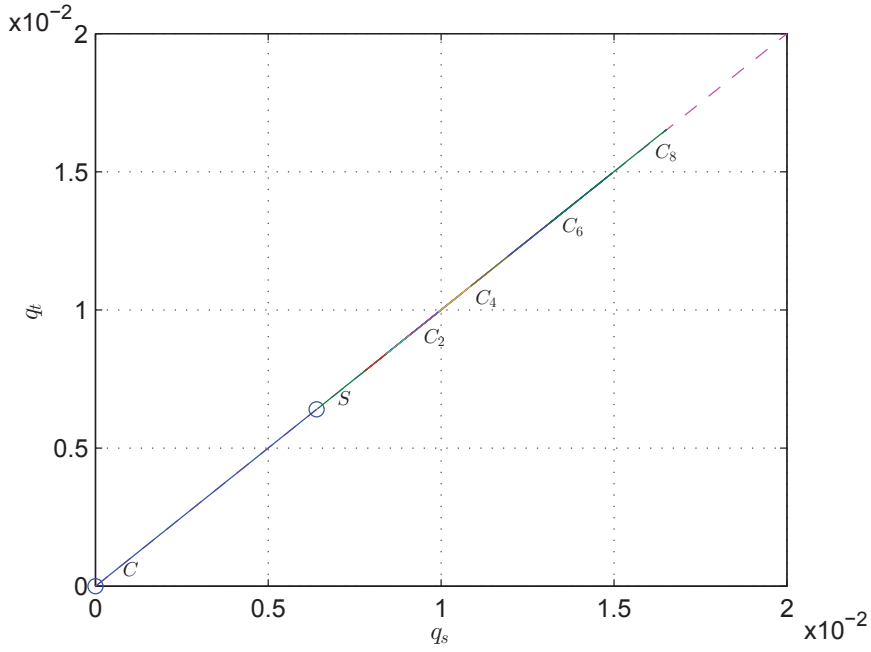

(b)

Figure 3.9: Numerical equilibrium paths for $c_p = 0$ Nmm/mm: (a) local versus global modes: $w_{\max}/t_s$ versus q_s; (b) amplitudes of sway q_s versus tilt q_t with the dashed line showing $q_s = q_t$.

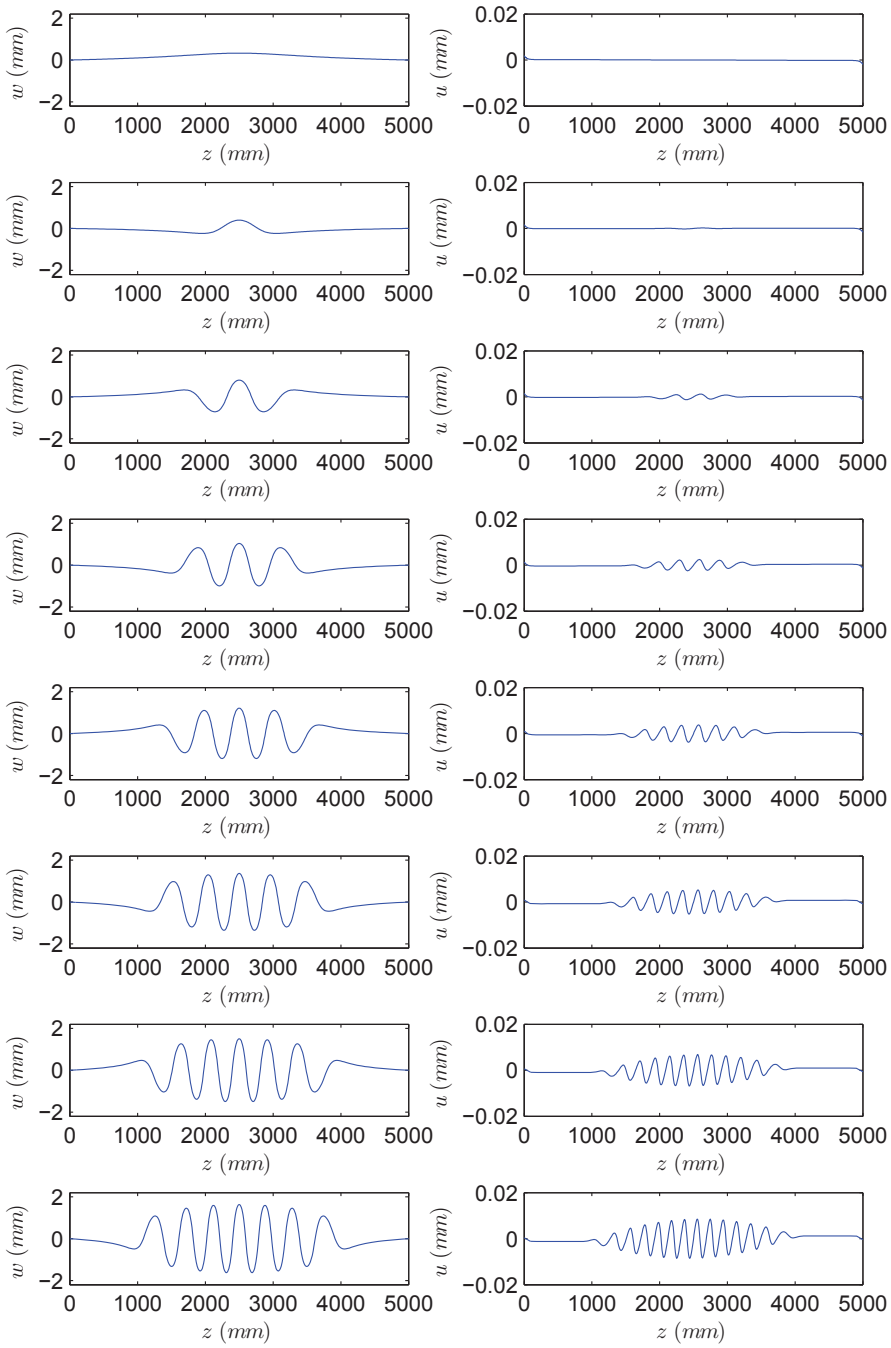

Figure 3.10: Numerical solutions for the stiffener local out-of-plane displacement w (left) and local in-plane displacement u (right) with $c_p = 0$ Nmm/mm for the equilibrium paths at the secondary bifurcation point S and cells C_2–C_8 from top to bottom respectively.

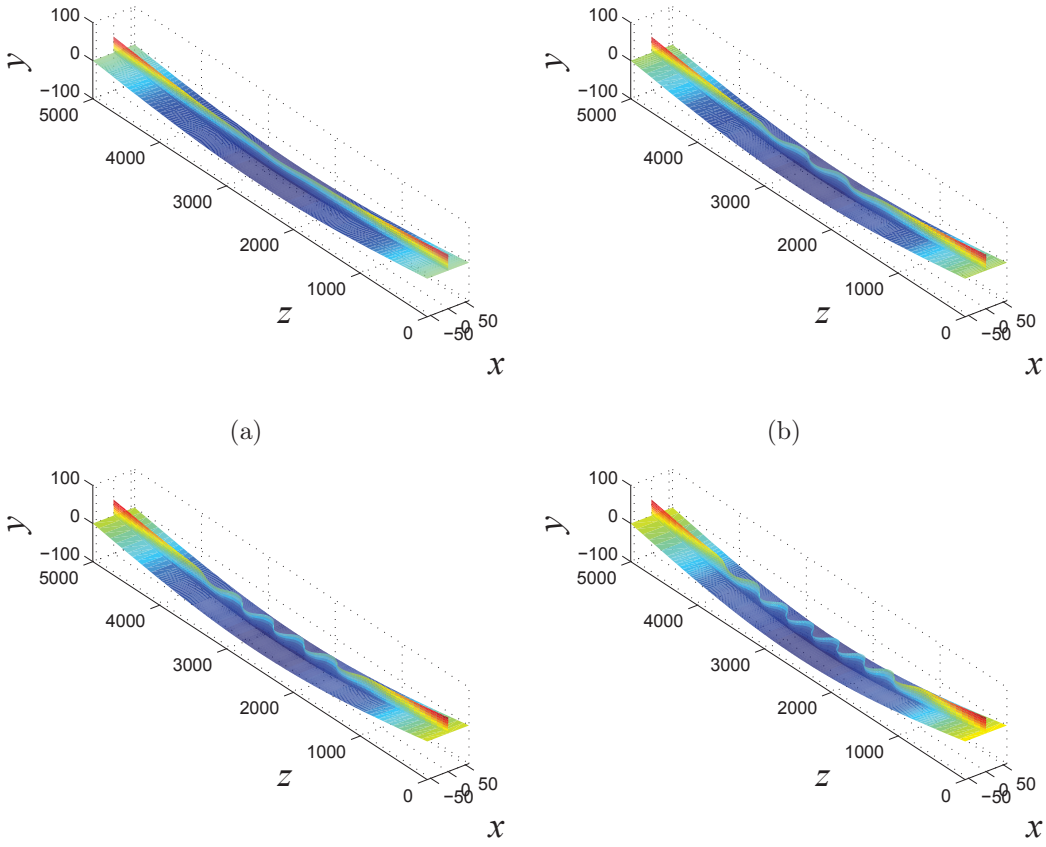

(a) (b)

(c) (d)

Figure 3.11: Numerical solutions from the analytical model with $c_p = 0$ Nmm/mm visualized on 3-dimensional representations of the strut for (a) cell C_2 ($p = 0.9995$), (b) cell C_4 ($p = 0.9829$), (c) cell C_6 ($p = 0.9440$) and (d) cell C_8 ($p = 0.8894$). All dimensions are in millimetres, but the local buckling displacements in the stiffener are scaled by a factor of 5 to aid visualization.

Hitherto, the results have been presented for the case where the joint between the main plate and the stiffener was pinned ($c_p = 0$). Figure 3.12 shows how the introduction of the joint stiffness affects the response. First of all, the value of $\sigma_{l,s}^{\mathrm{C}}$ is increased since rotation at the joint is more restrained. This, in turn, increases the value of q_s^{S} and q_s^{T} at different rates, as shown in Figure 3.13(a). It can be seen that as c_p

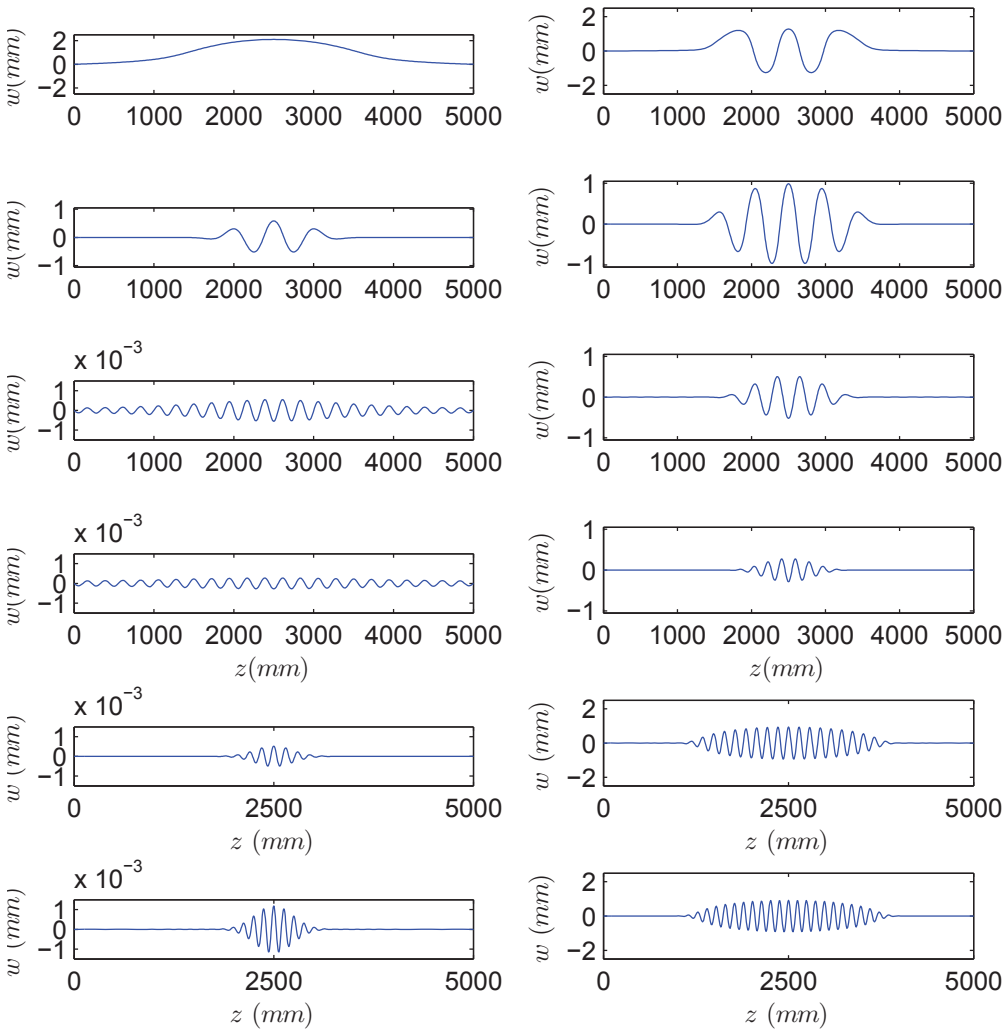

(a) $p = 0.99$ (b) $p = 0.96$

Figure 3.12: (a–b) Numerical solutions from the analytical model for the local out-of-plane deflection w in the initial interactive buckling stage, where cases for $c_p = 0, 10, 10^2, 10^3, 10^4$ Nmm/mm and when $c_p \to \infty$ are shown from top to bottom respectively.

is increased the initial interactive mode that emerges from the secondary bifurcation S is more localized with a smaller wavelength (Figure 3.12) and resembles the more advanced cells shown in Figure 3.10 directly. Moreover, it is demonstrated that the snap-backs occur later in the interactive buckling process.

As expected, the cellular buckling behaviour in the post-buckling response, is rapidly eroded by increasing the rotational stiffness. In other words, by comparing the equilibrium paths against the equilibrium paths when $c_p = 0$ Nmm/mm, it is observed that the snap-backs start to vanish from the first cell to the last, as c_p increases. For larger values of c_p (*i.e.* $c_p \geq 1000$ Nmm/mm), no cellular behaviour is observed in the post-buckling paths. Figure 3.13(b) shows the normalized axial load p versus the normalized total end-shortening, $\mathcal{E}/L$, that is given by the Equation (4.32). It is observed that the total end-shortening increases significantly, when $c_p \to \infty$. Figure 3.13(c) shows the global versus the local amplitude of deflections for different values of c_p. For the normalized maximum local out-of-plane displacement $w_{\max}/t_s$, the post-buckling path shows a stiffer response for higher values of c_p. At $p = 0.85$, the normalized maximum out-of-plane displacement $w_{\max}/t_s$ is decreased by 39% from 1.742 when $c_p = 0$ to 1.068 when $c_p \to \infty$ approximately. Figure 3.13(d) shows p versus q_s. It is observed that the position of the secondary bifurcation point S is increased by 71% from 0.0064 for the pinned case ($c_p = 0.0$ Nmm/mm) to 0.0215 for the rigid case ($c_p \to \infty$) approximately. In addition, as c_p increases, a significant reduction in both the amplitude and the wavelengths of the local displacement is observed at the same load level. The interactive buckling wavelength Λ can also be then compared, which is defined in Figure 3.14. It is found that the wavelength Λ is 205.73 mm and 62.6 mm at $p = 0.89$ for $c_p = 0$ and when $c_p \to \infty$ respectively, showing a reduction of approximately 70%.

The detailed numerical results are also presented when the rotational spring stiffness $c_p > 0$. In these cases, the joint between the main plate and the stiffener is considered

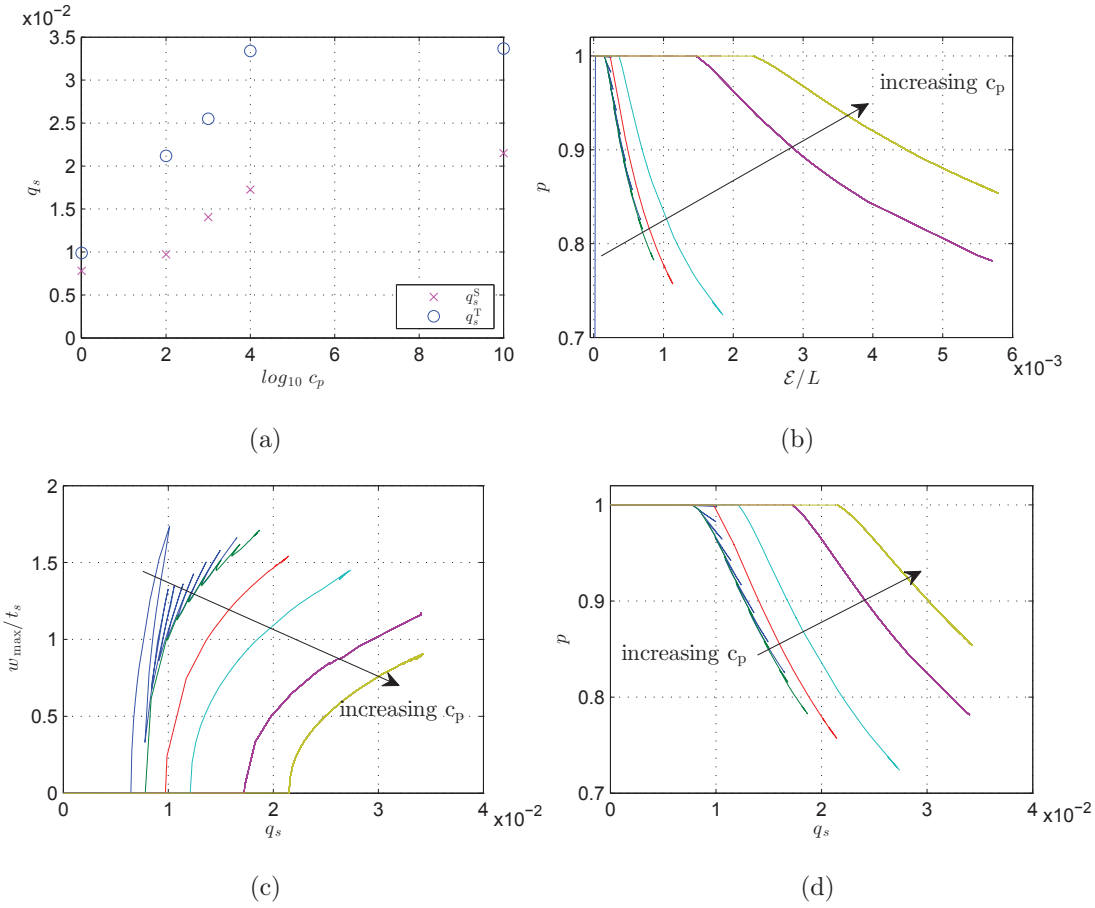

Figure 3.13: Variation of the equilibrium paths for increasing rigidities of the main plate–stiffener joint ($c_p = 1, 10^2, 10^3, 10^4$ Nmm/mm and $c_p \to \infty$). Graphs show (a) the distribution of q_s^{S} and q_s^{T} by increasing c_p value. (b) The normalized force ratio p ($= P/P_o^{\mathrm{C}}$) versus the normalized end-shortening $\mathcal{E}/L$, (c) the local mode amplitude $w_{\max}/t_s$, (d) the global mode amplitude q_s for the increasing values of c_p given in (a). Note that in (b–d) the pinned case ($c_p = 0$) is included.

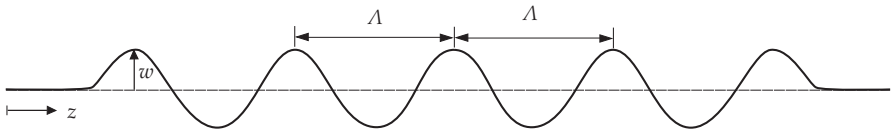

Figure 3.14: Definition of local buckling wavelength Λ from the variational model.

as a semi-rigid connection when c_p=1, 10, 10^2 and 10^4 Nmm/mm and effectively a fully-fixed junction when c_p tends to infinity. For the case where $c_p \to \infty$, the strain energy due to the rotational spring tends to zero since the relative rotation between the stiffener and the main plate tends to zero. The parameter S_4 in the stiffener deflection function given in Equation (3.10) is therefore:

$$\begin{aligned} \lim_{c_p \to \infty} S_4 &= \lim_{c_p \to \infty} \frac{3c_p h_1}{3D_s\pi^3 + c_p h_1 \pi^3 - 3\pi c_p h_1} \\ &= \frac{3}{\pi(\pi^2 - 3)} \\ &\approx 0.13901. \end{aligned} \tag{3.37}$$

Figures 3.15–3.26 illustrate the equilibrium paths when c_p is set to be 1, 10, 10^2 and 10^4 Nmm/mm and when $c_p \to \infty$ respectively. According to the results, it is found that the effect of the snap-backs is reduced by increasing the spring stiffness and it turns into a smooth path when a fully-fixed junction is considered between the main plate and the stiffener. Figure 3.17 illustrates the corresponding progression of the numerical solutions for the local buckling functions w and u at the secondary bifurcation point S and cells C_2–C_{10} from top to bottom. Figure 3.18 shows a selection of 3-dimensional representations of the deflected stiffened plate at a specific state on paths S, C_2 to C_4, C_6, C_8 and C_{10}. Figures 3.19, 3.21, 3.23 and 3.25 are identical to Figure 3.15 but are for cases of c_p = 10, 10^2 and 10^4 Nmm/mm and $c_p \to \infty$ respectively. In addition, Figures 3.20, 3.22, 3.24 and 3.26 are identical to Figure 3.16 but are for cases of c_p = 10, 10^2 and 10^4 Nmm/mm and $c_p \to \infty$ respectively. Moreover, Figures 3.27 and 3.28 present the local out-of-plane deflection profiles w as well as local in-plane deflection of the stiffener u and the corresponding 3-dimensional representations of the deflected stiffened plate respectively, for the case where $c_p \to \infty$.

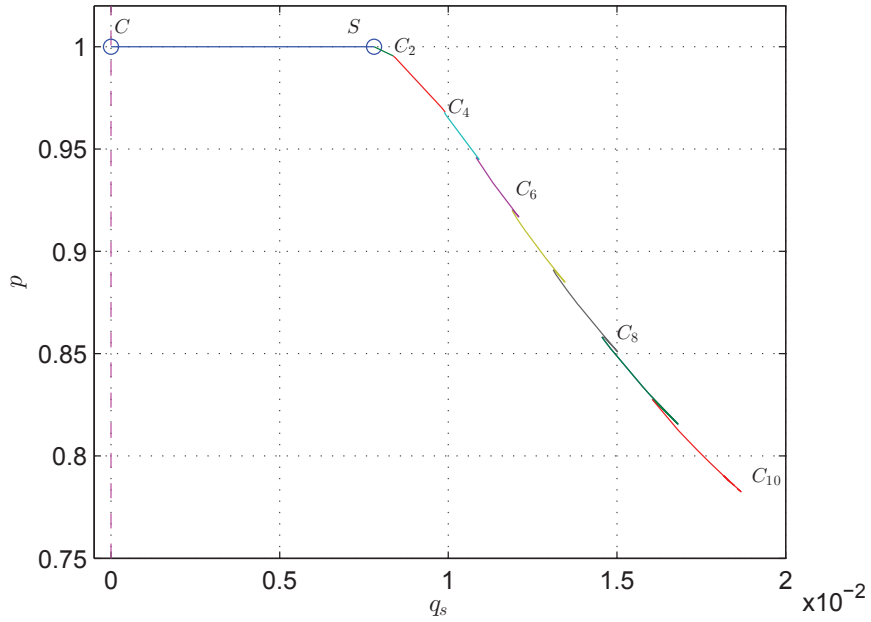

(a)

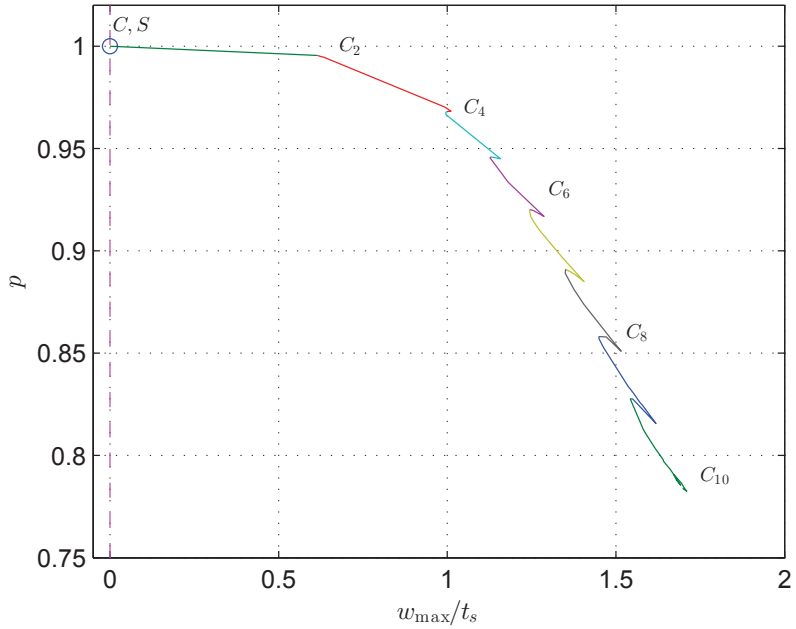

(b)

Figure 3.15: Numerical equilibrium paths with $c_p = 1$ Nmm/mm: normalized force ratio p versus (a) the sway amplitude q_s and (b) the normalized maximum out-of-plane deflection of the stiffener $w_{\max}/t_s$.

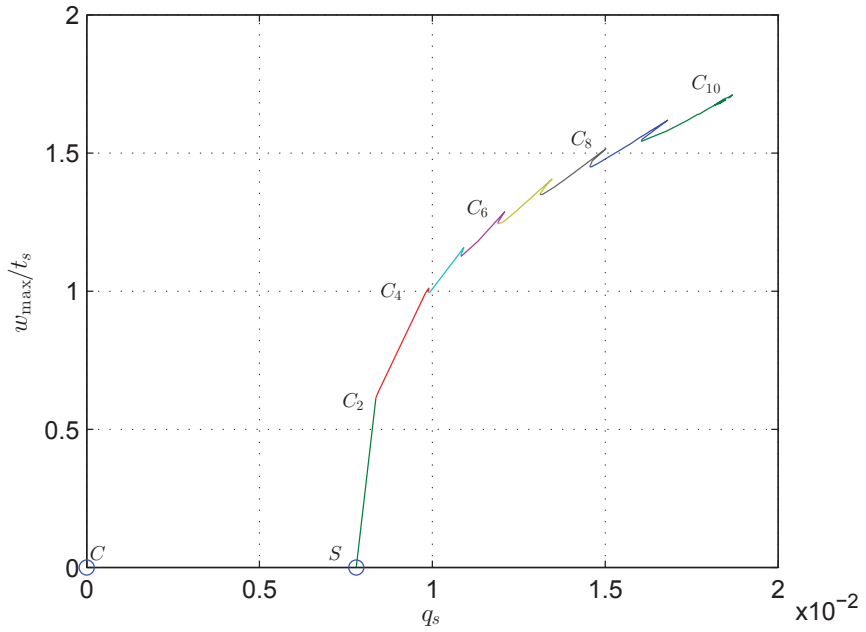

(a)

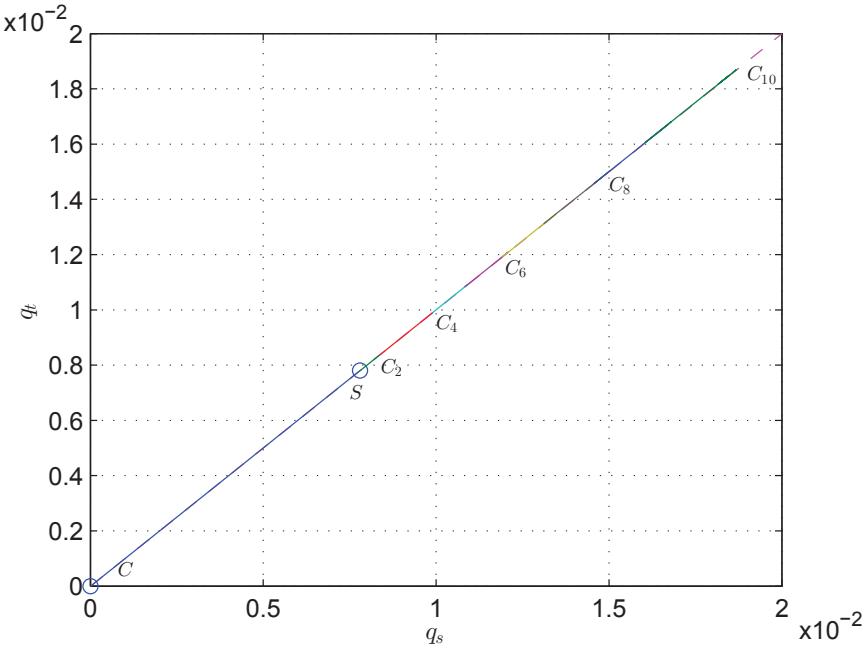

(b)

Figure 3.16: Numerical equilibrium paths for $c_p = 1$ Nmm/mm: (a) local versus global modes: $w_{\max}/t_s$ versus q_s; (b) amplitudes of sway q_s versus tilt q_t with the dashed line showing $q_s = q_t$.

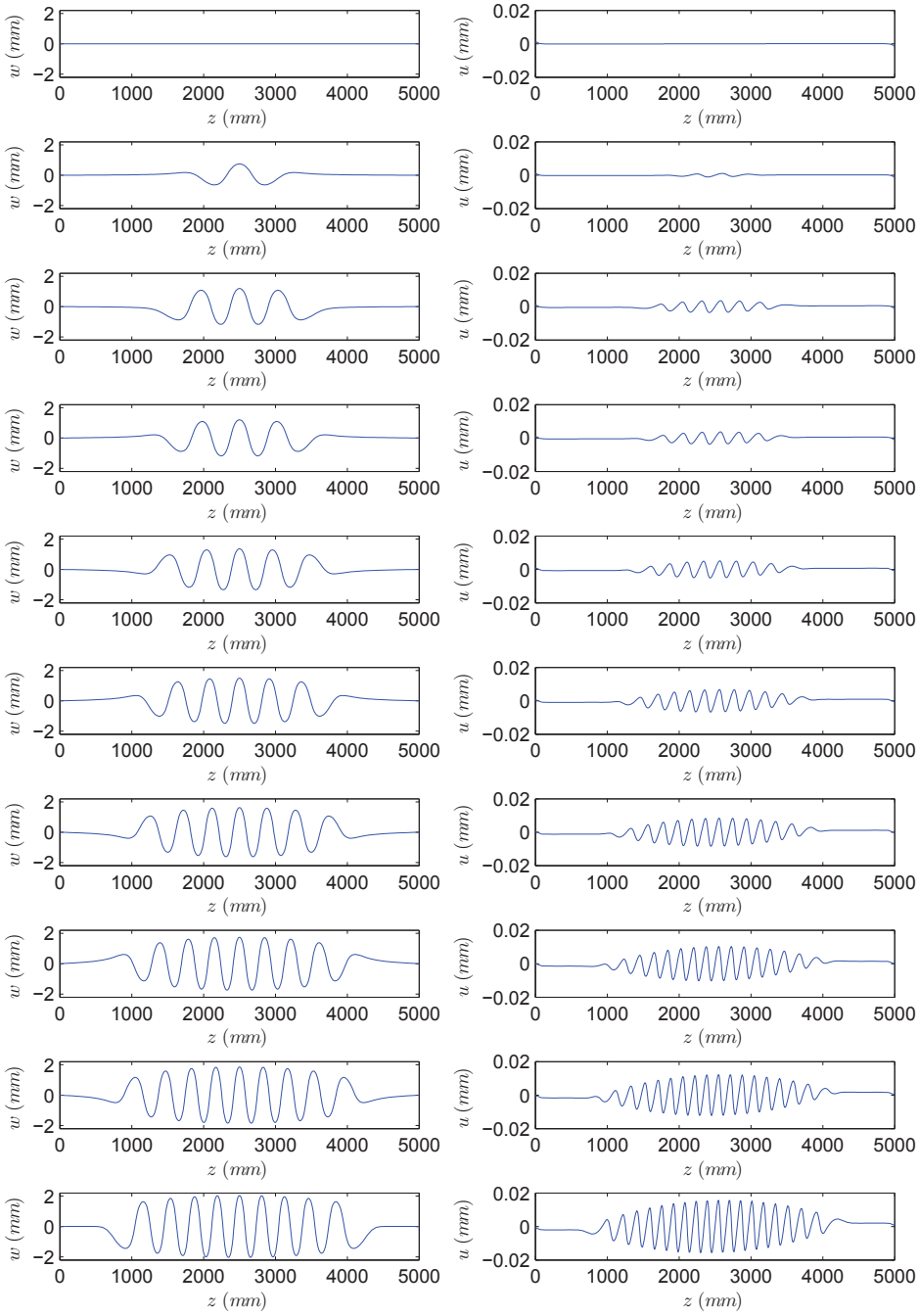

Figure 3.17: Numerical solutions for the stiffener local out-of-plane displacement w (left) and the local in-plane displacement u (right) with $c_p = 1$ Nmm/mm for the equilibrium paths at the secondary bifurcation point S and cells C_2–C_{10} from top to bottom respectively.

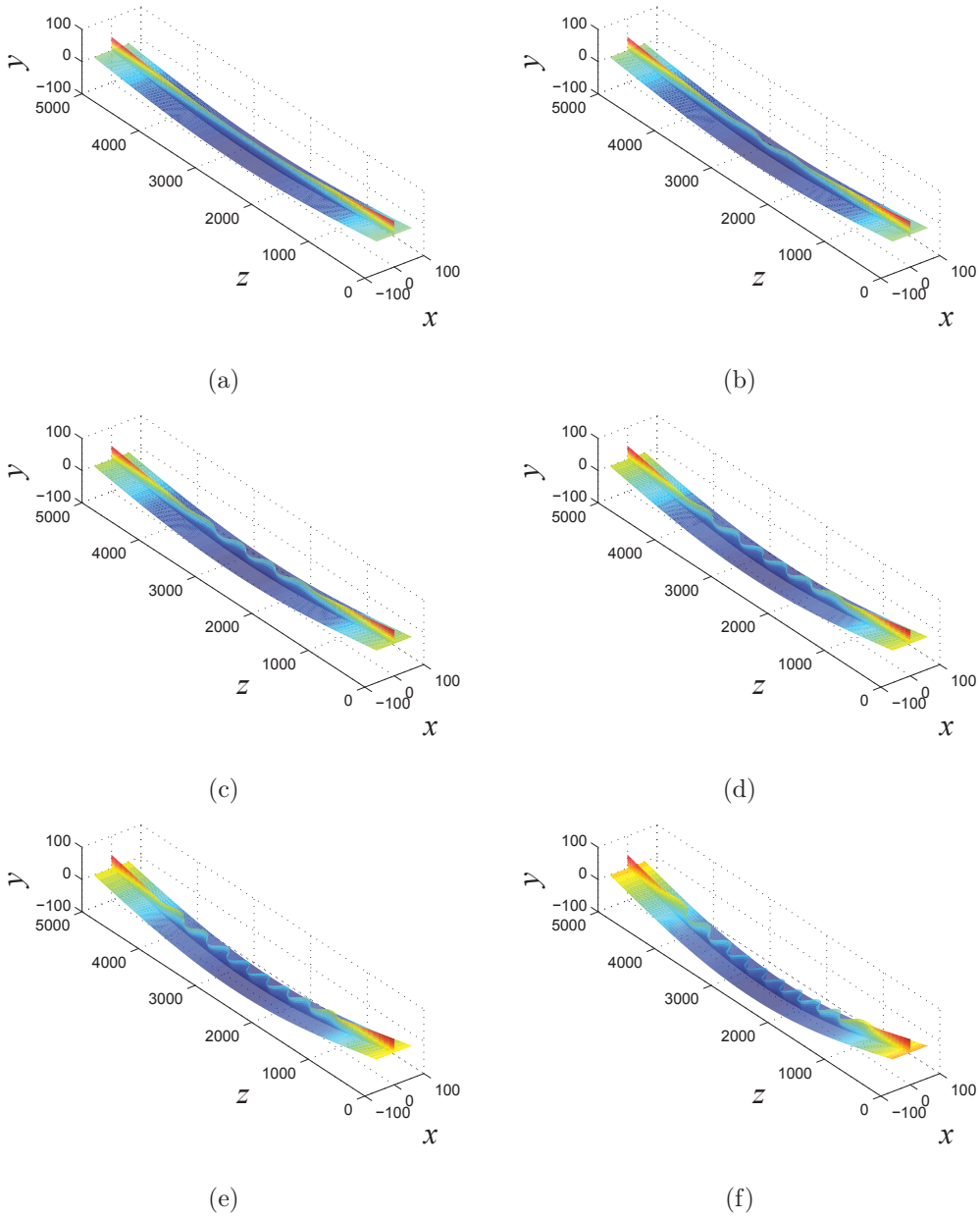

Figure 3.18: Numerical solutions from the analytical model visualized on 3-dimensional representations of the strut with $c_p = 1$ Nmm/mm. (a) Secondary bifurcation point S ($p = 1.000$), and cell C_2 ($p = 0.9955$), (b) cell C_4 ($p = 0.9680$), (c) cell C_6 ($p = 0.9459$), (d) cell C_8 ($p = 0.8910$) and (e) cell C_{10} ($p = 0.8277$). All dimensions are in millimetres, but the local buckling displacements in the stiffener are scaled by a factor of 5 to aid visualization.

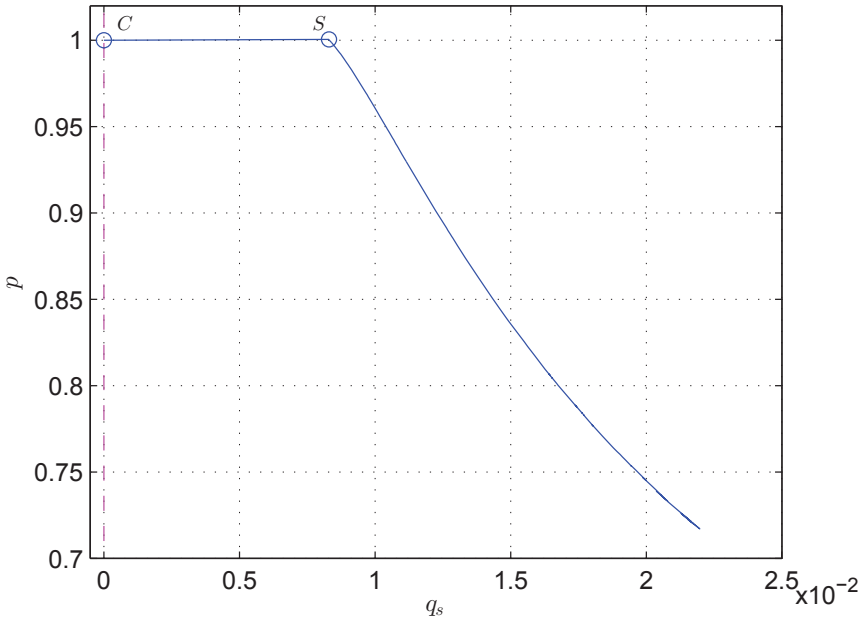

(a)

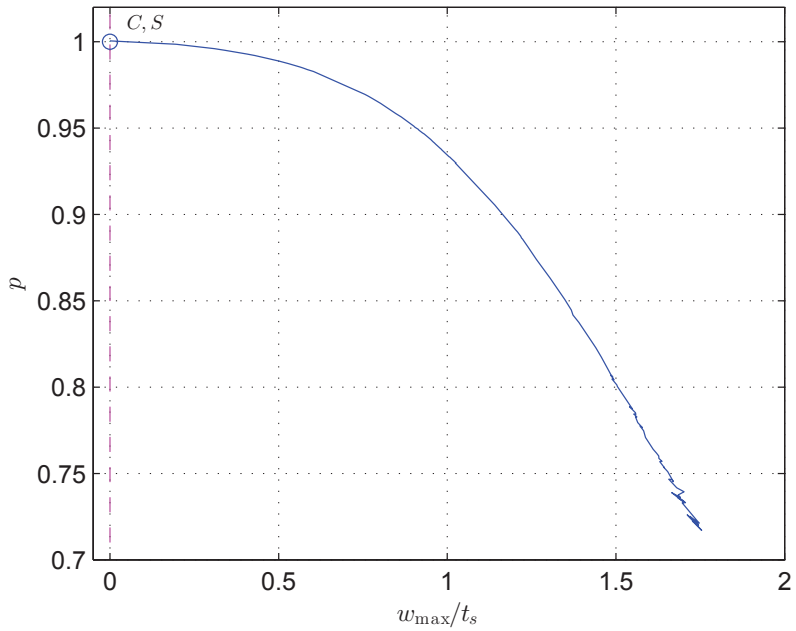

(b)

Figure 3.19: Numerical equilibrium paths with $c_p = 10$ Nmm/mm: normalized force ratio p versus (a) the sway amplitude q_s and (b) the normalized maximum out-of-plane deflection of the stiffener $w_{\max}/t_s$.

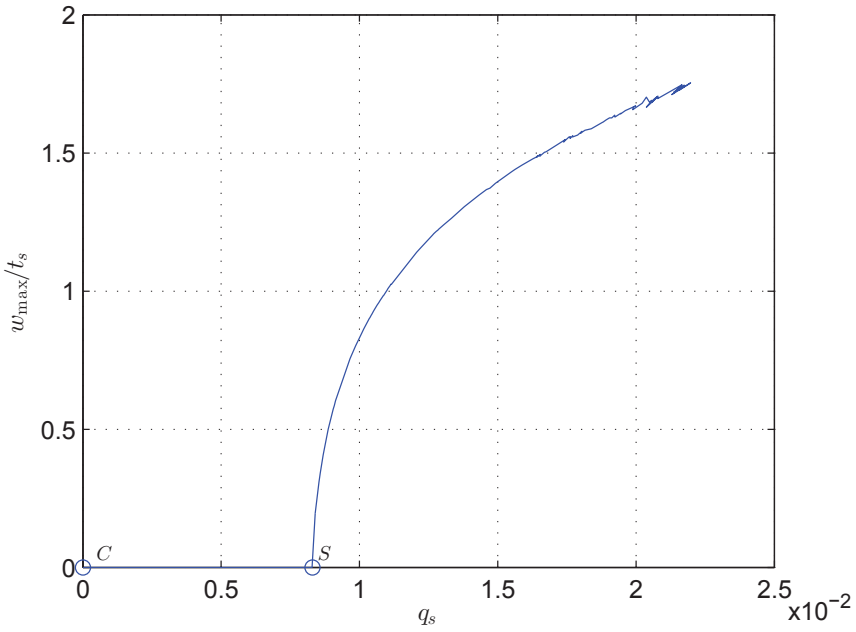

(a)

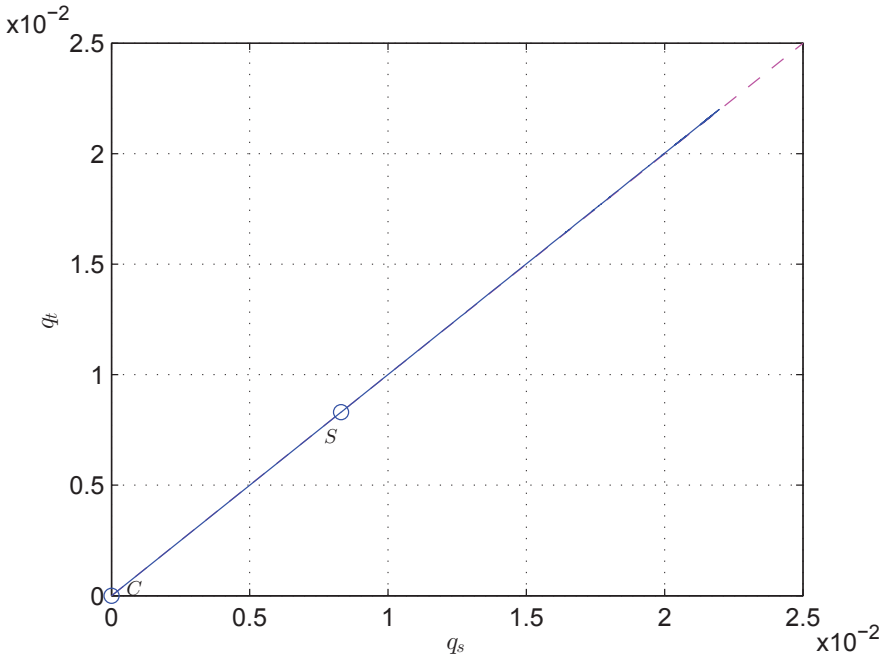

(b)

Figure 3.20: Numerical equilibrium path for $c_p = 10$ Nmm/mm: (a) local versus global modes: $w_{\max}/t_s$ versus q_s; (b) amplitudes of sway q_s versus tilt q_t with the dashed line showing $q_s = q_t$.

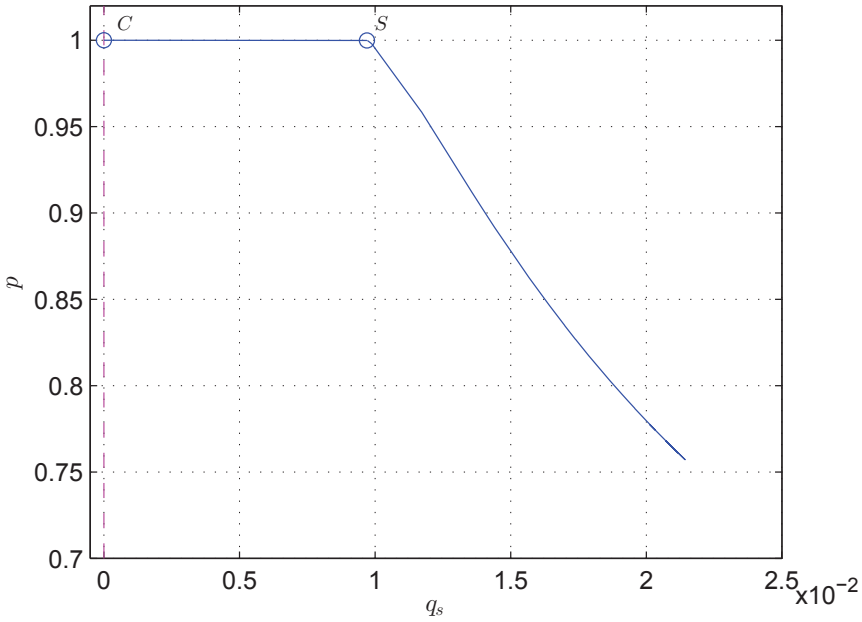

(a)

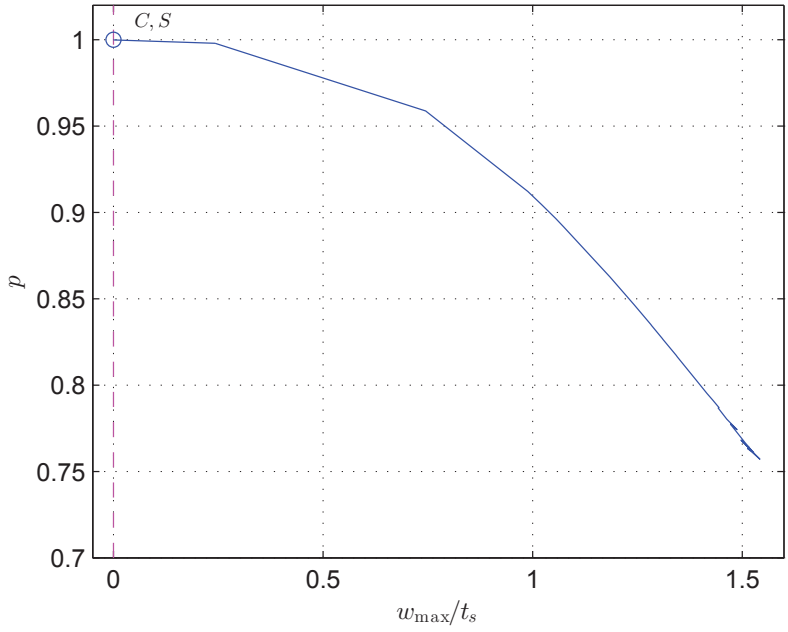

(b)

Figure 3.21: Numerical equilibrium paths with $c_p = 100$ Nmm/mm: normalized force ratio p versus (a) the sway amplitude q_s and (b) the normalized maximum out-of-plane deflection of the stiffener $w_{\max}/t_s$.

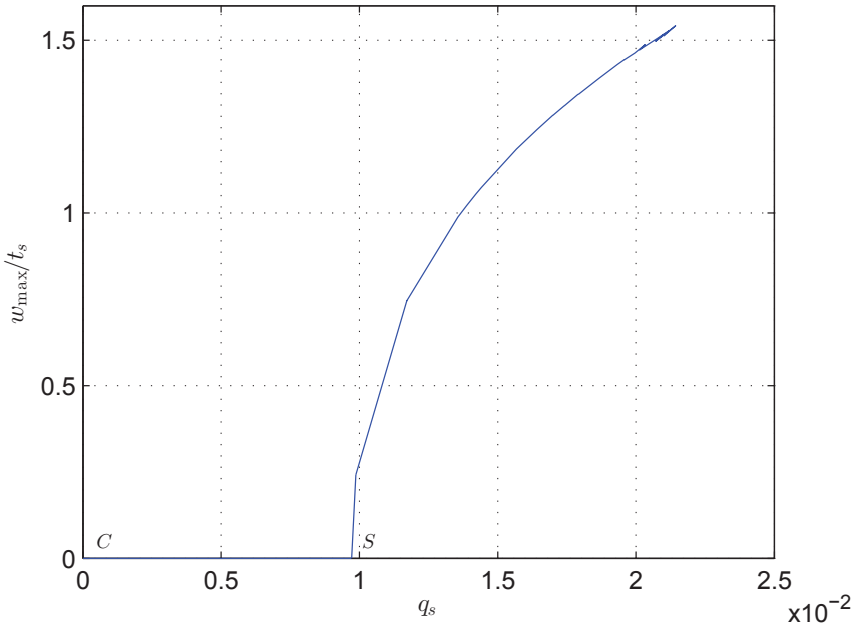

(a)

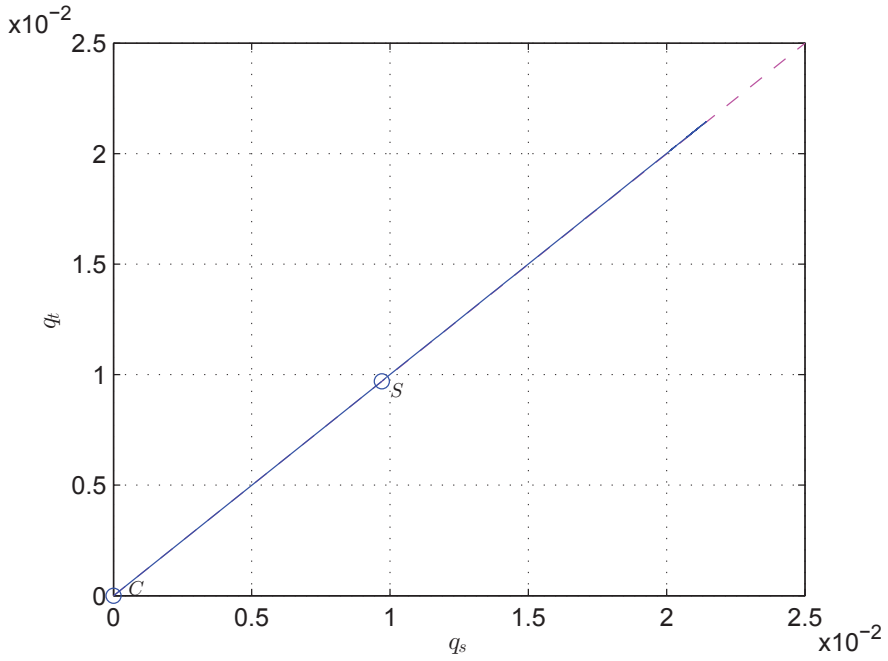

(b)

Figure 3.22: Numerical equilibrium path with $c_p = 100$ Nmm/mm: (a) local versus global modes: $w_{\max}/t_s$ versus q_s; (b) amplitudes of sway q_s versus tilt q_t with the dashed line showing $q_s = q_t$.

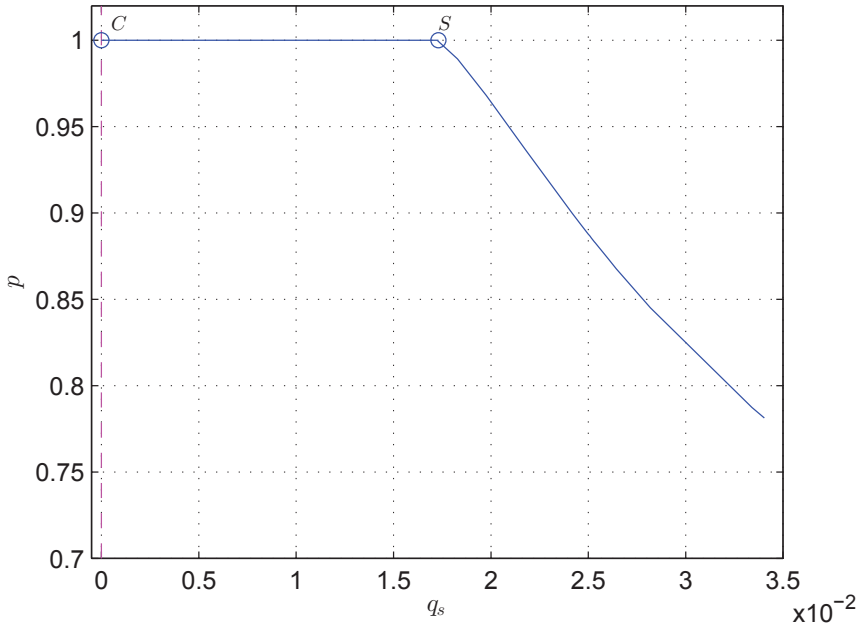

(a)

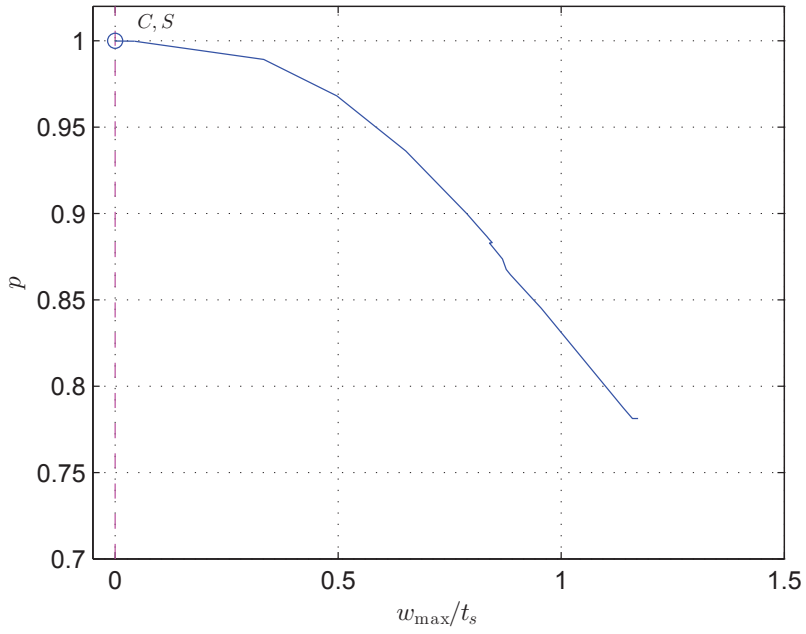

(b)

Figure 3.23: Numerical equilibrium paths with $c_p = 10^4$ Nmm/mm: normalized force ratio p versus (a) the sway amplitude q_s and (b) the normalized maximum out-of-plane deflection of the stiffener $w_{\max}/t_s$.

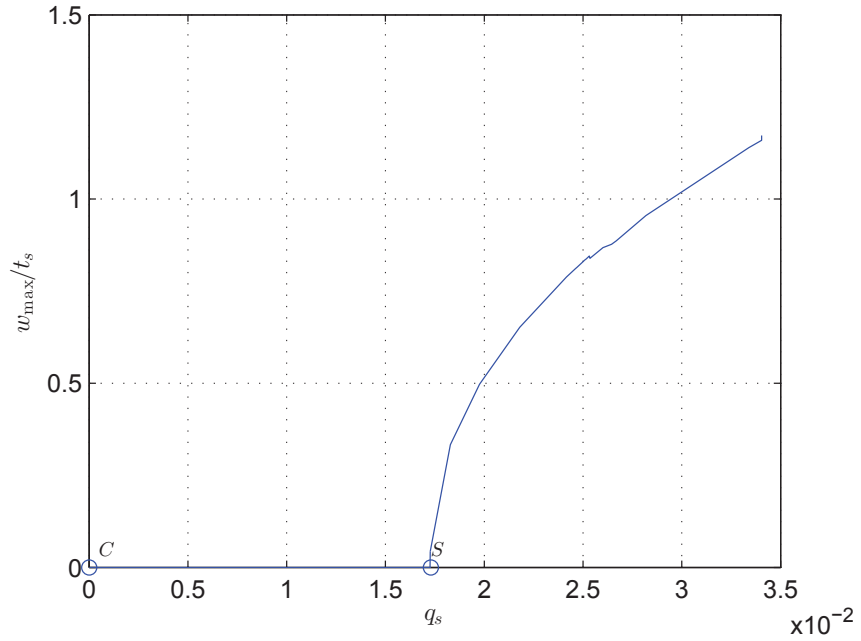

(a)

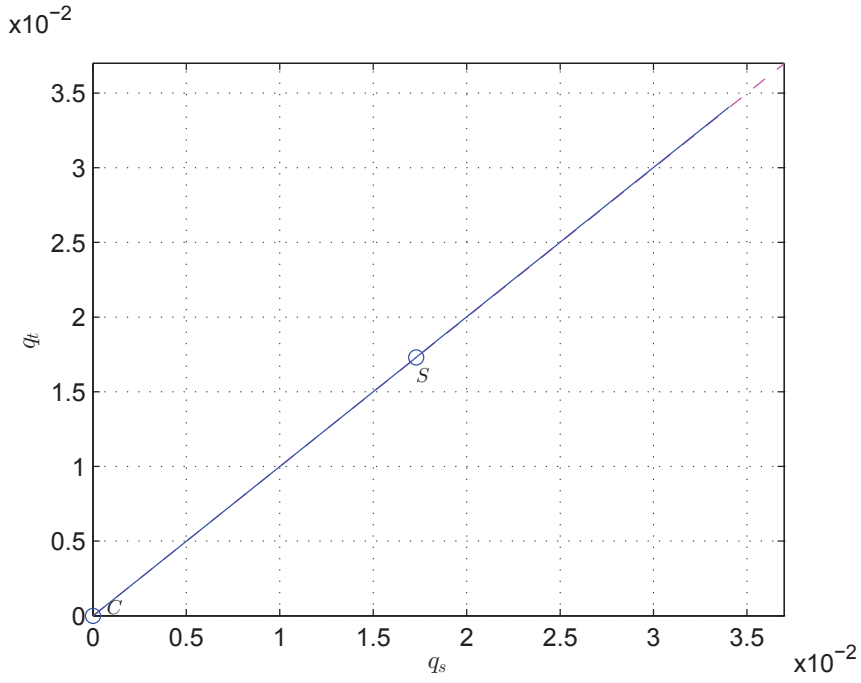

(b)

Figure 3.24: Numerical equilibrium path with $c_p = 10^4$ Nmm/mm: (a) local versus global modes: $w_{\max}/t_s$ versus q_s; (b) amplitudes of sway q_s versus tilt q_t with the dashed line showing $q_s = q_t$.

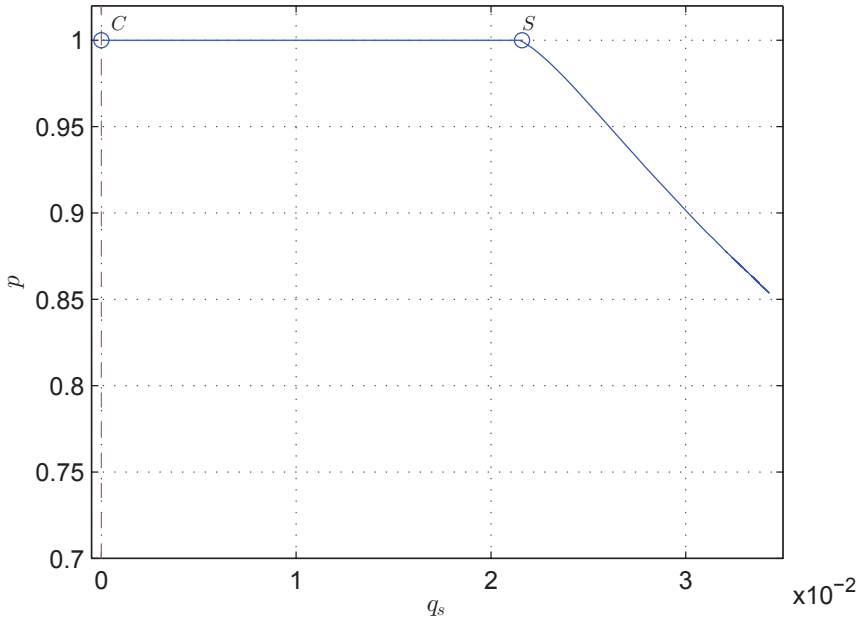

(a)

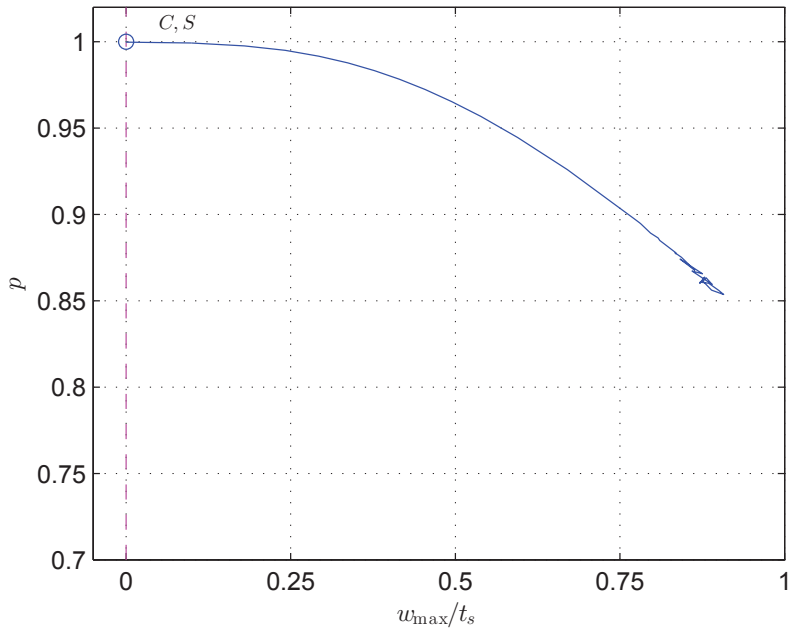

(b)

Figure 3.25: Numerical equilibrium paths with $c_p \to \infty$: normalized force ratio p versus (a) the sway amplitude q_s and (b) the normalized maximum out-of-plane deflection of the stiffener $w_{\max}/t_s$.

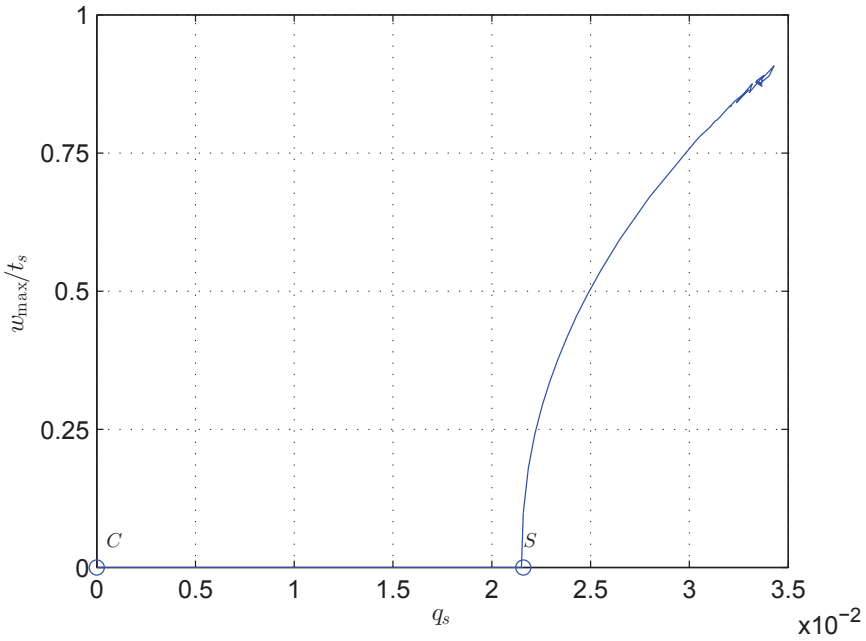

(a)

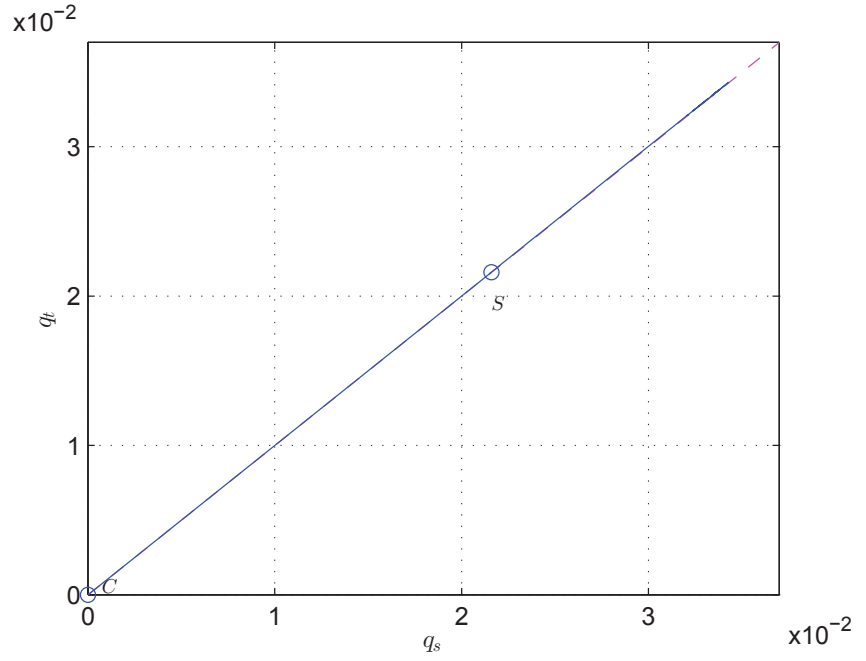

(b)

Figure 3.26: Numerical equilibrium path with $c_p \to \infty$: (a) local versus global modes: $w_{\max}/t_s$ versus q_s; (b) amplitudes of sway q_s versus tilt q_t with the dashed line showing $q_s = q_t$.

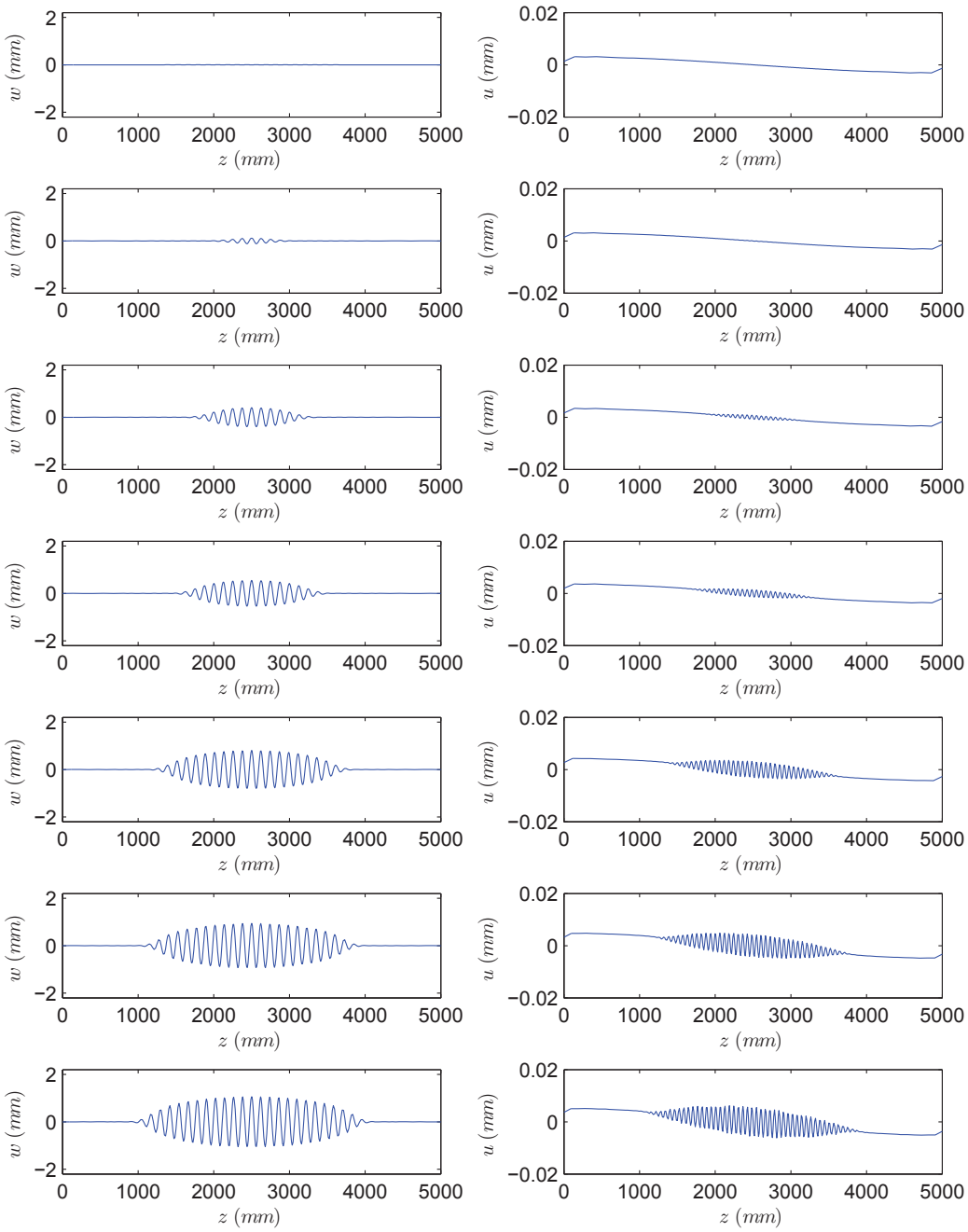

Figure 3.27: Numerical solutions for the stiffener local out-of-plane displacement w (left) and the local in-plane displacement u (right) with $c_p \to \infty$ for the equilibrium paths at the secondary bifurcation point S ($p = 1.000$) and at the normalized load levels equal to 0.9992, 0.9877, 0.9723, 0.9259, 0.8943 and 0.8619 from top to bottom respectively.

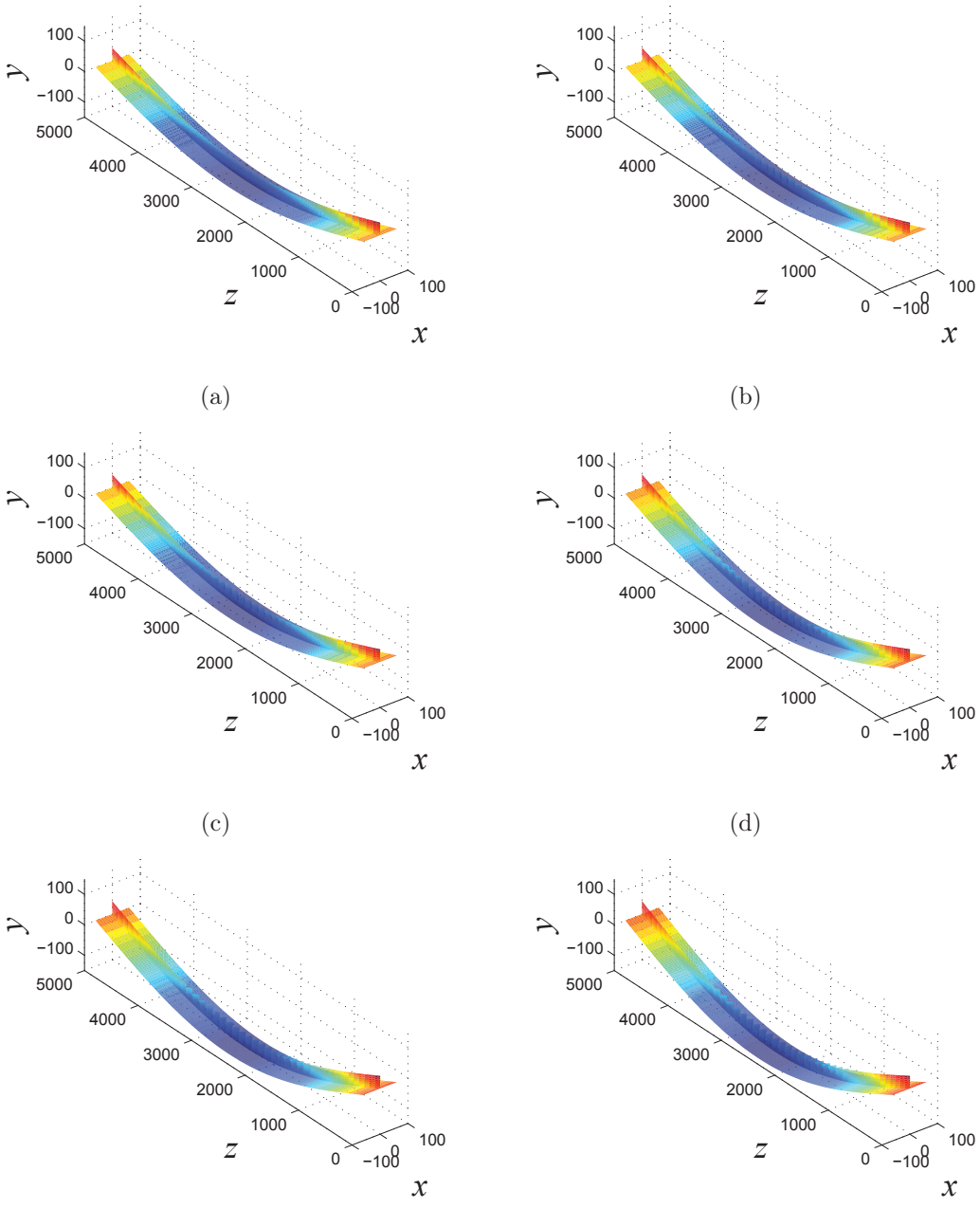

Figure 3.28: Numerical solutions from the analytical model visualized on 3-dimensional representations of the strut with $c_p \to \infty$. All dimensions are in millimetres, but the local buckling displacements in the stiffener are scaled by a factor of 5 to aid visualization.

3.3 Concluding remarks

A nonlinear analytical model for a representative portion of a wide stiffened plate with a perfect geometry has been presented. The structure is subjected to uniaxial compression that is loaded at the centroid of the whole cross-section. A form of cellular buckling, with a characteristic sequence of snap-backs in the mechanical response, has been found that arises from a potentially dangerous interaction of local and global modes of buckling. To model a more realistic joint condition between the main plate and the stiffener, a rotational spring was considered along the strut length with stiffness c_p. It can have a full range of positive values from zero, to model a fully-pinned connection, to effectively infinity for a fully-rigid joint. The full equations of equilibrium were solved numerically by the continuation and bifurcation software Auto-07p (Doedel & Oldeman, 2011). The numerical examples, representing the cases where $c_p = 0$ (fully-pinned), 1, 10, 10^2, 10^4 Nmm/mm and where $c_p \to \infty$ (fully-fixed), have been presented.

For the fully-pinned case, cellular buckling was found with a characteristic sequence of snap-backs in the mechanical response. The buckling mode of the stiffener went from localized to periodic with a progressively reducing wavelength. It was also found that although the effect of the snap-backs can be reduced by increasing the rotational stiffness c_p, the mode interaction persisted and the local buckling profile still changed wavelength as has been found in related experimental studies (Becque & Rasmussen, 2009a; Wadee & Gardner, 2012; Wadee & Bai, 2014). It was also evident that the out-of-straightness at the secondary bifurcation point (q_s^{S}) and at the first snap-back location (q_s^{T}), increased when a greater value of c_p was used. Moreover, it has been found that the number of local buckling waves increases with higher values of c_p. The maximum deflection of the stiffener at mid-span ($w_{\max}$) also decreased as c_p was increased.

In the following chapter, the model presented currently is extended by including the consideration of local buckling of the main plate in combination with the stiffener. Moreover, initial geometric imperfections are also introduced to the model with aim of making the model more practically applicable to the real situation.

Chapter 4

Main plate local buckling and imperfection modelling

In the previous chapter, the perfect elastic post-buckling response of an axially loaded plated panel made from a linear elastic material was considered. The nonlinear mode interaction between the weakly stable global Euler buckling mode and the strongly stable local buckling mode of the stiffener was fully described. However, it was assumed that the main plate was fully-rigid and it had no local deformation. The primary focus was on capturing the perfect elastic post-buckling response with the highly unstable cellular buckling behaviour and the steadily changing buckling wavelength being highlighted. Since real structures contain imperfections, considering these is an important aspect (Thompson, 1967; van der Neut, 1974; Koiter & Pignataro, 1976). It has been shown in the past that such systems are highly imperfection sensitive when the global critical load and the local critical load are sufficiently close. In the current chapter, the previous analytical model is extended to study the behaviour of imperfect systems. Moreover, nonlinear mode interaction between global Euler buckling of the entire cross-section with the local in-plane and out-of-plane deflec-

tion of the stiffener and the main plate is modelled to act in sympathy with each other. The initial global out-of-straightness of the stiffened plate as well as the local out-of-straightness of the stiffener and the main plate are also considered.

4.1 Development of the analytical model

4.1.1 Modal Description

The same definitions for the section and material properties are used as described in the previous chapter (see Figure 3.2). It is also considered that there is a rotational spring with the stiffness c_p along the stiffened plate, as shown in Figure 3.5(a), which models the rigidity of the junction between the stiffener to the main plate. The lateral displacement $W(z)$ and the rotation of the plane section $\theta(z)$ about the x-axis are given in Equation (3.2). The general form of the equations for the local in-plane displacement $u(y, z)$ and out-of-plane displacement of the stiffener $w_s(y, z)$ based on the corresponding boundary conditions, are the same as the ones presented in Equations (3.4)–(3.10). In the current chapter, the local out-of-plane deflection of the main plate $w_p(x, z)$ is introduced with appropriate boundary conditions. The shape of the local buckling mode along the width of the main plate can be estimated by a nonlinear function that is a summation of trigonometric and polynomial terms. The general form of this approximation can be expressed by the following equations:

$$w_p(x, z) = g(x)w_p(z), \tag{4.1}$$

where:

$$g(x) = C_0 + C_1X + (-1)^iC_2X^2 + C_3X^3 + C_4 \sin(\pi X), \tag{4.2}$$

and $X(x) = x/b$. Moreover, for $i = 1$, the range for $x = [0, b/2]$ and for $i = 2$, the range for $x = [-b/2, 0]$. To establish $g(x)$, the constant coefficients C_0, C_1, C_2, C_3

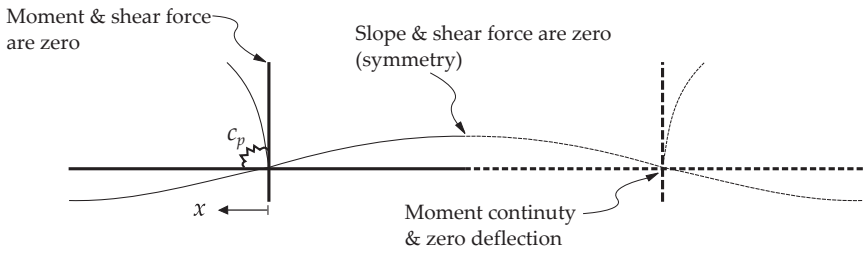

Figure 4.1: Boundary conditions for the stiffener and the main plate.

and C_4 are determined again by applying appropriate boundary conditions for the main plate as shown in Figure 4.1. At the junction between the stiffener and the main plate $x = 0$, there is no relative deflection and the moment is dependent on the joint stiffness c_p. Therefore:

$$w_p(x,z) = 0, \quad D_p \frac{\partial^2}{\partial x^2} w_p(x,z) = c_p \frac{\partial}{\partial x} w_p(x,z), \tag{4.3}$$

whereas at the tips of the main plate at $x = b/2$ and $x = -b/2$, the slope and the shear force are zero and thus:

$$\frac{\partial}{\partial x} w_p(x,z) = 0, \quad D_p \frac{\partial^3}{\partial x^3} w_p(x,z) = 0, \tag{4.4}$$

where D_p is the main plate flexural rigidity given by the expression $Et_p^3/[12(1-\nu^2)]$. The function for the deflected shape $w_p(x,z)$ can be deduced from the above conditions and written thus:

$$w_p(x,z) = -\left\{ \sin(\pi X) + J_p \left[X + (-1)^i X^2 - \frac{1}{4} \sin(\pi X) \right] \right\} w_p(z), \tag{4.5}$$

where:

$$J_p = \left\{ [1/4 - (2D_p)/(c_p b\pi) - 1/\pi] \right\}^{-1}. \tag{4.6}$$

In physical experiments it is often observed that the main plate deflects in sympathy with the stiffener to some extent. In the current work, the following relationship is assumed, $w_p(z) = \lambda_p w(z)$. Moreover, by adding the moment equilibrium relationships

for the stiffener, given in Equation (3.6), and the main plate, given in Equation (4.3), at the joint, an explicit relationship can be derived for the relating parameter λ_p, thus:

$$D_s \frac{\partial^2}{\partial y^2} w_s(-\bar{y}, z) + D_p \frac{\partial^2}{\partial x^2} w_p(0, z) = c_p \left[\frac{\partial}{\partial y} w_s(-\bar{y}, z) + \frac{\partial}{\partial x} w_p(0, z) \right], \tag{4.7}$$

and this leads to the following expression for λ_p after a little bit of manipulation:

$$\lambda_p = \left(\frac{2b^2}{3h_1^2} \right) \left[\frac{c_p h_1 \left(3 - S_4 \pi^3 + 3 S_4 \pi\right) - 3 D_s S_4 \pi^3}{c_p b \left(4 J_p + 4\pi - \pi J_p\right) + 8 D_p J_p} \right]. \tag{4.8}$$

This simplifies the formulation considerably by allowing the system to be modelled with effectively only one out-of-plane displacement function $w(z)$.

4.1.2 Introducing imperfections

The consideration of initial geometric imperfections within the system, leads to more accurate modelling of the actual practical situation. In the current chapter, both initial global and local imperfections are introduced. A lateral displacement W_0 is introduced as a global imperfection as well as an initial rotation of the plane section θ_0. The corresponding expressions are thus:

$$W_0(z) = -q_{s0} L \sin \frac{\pi z}{L}, \quad \theta_0 = q_{t0} \pi \cos \frac{\pi z}{L}, \tag{4.9}$$

with q_{s0} and q_{t0} defining the amplitude of the generalized coordinates defining the initial global imperfection. The function for the local out-of-plane imperfection for the stiffener and the main plate is expressed as:

$$w_0(z) = A_0 \operatorname{sech} \left[\frac{\alpha \left(z - \eta\right)}{L} \right] \cos \left[\frac{\beta \pi \left(z - \eta\right)}{L} \right]. \tag{4.10}$$

The form of the local imperfection closely matches that of the least stable localized buckling mode for the strut on a softening foundation. This is derived from a first

order approximation of a multiple scale perturbation analysis (Wadee *et al.*, 1997), where $z = [0, L]$ and w_0 is symmetric about $z = \eta$. This form for w_0 enables the study of periodic and localized imperfections; the degree of localization and the number of waves can be changed by varying the parameters α and β respectively. It is worth noting that the relationship between w_{p0} and w_0 corresponds to that for the perfect case; hence, $w_{p0} = \lambda_p w_0$ is assumed. The shape of the initial imperfection is illustrated in Figure 4.2. By increasing the α value, the initial imperfection forms into a localized shape; Figure 4.2(a). The value of β controls the number of half sine-waves, as shown in Figure 4.2(b). Note that the imperfection is always assumed to be symmetric about the mid-span of the stiffened plate. This type of study using such a shape of imperfection, has been shown to provide a good approximation of the worst case imperfection in other situations of local–global mode interaction (Wadee, 2000; Wadee & Simões Da Silva, 2005; Wadee *et al.*, 2010).

4.1.3 Total potential energy

The full formulation of the total potential energy V of the perfect stiffened plate was established in the previous chapter. Currently, the global and the local imperfections are introduced, as shown in Figure 4.3(a). It is assumed that the initial out-of-plane deflections of the stiffener w_0 and the main plate w_{p0} are stress-relieved (Thompson & Hunt, 1984), implying that the elemental moment M and thus the local bending energy for both elements drops to zero (Wadee, 2000), as illustrated in Figure 4.3(b). The introduction of the global and the local imperfections provide additional expressions to the global and the local bending strain energy expressions. The global strain energy U_{bo} of bending involves the second derivative of W and W_0, and is hence calculated from the equation below:

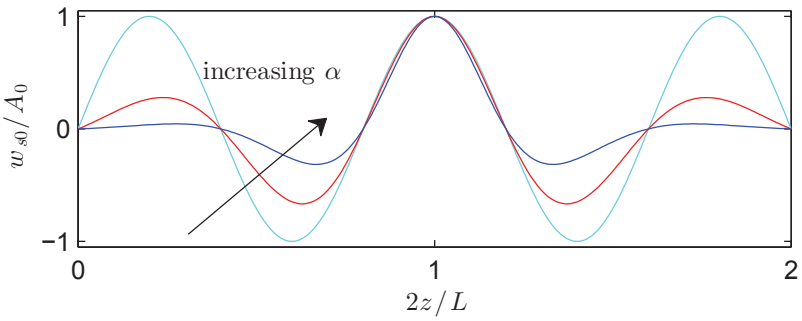

(a)

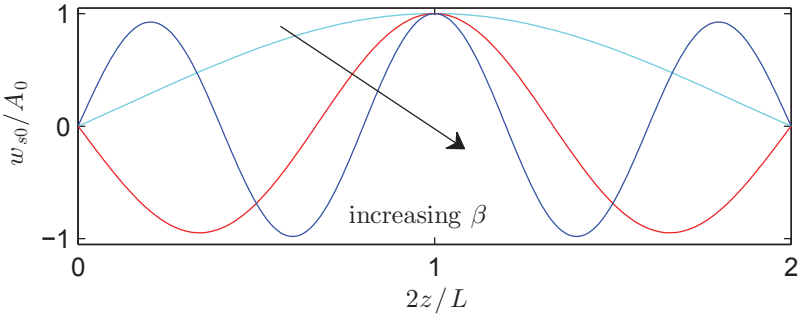

(b)

Figure 4.2: (a) Localized imperfection shape produced by increasing α; (b) periodic imperfection shape ($\alpha = 0$) with different number of half sine-waves $\beta\pi/L$ by increasing β. In both cases $\eta = L/2$.

$$U_{bo} = \frac{1}{2} EI_p \int_0^L \left(\ddot{W} - \ddot{W}_0\right)^2 \mathrm{d}z = \frac{1}{2} EI_p \int_0^L (q_s - q_{s0})^2 \frac{\pi^4}{L^2} \sin^2 \frac{\pi z}{L} \mathrm{d}z, \tag{4.11}$$

where dots again represent differentiation with respect to z. Based on plate theory, to obtain the full expression of the strain energy from local bending U_{bl}, the second derivative terms of the local out-of-plane deflection of the main plate are added to Equation (3.12). The resulting local bending energy expression is thus:

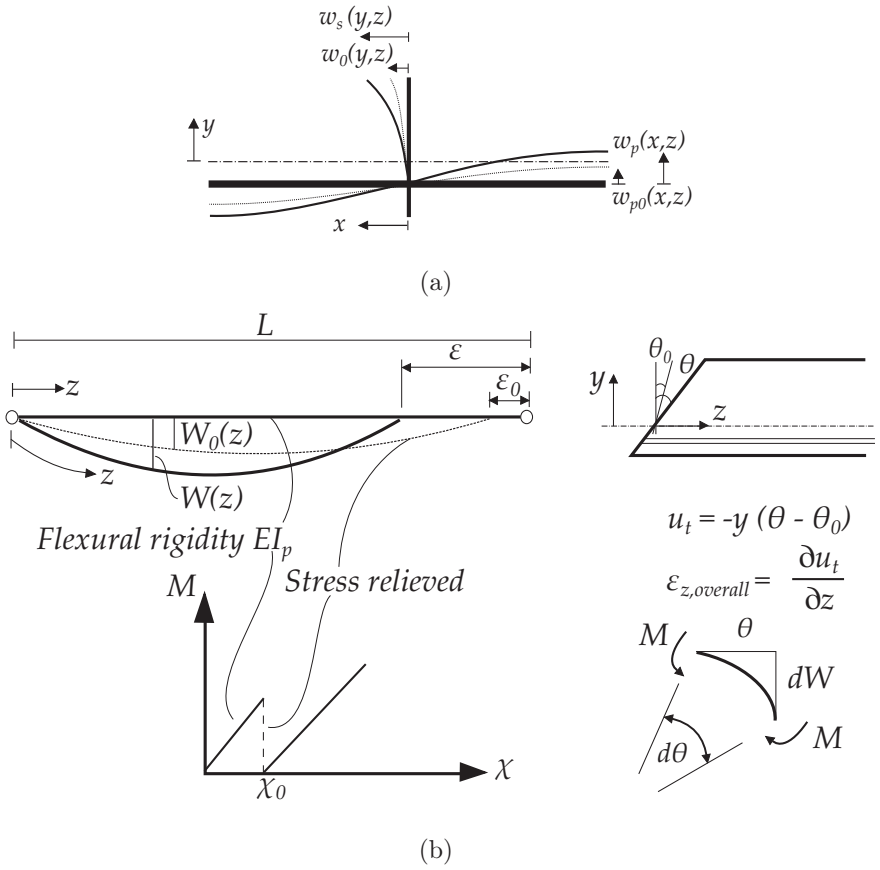

Figure 4.3: (a) Local out-of-plane deflection of the stiffener $w_s(y, z)$ with the initial imperfection $w_0(y, z)$ and local out-of-plane deflection of the plate $w_p(x, z)$ with the initial imperfection $w_{p0}(x, z)$. (b) Incorporation of the global imperfection functions W_0 and θ_0 where the strut is stress-relieved. To incorporate w_0 or w_{p0}, the process is simply to replace W_0 with w_0 or w_{p0}.

$$
\begin{aligned}
U_{bl} = \frac{D_s}{2}\int_0^L \int_{-\bar{y}}^{h_1-\bar{y}} \Bigg\{ & \left[\frac{\partial^2(w_s-w_0)}{\partial z^2} + \frac{\partial^2(w_s-w_0)}{\partial y^2}\right]^2 \\
& -2\,(1-\nu)\left[\frac{\partial^2(w_s-w_0)}{\partial z^2}\frac{\partial^2(w_s-w_{s0})}{\partial y^2} - \left(\frac{\partial^2(w_s-w_0)}{\partial z \partial y}\right)^2\right]\Bigg\}\,\mathrm{d}y\,\mathrm{d}z, \\
+ \frac{D_p}{2}\int_0^L \int_{-b/2}^{b/2} \Bigg\{ & \left[\frac{\partial^2(w_p-w_{p0})}{\partial z^2} + \frac{\partial^2(w_p-w_{p0})}{\partial x^2}\right]^2 \\
& -2\,(1-\nu)\left[\frac{\partial^2(w_p-w_{p0})}{\partial z^2}\frac{\partial^2(w_p-w_{p0})}{\partial x^2} - \left(\frac{\partial^2(w_p-w_{p0})}{\partial z \partial x}\right)^2\right]\Bigg\}\,\mathrm{d}x\,\mathrm{d}z, \\
= \frac{D_s}{2}\int_0^L \Big[& \{f^2\}_y(\ddot{w}-\ddot{w}_0)^2 + \{f''^2\}_y(w-w_0)^2 + 2\nu\{ff''\}_y(w-w_0)(\ddot{w}-\ddot{w}_0) \\
& +2(1-\nu)\{f'^2\}_y(\dot{w}-\dot{w}_0)^2\Big]\,\mathrm{d}z, \\
+ \frac{D_p}{2}\int_0^L \Big[& \{g^2\}_x(\ddot{w}_p-\ddot{w}_{p0})^2 + \{g''^2\}_x(w_p-w_{p0})^2 + 2\nu\{gg''\}_x(w_p-w_{p0})(\ddot{w}_p-\ddot{w}_{p0}) \\
& +2(1-\nu)\{g'^2\}_x(\dot{w}_p-\dot{w}_{p0})^2\Big]\,\mathrm{d}z,
\end{aligned}
\tag{4.12}
$$

where primes denote differentiation with respect to the respective subscript outside the closing brace, with the terms within the braces being definite integrals, thus:

$$
\{F(y)\}_y = \int_{-\bar{y}}^{h_1-\bar{y}} F(y)\,\mathrm{d}y, \qquad \{H(x)\}_x = \int_{-b/2}^{b/2} H(x)\,\mathrm{d}x, \tag{4.13}
$$

where $F(y)$ and $H(x)$ are example functions representing the actual expressions within the braces. Considering the local deflection of the main plate as well as the global deflection along with the imperfection within the stiffener, a series of extended expressions for the global and local direct strains of the stiffeners and the main plate are obtained. Subsequently, the global buckling distribution of the longitudinal strain ε_z, the direct strains for the top and bottom stiffeners ε_{zt} and ε_{zb} respectively and

the main plate ε_{zp} are thus:

$$\begin{aligned}
\varepsilon_{z,\text{global}} &= -y\frac{\mathrm{d}(\theta-\theta_0)}{\mathrm{d}z} = -y\left(q_t-q_{t0}\right)\frac{\pi^2}{L}\sin\frac{\pi z}{L}.\\
\varepsilon_{zt} &= \varepsilon_{z,\text{global}} - \Delta + \frac{\partial u}{\partial z} + \frac{1}{2}\left(\frac{\partial w_s}{\partial z}\right)^2 - \frac{1}{2}\left(\frac{\partial w_0}{\partial z}\right)^2,\\
&= -y\left(q_t-q_{t0}\right)\frac{\pi^2}{L}\sin\frac{\pi z}{L} - \Delta + Y\dot{u} + \frac{1}{2}\{f^2\}_y\left(\dot{w}^2-\dot{w}_0^2\right),\\
\varepsilon_{zb} &= \varepsilon_{z,\text{global}} - \Delta\\
\varepsilon_{zp} &= -\Delta + \frac{1}{2}\left(\frac{\partial w_p}{\partial z}\right)^2 - \frac{1}{2}\left(\frac{\partial w_{p0}}{\partial z}\right)^2.
\end{aligned} \tag{4.14}$$

The derivation of the final terms in the expression for ε_{zt} and ε_{zb} may be found in Appendix A. The membrane energy due to the direct strains U_d is thus:

$$\begin{aligned}
U_d = \frac{E}{2}\int_0^L \Bigg\{ &\int_{-t_s/2}^{t_s/2}\left[\int_{-\bar{y}}^{h_1-\bar{y}}\varepsilon_{zt}^2\,\mathrm{d}y + \int_{-(h_2+\bar{y})}^{-\bar{y}}\varepsilon_{zb}^2\,\mathrm{d}y\right]\mathrm{d}x\\
&+ \int_{-t_p/2}^{t_p/2}\int_{-(b-t_s)/2}^{(b-t_s)/2}\varepsilon_{zp}^2\,\mathrm{d}x\,\mathrm{d}y\Bigg\}\,\mathrm{d}z,\\
= \frac{1}{2}Et_s\int_0^L\Bigg\{ &\frac{1}{3}\left[(h_1-\bar{y})^3+(h_2+\bar{y})^3\right]\left(q_t-q_{t0}\right)^2\frac{\pi^4}{L^2}\sin^2\frac{\pi z}{L} + \Delta^2\left(h_1+h_2\right)\\
&+ \left[(h_1-\bar{y})^2-(h_2+\bar{y})^2\right]\Delta\left(q_t-q_{t0}\right)\frac{\pi^2}{L}\sin\frac{\pi z}{L}\\
&+ h_1\left[\frac{1}{3}\dot{u}^2 + \frac{1}{4h_1}\{f^4\}_y\left(\dot{w}^2-\dot{w}_0^2\right)^2 + \left\{\frac{Yf^2}{h_1}\right\}_y\dot{u}\left(\dot{w}^2-\dot{w}_0^2\right)\right]\\
&- \left(q_t-q_{t0}\right)\frac{h_1\pi^2}{L}\sin\frac{\pi z}{L}\left[\left(\frac{2}{3}h_1-\bar{y}\right)\dot{u} + \frac{1}{h_1}\{yf^2\}_y\left(\dot{w}^2-\dot{w}_0^2\right)\right]\\
&- h_1\Delta\left[\dot{u} + \frac{1}{h_1}\{f^2\}_y\left(\dot{w}^2-\dot{w}_0^2\right)\right]\\
&+ \left(\frac{t_p}{t_s}\right)\left[(b-t_s)\Delta^2 + \frac{1}{4}\{g^4\}_x\left(\dot{w}_p^2-\dot{w}_{p0}^2\right)^2 - \Delta\{g^2\}_x\left(\dot{w}_p^2-\dot{w}_{p0}^2\right)\right]\Bigg\}\,\mathrm{d}z.
\end{aligned} \tag{4.15}$$

The shear strains in the stiffeners γ_{yzi} and the plate γ_{xz}, including the contribution from q_{s0}, w_0 and w_{p0} are given by the following expressions (Bazant & Cedolin, 1991):

$$\begin{aligned}\gamma_{yzi} &= \frac{\partial}{\partial z}(W - W_0) + (\theta - \theta_0) + \frac{\partial u}{\partial y} + \frac{\partial w_s}{\partial z}\frac{\partial w_s}{\partial y} - \frac{\partial w_0}{\partial z}\frac{\partial w_0}{\partial y} \\ \gamma_{xz} &= \frac{\partial w_p}{\partial z}\frac{\partial w_p}{\partial x} - \frac{\partial w_{p0}}{\partial z}\frac{\partial w_{p0}}{\partial x},\end{aligned} \tag{4.16}$$

the expressions for the top and bottom stiffeners are given respectively:

$$\begin{aligned}\gamma_{yzt} &= -\left[(q_s - q_{s0}) - (q_t - q_{t0})\right]\pi\cos\frac{\pi z}{L} + \frac{u}{h_1} + \{ff'\}_y(w\dot{w} - w_0\dot{w}_0), \\ \gamma_{yzb} &= -\left[(q_s - q_{s0}) - (q_t - q_{t0})\right]\pi\cos\frac{\pi z}{L},\end{aligned} \tag{4.17}$$

with the explicit expression for the main plate shear strain:

$$\gamma_{xz} = \{gg'\}_x(w_p\dot{w}_p - w_{p0}\dot{w}_{p0}), \tag{4.18}$$

the membrane energy contribution from the shear strains U_s is therefore:

$$\begin{aligned}U_s = \frac{1}{2}Gt_s\int_0^L \Bigg\{ & \left[(q_s - q_{s0}) - (q_t - q_{t0})\right]^2\pi^2\cos^2\frac{\pi z}{L}(h_1 + h_2) \\ & + \frac{1}{h_1}\left[u^2 + h_1\{(ff')^2\}_y(w\dot{w} - w_0\dot{w}_0)^2 + 2\{ff'\}_y u(w\dot{w} - w_0\dot{w}_0)\right] \\ & - \left[(q_s - q_{s0}) - (q_t - q_{t0})\right]\left[2u + 2\{ff'\}_y(w\dot{w} - w_0\dot{w}_0)\right]\pi\cos\frac{\pi z}{L} \\ & + \left(\frac{t_p}{t_s}\right)\{(gg')^2\}_x(w_p\dot{w}_p - w_{p0}\dot{w}_{p0})^2\Bigg\}\,\mathrm{d}z.\end{aligned} \tag{4.19}$$

The final component of strain energy is that stored in the rotational spring of the stiffness c_p representing the rigidity of the main plate–stiffener joint. It is expressed as:

$$\begin{aligned}U_{sp} &= \frac{1}{2}c_p\int_0^L\left\{\left[\frac{\partial}{\partial y}\left[w_s(-\bar{y}) - w_0(-\bar{y})\right] - \frac{\partial}{\partial x}\left[w_p(0) - w_{p0}(0)\right]\right]^2\right\}\mathrm{d}z, \\ &= \frac{1}{2}c_p\int_0^L\left\{\left[f'(-\bar{y})\,(w - w_0) - g'(0)(w_p - w_{p0})\right]^2\right\}\mathrm{d}z,\end{aligned} \tag{4.20}$$

where $f'(-\bar{y})$ and $g'(0)$ indicate the value of f' and g' at $y = -\bar{y}$ and $x = 0$ respectively. The final component is the work done by the axial load P, which is given by:

$$P\mathcal{E} = \frac{P}{2}\int_0^L \left[2\Delta + q_s^2\pi^2\cos^2\frac{\pi z}{L} - 2\left(\frac{h_2+\bar{y}}{h_1+h_2}\right)\dot{u}\right]\mathrm{d}z, \tag{4.21}$$

where the end-shortening $\mathcal{E}$ again comprises components from pure squash and sway from global buckling combined with the local buckling of the stiffener. Therefore, the total potential energy V is given by the summation of all the strain energy terms minus the work done, assembled as:

$$V = U_{bo} + U_{bl} + U_d + U_s + U_{sp} - P\mathcal{E}. \tag{4.22}$$

4.1.4 Variational Formulation

The governing differential equations are obtained by performing the calculus of variations on the total potential energy V. The integrand of the total potential energy V can be expressed as the Lagrangian ($\mathcal{L}$) of the form:

$$V = \int_0^L \mathcal{L}\left(\ddot{w}, \dot{w}, w, \ddot{w}_p, \dot{w}_p, w_p, \dot{u}, u, z\right)\mathrm{d}z. \tag{4.23}$$

Note that the local deflection of the main plate w_p and the stiffener w relate to each other by the following relationship $w_p = \lambda_p w$ and therefore the first variation of the total potential energy V has the same expression as Equation (3.25). Subsequently, partial derivatives of the Lagrangian ($\mathcal{L}$) function with respect to the corresponding variables, leads to the following expression for the first variation δV:

$$
\begin{aligned}
\delta V = \int_0^L \Bigg\{ & D_s \Big[\{f^2\}_y (\ddot{w} - \ddot{w}_0) + \nu \{ff''\}_y (w - w_0) \Big] \\
& + D_p \lambda_p^2 \Big[\{g^2\}_x (\ddot{w} - \ddot{w}_0) + \nu \{gg''\}_x (w - w_0) \Big] \Bigg\} \delta \ddot{w} \\
& + \Bigg\{ D_s \Big[2(1-\nu) \{f'^2\}_y (\dot{w} - \dot{w}_0) \Big] + D_p \lambda_p^2 \Big[2(1-\nu) \{g'^2\}_x (\dot{w} - \dot{w}_0) \Big] \\
& + \frac{1}{2} E t_s \Big[\{f^4\}_y \left(\dot{w}^3 - \dot{w} \dot{w}_0^2 \right) + 2 \{Y f^2\}_y \dot{w} \dot{u} - 2\Delta \{f^2\}_y \dot{w} \\
& - (q_t - q_{t0}) \frac{\pi^2}{L} \sin\left(\frac{\pi z}{L} \right) \Big] + G t_s \Big[\{(ff')^2\}_y \left(w^2 \dot{w} - w w_0 \dot{w}_0 \right) \\
& + \frac{1}{h_1} \{ff'\}_y w u - \big[(q_s - q_{s0}) - (q_t - q_{t0}) \big] \pi \cos\left(\frac{\pi z}{L} \right) \{ff'\}_y w \Big] \\
& + E t_p \Big[\frac{1}{2} \lambda_p^4 \{g^4\}_x \left(\dot{w}^3 - \dot{w} \dot{w}_0^2 \right) - 2\Delta \lambda_p^2 \{g^2\}_x \dot{w} \Big] \\
& + G t_p \lambda_p^4 \{(gg')^2\}_x \left(w^2 \dot{w} - w w_0 \dot{w}_0 \right) \Bigg\} \delta \dot{w} \\
& + \Bigg\{ D_s \Big[\{f''^2\}_y w + \nu \{ff''\}_y \ddot{w} \Big] + D_p \lambda_p^2 \Big[\{g''^2\}_x w + \nu \{gg''\}_x \ddot{w} \Big] \\
& + G t_s \Big[\{(ff')^2\}_y \left(w \dot{w}^2 - w_0 \dot{w}_0 \dot{w} \right) + \frac{1}{h_1} \{ff'\}_y \dot{w} u \\
& - (q_s - q_t) \pi \cos\left(\frac{\pi z}{L} \right) \{ff'\}_y \dot{w} \Big] + G t_p \lambda_p^4 \{(gg')^2\}_x \left(w \dot{w}^2 - w_0 \dot{w}_0 \dot{w} \right) \\
& + c_p \Big[f'(-\bar{y})^2 - \lambda_p g'(0)^2 \Big] (w - w_0) \Bigg\} \delta w \\
& + \Bigg\{ \frac{1}{2} E t_s h_1 \Big[\frac{2}{3} \dot{u} + \left\{ \frac{Y f^2}{h_1} \right\}_y \left(\dot{w}^2 - \dot{w}_0^2 \right) - \Delta - (q_t - q_{t0}) \frac{\pi^2}{L} \sin\left(\frac{\pi z}{L} \right) \left(\frac{2}{3} h_1 - \bar{y} \right) \Big] \\
& - \frac{h_2 + \bar{y}}{h_1 + h_2} P \Bigg\} \delta \dot{u} + \Bigg\{ G t_s \Big[\frac{1}{h_1} u + \frac{1}{h_1} \{ff'\}_y (w \dot{w} - w_0 \dot{w}_0) \\
& - \big[(q_s - q_{s0}) - (q_t - q_{t0}) \big] \pi \cos\left(\frac{\pi z}{L} \right) \Big] \Bigg\} \delta u \, \mathrm{d}z,
\end{aligned}
\tag{4.24}
$$

where the terms in the braces can be found in Appendix B. Using the same procedure detailed in Chapter 3, the nondimensional differential equations are obtained thus:

$$\begin{aligned}
&\ddot{\tilde{w}} - \ddot{\tilde{w}}_0 + \frac{L^2}{2\{f^2\}_y}\left[\nu\{ff''\}_y - (1-\nu)\{f'^2\}_y\right]\left(\tilde{\tilde{w}} - \tilde{\tilde{w}}_0\right) + \tilde{k}\left(\tilde{w} - \tilde{w}_0\right) \\
&\quad - \tilde{D}\left[\frac{\{f^4\}_y}{\{f^2\}_y}\left(3\tilde{\dot{w}}^2\tilde{\tilde{w}} - \tilde{\tilde{w}}\dot{\tilde{w}}_0^2 - 2\tilde{\tilde{w}}_0\dot{\tilde{w}}_0\tilde{\dot{w}}\right) + \frac{\{2Yf^2\}_y}{\{f^2\}_y}\left(\tilde{\tilde{u}}\tilde{\dot{w}} + \tilde{\tilde{w}}\tilde{\dot{u}}\right)\right. \\
&\quad \left. - 2\Delta\tilde{\tilde{w}} - 2\left(q_t - q_{t0}\right)\frac{\pi^2}{L}\frac{\{yf^2\}_y}{\{f^2\}_y}\left(\sin\frac{\pi\tilde{z}}{2}\tilde{\tilde{w}} + \frac{\pi}{2}\cos\frac{\pi\tilde{z}}{2}\tilde{\dot{w}}\right)\right] \\
&\quad - \frac{\tilde{G}L^2\tilde{w}}{2\{f^2\}}\left[\{(ff')^2\}_y\left(\tilde{\dot{w}}^2 + \tilde{w}\tilde{\tilde{w}} - \tilde{\dot{w}}_0^2 - \tilde{w}_0\tilde{\tilde{w}}_0\right) + \frac{1}{h_1}\{ff'\}_y\tilde{\tilde{u}}\right. \\
&\quad \left. + \left[\left(q_s - q_{s0}\right) - \left(q_t - q_{t0}\right)\right]\frac{\pi^2}{L}\{ff'\}_y\sin\frac{\pi\tilde{z}}{2}\right] \\
&\quad + \left(\frac{t_p}{t_s}\right)^3\frac{\lambda_p^2}{\{f^2\}_y}\left[\{g^2\}_x\left(\ddot{\tilde{w}} - \ddot{\tilde{w}}_0\right) + \frac{L^2}{2}\left[\nu\{gg''\}_x - (1-\nu)\{g'^2\}_x\right]\left(\tilde{\tilde{w}} - \tilde{\tilde{w}}_0\right)\right] \\
&\quad - \left(\frac{t_p}{t_s}\right)\frac{\tilde{D}\lambda_p^2}{\{f^2\}_y}\left[\lambda_p^2\{g^4\}_x\left(3\tilde{\dot{w}}^2\tilde{\tilde{w}} - \tilde{\tilde{w}}\dot{\tilde{w}}_0^2 - 2\tilde{\tilde{w}}_0\dot{\tilde{w}}_0\tilde{\dot{w}}\right) - 2\Delta\{g^2\}_x\tilde{\tilde{w}}\right] \\
&\quad - \left(\frac{t_p}{t_s}\right)\frac{L^2\tilde{G}\lambda_p^4\tilde{w}}{2\{f^2\}_y}\left[\{(gg')^2\}_x\left(\tilde{\dot{w}}^2 + \tilde{w}\tilde{\tilde{w}} - \tilde{\dot{w}}_0^2 - \tilde{w}_0\tilde{\tilde{w}}_0\right)\right] = 0,
\end{aligned} \tag{4.25}$$

$$\begin{aligned}
&\tilde{\tilde{u}} - \frac{3}{4}\frac{\tilde{G}}{\tilde{D}}\psi\left[\psi\left(\tilde{u} + \{ff'\}_y\left(\tilde{w}\tilde{\dot{w}} - \tilde{w}_0\tilde{\dot{w}}_0\right)\right) - 2\pi\left[\left(q_s - q_{s0}\right) - \left(q_t - q_{t0}\right)\right]\cos\frac{\pi\tilde{z}}{2}\right] \\
&\quad - \left\{\frac{3Yf^2}{h_1}\right\}_y\left(\tilde{\tilde{w}}\tilde{\dot{w}} + \tilde{\dot{w}}_0\tilde{\tilde{w}}_0\right) + \frac{1}{2}\left(q_t - q_{t0}\right)\pi^3\left(\psi - \frac{3\bar{y}}{2L}\right)\cos\frac{\pi\tilde{z}}{2} = 0,
\end{aligned} \tag{4.26}$$

where the updated non-dimensional parameters are:

$$\tilde{k} = \frac{L^4}{16\left\{f^2\right\}_y}\left[\left\{f''^2\right\}_y + \lambda_p^2\left(t_p/t_s\right)^3\left\{g''^2\right\}_x + c_p\left[f'(-\bar{y}) - \lambda_p g'(0)\right]^2/D_s\right], \tag{4.27}$$

and $\tilde{w}_0 = 2w_0/L$. The three integral conditions in non-dimensional form are as follows:

$$
\begin{aligned}
\frac{\partial V}{\partial q_s} &= \pi^2 \left(q_s - q_{s0}\right) + \tilde{s}\left[\left(q_s - q_{s0}\right) - \left(q_t - q_{t0}\right)\right] - \frac{PL^2}{EI_p} q_s \\
&\quad - \frac{\tilde{s}\tilde{\phi}}{2\pi} \int_0^2 \cos\frac{\pi\tilde{z}}{2} \left[\tilde{u} + \left\{ff'\right\}_y \left(\tilde{w}\tilde{\dot{w}} - \tilde{w}_0\tilde{\dot{w}}_0\right)\right] \mathrm{d}\tilde{z} = 0, \\
\frac{\partial V}{\partial q_t} &= \pi^2 \left(q_t - q_{t0}\right) + \tilde{\Gamma}_3\Delta - \tilde{t}\left[\left(q_s - q_{s0}\right) - \left(q_t - q_{t0}\right)\right] - \frac{1}{2}\int_0^2 \left\{ \sin\frac{\pi\tilde{z}}{2} \left[\tilde{\Gamma}_1\tilde{\dot{u}}\right.\right. \\
&\quad \left.\left. + \tilde{\Gamma}_2\left(\tilde{\dot{w}}^2 - \tilde{\dot{w}}_0^2\right)\right] + \frac{\tilde{t}\tilde{\phi}}{\pi}\cos\frac{\pi\tilde{z}}{2}\left[\tilde{u} + \left\{ff'\right\}_y\left(\tilde{w}\tilde{\dot{w}} - \tilde{w}_0\tilde{\dot{w}}_0\right)\right] \right\} \mathrm{d}\tilde{z} = 0, \\
\frac{\partial V}{\partial \Delta} &= \Delta\left[1 + \frac{h_2}{h_1} + \frac{t_p(b - t_s)}{t_s h_1}\right] - \frac{P}{Et_s h_1} + \left(q_t - q_{t0}\right)\frac{\pi}{Lh_1}\left[\left(h_1 - \bar{y}\right)^2 - \left(h_2 + \bar{y}\right)^2\right] \\
&\quad - \frac{1}{4}\int_0^2 \left[\tilde{\dot{u}} + \frac{1}{h_1}\left\{f^2\right\}_y\left(\tilde{\dot{w}}^2 - \dot{w}_0^2\right)\right] \mathrm{d}\tilde{z} - \left(\frac{t_p}{t_s}\right)\frac{\lambda_p^2}{4h_1}\int_0^2 \left[\left\{g^2\right\}_x\left(\tilde{\dot{w}}^2 - \dot{w}_0^2\right)\right] \mathrm{d}\tilde{z} \\
&= 0,
\end{aligned}
\tag{4.28}
$$

where the rescaled quantities are the same expressions given in Equation (3.32). Since the column is an integral member, Equation (4.28) provides a relationship linking q_s and q_t before any interactive buckling occurs, *i.e.* when $w = u = 0$. This relationship is assumed to hold also between q_{s0} and q_{t0}, which has the beneficial effect of reducing the number of imperfection amplitude parameters associated with the global mode to one; the relationship is given by:

$$
q_{s0} = \left(1 + \pi^2/\tilde{t}\right) q_{t0}. \tag{4.29}
$$

The boundary conditions for $\tilde{w}$ and $\tilde{u}$ and their derivatives are for pinned conditions for $\tilde{z} = 0$ and for symmetry at $\tilde{z} = 1$:

$$
\tilde{w}(0) = \tilde{\ddot{w}}(0) = \tilde{\dot{w}}(1) = \tilde{\dddot{w}}(1) = \tilde{u}(1) = 0, \tag{4.30}
$$

with a further condition from matching the in-plane strain:

$$
\frac{1}{3}\tilde{\dot{u}}(0) + \frac{1}{2}\left\{\frac{Y}{h_1}f^2\right\}_y \left[\tilde{\dot{w}}^2(0) - \dot{w}_0^2(0)\right] - \frac{1}{2}\Delta + \frac{P}{Et_s h_1}\left(\frac{h_2 + \bar{y}}{h_1 + h_2}\right) = 0, \tag{4.31}
$$

which is obtained in precisely the same way as in Chapter 3. The global critical load, P_o^{C}, determined by the linear eigenvalue analysis of the perfect system, remains the same as before and is given by Equation (3.36).

4.2 Numerical results

In this section, representative numerical examples are presented. The material and section properties used throughout the current chapter are the same as the properties that were used in Chapter 3. Note that the following numerical examples consider the case where global buckling is critical ($L = 5$ m). The continuation and bifurcation software Auto-07p (Doedel & Oldeman, 2011) is again utilized to solve the full equations of equilibrium numerically. The numerical results are presented for an imperfect stiffened plate with an initial out-of-straightness only in terms of the global mode ($q_{s0} \neq 0$ and $A_0 = 0$), and for an imperfect case with both global and local imperfections in the stiffener as well as in the main plate ($q_{s0} \neq 0$ and $A_0 \neq 0$). The results are presented into two limiting values for c_p where the joint between the main plate and the stiffener is described as fully-pinned (*i.e.* $c_p = 0$) and fully-rigid (*i.e.* $c_p \to \infty$).

To find the equilibrium path for the fundamental and post-buckling states, a similar solution strategy is performed as in Chapter 3 (see Figure 3.7), which is illustrated diagrammatically in Figure 4.4. However, for an imperfect panel, the equilibrium path is computed initially from zero axial load and then the load P is increased up to the maximum value where the limit point is detected. The load subsequently drops and the path is asymptotic to the perfect path, as shown in Figure 4.4. Note that, in the case where there is only a global imperfection, the location of the secondary bifurcation point S is obtained in the first run and then the full post-buckling path is generated from this point with branch switching. The case with both initial global and local imperfections, however, only requires a single run without branch switching.

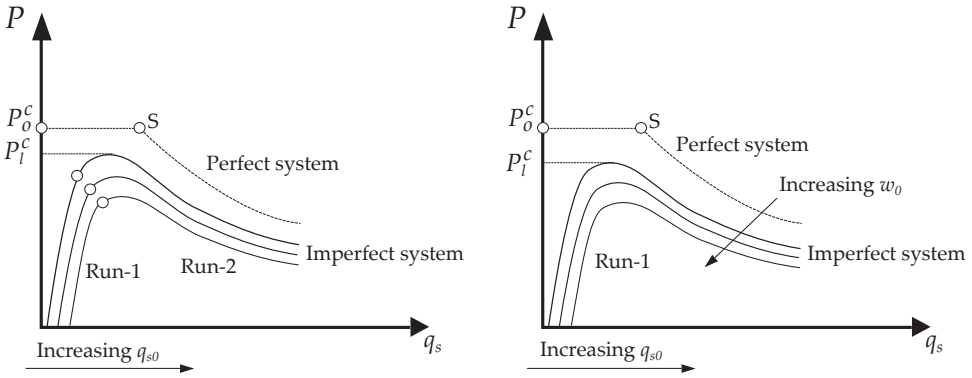

Figure 4.4: Numerical continuation procedures when global buckling is critical with (a) initial out-of straightness q_{s0} only and (b) both q_{s0} and initial out-of-plane displacement w_0 present in the stiffener and the main plate.

4.2.1 Pinned stiffener–plate connection

The study is first conducted for an imperfect system of the stiffened plate with a pinned connection ($c_p = 0$). In this section, two sets of numerical examples are considered. The initial example focuses on the stiffened plate with a global imperfection only with $q_{s0} = 0.001$. However, the second numerical example focuses on the case with both initial global and local imperfections in the stiffener and the main plate, *i.e.* $A_0 \neq 0$. The initial out-of-straightness of the stiffened plate q_{s0} remains the same as in the initial case. The local imperfection amplitude A_0 is $t_s/10$ (= 0.12 mm). Note that for this case, the initial imperfection shape is the first linear eigenmode with $\alpha = 0$ and $\beta = 1$. In addition, the applied imperfection is symmetric about mid-span and therefore η is $L/2$ in both cases. The corresponding numerical results are presented in Figures 4.5–4.8 for the case with a global imperfection only, and Figures 4.9–4.12 are for the case with the combined global and local imperfections. Figures 4.5 and 4.9 show the equilibrium path of the normalized axial load $p = P/P_o^{\mathrm{C}}$ versus (a) the generalized coordinate of the sway component q_s and (b) the maximum out-of-plane normalized deflection of the buckled stiffener ($w_{\max}/t_s$). The graphs in

Figures 4.6 and 4.10 show respectively in (a) the relative amplitudes of global and the local buckling modes and in (b) the relationship between sway q_s and tilt q_t components of the global buckling mode, which are almost equal; this indicates again that the shear strain is small but, importantly, not zero. Figures 4.7 and 4.11 illustrate the corresponding progression of the numerical solutions for the local buckling functions w and u for the secondary bifurcation point S and cells C_2–C_8. Furthermore, a selection of 3-dimensional representations of the deflected stiffened plate are illustrated in Figures 4.8 and 4.12 respectively. These graphs correspond to specific states on the equilibrium path labelled as C_2, C_4, C_6 and C_8.

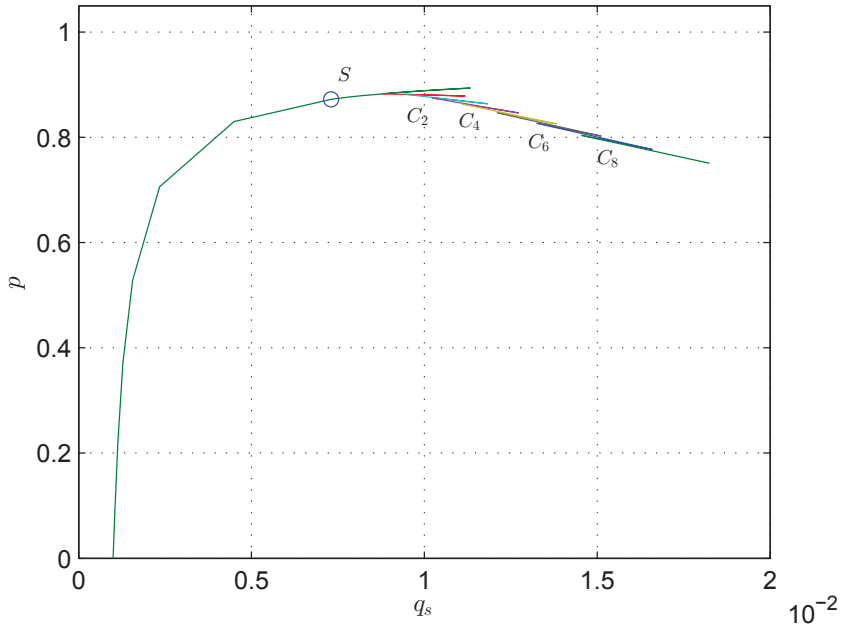

(a)

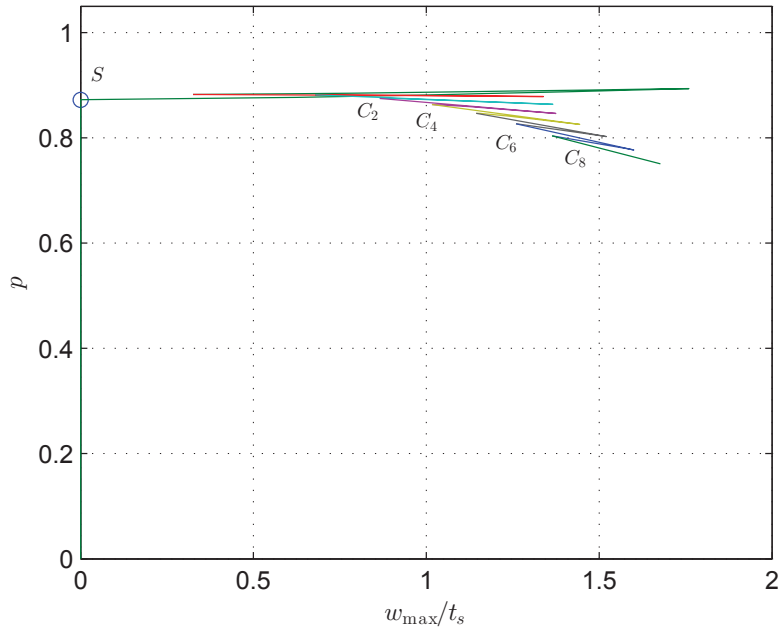

(b)

Figure 4.5: Numerical equilibrium paths for the pinned case ($c_p = 0$ Nmm/mm) where $q_{s0} \neq 0$ and $w_0 = 0$; normalized force ratio p ($= P/P_o^{\mathrm{C}}$) versus (a) the sway amplitude q_s and (b) the normalized maximum out-of-plane deflection of the stiffener $w_{\max}/t_s$.

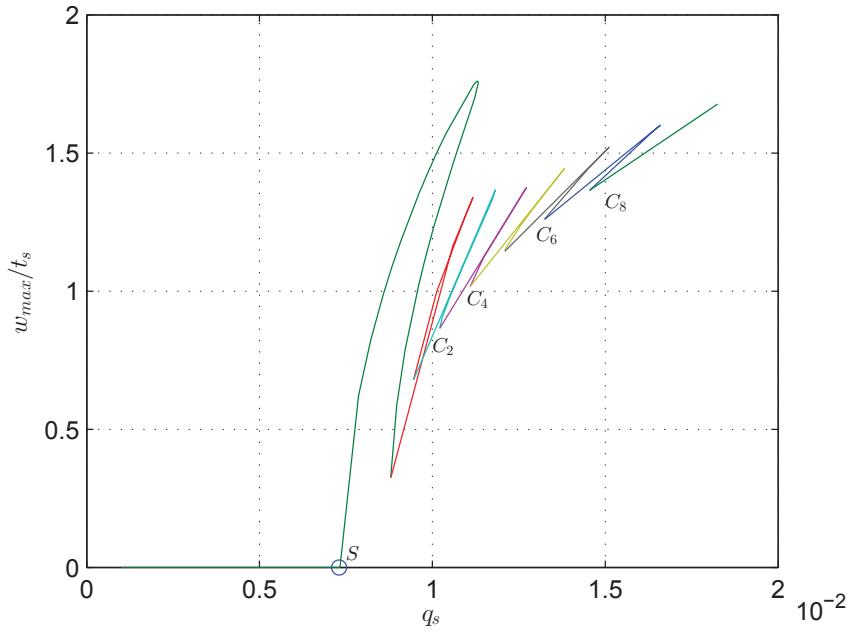

(a)

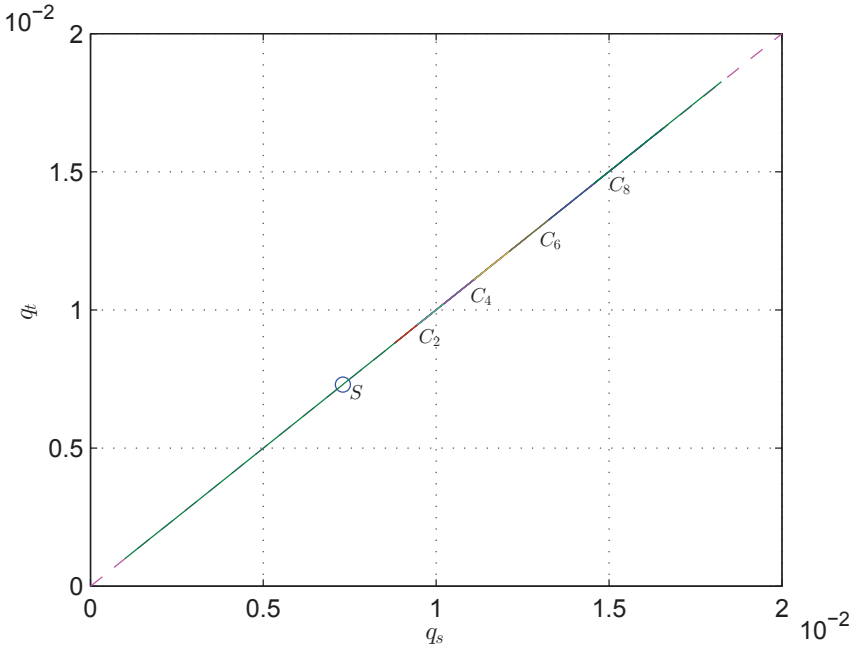

(b)

Figure 4.6: Numerical equilibrium paths for $c_p = 0$ Nmm/mm where $q_{s0} \neq 0$ and $w_0 = 0$: (a) local versus global modes: $w_{\max}/t_s$ versus q_s; (b) amplitudes of sway q_s versus tilt q_t with the dashed line showing $q_s = q_t$.

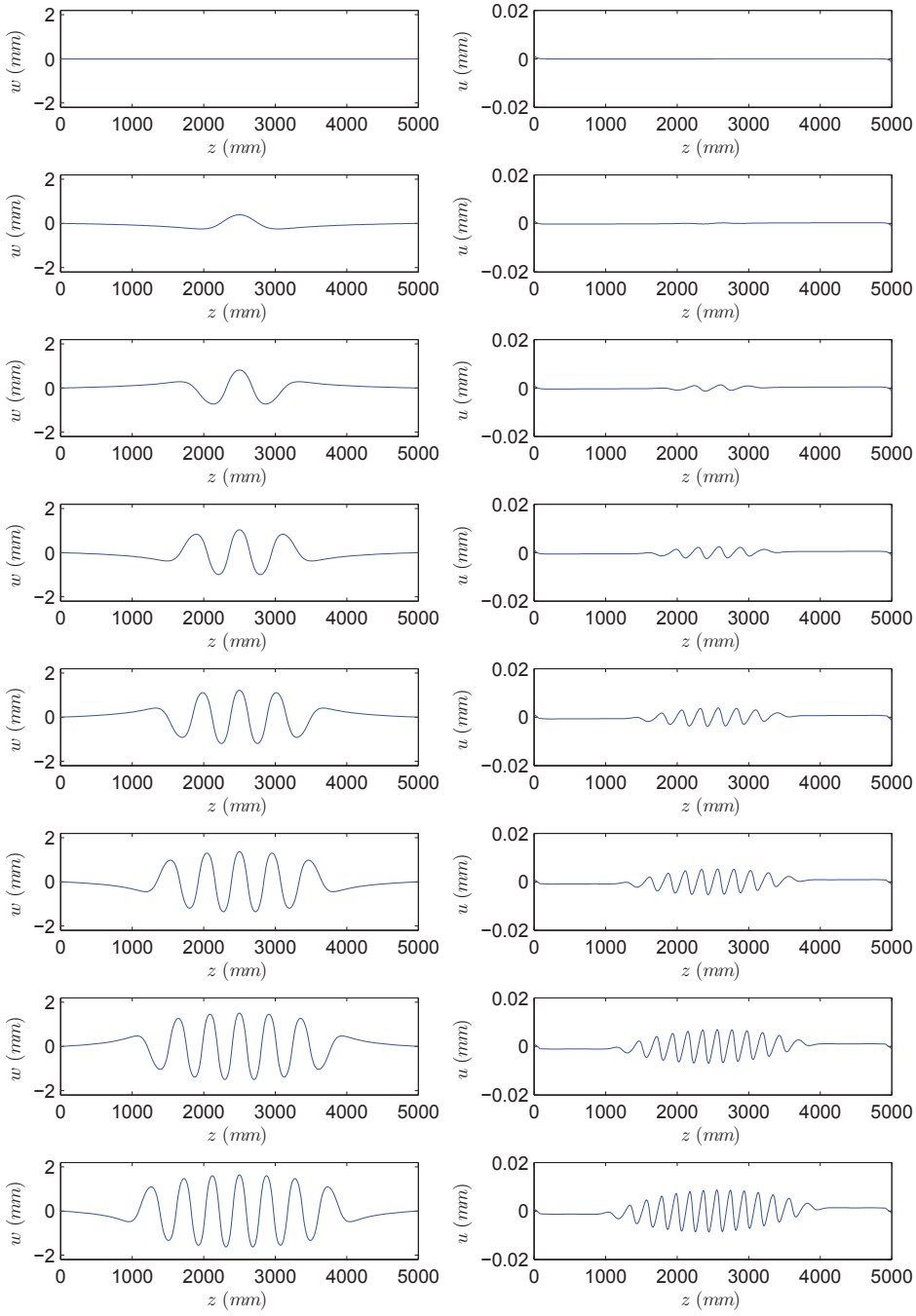

Figure 4.7: Numerical solutions for the local out-of-plane deflection w (left) and the local in-plane deflection u (right) with $c_p = 0$ Nmm/mm, where $q_{s0} \neq 0$ and $w_0 = 0$, shown for the equilibrium paths at the secondary bifurcation point S and cells C_2–C_8 from top to bottom respectively.

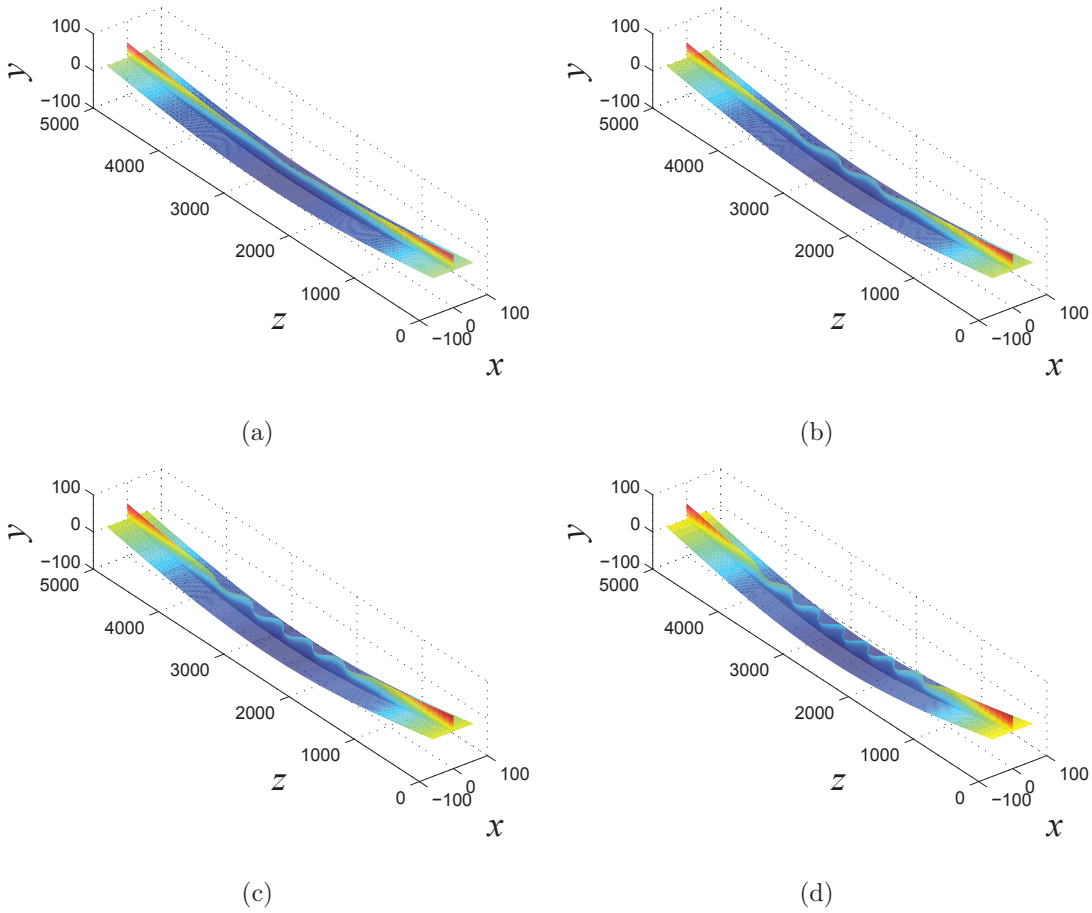

Figure 4.8: Numerical solutions from the analytical model with $c_p = 0$ Nmm/mm visualized on 3-dimensional representations of the stiffened plate where $q_{s0} \neq 0$ and $w_0 = 0$. (a) cell C_2 ($p = 0.8827$) (b) cell C_4 ($p = 0.8750$), (c) cell C_6 ($p = 0.8468$) and (d) cell C_8 ($p = 0.8036$). All dimensions are in millimetres, but the local buckling displacements in the stiffener are scaled by a factor of 5 to aid visualization.

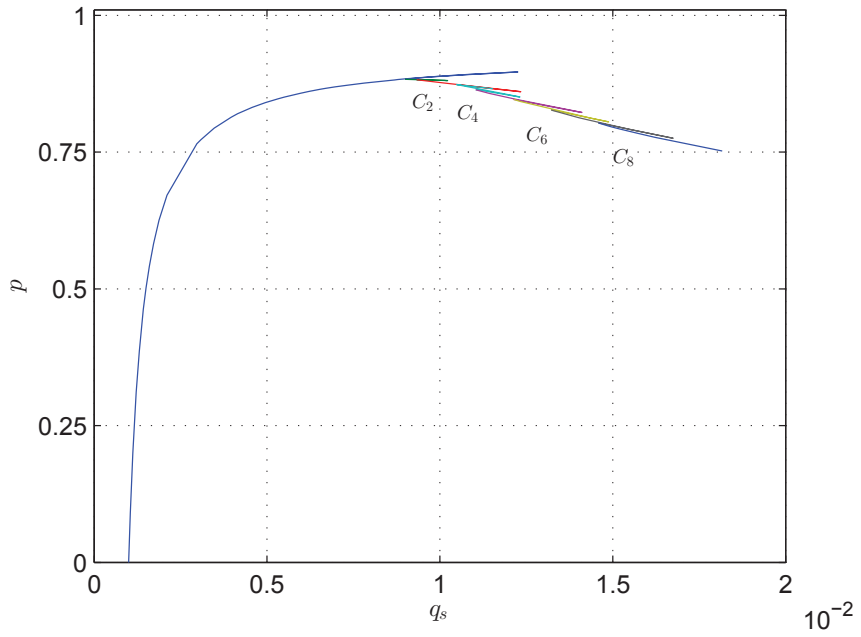

(a)

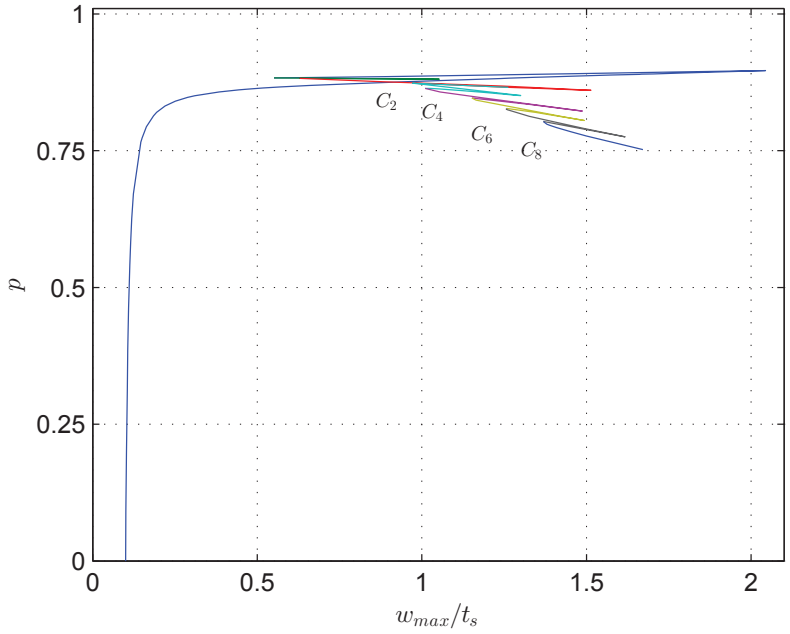

(b)

Figure 4.9: Numerical equilibrium path for $c_p = 0$ Nmm/mm where $q_{s0} \neq 0$ and $w_0 \neq 0$: Normalized force ratio p versus (a) the sway amplitude q_s and (b) the normalized maximum out-of-plane deflection of the stiffener $w_{\max}/t_s$.

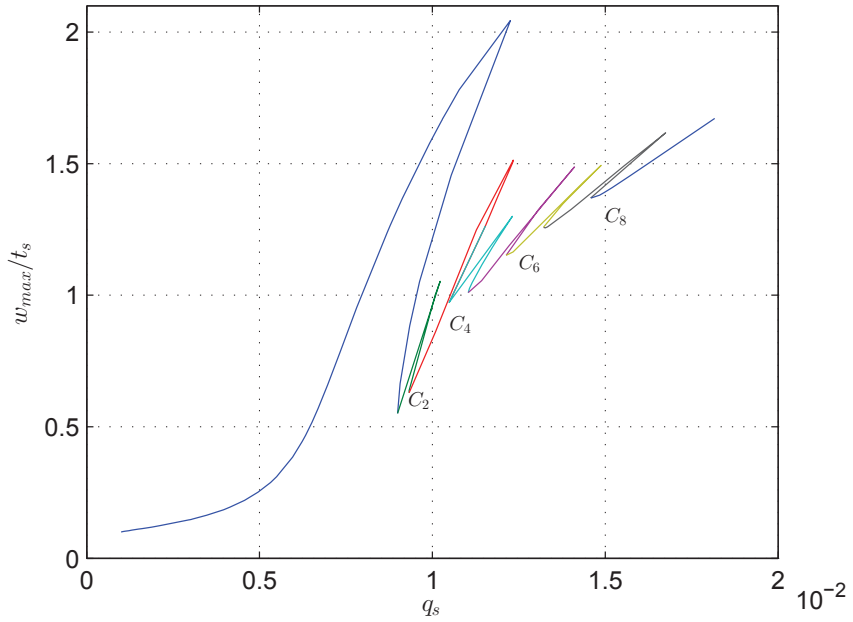

(a)

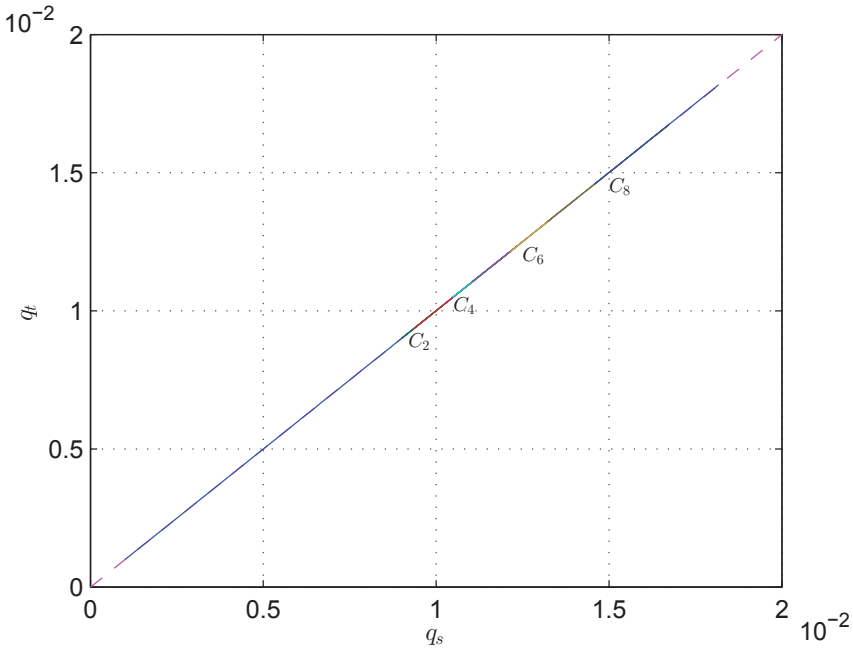

(b)

Figure 4.10: Numerical equilibrium paths for $c_p = 0$ Nmm/mm where $q_{s0} \neq 0$ and $w_0 \neq 0$. (a) Local versus global modes: $w_{\max}/t_s$ versus q_s; (b) amplitudes of sway q_s versus tilt q_t with the dashed line showing $q_s = q_t$.

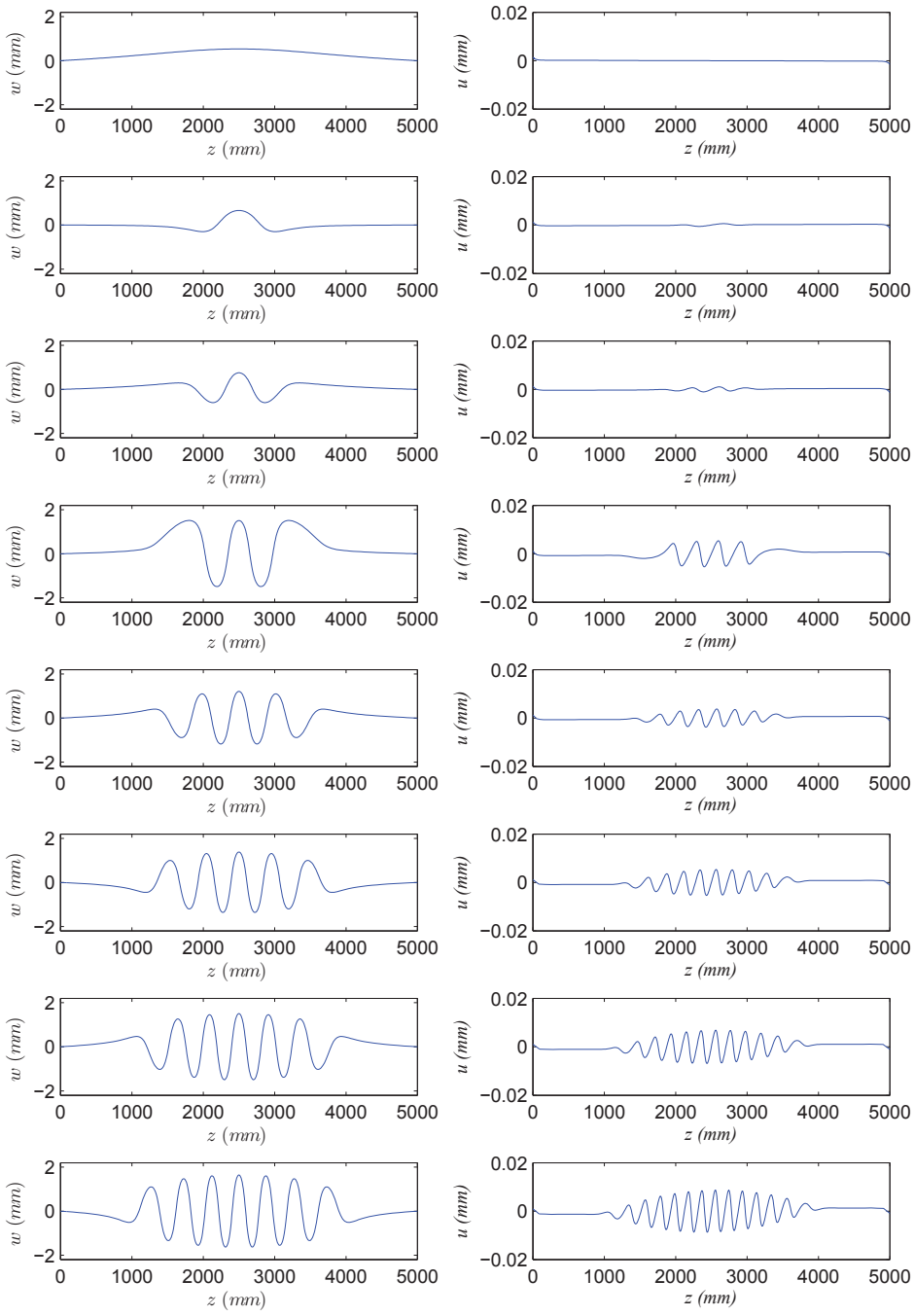

Figure 4.11: Numerical solutions for the local out-of-plane deflection w (left) and the local in-plane deflection u (right) with $c_p = 0$ Nmm/mm where $q_{s0} \neq 0$ and $w_0 \neq 0$; for the equilibrium paths at the secondary bifurcation point S and cells C_2–C_8 from top to bottom respectively.

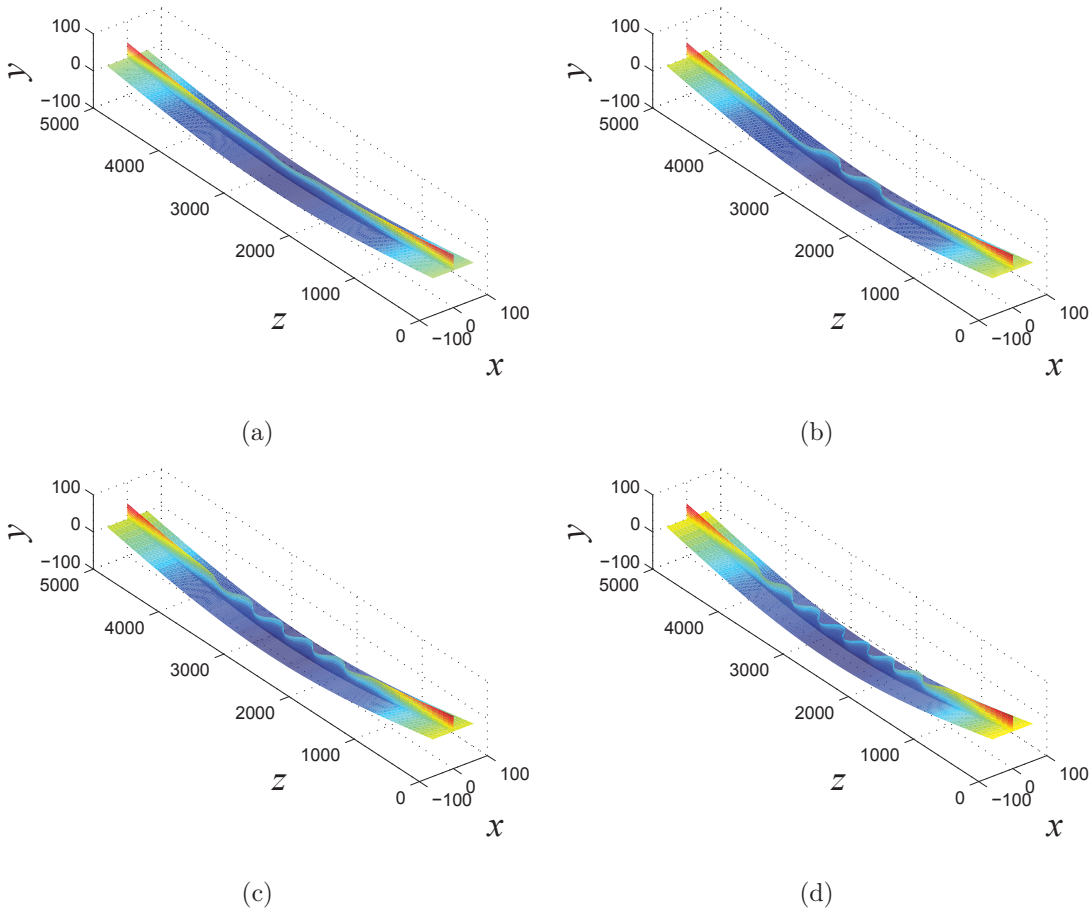

Figure 4.12: Numerical solutions from the analytical model with $c_p = 0$ Nmm/mm visualized on 3-dimensional representations of the stiffened plate where $q_{s0} \neq 0$ and $w_0 \neq 0$. (a) cell C_2 ($p = 0.8832$), (b) cell C_4 ($p = 0.8658$), (c) cell C_6 ($p = 0.8462$) and (d) cell C_8 ($p = 0.8031$). All dimensions are in millimetres, but the local buckling displacements in the stiffener are scaled by a factor of 5 to aid visualization.

4.2.2 Rigid stiffener–plate connection

The analytical model for the perfect system of the stiffened plate with a fully rigid connection for the stiffener to the main plate (*i.e.* $c_p \to \infty$) was developed in Chapter 3. The same material and section properties are used in the following numerical exam-

ples. In this section, two sets of numerical examples are considered. As in the previous section, the initial example focuses on the structure with a global imperfection only but the second set contains both global and local imperfections in the stiffener and the main plate. In these cases, the amount of q_{s0} and A_0 remain the same as in the previous section. However, in this case, $\alpha = 3$, $\beta = 53$ and $\eta = L/2$ for w_0. This form for w_0 is used since it replicates the interactive buckling mode relatively close to the secondary instability. The corresponding numerical results are presented in Figures 4.13–4.16 for the case with a global imperfection only, and Figures 4.17–4.20 are for the case with the combined global and local imperfections. Figures 4.13 and 4.17 show the equilibrium path of the normalized axial load $p = P/P_o^{\mathrm{C}}$ versus (a) the generalized coordinate of the sway component q_s and (b) the maximum out-of-plane normalized deflection of the buckled stiffener ($w_{\max}/t_s$). The graphs in Figures 4.14 and 4.18 show respectively in (a) the relative amplitudes of the global and the local buckling modes and in (b) the relationship between sway q_s and tilt q_t components of the global buckling mode, which again are almost equal. Figures 4.15 and 4.19 respectively illustrate the corresponding progression of the numerical solutions for the local buckling functions w and u for the secondary bifurcation point S and cells C_2–C_8. Furthermore, a selection of 3-dimensional representations of the deflected stiffened plate are shown in Figures 4.16 and 4.20 respectively.

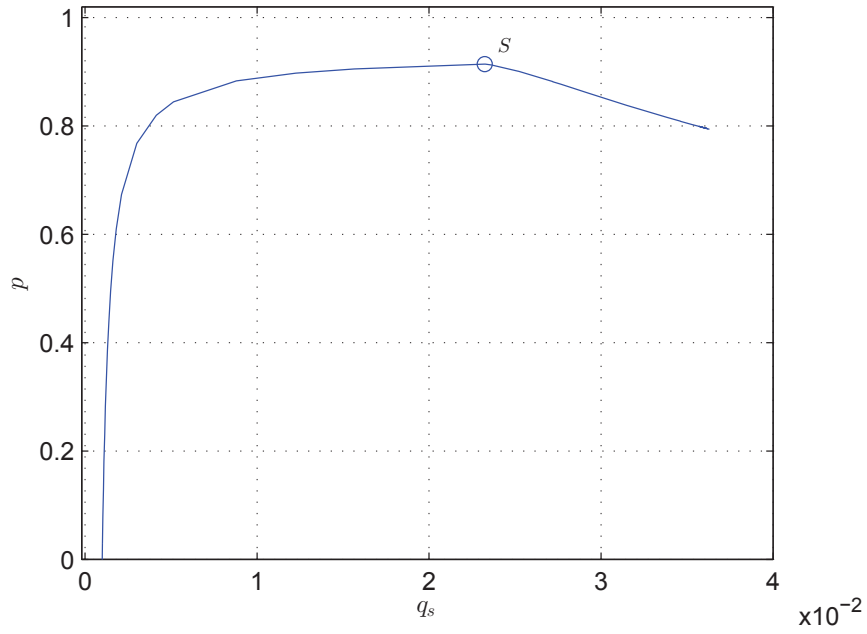

(a)

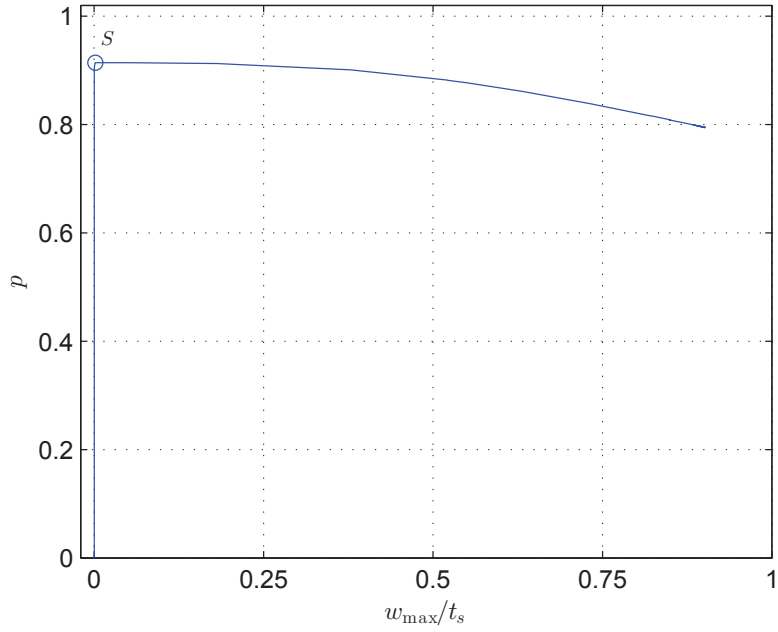

(b)

Figure 4.13: Numerical equilibrium paths for the rigid case ($c_p \to \infty$) where $q_{s0} \neq 0$ and $w_0 = 0$; normalized force ratio p ($= P/P_o^{\mathrm{C}}$) versus (a) the sway amplitude q_s and (b) the normalized maximum out-of-plane deflection of the stiffener $w_{\max}/t_s$.

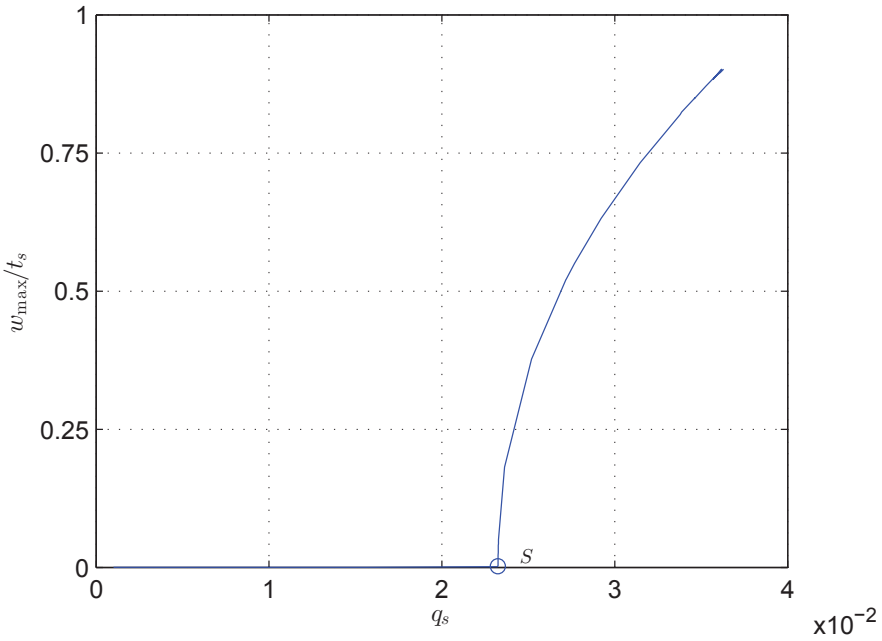

(a)

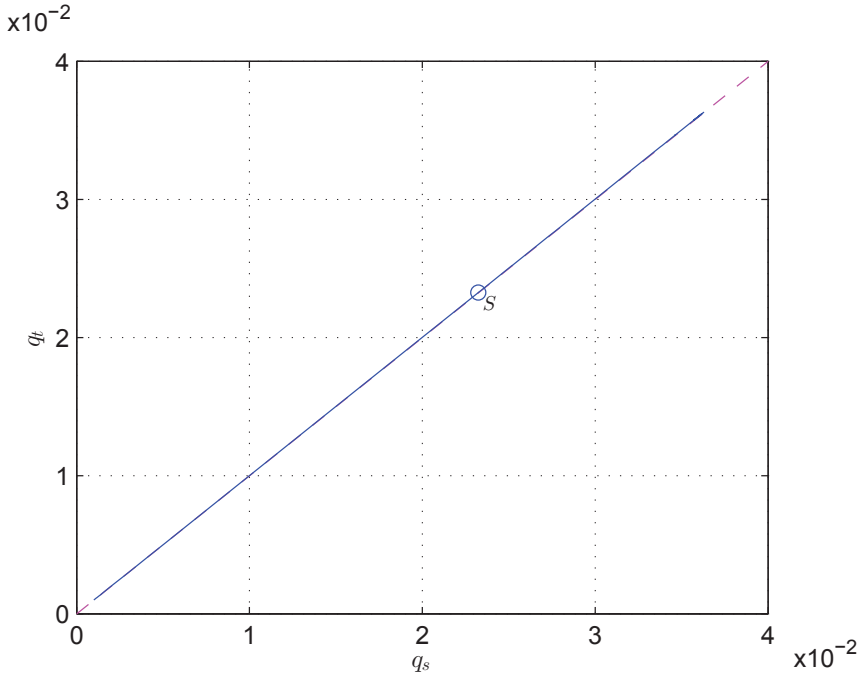

(b)

Figure 4.14: Numerical equilibrium paths for $c_p \to \infty$ where $q_{s0} \neq 0$ and $w_0 = 0$: (a) local versus global modes: $w_{\max}/t_s$ versus q_s; (b) amplitudes of sway q_s versus tilt q_t with the dashed line showing $q_s = q_t$.

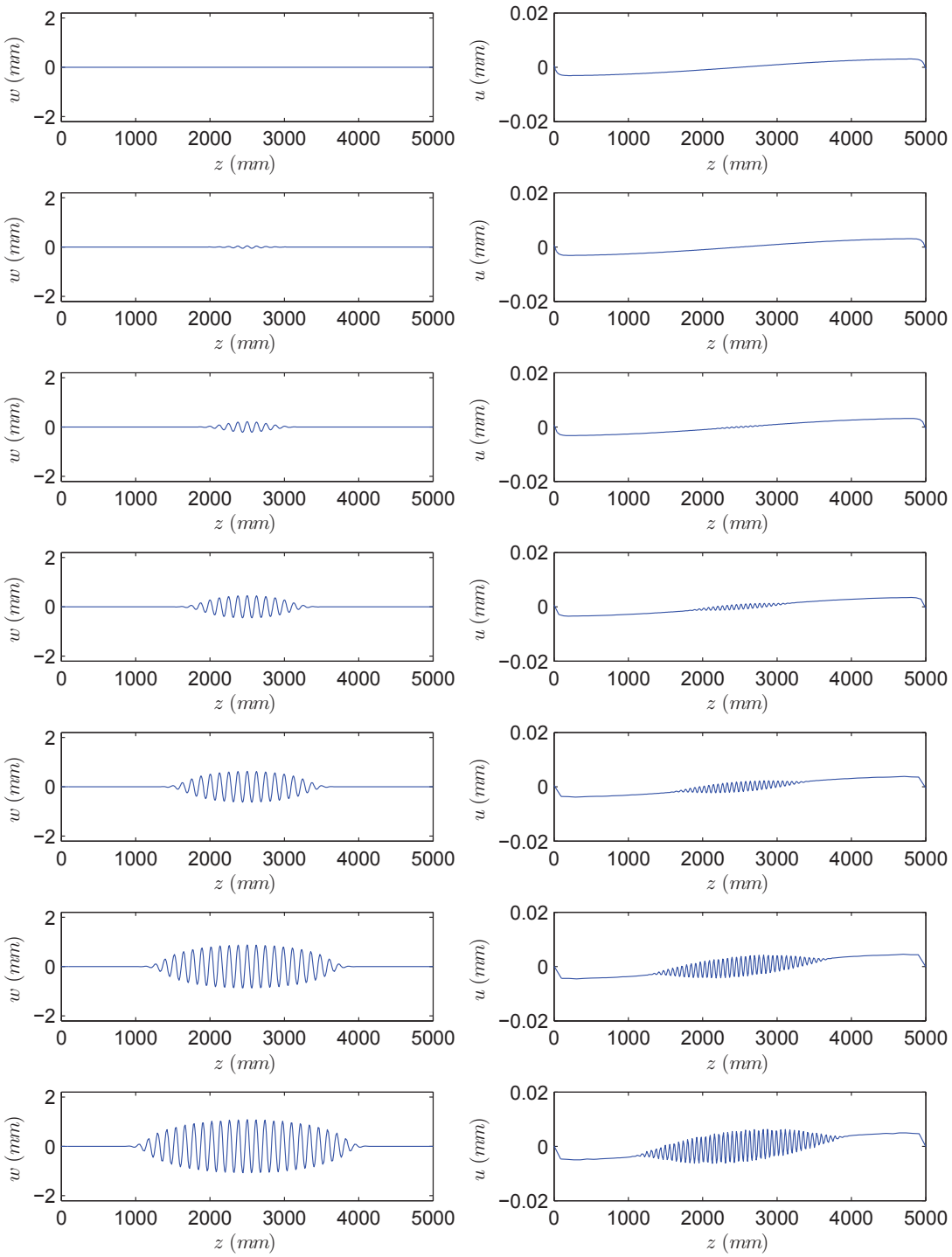

Figure 4.15: Numerical solutions for the local out-of-plane deflection w (left) and the local in-plane deflection u (right) with $c_p \to \infty$ where $q_{s0} \neq 0$ and $w_0 = 0$.

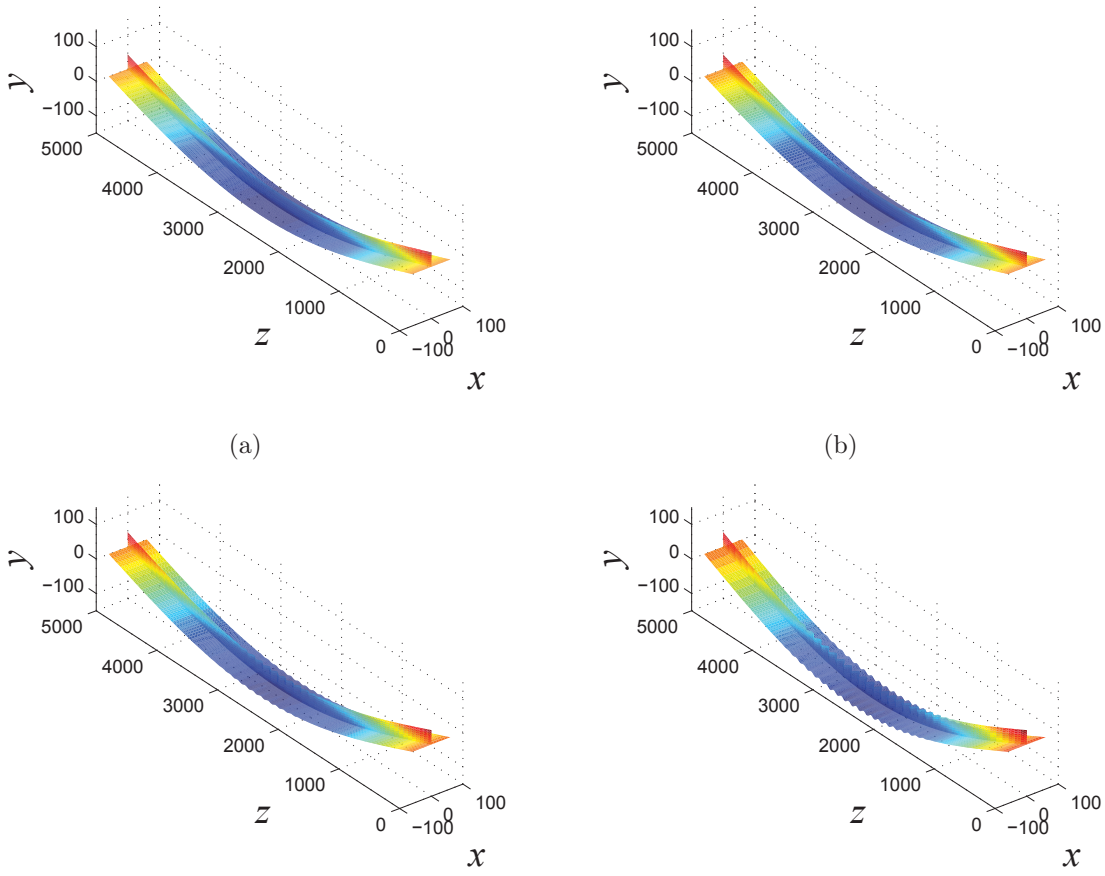

(a) (b)

(c) (d)

Figure 4.16: Numerical solutions from the analytical model with $c_p \to \infty$ visualized on 3-dimensional representations of the stiffened plate where $q_{s0} \neq 0$ and $w_0 = 0$ for the normalized load levels equal to(a) $p = 0.9141$, (b) $p = 0.9124$, (c) $p = 0.9001$ and (d) $p = 0.8384$. All dimensions are in millimetres, but the local buckling displacements in the stiffener and the main plate are scaled by a factor of 3 to aid visualization.

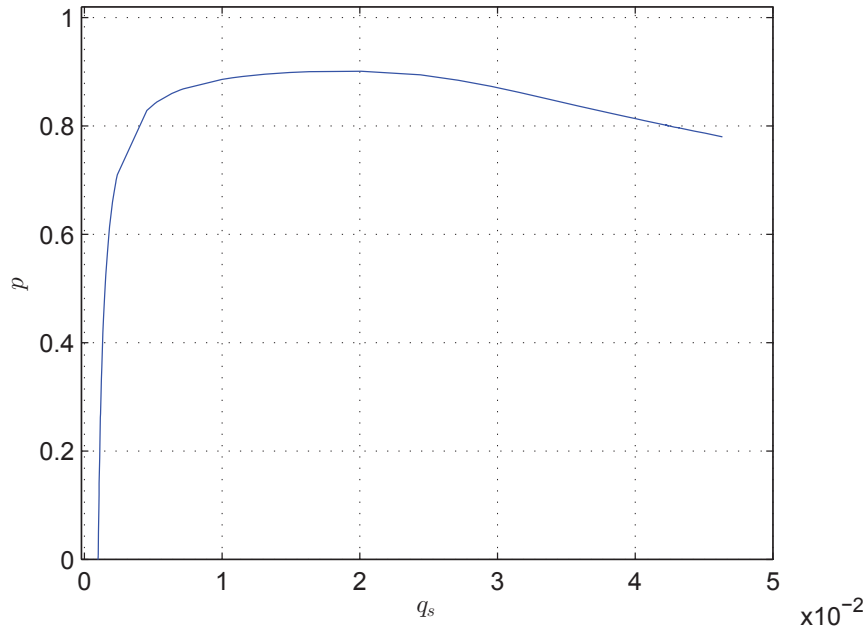

(a)

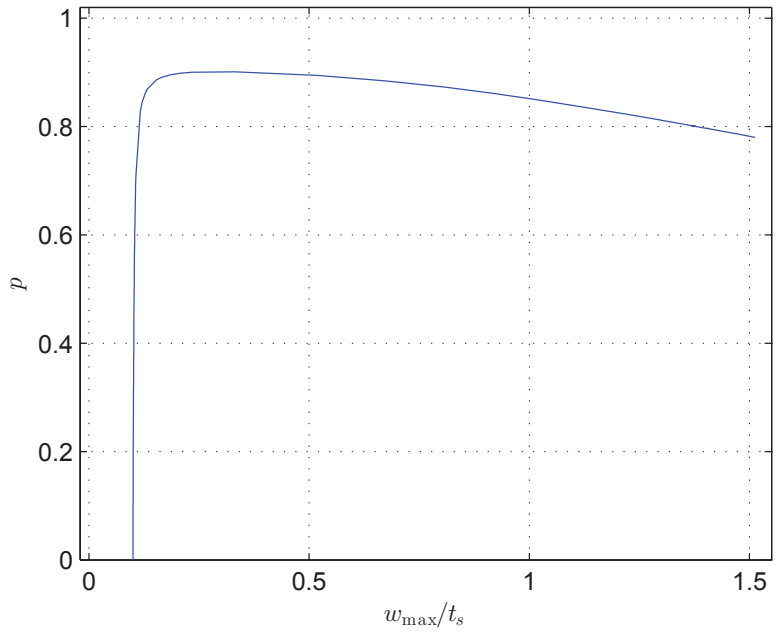

(b)

Figure 4.17: Numerical equilibrium paths for $c_p \to \infty$ where $q_{s0} \neq 0$ and $w_0 \neq 0$; normalized force ratio p versus (a) the sway amplitude q_s and (b) the normalized maximum out-of-plane deflection of the stiffener $w_{\max}/t_s$.

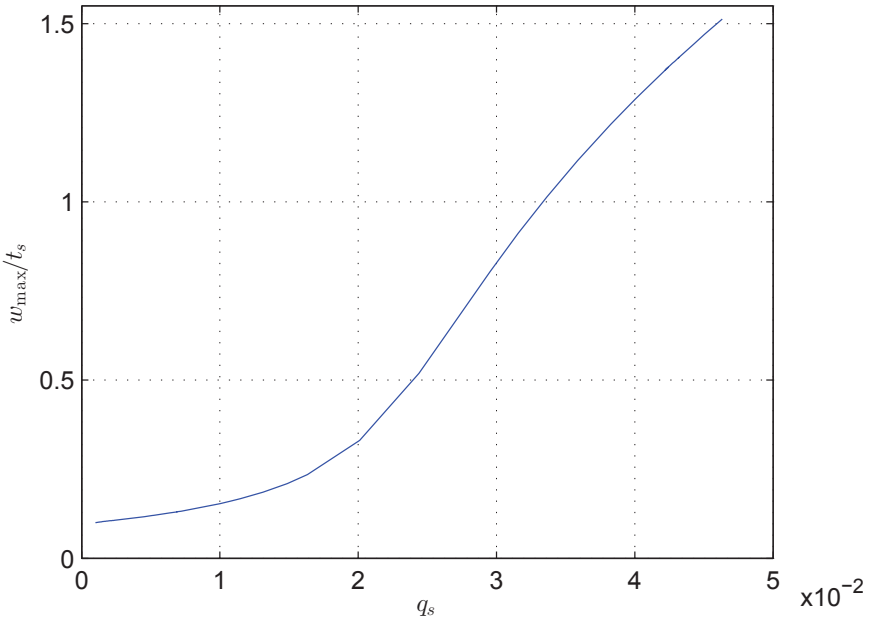

(a)

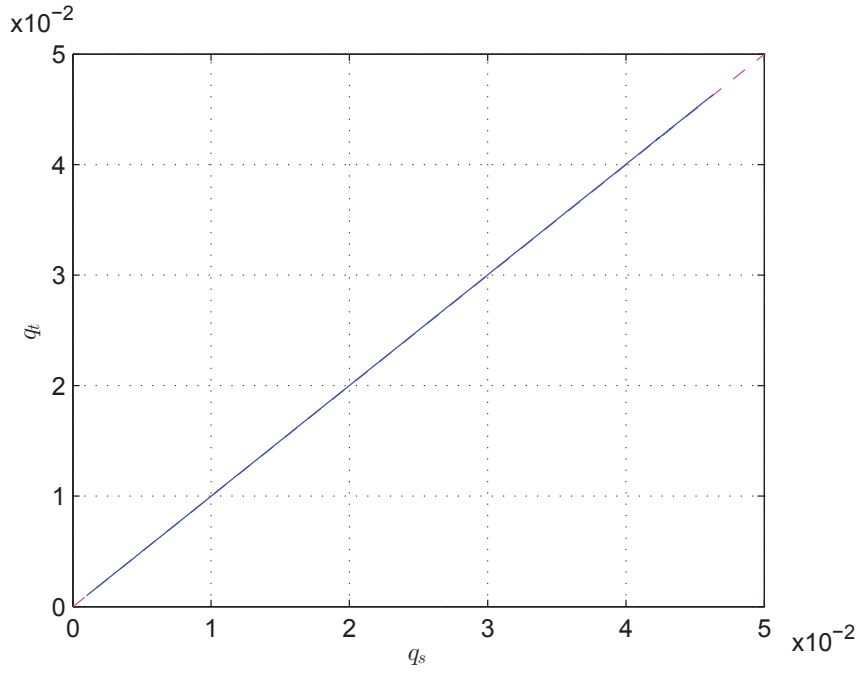

(b)

Figure 4.18: Numerical equilibrium paths for $c_p \to \infty$ where $q_{s0} \neq 0$ and $w_0 \neq 0$. (a) Local versus global modes: $w_{\max}/t_s$ versus q_s; (b) amplitudes of sway q_s versus tilt q_t with the dashed line showing $q_s = q_t$.

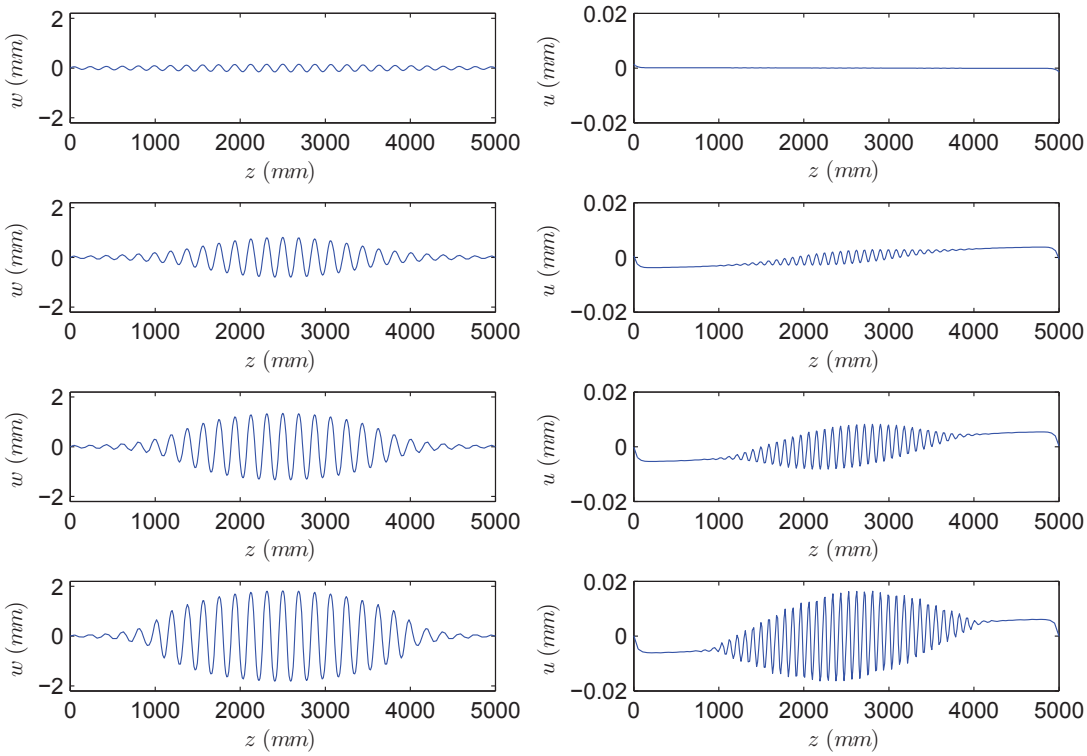

Figure 4.19: Numerical solutions for the local out-of-plane deflection w (left) and the local in-plane deflection u (right) with $c_p \to \infty$ where $q_{s0} \neq 0$ and $w_0 \neq 0$. The normalized load level p is equal to 0.8845, 0.8657, 0.8369 and 0.7800 from top to bottom respectively.

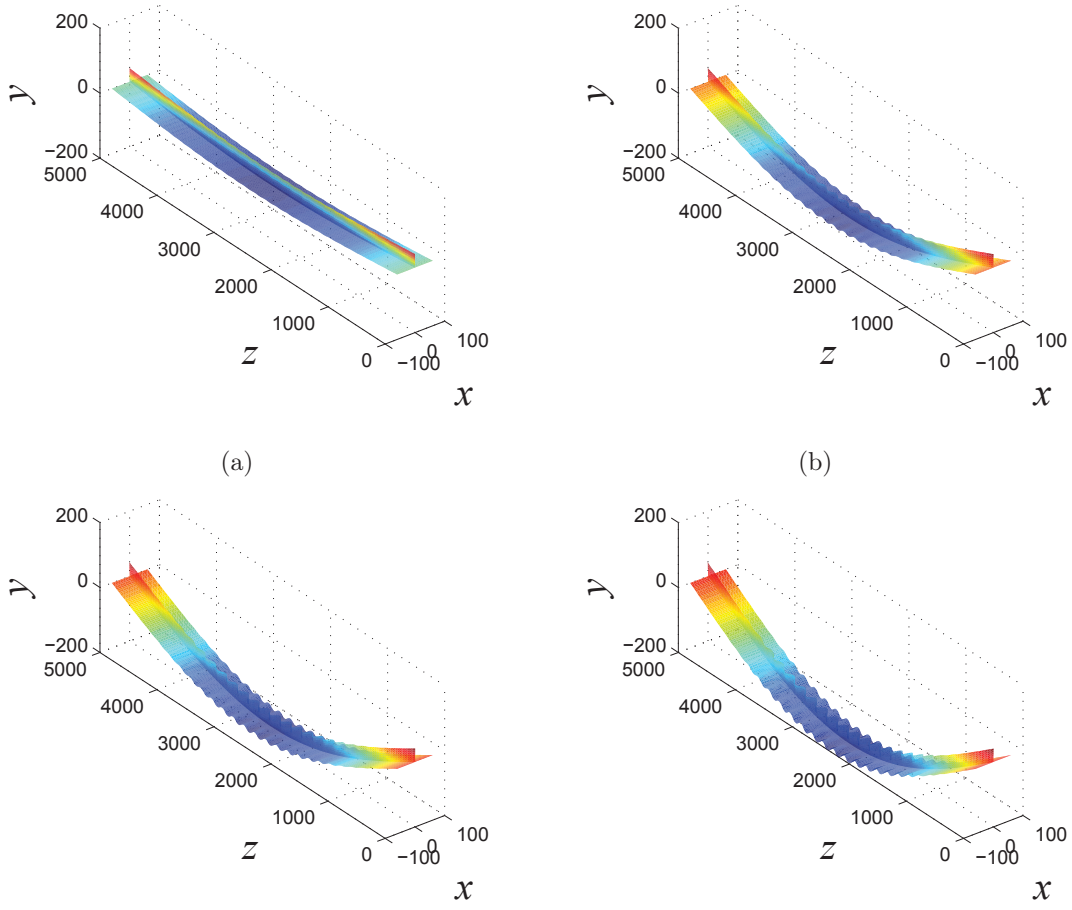

Figure 4.20: Numerical solutions from the analytical model with $c_p \to \infty$ visualized on 3-dimensional representations of the stiffened plate where $q_{s0} \neq 0$ and $w_0 \neq 0$. All dimensions are in millimetres, but the local buckling displacements in the stiffener and the main plate are scaled by a factor of 3 to aid visualization.

The work-done expression given in Equation (4.21), provides the expression for the total end shortening $\mathcal{E}$ given by:

$$\mathcal{E} = \int_0^L \left[\Delta + \frac{1}{2} q_s^2 \pi^2 \cos^2 \frac{\pi z}{L} - \left(\frac{h_2 + \bar{y}}{h_1 + h_2} \right) \dot{u} \right] \mathrm{d}z. \tag{4.32}$$

Figures 4.21 and 4.22, show the normalized axial load p versus the normalized total end-shortening $\mathcal{E}/L$ for the stiffened plate with pinned and rigid main plate–stiffener connections respectively. The corresponding graphs in (a) are for the case with the global imperfection only and in (b) with both the global and local imperfections. It is clearly observed that at the same load level, the normalized end-shortening $\mathcal{E}/L$ has a larger value when c_p tends to infinity.

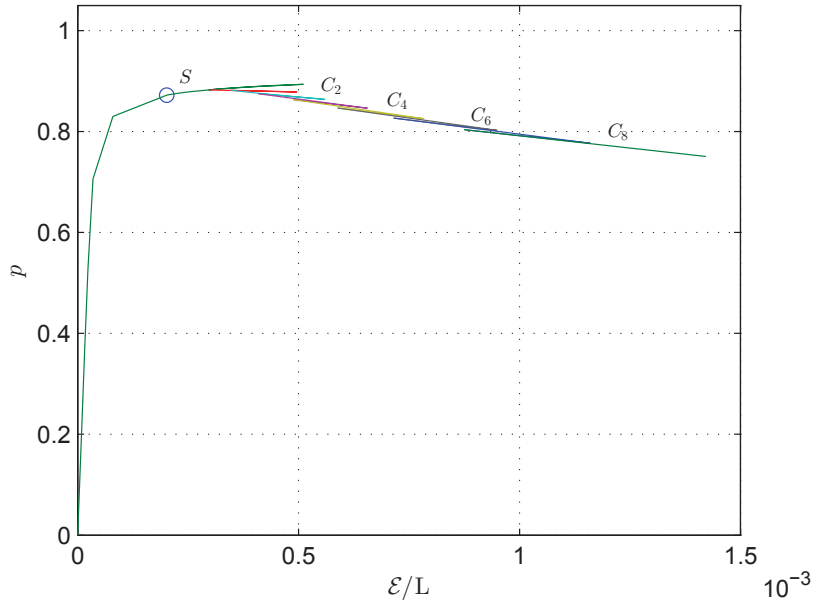

(a)

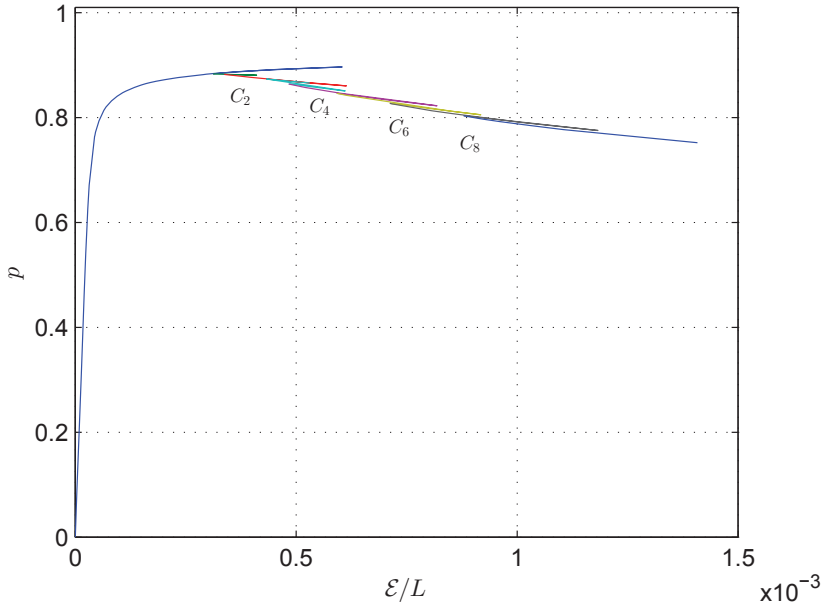

(b)

Figure 4.21: Numerical equilibrium paths for the pinned case ($c_p = 0$). It shows the normalized load p versus the normalized end-shortening $\mathcal{E}/L$ for the case with (a) the global imperfection only ($q_{s0} \neq 0$ and $w_0 = 0$) and (b) both global and local imperfections ($q_{s0} \neq 0$ and $w_0 \neq 0$).

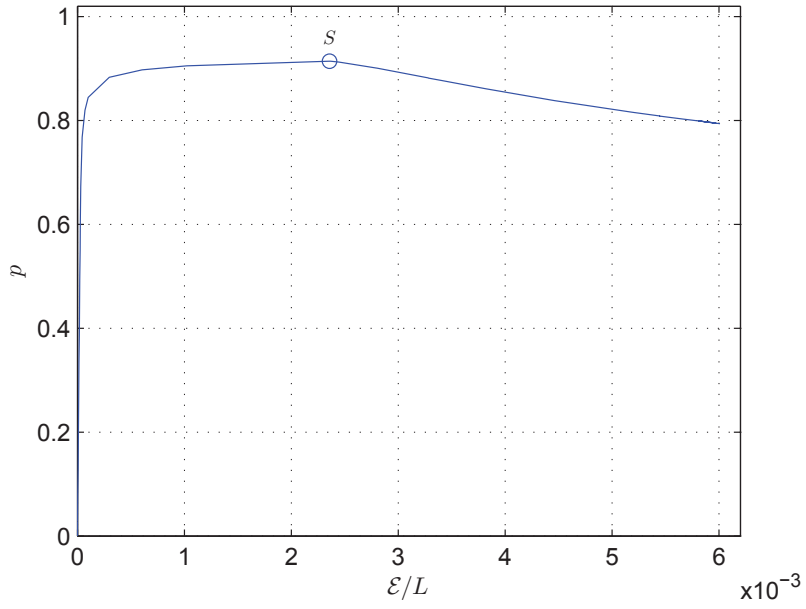

(a)

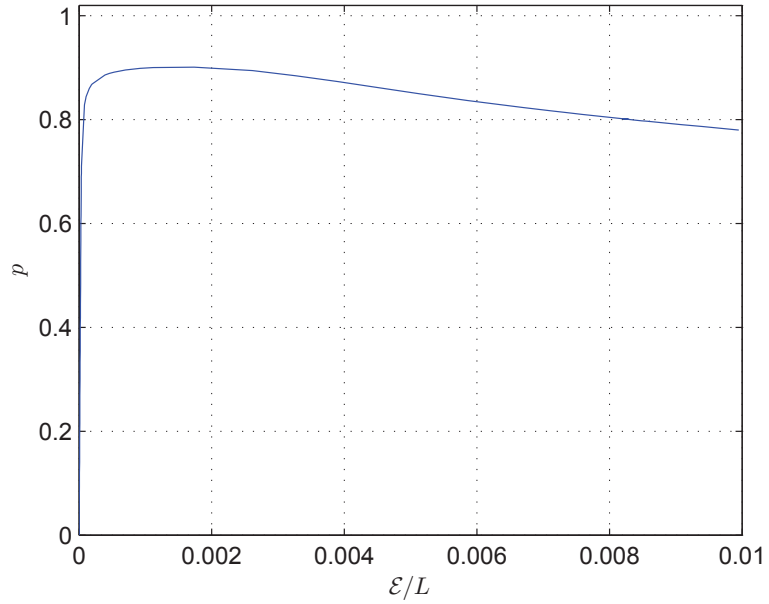

(b)

Figure 4.22: Numerical equilibrium path for the rigid case ($c_p \to \infty$). It shows the normalized load p versus the normalized end-shortening $\mathcal{E}/L$ for the case with (a) the global imperfection only ($q_{s0} \neq 0$ and $w_0 = 0$) and (b) both global and local imperfections ($q_{s0} \neq 0$ and $w_0 \neq 0$).

4.3 Concluding remarks

A nonlinear analytical model for an axially-loaded thin-walled stiffened plate in Chapter 3 has been developed by including the local deflection of the main plate in the formulation. In addition, an initial global out-of-straightness and local out-of-plane displacement of the stiffener and the main plate were also considered. Significant reduction in the load-carrying capacity was observed for the structure with a small initial global imperfection or both global and local imperfection components. A rapid increase in the normalized end-shortening of the strut $\mathcal{E}/L$ when the c_p value tends to infinity was also found.

In the next chapter, the studied analytical models presented hitherto are validated against physical experiments from the literature as well as finite element models formulated in the commercial code Abaqus (2011).

Chapter 5

Validation of analytical models

The analytical model of the perfect and imperfect stiffened plate are now validated by comparing the model results against results from physical experiments from the literature as well as using finite element analysis conducted in the commercial code ABAQUS (2011). The continuation and bifurcation software AUTO-07P (Doedel & Oldeman, 2011) is used to solve the system of equilibrium equations presented in the previous chapters. Once validated, the analytical model can be exploited to determine imperfection sensitivity and the zone where the mode interaction is the strongest.

An axially loaded portion representative of a stiffened plate with length L, stiffener heights h_1 and h_2 at the top and the bottom of the main plate respectively with thickness t_s and the main plate breadth b with thickness t_p is considered. Sets of section and material properties is chosen in each of the following examples. The same coordinate system, as in previous chapters, is used currently as was shown in Figure 3.2. The global critical load P_o^{C} is again calculated using Equation (3.36), whereas the local buckling critical stress σ_l^C is evaluated using the well-known formula expressed in Equation (2.26), where the coefficient k_p depends on plate buckling conditions. Since the rotational spring with stiffness c_p again represents the relative rigidity at

the main plate–stiffener junction, by increasing the c_p value, the relative rigidity can vary from being pinned ($c_p = 0$) to being fully-fixed ($c_p \to \infty$). However, the value of the global critical buckling load, P_o^{C} remains the same, since it is independent of c_p. To find the equilibrium path in the fundamental and post-buckling states, a similar solution strategy is performed as in previous chapters for the perfect and imperfect cases, as described in Figures 3.6 and 4.4 respectively.

5.1 Finite element modelling

In this section, the numerical results from the analytical model are compared to the results from the numerical model using finite element (FE) analysis facilitated by the commercial software Abaqus (2011). Consider an axially loaded stiffened plate with cross-section and material properties as was shown in Table 3.1. The two parts of the stiffened plate, *i.e.* the stiffener and the main plate, were modelled separately with linear quadrilateral $S4R$ elements with an 8 mm mesh along the panel (see later).

The stiffener and the main plate were then tied together at their junction. To model the fully-pinned connection (*i.e.* when $c_p = 0$), the rotational degree of freedom in the z direction was released with the tie constraint. In the semi-rigid case as well as the fully-rigid main plate–stiffener connection case, a series of linear rotational spring elements was modelled along the length of the strut at each node with the exception of the nodes at the supports to avoid clashes with the boundary conditions. The rotational springs all had the same stiffness equal to mc_p, where m is the mesh size. They restrain the rotation about the longitudinal axis z.

The stiffened plate was modelled with simply supported boundary conditions at the supports. The corresponding boundary conditions at the ends, restrained the displacement in the x and y directions and the rotation about the y and z axes. It is

worth noting that the half length was simulated to retain symmetry. Therefore, an appropriate boundary condition, with reference "ZSYMM" was also applied at mid-span. Consequently, the axial displacement in the z direction, u, was zero as well as the rotations about x and y axes. Since the stiffened plate is part of a multi-stiffener panel, there is a compatible boundary condition for the main plate edges as explained in Chapter 4. Therefore, the main plate displacement in the x-direction and rotations in the y and z-directions were restrained in the FE model. The axial load was applied at the centroid of the whole cross-section which generated a uniform in-plane pressure on the stiffened plate (see Figure 5.1). The FE analysis procedure in Abaqus is also illustrated as a flowchart in Figure 5.2.

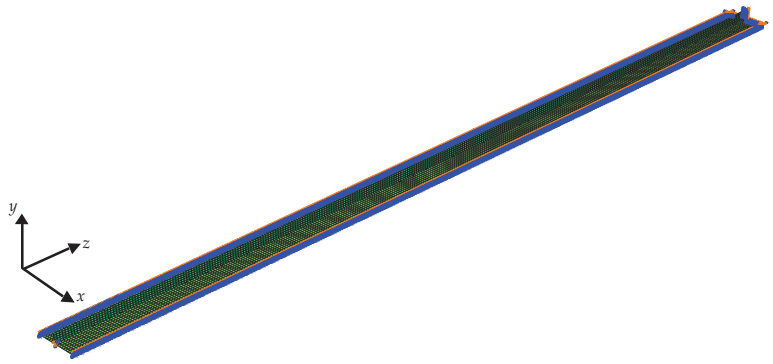

Figure 5.1: FE model for a simply-supported and axially loaded stiffened plate in Abaqus. The FE model is shown for half of the strut length.

Once the model was constructed, a linear eigenvalue buckling analysis was conducted to estimate the critical buckling load. This type of analysis is a linear perturbation procedure, and the buckling load is calculated relative to the fundamental state of the structure. The Riks method (Riks, 1972), with reference "STATIC, RIKS" in

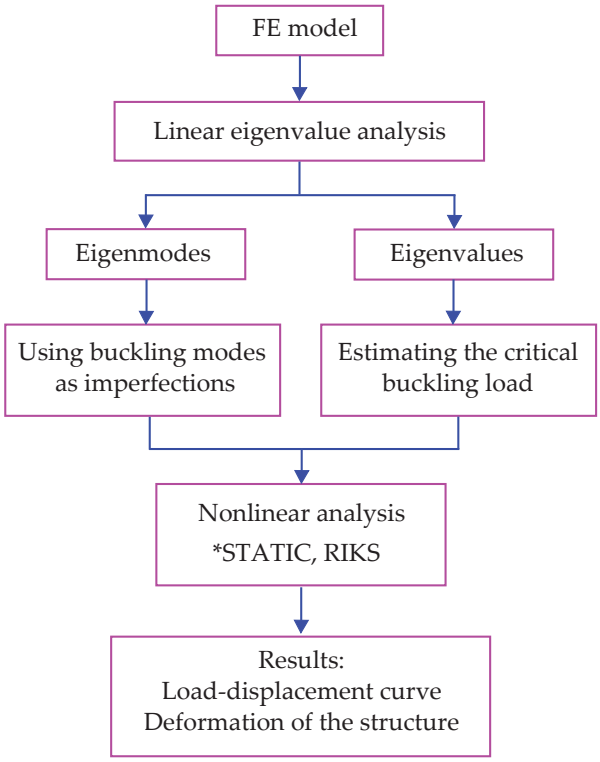

Figure 5.2: FE analysis procedure in Abaqus.

the Abaqus commands, was then used to determine the post-buckling path. The command "STEP, NLGEOM" was applied to account for geometric nonlinearities. An initial imperfection from the linear eigenvalue analysis was applied to the perfect geometry so that there was some displacement prior to the critical load being reached. Thus the post-buckling analysis was based on the initial imperfection in the stiffened plate obtained from introducing an initial displacement that was affine to the solution of the eigenvalue buckling analysis.

A mesh sensitivity study was conducted on the FE model in order to optimize the simulation. The graph in Figure 5.3 shows the normalized critical load $p = P/P_o^{\mathrm{C}}$ from the numerical simulation in Abaqus against mesh size m. It was found that the mesh size $m = 8$ mm provides a sufficiently high degree of accuracy versus computational costs. The total number of elements in the stiffener and the main plate were 1565

and 5008 respectively. Although by decreasing the mesh size to less than 8 mm the results become more accurate, but the mesh sensitivity results show that the error for the critical load is approximately 0.6% for the 8 mm mesh. Moreover, halving the mesh size does not change the error very much but increases computation time considerably.

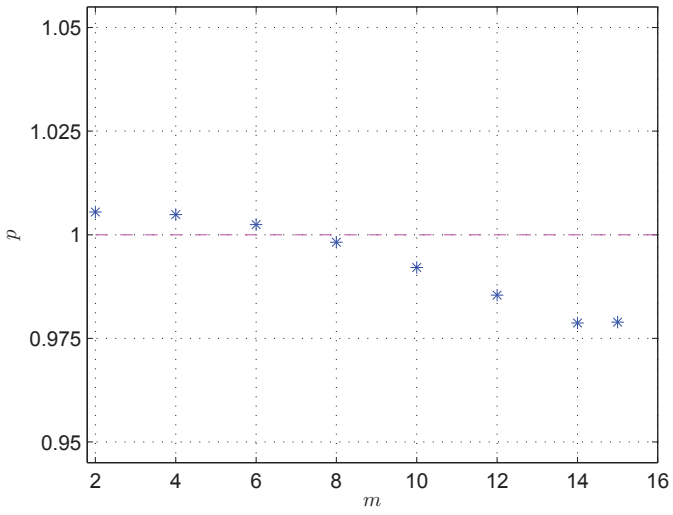

Figure 5.3: Mesh sensitivity study from the numerical FE model in Abaqus. Comparison of the global critical buckling load versus the mesh size m.

In the current validation study, the focus is on intermediate and large values of the rotational stiffness c_p in order to simulate semi-rigid and fully-rigid connections respectively. In the analytical equations, c_p is the rotational stiffness per unit length and since it is assumed to be uniform along the length of the stiffened plate, the total rotational stiffness is thus: $c_p L$. However, in the finite element model, since the rotational spring is applied at each individual node along the length with the same stiffness, the total stiffness of the spring element in the numerical model is therefore mc_p.

5.1.1 Perfect stiffened plate

In this section, numerical results from the analytical model for a perfect stiffened plate are compared to the FE solution conducted in Abaqus. The initial imperfections that are introduced into the static Riks analysis within the FE model are sufficiently small and therefore, the almost perfect response is studied and compared against the perfect system of the analytical model. The rotational stiffness c_p tends to infinity to provide a fully-rigid main plate–stiffener connection in the analytical solution. The corresponding equations for the stiffener and the main plate are the same as the ones discussed in the previous chapter. However, for the FE model, the rotational spring stiffness c_p is set to a sufficiently high value of 10^{10} Nmm/mm. According to the geometric properties of the stiffened plate, Table 3.1, this level of stiffness provides a similar joint rigidity as in the analytical model evaluated from the following equations:

$$\begin{aligned}
(S_4)_{\text{Auto}} &= \lim_{c_p \to \infty} \frac{3c_p h_1}{3D_s\pi^3 + c_p h_1 \pi^3 - 3\pi c_p h_1} \\
&= \frac{3}{\pi(\pi^2 - 3)}, \\
(S_4)_{\text{Abaqus}} &= \frac{3(10^{10})h_1}{3D_s\pi^3 + (10^{10})h_1\pi^3 - 3\pi(10^{10})h_1}, \\
&\approx 0.13901.
\end{aligned} \tag{5.1}$$

Comparing this to Equation (3.37), the approximation matches the exact value to 5 decimal places showing that $c_p = 10^{10}$ Nmm/mm is a suitable value to use. Hence,

J_p and λ_p are thus:

$$\begin{aligned}
(J_p)_{\text{AUTO}} &= \lim_{c_p \to \infty} \frac{4c_p b\pi}{8(-1)^i D_p - 4c_p b + c_p b\pi} \\
&= \frac{4\pi}{\pi - 4}, \\
(J_p)_{\text{ABAQUS}} &= \frac{4(10^{10})b\pi}{8(-1)^i D_p - 4(10^{10})b + (10^{10})b\pi}, \\
&\approx -14.63917, \\
(\lambda_p)_{\text{AUTO}} &= \lim_{c_p \to \infty} \left(\frac{2b^2}{3h_1^2}\right) \left\{\frac{3D_s S_4 \pi^3 - c_p h_1 \left(3 - S_4\pi^3 + 3S_4\pi\right)}{-8D_p J_p - c_p b \left(4J_p + 4\pi - \pi J_p\right)}\right\}, \\
(\lambda_p)_{\text{ABAQUS}} &= \left(\frac{2b^2}{3h_1^2}\right) \left\{\frac{3D_s S_4 \pi^3 - (10^{10})h_1 \left(3 - S_4\pi^3 + 3S_4\pi\right)}{-8D_p J_p - (10^{10})b \left(4J_p + 4\pi - \pi J_p\right)}\right\} \\
&\approx 0.674.
\end{aligned} \tag{5.2}$$

Moreover, Figure 5.4 shows the relationship between the ratio of the out-of-plane

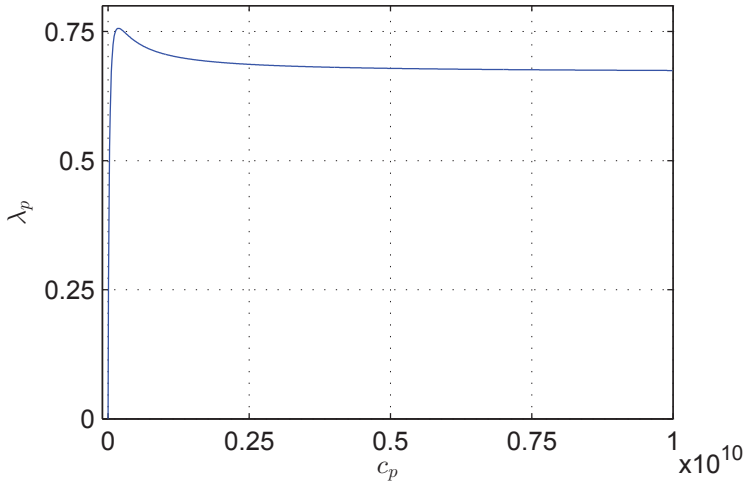

Figure 5.4: Plot of the ratio of the out-of-plane displacements in the main plate to the stiffener λ_p versus the joint rigidity modelling of rotational stiffness c_p.

deflections in the main plate to the stiffener λ_p and the c_p values. It shows that the level of c_p selected for FE model is on the plateau region of λ_p, which seems to mimic a fixed joint.

A linear eigenvalue analysis is first conducted in Abaqus (2011). The corresponding eigenvalue is found to be 1.61 kN, which is approximately 1% lower than P_o^{C} determined by the analytical model, as given in Equation (3.36). Figure 5.5 shows equilibrium plots of the normalized axial load $p = P/P_o^{\mathrm{C}}$ versus the normalized buckling amplitudes of (a) the global mode of the strut q_s and (b) the normalized local mode deflection of the stiffener $w_{\max}/t_s$. The graph in (c) shows the relative amplitudes of the global and local buckling modes for the studied perfect case. Figure 5.6 shows the local out-of-plane deflection profiles w at the respective locations (i)–(iii), shown in Figure 5.5(a–c), the comparison being for the same value of p. In addition, the visual comparisons of the 3-dimensional representation of the stiffened plate from the analytical and the FE models are also presented in Figure 5.7.

5.1.2 Imperfect stiffened plates

In this section, three examples of the FE model results are considered and compared against the corresponding analytical solutions in Auto-07p (Doedel & Oldeman, 2011). The first FE model with rotational stiffness, $c_p = 1000$ Nmm/mm is considered for the case where local buckling deflections are confined to the stiffener only ($\lambda_p = 0$). The initial amplitude for the local out-of-plane displacement in the analytical model A_0 is set to be $t_s/10$ (= 0.12 mm) with $\alpha = 8.0$, $\beta = 35$ and $\eta = L/2$, to be compatible with the eigenvalue analysis from Abaqus. However, in the second and the third examples, the local buckling deflection of the main plate is included alongside the stiffener ($\lambda_p \neq 0$). The rotational spring stiffnesses c_p are set to be 500 and 1000 Nmm/mm respectively. In addition, the local imperfections have the same amplitude as in the first model with $\alpha = 5.0$, $\beta = 75$ and $\eta = L/2$, for the same reason as described for the first example. For the two latter examples, the corresponding initial deflection amplitude ratios λ_p are approximately 0.1533 and 0.2687 respectively, which have been evaluated from Equation (4.8). The amplitudes of the global out-

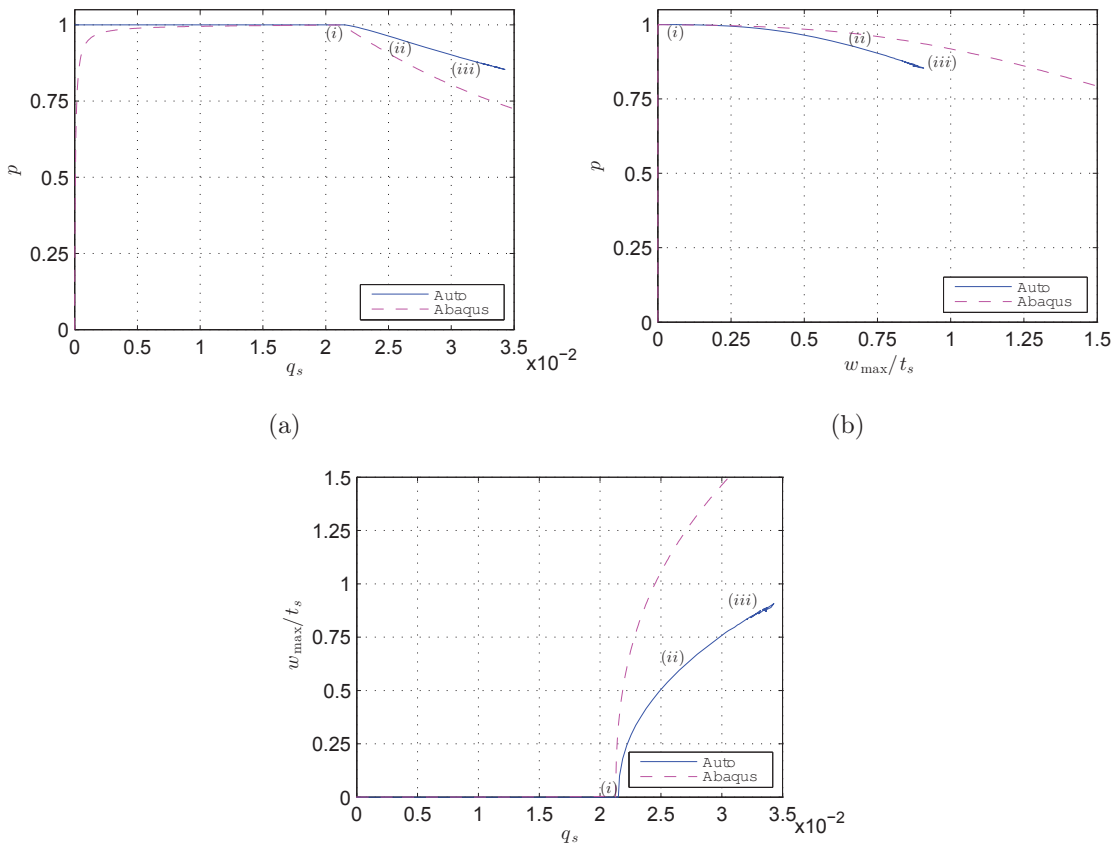

Figure 5.5: Comparisons of the analytical model (solid line) versus the FE model (dashed line) solutions for the perfect case ($q_{s0} = 0, w_0 = 0$), both with $c_p \to \infty$; Normalized force ratio p versus (a) the global mode amplitudes q_s and (b) the maximum normalized out-of-plane deflection $w_{\max}/t_s$; (c) local versus global mode amplitudes.

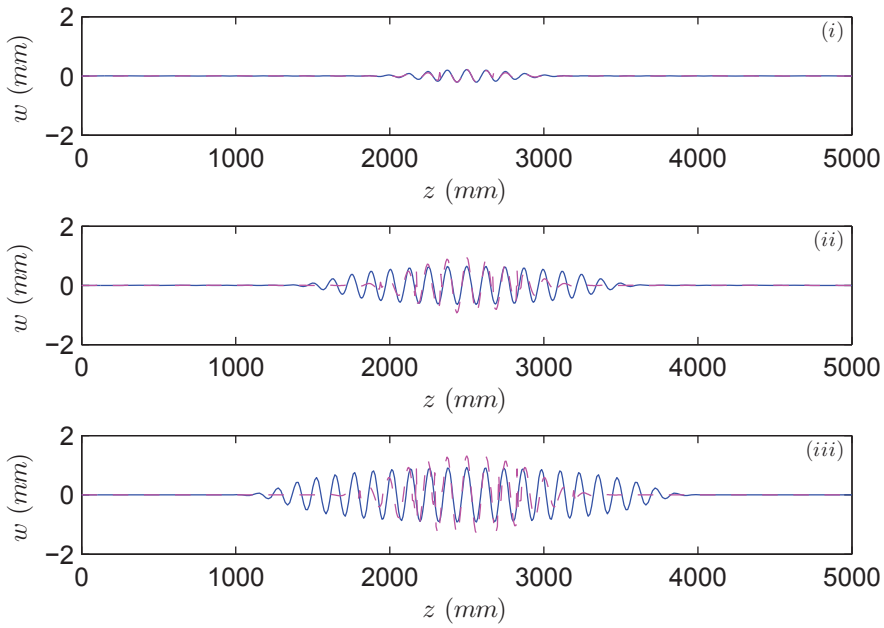

Figure 5.6: Comparisons of the analytical results (solid line) versus the FE model (dashed line) solutions for the local out-of-plane deflection of the stiffener w, both with $c_p \to \infty$ where (i)–(iii) correspond to the equilibrium states at $p = 0.99$, $p = 0.95$ and $p = 0.89$ respectively.

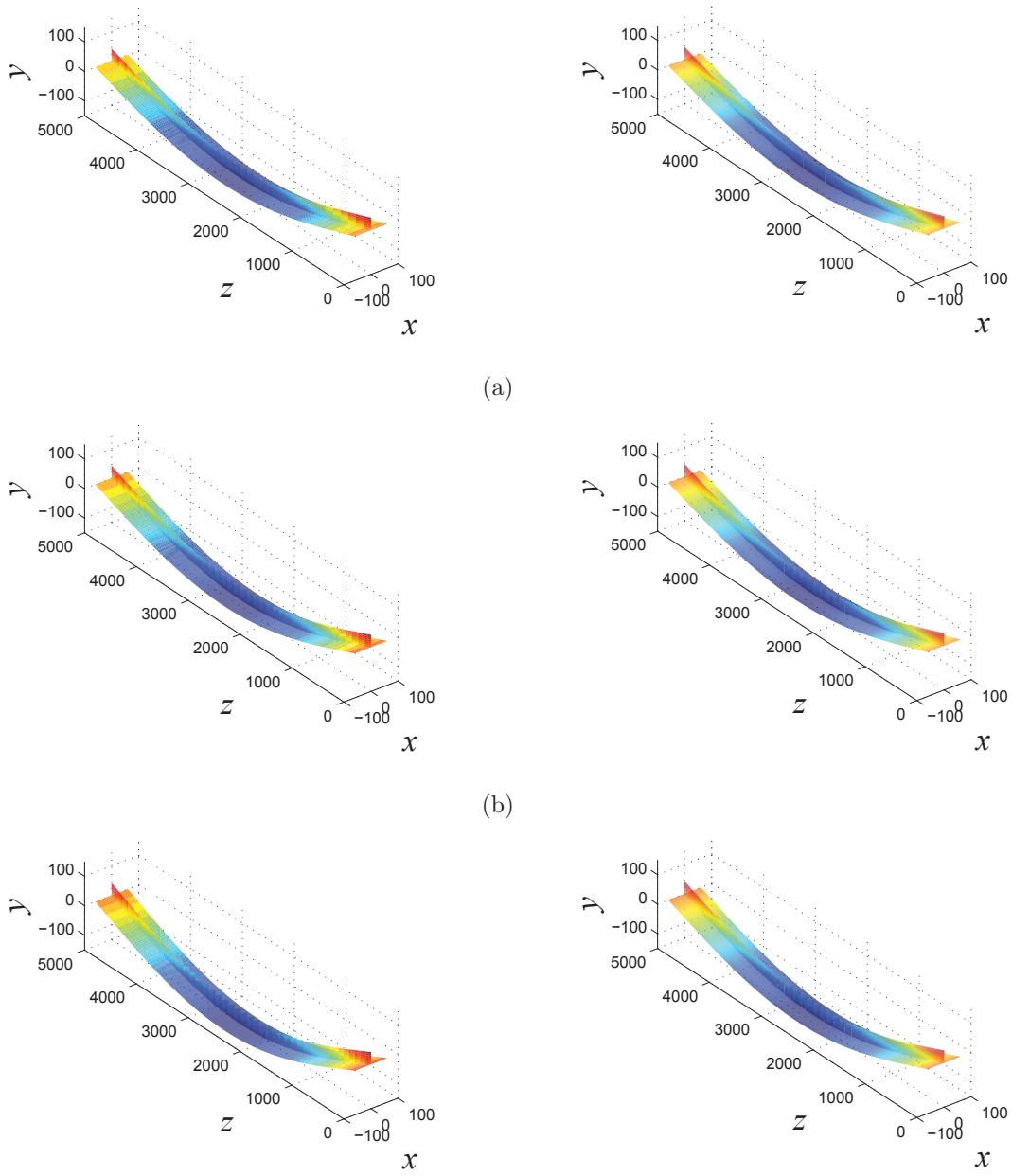

Figure 5.7: Comparisons of the numerical solutions from the analytical (left) and the FE (right) models when $c_p \to \infty$ visualized on 3-dimensional representations of the strut. The results are shown for equilibrium states at the points shown in Figure 5.5 (a–c) defined as (i)–(iii). All dimensions are in millimetres but the local buckling displacements in the stiffener are scaled by a factor of 5 to aid visualization.

of-straightness q_{s0} are set to be 0.001 in all three FE models. Table 5.1 presents the

Source	σ_o^{C} (N/mm^2)	$\sigma_{l,s}^{\mathrm{C}}$ (N/mm^2)	$\sigma_{l,p}^{\mathrm{C}}$ (N/mm^2)	Critical mode
Theory	4.89	236.02	309.85 – 539.91	Global
FE-1	4.942	215.69	–	Global
% difference	+0.12	-9.42	-	N/A
FE-2	4.942	227.81	–	Global
% difference	+0.12	-3.60	-	N/A
FE-3	4.942	228.94	503.15	Global
% difference	+0.12	-3.09	+7.31	N/A

Table 5.1: Theoretical and FE values of the global and local critical buckling stresses (σ_o^{C} and σ_l^{C}) respectively; subscripts "p" and "s" refer to the main plate and the stiffener respectively and k_p is taken to be 1.247. The expression for $\sigma_o^{\mathrm{C}} = P_o^{\mathrm{C}}/A$, where A is the cross-sectional area of the strut.

corresponding critical global stresses σ_o^C as well as the local critical stresses for the stiffener and the main plate $\sigma_{l,s}^C$ and $\sigma_{l,p}^C$ respectively, for all the components from the analytical and the FE models. The corresponding difference between the FE and the analytical values are also evaluated for each example.

Figure 5.8 shows the equilibrium path for the first example with $c_p = 1000$ Nmm/mm. The graphs in (a–b) show the normalized load p versus the global mode amplitude q_s and the maximum normalized local out-of-plane deflection $w_{\max}/t_s$ respectively. The graph in (c) shows the global amplitude q_s versus the local amplitude $w_{\max}/t_s$. Figure 5.9 shows the local out-of-plane deflection profiles w at the respective locations (i)–(iii), shown in Figure 5.8(a–c), the comparison being for the same value of p. A visual comparison between the 3-dimensional representations of the stiffened plate from the analytical and the FE models is also presented in Figure 5.10.

Moreover, Figures 5.11 and 5.14 show a series of equilibrium paths when $c_p = 500$

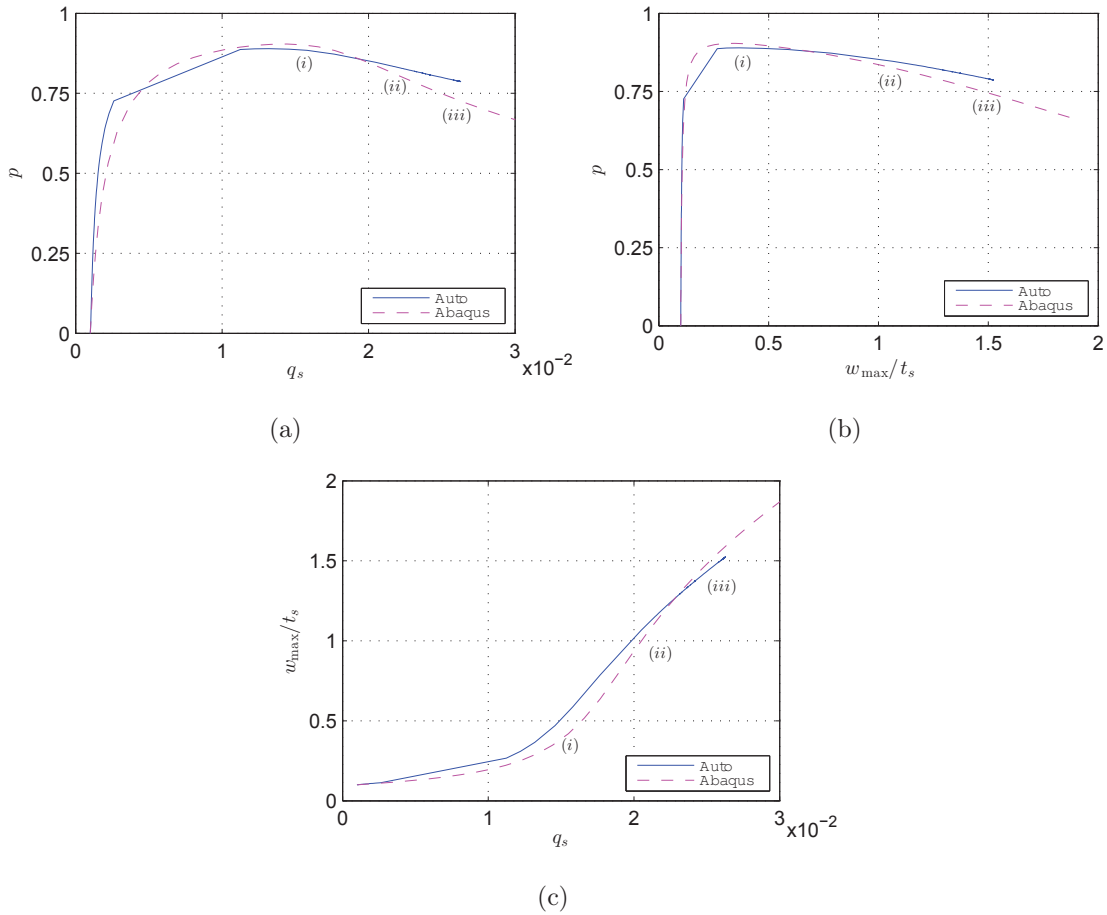

Figure 5.8: Comparison of the analytical model (solid line) versus the FE model (dashed line) solutions, both with $c_p = 1000$ Nmm/mm ($\lambda_p = 0$), $q_{s0} = 0.001$, and $A_0 = t_s/10$. Normalized force ratio p versus (a) the global mode amplitude q_s and (b) the maximum normalized out-of-plane stiffener deflection $w_{\max}/t_s$; (c) local versus global mode amplitudes. Note that, the local imperfection is only for the stiffener for this case.

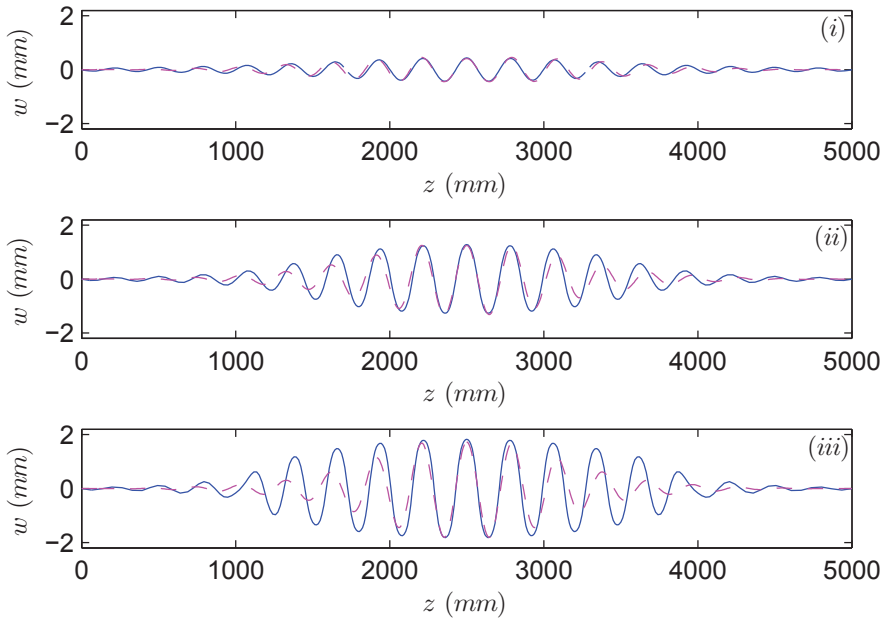

(a)

Figure 5.9: Comparison of the analytical model (solid line) versus the FE model (dashed line) solutions, both with $c_p = 1000$ Nmm/mm ($\lambda_p = 0$), $q_{s0} = 0.001$, and $A_0 = t_s/10$. The out-of-plane deflection of the stiffener w for the points shown in Figure 5.8(a–c), defined as (i)–(iii), corresponding to the equilibrium states at $p = 0.89$, $p = 0.84$ and $p = 0.81$ respectively.

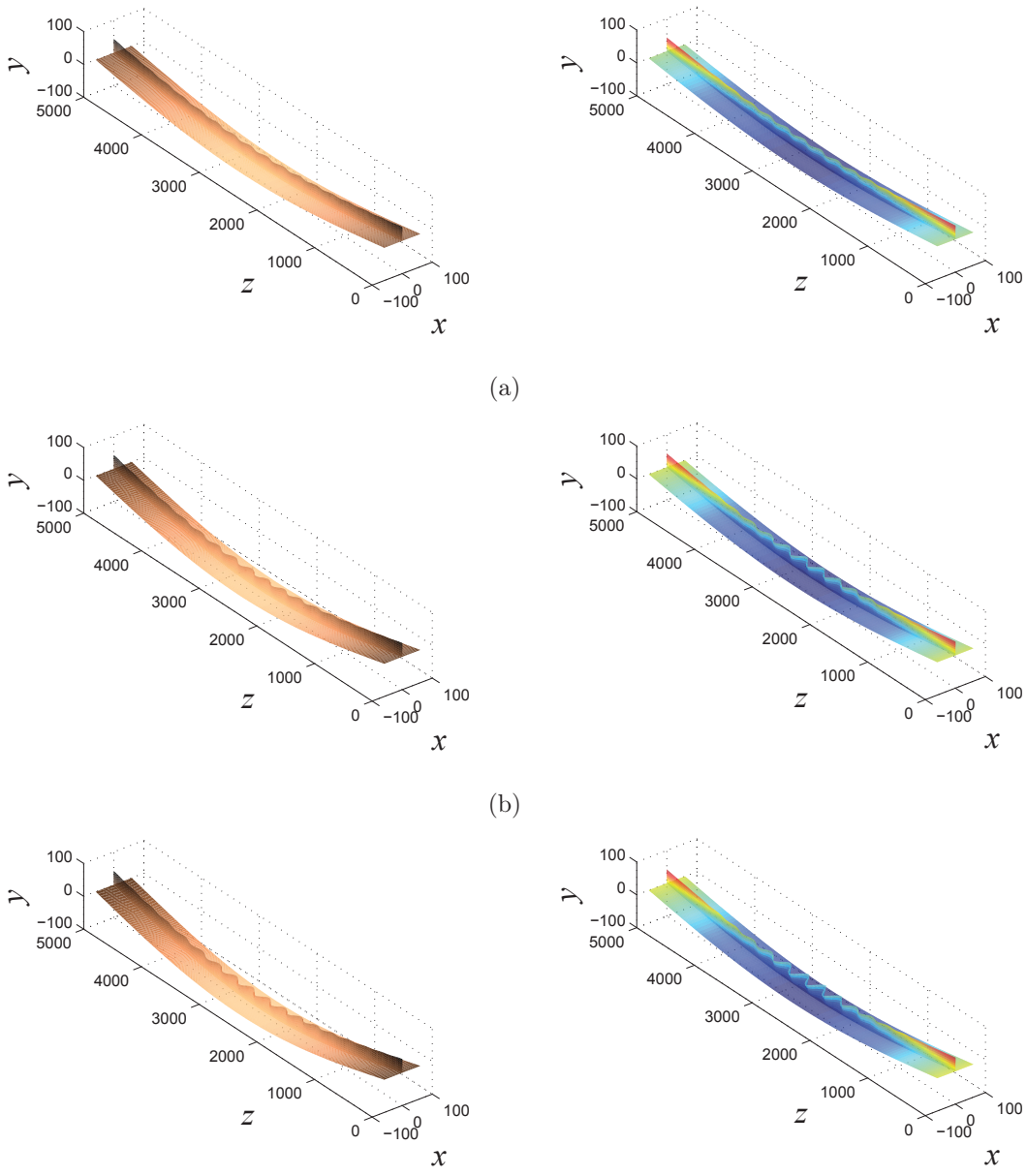

Figure 5.10: Comparisons of the numerical solutions from the analytical (left) and the FE (right) models with $c_p = 1000$ Nmm/mm ($\lambda_p = 0$). Visualized on 3-dimensional representations of the strut. The results are shown for equilibrium states at the points shown in Figure 5.8 (a–c), defined as (i)–(iii). All dimensions are in millimetres, but the local buckling displacements in the stiffener are scaled by a factor of 5 to aid visualization.

and $c_p = 1000$ Nmm/mm respectively with the initial imperfection in the main plate as well as in the stiffener. The graphs show the normalized load $p = P/P_o^{\mathrm{C}}$ versus (a) the global mode amplitude q_s and (b) the maximum normalized local out-of-plane deflection of the stiffener $w_{\max}/t_s$. The graphs in (c) show modal amplitudes q_s versus $w_{\max}/t_s$. Figures 5.12 and 5.15 show the local out-of-plane deflection profiles w at the respective locations (i)–(iii), shown in Figures 5.11 and 5.14 (a–c) respectively. In addition, visual comparisons between the 3-dimensional representations of the stiffened plate from the analytical and the FE models are also presented in Figures 5.13 and 5.16. As it can be seen in the aforementioned figures, all sets of graphs show very good correlation in terms of the mechanical response; the results for w from the analytical and the FE models being almost indistinguishable. In particular, by including the main plate local deflection as well as that of the stiffener (*i.e.* the second and third examples), the number of waves in the interactive mode (w) are increased and therefore, the comparison between the analytical results and the FE models (*i.e.* FE-2 and FE-3 in the Table 5.1) are improved in terms of the maximum out-of-plane deflection and the wavelengths. Although, it seems that the FE model is unable to capture the changing wavelength of the post-buckling mode that has been observed in physical experiments (Becque & Rasmussen, 2009a; Wadee & Gardner, 2012; Wadee & Bai, 2014). Nevertheless with increasing c_p, the rate of reduction in local buckling wavelength is reduced, hence the better quantitative comparison.

5.2 Comparison with experimental results

An experimental study of thin-walled stiffened plates by Fok *et al* (1976) focused on the case where global buckling was critical. In this section, two specific tests conducted on a panel with multiple stiffeners, are considered. The corresponding experimental results are then compared with the numerical results from the analytical

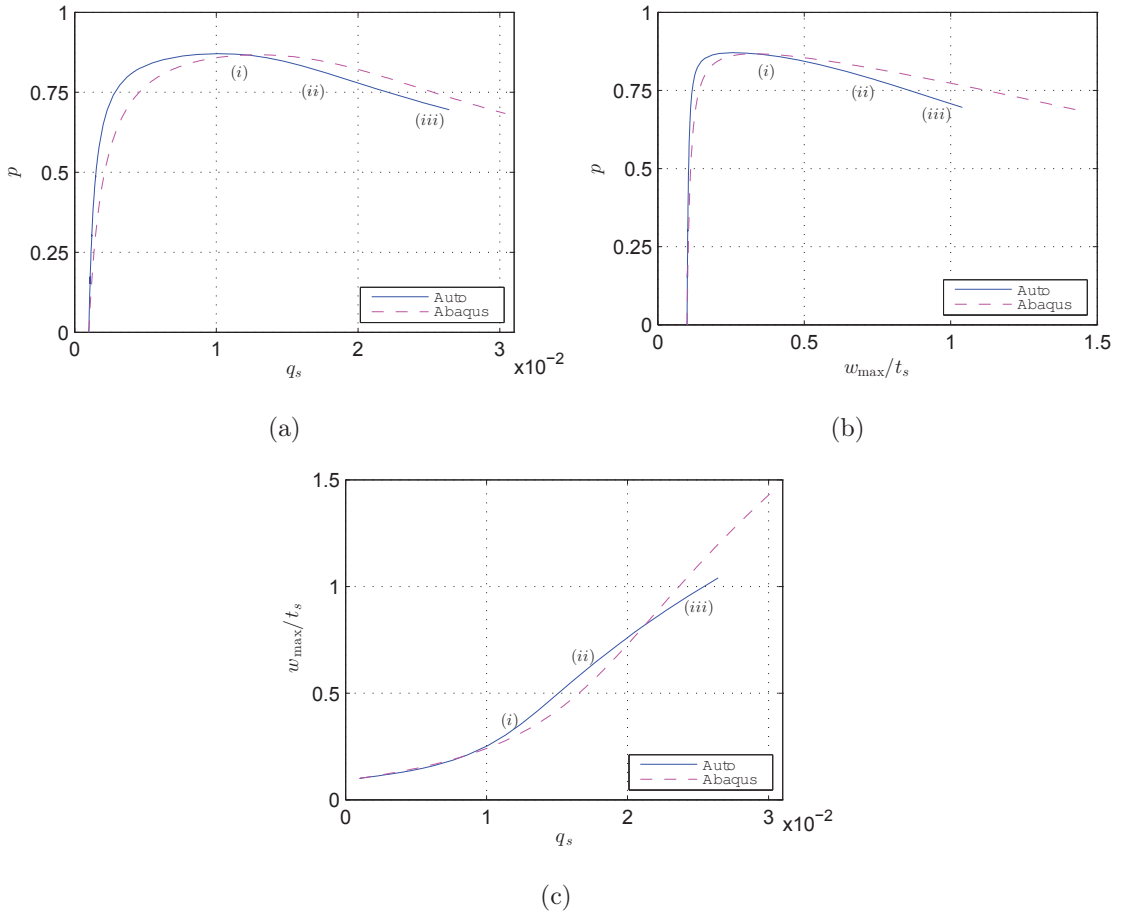

Figure 5.11: Comparison of the analytical model (solid line) versus the FE model (dashed line) solutions, both with $c_p = 500$ Nmm/mm ($\lambda_p = 0.1533$), $q_{s0} = 0.001$, and $A_0 = t_s/10$. Normalized force ratio p versus (a) the global mode amplitude q_s and (b) the maximum out-of-plane normalized stiffener deflection $w_{\max}/t_s$; (c) local versus global mode amplitudes. Note that the local imperfection is introduced in both the stiffener and the main plate for this case.

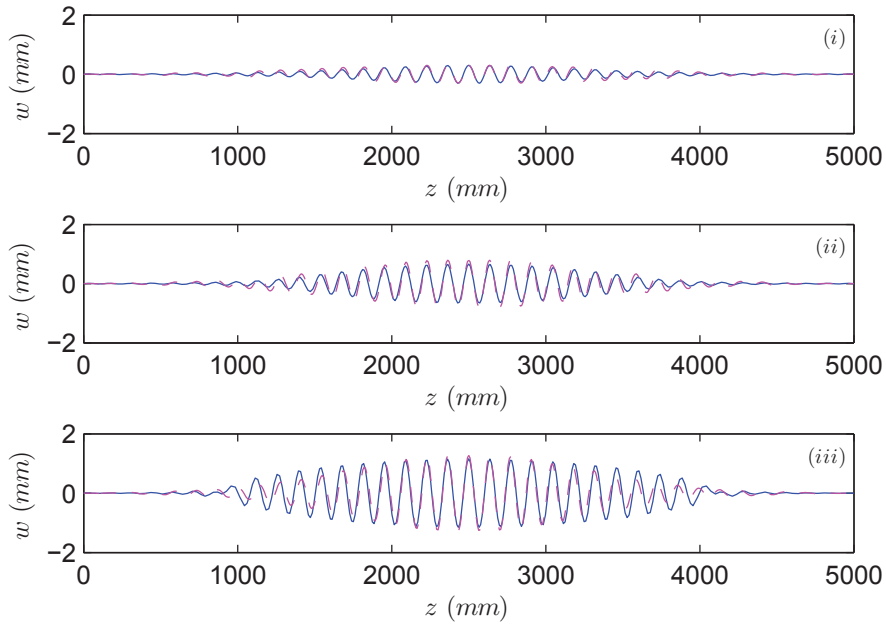

(a)

Figure 5.12: Comparison of the analytical model (solid lines) versus the FE model (dashed lines) solutions, both with $c_p = 500$ Nmm/mm ($\lambda_p = 0.1533$) for the out-of-plane deflection of the stiffener w for the points as shown in Figure 5.11(a–c), defined as (i)–(iii), corresponding to the equilibrium states at $p = 0.87$, $p = 0.82$ and $p = 0.72$ respectively.

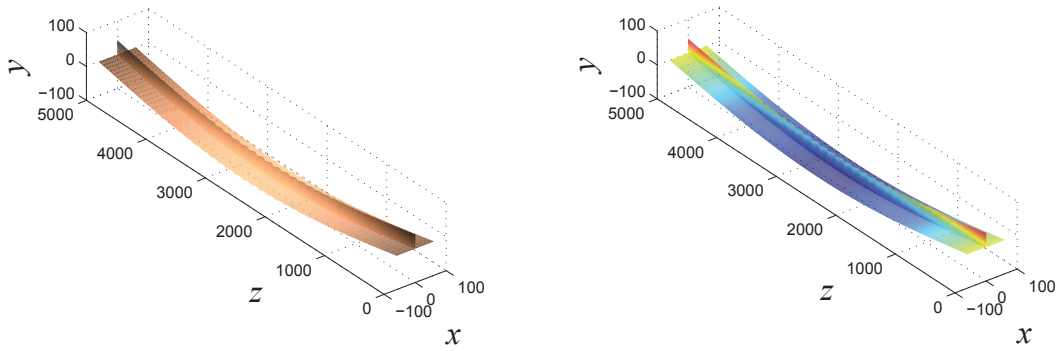

(a)

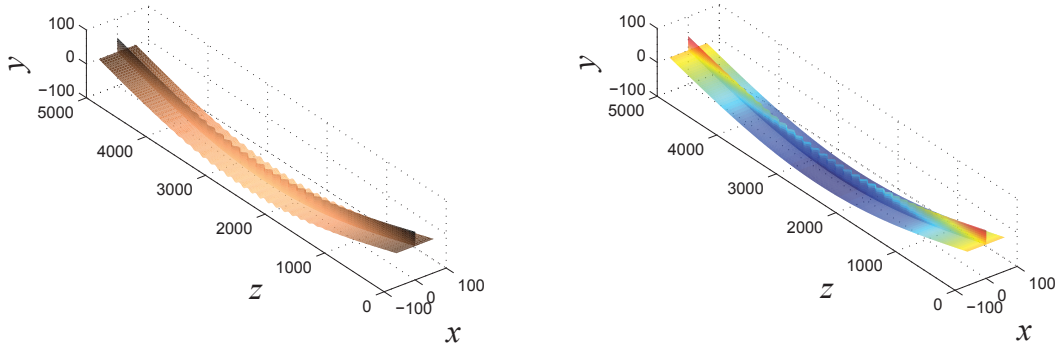

(b)

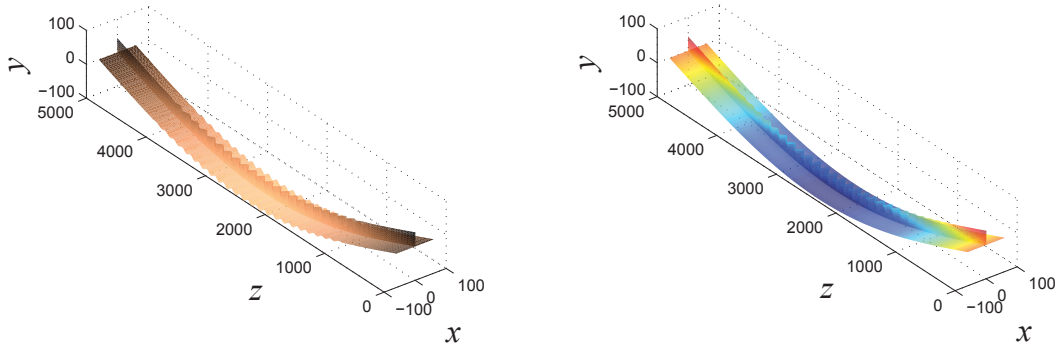

(c)

Figure 5.13: Comparisons of the numerical solutions from the analytical (left) and the FE (right) models with $c_p = 500$ Nmm/mm ($\lambda_p = 0.1533$) visualized on 3-dimensional representations of the strut. The results are shown for equilibrium states at the points shown in Figure 5.11(a–c), defined as (i)–(iii). All dimensions are in millimetres, but the local buckling displacements in the stiffener and the main plate are scaled by a factor of 3 to aid visualization.

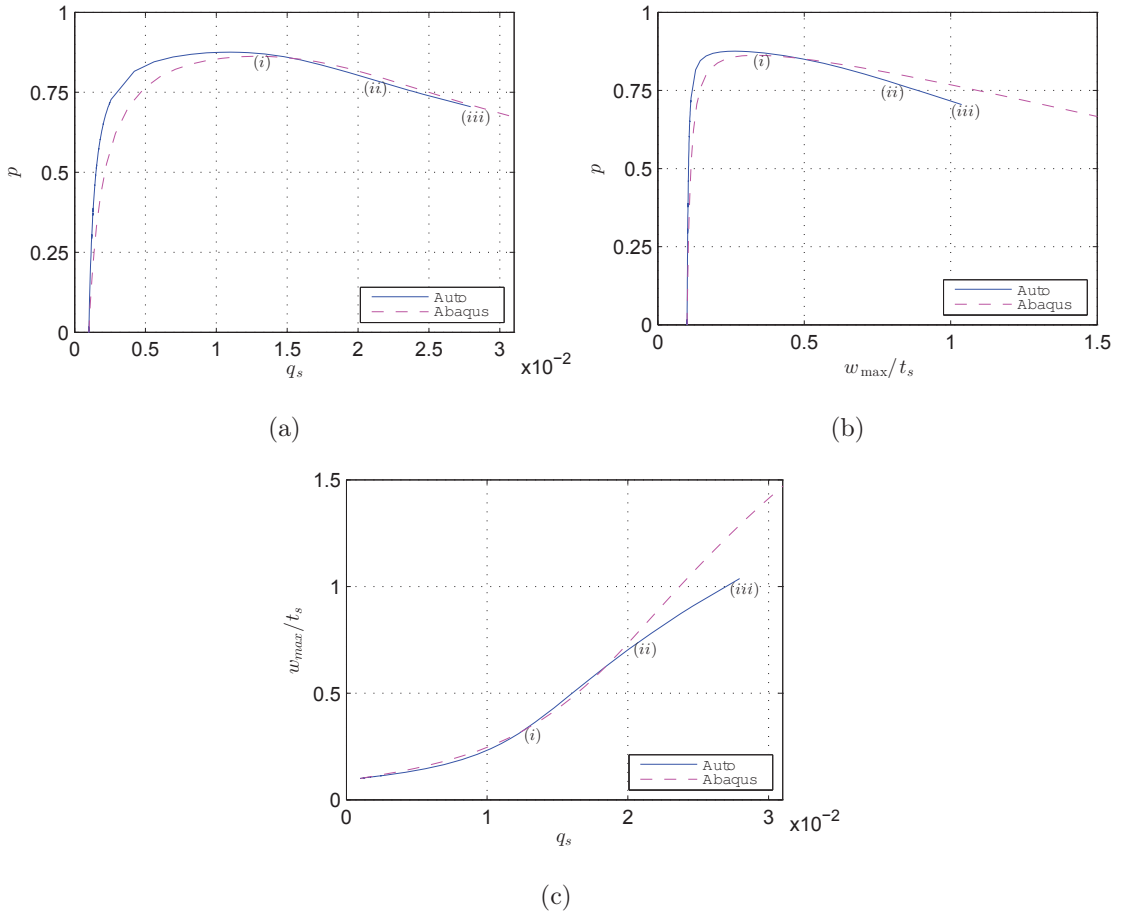

Figure 5.14: Comparison of the analytical model (solid line) versus the FE model (dashed line) solutions, both with $c_p = 1000$ Nmm/mm ($\lambda_p = 0.2687$), $q_{s0} = 0.001$, and $A_0 = t_s/10$. Normalized force ratio p versus (a) the global mode amplitude q_s and (b) the maximum out-of-plane normalized stiffener deflection $w_{\max}/t_s$; (c) local versus global mode amplitudes. Note that the local imperfection is introduced in both the stiffener and the main plate for this case.

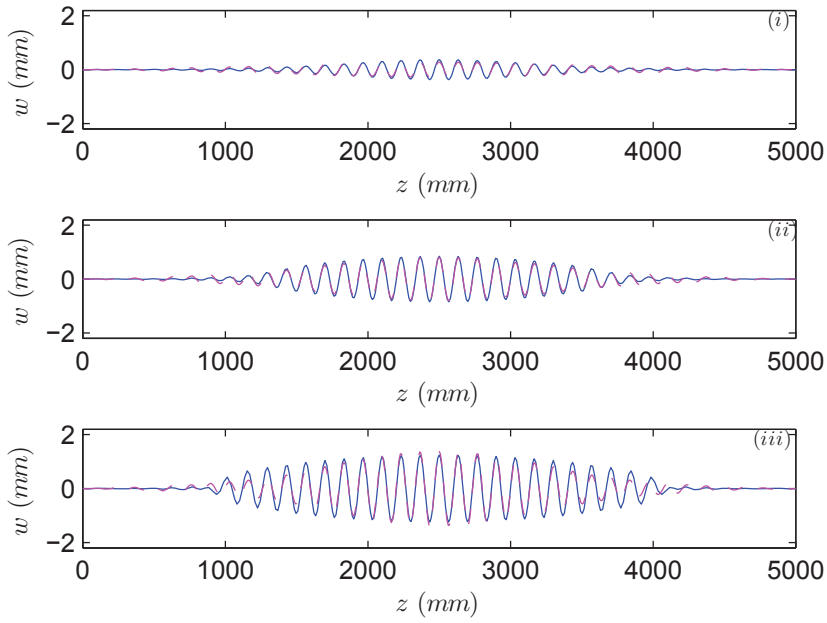

(a)

Figure 5.15: Comparison of the analytical model (solid lines) versus the FE model (dashed lines) solutions, both with $c_p = 1000$ Nmm/mm ($\lambda_p = 0.2687$) for the out-of-plane deflection of the stiffener w for the points shown in Figure 5.14(a–c), defined as (i)–(iii), corresponding to the equilibrium states at $p = 0.82$, $p = 0.72$ and $p = 0.69$ respectively.

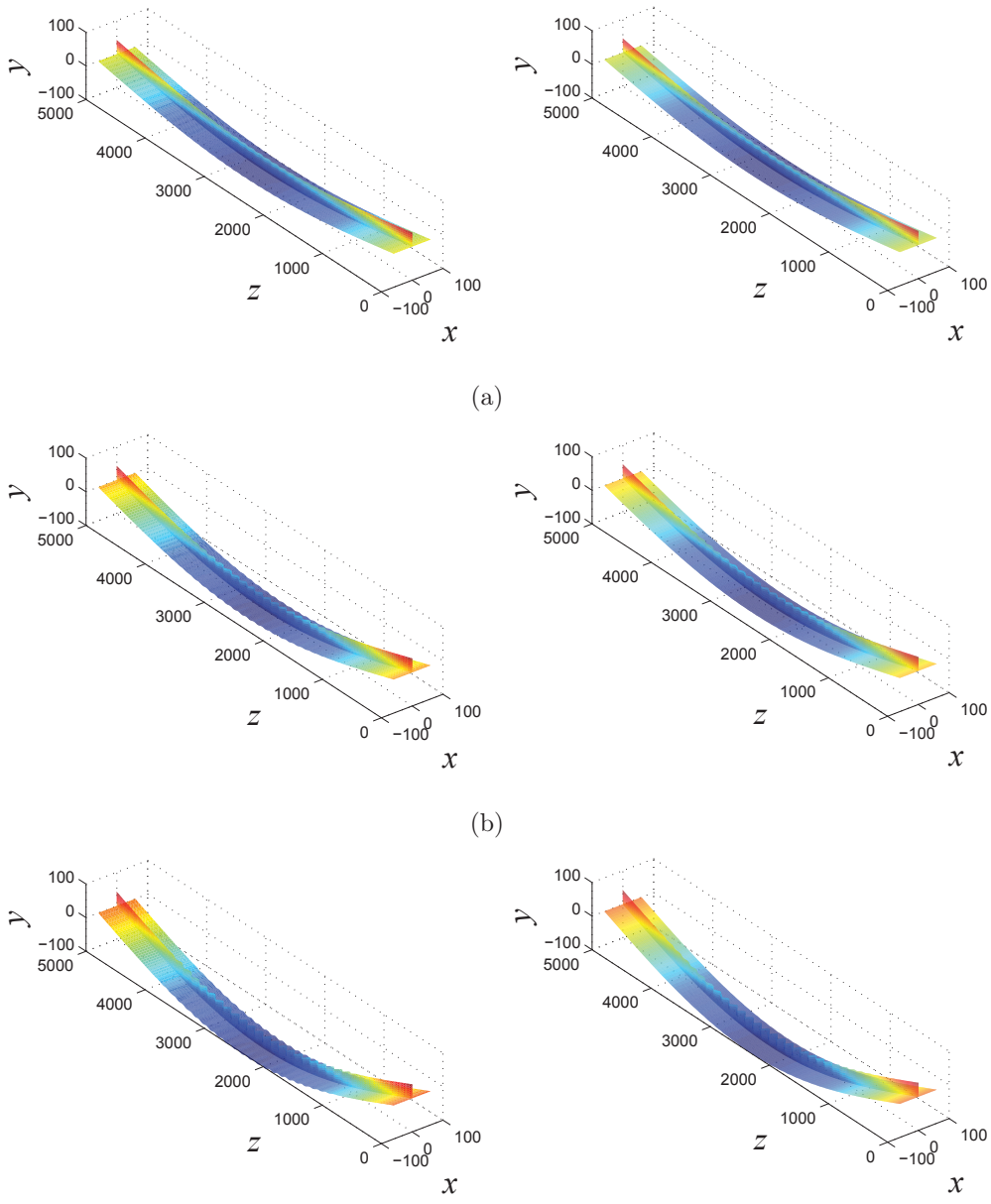

Figure 5.16: Comparisons of the numerical solutions from the analytical (left) and the FE (right) models with $c_p = 1000$ Nmm/mm ($\lambda_p = 0.2687$) visualized on 3-dimensional representations of the strut. The results are shown for equilibrium states at the points shown in Figure 5.14(a–c), defined as (i)–(iii). All dimensions are in millimetres, but the local buckling displacements of the stiffener and the main plate are scaled by a factor of 3 to aid visualization.

model in Auto and the FE model in Abaqus. The cross-section of the stiffened panel investigated by Fok *et al* (1976) is shown in Figure 5.17. The corresponding experimental specimen had 10 blade stiffeners with length L. The geometric properties were thus: $b = 45.5$ mm, $h_1 = 13.5$ mm, and $t_s = t_p = 0.735$ mm. The studied model was made of cold-setting Araldite® (epoxy resin) and the material had an elastic constitutive relationship, but unfortunately no material properties were provided. Hence, in the analytical and numerical studies, nominal values of E and ν are used. Given that the behaviour was elastic and only ratios of loads and displacements were presented as the results, this does not pose a problem as long as the same values are used in the analytical and FE models.

In the first test, the length L of the panel was 400 mm, ensuring that the global critical buckling load was much less than the local buckling load. As in the Fok *et al* (1976) article, the initial global out-of-straightness of the strut was taken as $W_0 = 1.2t_s$ and no out-of-plane imperfection in the stiffeners nor in the main plate was considered (*i.e.* $w_0 = w_{p0} = 0$). In the second test, however, the length of the stiffened panel was reduced to $L = 320$ mm. Although, the ratio of P_o^{C} to P_l^{C} decreased by about 15%, the global buckling mode remained critical. The corresponding stresses for both tests are summarized in Table 5.2.

	L (mm)	σ_o^{C} (N/mm^2)	$\sigma_{l,s}^{\mathrm{C}}$ (N/mm^2)	$\sigma_{l,p}^{\mathrm{C}}$ (N/mm^2)
Test 1	400	$7.122 \times 10^{-4}E$	$3.34 \times 10^{-3}E$	$1.176 \times 10^{-3}E$
Test 2	320	$1.109 \times 10^{-3}E$	$3.34 \times 10^{-3}E$	$1.176 \times 10^{-3}E$

Table 5.2: Theoretical values of the global and local critical buckling stresses (σ_o^{C} and σ_l^{C}) respectively; subscripts "p" and "s" refer to the main plate and the stiffener respectively. The expression for $\sigma_o^{\mathrm{C}} = P_o^{\mathrm{C}}/A$, where A is the cross-sectional area of the panel.

For the $L = 320$ mm panel, the initial global buckling mode imperfection W_0 was set to $0.8t_s$ and the amplitude of the out-of-plane imperfection $A_0 = 0.01t_s$ with $\alpha = 4$,

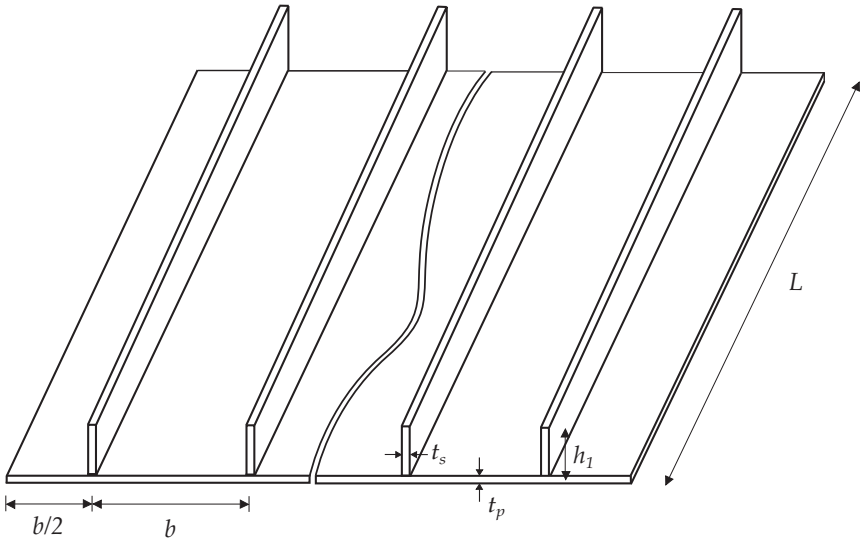

Figure 5.17: Stiffened panel dimensions in Fok *et al* (1976) tests.

$\beta = 11$ and $\eta = L/2$, giving a similar interactive mode as the FE model. The relative rigidity between the stiffeners and the main plate was again defined by rotational springs with stiffness c_p. For both models, the stiffness of the rotational spring c_p was set to be 300 Nmm/mm since this gave the best match with the peak load of the experimental results. To find the equilibrium path, the numerical continuation process was initiated from zero load as for an imperfect case (see §4.2).

Figure 5.18 shows the comparisons between the experimental results from Fok *et al* (1976), the results from the analytical and the FE models. The comparisons show strong agreement between all three sets of results. The graphs in Figure 5.18(a–b) show the normalized force ratio p versus the normalized global mode deflection $(W - W_0)/t_s$ in tests 1 and 2 respectively. Since there was no information provided about the local out-of-plane deflection magnitude, the results from the analytical model are best compared to the results of numerical model in Abaqus. Figure 5.19(a) presents the comparison of the normalized force ratio p versus the maximum normalized out-of-plane deflection $w_{\max}/t_s$ of the stiffener. However, Figure 5.19(b) shows the comparisons of the analytical and the FE model results for the local out-

of-plane displacement of the stiffener w. Note that the results are obtained when (i) $p = 0.80$ and (ii) $p = 0.65$. The visual comparison between the local buckling amplitudes and wavelength is excellent. Of course at lower loads, in the advanced post-buckling range, there is divergence between the non-midspan peaks; this is a further example of the the FE model locking the modal wavelength, as found in earlier studies, even though actual experimental evidence points to the contrary (Becque, 2008; Wadee & Gardner, 2012; Wadee & Bai, 2014).

5.3 Concluding remarks

The analytical model based on variational principles was introduced in Chapter 3 and extended to include global and local imperfections and the buckling of the main plate, in Chapter 4. By introducing the sympathetic deflection of the main plate along with the locally buckling stiffener, the currently developed model could now be compared to published experiments (Fok *et al.*, 1976) and a finite element model formulated in Abaqus (2011). The comparison between the analytical model and the corresponding results from both the FE model and the physical experimental results are found to be excellent. The comparisons are seen to be the best where the main plate buckles in sympathy with the stiffener and where the rigidity of the joint connecting the stiffener to the main plate is high. It is also found that the static FE model formulated in Abaqus, compares very well to the analytical model in the neighbourhood of the secondary instability. The FE model, however, seems to have problems by not allowing the local buckling wavelength to change. In particular, it is unable to track any cellular buckling, even though, it is clearly seen in experiments of closely related structural components (Becque, 2008; Wadee & Gardner, 2012; Wadee & Bai, 2014). A possible way to overcome this problem might be to perform dynamic (explicit) analysis within Abaqus, instead of Riks analysis, although for that a more

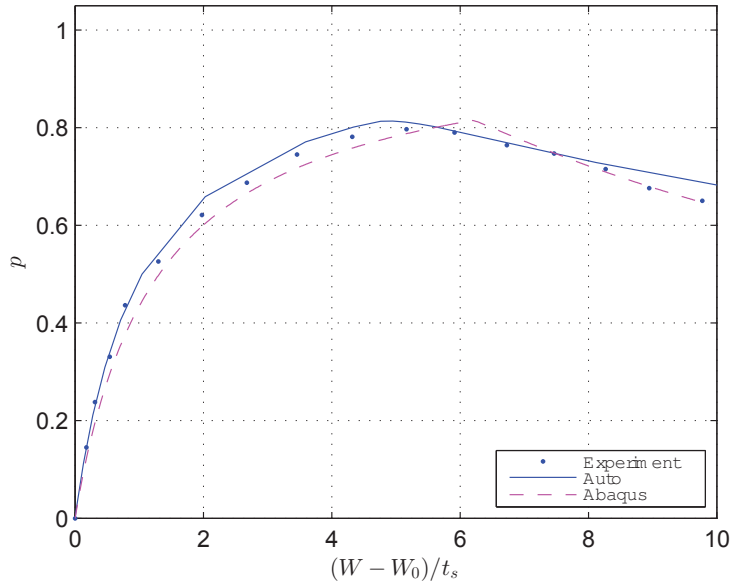

(a)

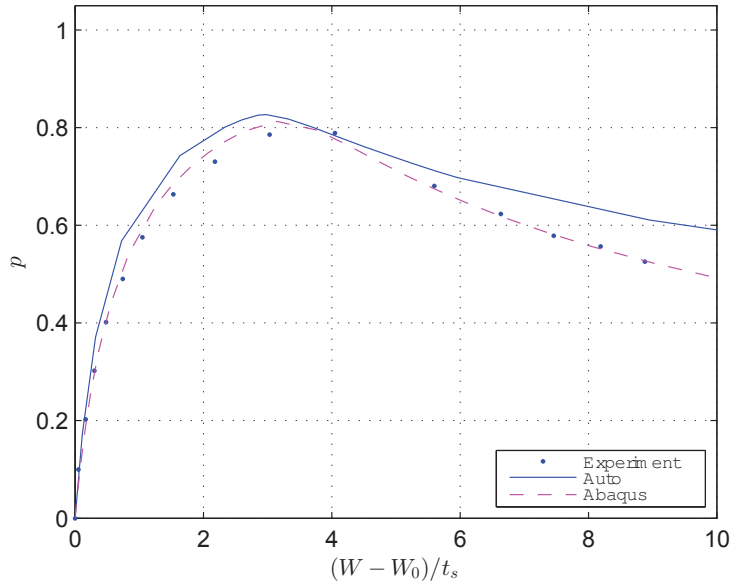

(b)

Figure 5.18: Comparison of the experimental results (dots), the analytical model (solid line) and the FE model (dashed line) solutions. Normalized force ratio p ($= P/P_o^{\mathrm{C}}$) versus the normalized relative global mode deflection $(W - W_0)/t_s$ for the panel with (a) $L = 400$ mm and (b) $L = 320$ mm.

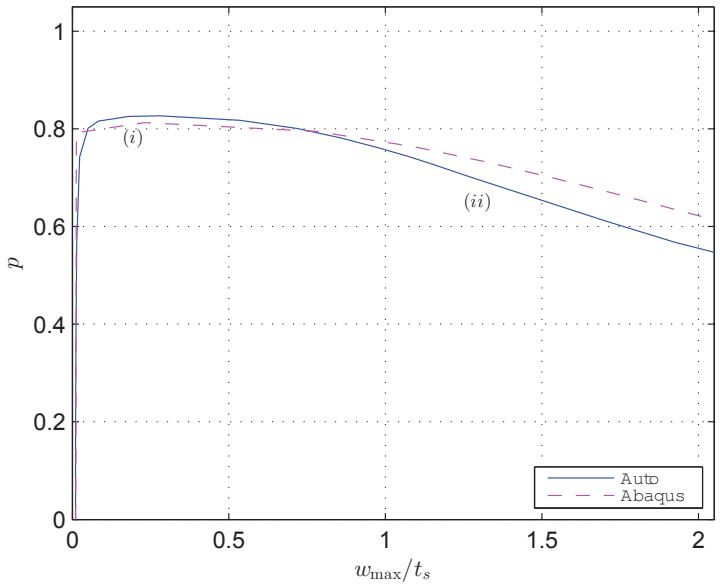

(a)

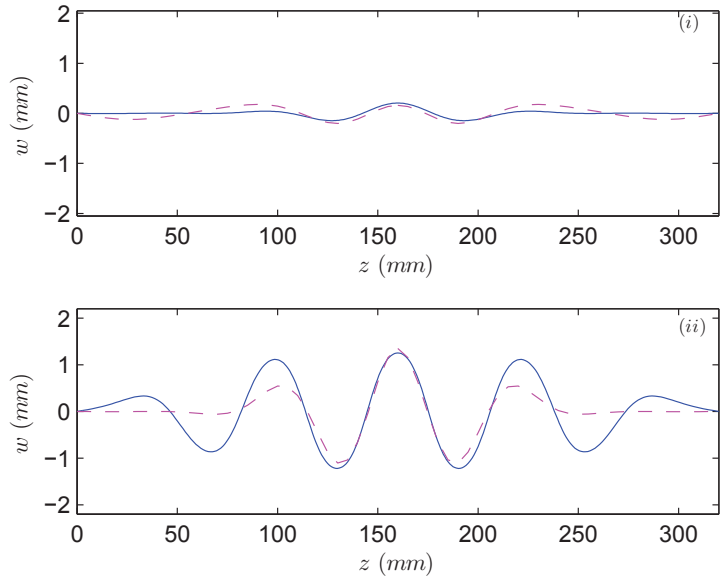

(b)

Figure 5.19: Comparison of the analytical model (solid line) and the FE model (dashed line). (a) Normalized force ratio p ($= P/P_o^{\mathrm{C}}$) versus the normalized maximum out-of-plane deflection $w_{\max}/t_s$; (b) local out-of-plane deflection of the stiffener w for the points shown in (a) defined as (i) and (ii).

intensive computational effort would be required.

In the next chapter, a more detailed imperfection sensitivity study is presented and a parametric investigation is conducted to provide greater understanding of the interactive buckling phenomena and to highlight the practical implications for design.

Chapter 6

Parametric study

A nonlinear analytical model for an axially loaded thin-walled stiffened plate, based on variational principles, was introduced in Chapter 3 and then developed in Chapter 4 by considering the local deflection of the main plate as well as the stiffener. The corresponding analytical results were validated against physical experiments, as well as finite element models, formulated in the commercial software ABAQUS (2011) in Chapter 5. Excellent agreement was found in terms of the mechanical response and the predicted deformation. So far, the numerical examples have been considered with a set of section and material properties that was focused on the case where global buckling was critical ($L = 5$ m). The highly unstable post-buckling behaviour was revealed for all cases including the cellular behaviour when the rigidity of the main plate–stiffener junction was modelled as pinned ($c_p = 0$ Nmm/mm) or semi-rigid ($c_p \leq 1000$ Nmm/mm) and the non-cellular buckling behaviour being observed for the cases where the aforementioned joint was assumed to be rigid, *i.e.* $c_p \to \infty$.

In this chapter, initially, imperfection sensitivity is studied by varying the amplitude of a local imperfection as well as varying the periodic and the localization factors that change the profile qualitatively. Moreover, an initial global buckling out-of-

straightness amplitude is also varied in order to study the effect of the initial global imperfection. After that, a parametric study is presented aimed at varying the length L of the stiffened plate and the height of the stiffener h_1, to obtain a better understanding of where the interactive buckling behaviour of the stiffened plate is important in terms of the geometric properties and where it can be practically neglected.

6.1 Effect of initial imperfections

In this section, an initial imperfection is considered in terms of the local deflection of the stiffener w_0 and the global out-of-straightness of the stiffened plate W_0. The stiffened plate cross-section properties are the same as were given in Table 3.1. The form of the local imperfection w_0 is obtained from Equation (4.10) and the global out-of-straightness W_0 is derived from Equation (4.9). It is worth reiterating that the initial local displacement of the main plate w_{p0} relates to the local out-of-straightness of the stiffener with $w_{p0} = \lambda_p w_0$, as discussed in Chapter 4. Numerical continuation is again performed in Auto. The solution strategies for the aforementioned cases are the same as those explained in previous chapters. The material properties of Young's modulus $E = 210$ kN/mm^2 and Poisson's ratio $\nu = 0.3$ are kept constant in all the following examples.

6.1.1 Pinned main plate–stiffener connection

In this section, local and global imperfection sensitivities are investigated for the case where the main plate–stiffener connection is assumed to be pinned ($c_p = 0$). The initial set of numerical examples focus on the local imperfections. Therefore, the initial local out-of-plane displacement w_0 is only considered in the equation of equilibrium and the initial out-of-straightness, q_{s0} is set to zero. The local imperfection

amplitude A_0, the periodicity and the localization parameters β and α respectively, are varied to determine the worst case combination that gives the lowest peak load. The subsequent set of numerical examples consider the post-buckling behaviour of the stiffened plate by varying the global imperfection amplitude q_{s0}. In the following examples global buckling is critical ($L = 5$ m).

Local imperfection only ($A_0 \neq 0$, $q_{s0} = 0$)

In this section, three types of local imperfection w_0 are studied in the stiffened plate. The initial end-shortening $\mathcal{E}_0$ due to the local imperfection, is also considered, which is evaluated from the first-order approximation:

$$\mathcal{E}_0 = \frac{1}{2}\int_0^L \dot{w}_0^2 \ \mathrm{d}z. \tag{6.1}$$

Initially, the periodicity and the localization parameters β and α respectively, are kept at constant values of 1 and 0 respectively. This type of imperfection also replicates the first local buckling eigenmode captured from the FE model. At this stage, the amplitude of local deflection A_0 and $\mathcal{E}_0$ are varied. The peak loads are recorded for each value of $\mathcal{E}_0$. This method is used since it does not bias the results against any particular imperfection profile (Wadee, 2000).

Figure 6.1(a) shows the normalized initial end-shortening $\mathcal{E}_0/L$ versus the normalized peak load $p_u = P/P_o^{\mathrm{C}}$. By increasing the $\mathcal{E}_0$ value, the corresponding normalized peak loads p_u are plotted with the ($\times$) symbol when $\beta = 1$ and $\alpha = 0$. A very small reduction is found in p_u, which indicates that the stiffened plate is insensitive to the purely periodic local imperfection when $\beta = 1$. In the second step, the initial end-shortening $\mathcal{E}_0$ is kept constant. Since, the imperfection is kept periodic (*i.e.* $\alpha = 0$), the β value and the amplitude A_0, are varied. This variation in A_0, as well as β, values are shown in Figures 6.1(b) and 6.2(a) respectively. It is worth noting that, the periodic amplitude parameter β, takes odd integer values only, in order to satisfy

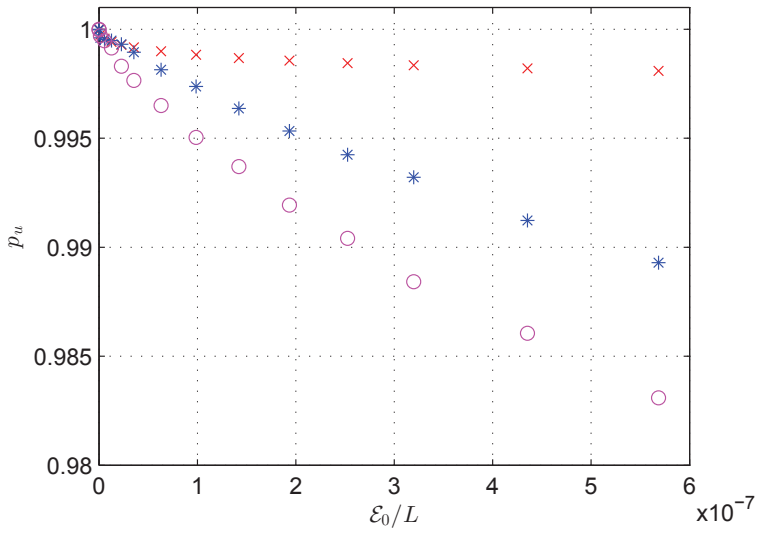

(a)

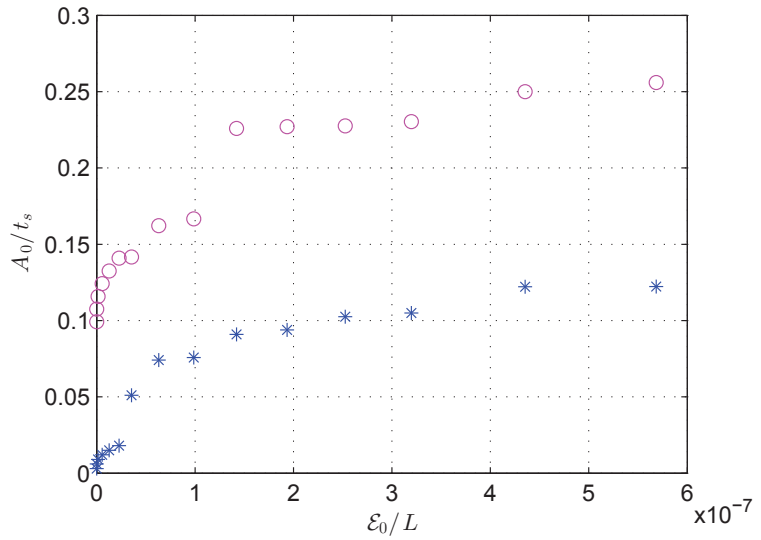

(b)

Figure 6.1: Imperfection sensitivity for the pinned case ($c_p = 0$). Normalized imperfection size $\mathcal{E}_0/L$ against: (a) the normalized peak load, p_u ($= P/P_o^{\mathrm{C}}$) and (b) the normalized local deflection amplitude A_0/t_s. The ($\times$) symbol corresponds to the imperfection form of the plate linear eigenvalue solution ($\alpha = 0$, $\beta = 1$), the ($*$) symbol corresponds to the periodic imperfection ($\alpha = 0$, $\beta > 1$) and the ($\circ$) symbol correspond to the modulated imperfection ($\alpha \neq 0$, $\beta > 1$).

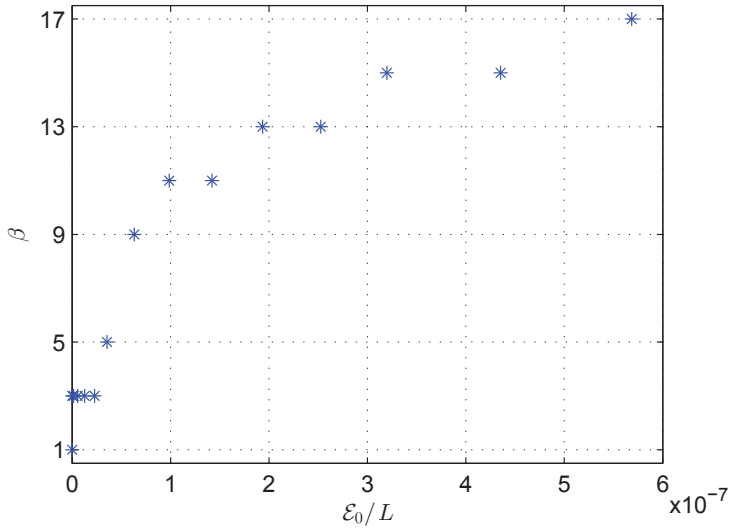

(a)

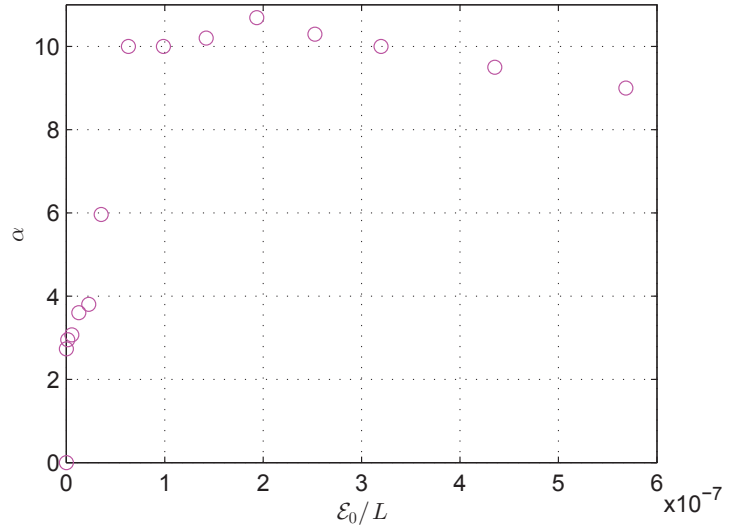

(b)

Figure 6.2: Worst case periodic and localized imperfections for the pinned case ($c_p = 0$). Normalized imperfection size $\mathcal{E}_0/L$ against: (a) the periodicity parameter β which gives the lowest peak loads and (b) the localization parameter α which gives the corresponding lowest peak loads.

the symmetry boundary conditions at mid-span. The combination of β and A_0 that gives the lowest peak load is determined as the critical peak load, as shown with the (*) symbol in both graphs of Figure 6.1. It is observed that, by increasing the β value, the peak load is reduced significantly as $\mathcal{E}_0$ increases.

In the final step, the localized imperfection is considered by varying the α value, while $\mathcal{E}_0$ is kept constant at the same value that was obtained in the second stage. In addition, β is also kept constant as the critical value determined in the previous stage. Therefore, an increase in the A_0 value is found by increasing the α value, as shown in Figure 6.1(b) with the circle ($\circ$) symbol. The combination of α and A_0 which gives the lowest peak load is also determined. A significant further reduction in the peak loads is observed when the imperfection is more localized (modulated) by varying α, for all values of $\mathcal{E}_0$ as shown in Figure 6.1(a). The corresponding α values for each value of normalized end-shortening $\mathcal{E}_0/L$ are also shown in Figure 6.2(b). For the largest $\mathcal{E}_0$ value, the amplitude A_0 for the worst case periodic imperfection is slightly more than $t_s/10$, whereas for the worst modulated imperfection, A_0 increases to approximately $t_s/4$. Note that for higher values of $\mathcal{E}_0/L$, α begins to reduce, this would be expected since the perfect case shows cellular buckling and hence the post-buckling mode amplitude envelope begins to spread outwards from the mid-span.

Global imperfection only ($q_{s0} \neq 0$, $A_0 = 0$)

In this section, only the initial out-of-straightness of the stiffened plate W_0 is introduced to the equilibrium equations. A set of values for the normalized initial out-of-straightness amplitude q_{s0} is assumed between zero (perfect case) and 1/500. Figure 6.3 shows a series of graphs of the normalized axial load p_u ($= P/P_o^{\mathrm{C}}$) versus (a) the global mode amplitude q_s and (b) the local mode amplitude $w_{\max}/t_s$. Moreover, the graphs in Figure 6.4 show the normalized axial load p_u versus the normalized

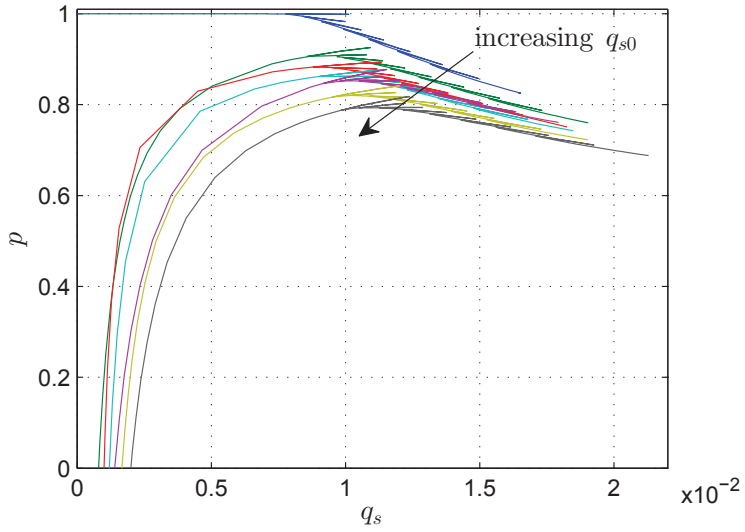

(a)

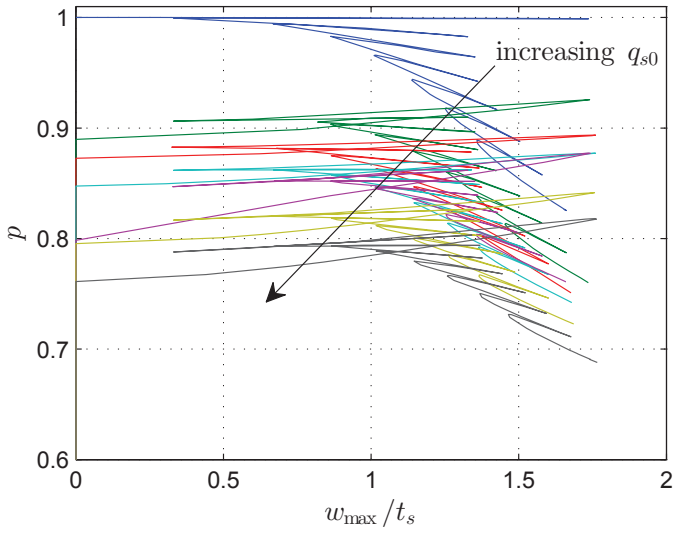

(b)

Figure 6.3: Numerical equilibrium paths for the pinned case ($c_p = 0$). The graphs show a family of curves of the normalized force ratio p ($= P/P_o^{\mathrm{C}}$) versus (a) the global mode amplitude q_s and (b) the normalized local mode amplitude $w_{\max}/t_s$.

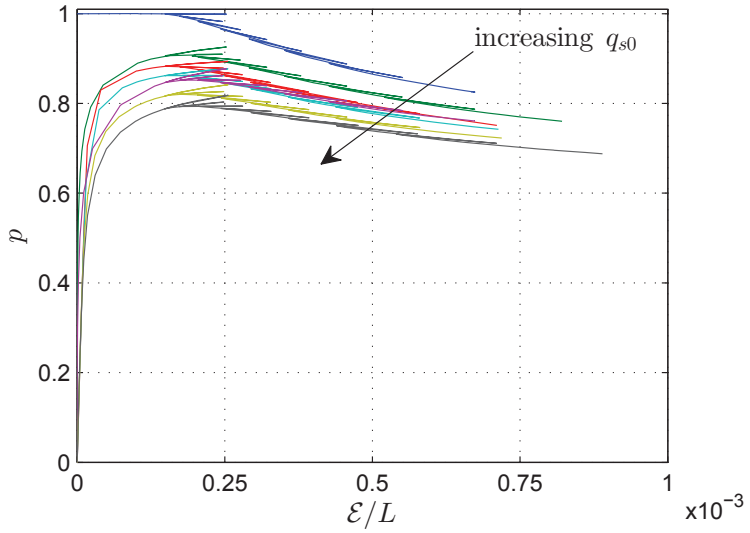

(a)

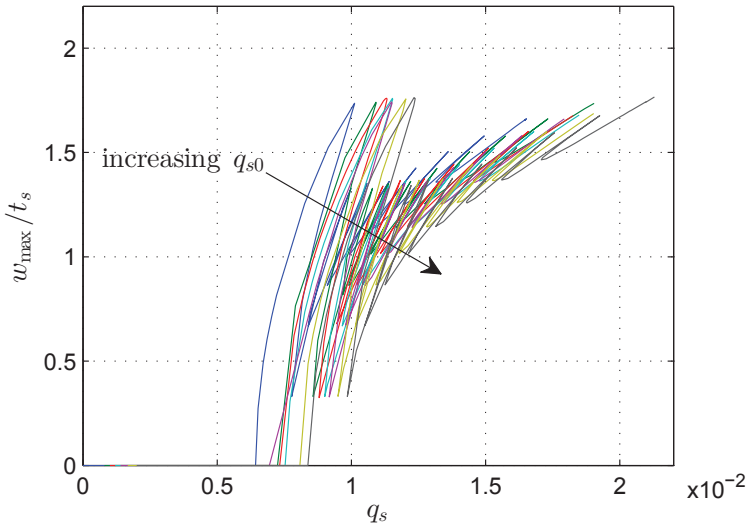

(b)

Figure 6.4: Numerical equilibrium paths for the pinned case ($c_p = 0$). The graphs show a family of curves of the (a) normalized force ratio p ($= P/P_o^{\mathrm{C}}$) versus the normalized end-shortening $\mathcal{E}/L$, (b) the local versus the global mode amplitude.

end-shortening $\mathcal{E}/L$ and the normalized local versus the global mode amplitudes, respectively.

Figure 6.5(a) shows a scatter plot of the normalized peak load, p_u against the initial global imperfection amplitudes. Moreover, Figure 6.5(b) shows the corresponding global out-of straightness q_s at the secondary bifurcation point q_s^{S} and the first snap-back location q_s^{T} versus q_{s0}. It is clearly observed that the peak load p_u decreases as the size of the imperfection increases beyond $q_{s0} = 4 \times 10^{-4}$, which shows that the stiffened plate is sensitive to global imperfections of sufficient size. Moreover, q_s^{S} and q_s^{T} values also increase as q_{s0} increases. In other words, as a result of both types of imperfection, the sensitivity studies show that the formation of the first new peak or trough (during cellular buckling) occurs further down the post-buckling path for larger initial imperfections. It is also observed that the formation of the new cell undergoes a similar restabilization path length.

6.1.2 Rigid main plate–stiffener connection

In this section, global imperfection sensitivity is studied for the case where the main plate–stiffener junction is assumed to be rigid ($c_p \to \infty$). The same set of material and geometric properties as the pinned case in the previous section is considered to study the buckling and post-buckling behaviour of the stiffened plate by varying the global imperfection amplitude q_{s0}. It is worth noting that, in the following examples, global buckling is still critical ($L = 5$ m). A set of values of the normalized initial out-of-straightness amplitude q_{s0} are assumed to be between zero (perfect case) and 1/500. Figure 6.6 shows a series of graphs of the normalized axial load $p_u = P/P_o^{\mathrm{C}}$ versus (a) the global mode amplitude q_s and (b) the local mode amplitude $w_{\max}/t_s$. Moreover, the graphs in Figure 6.7 show the normalized axial load $p_u = P/P_o^{\mathrm{C}}$ versus the normalized end-shortening $\mathcal{E}/L$ and the normalized local versus the global mode

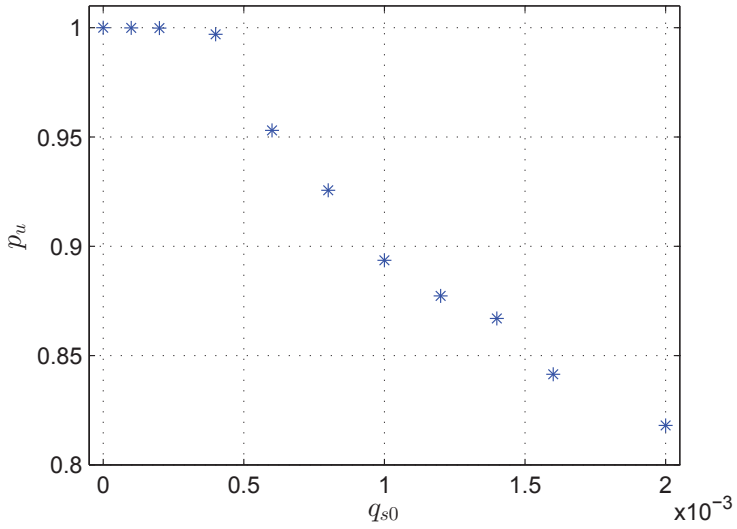

(a)

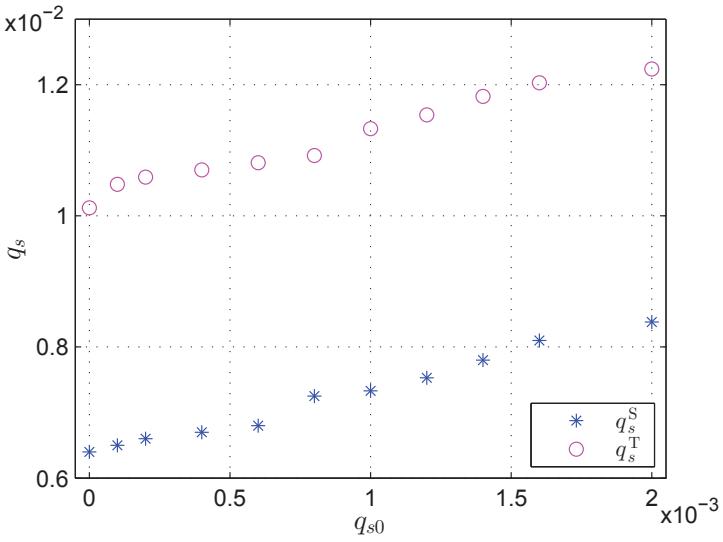

(b)

Figure 6.5: Imperfection sensitivity graphs. (a) Normalized peak load p_u ($= P/P_o^{\mathrm{C}}$) versus the initial out-of-straightness coordinate q_{s0}, (b) distribution of q_s^{S} and q_s^{T} versus q_{s0}.

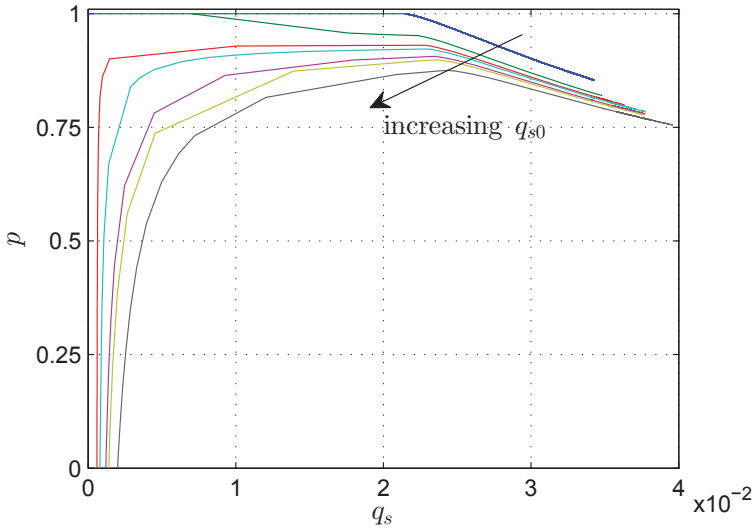

(a)

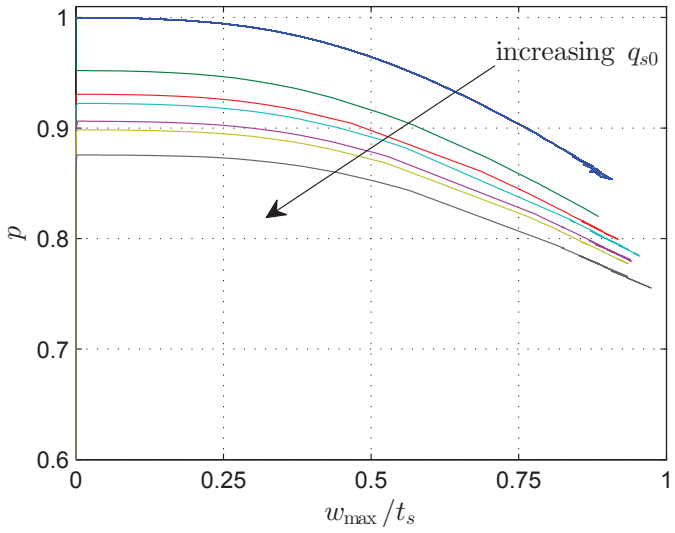

(b)

Figure 6.6: Numerical equilibrium paths for the rigid joint case ($c_p \to \infty$). The graphs show a family of curves of the normalized force ratio p ($= P/P_o^{\mathrm{C}}$) versus (a) the global mode amplitude q_s and (b) the normalized local mode amplitude $w_{\max}/t_s$.

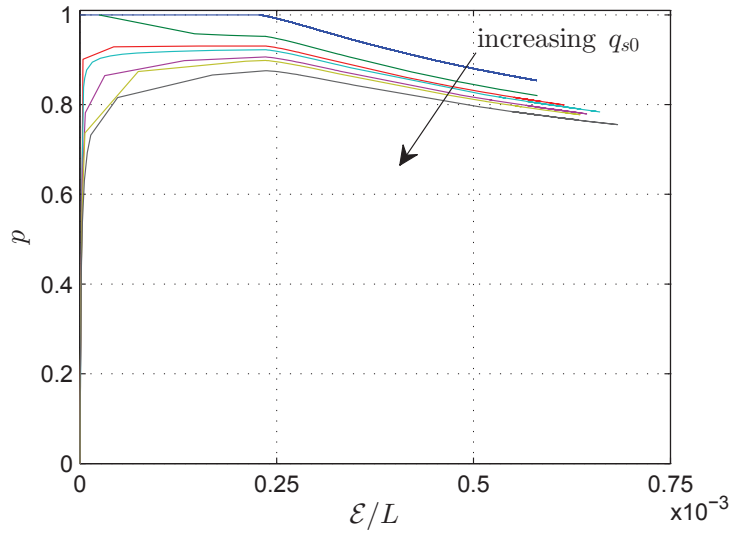

(a)

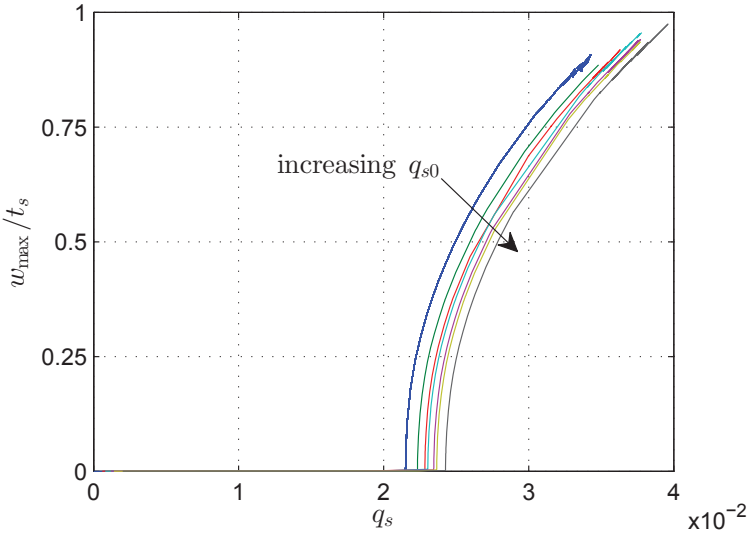

(b)

Figure 6.7: Numerical equilibrium paths for the rigid joint case ($c_p \to \infty$). The graphs show a family of curves of the (a) normalized force ratio p ($= P/P_o^{\mathrm{C}}$) versus the normalized end-shortening $\mathcal{E}/L$ and (b) the local versus the global mode amplitude.

amplitudes, respectively.

In addition, Figure 6.8(a) shows a scatter plot of the normalized peak load, p_u against the initial global imperfection amplitudes. Moreover, Figure 6.8(b) shows the corresponding value of q_s at the secondary bifurcation point q_s^{S} and the first snap-back location q_s^{T} versus q_{s0}. It is clearly observed that the peak load p_u decreases as the size of the imperfection increases, which shows that the stiffened plate is highly sensitive to global imperfections. Moreover, the q_s^{S} and q_s^{T} values also increases as q_{s0} increases. In other words, as a result of both types of imperfection, again, the sensitivity studies show that the formation of the first new peak or trough (snap-back) occurs even further down the post-buckling path for larger initial imperfections; this is similar to the perfect case yet no cellular buckling was found.

6.2 Effect of stiffener aspect ratio

The axially loaded stiffened plate with the geometric properties as summarized in Table 3.1 has been considered thus far. The corresponding aspect ratio L/h_1, was 131.57 and global buckling was the initial instability mode. In this section, a parametric study on the aspect ratio of the stiffened plate is conducted by varying the length of the stiffened plate L as well as the height of the stiffener h_1. Moreover, the effects of varying the aspect ratio on the normalized global and local panel slenderness ratios $\bar{\lambda}_o$ and $\bar{\lambda}_l$ are then discussed. It is worth noting that, in the proceeding sections, an imperfect stiffened plate with an initial global amplitude q_{s0} equivalent to a maximum mid-span deflection of $L/2000$ and the initial local amplitude A_0 equal to $t/100$ with $\beta = 1$ and $\alpha = 0$ is considered.

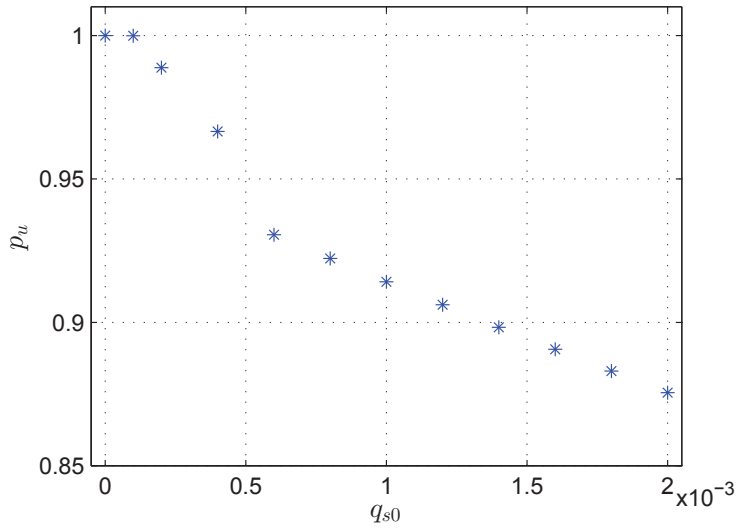

(a)

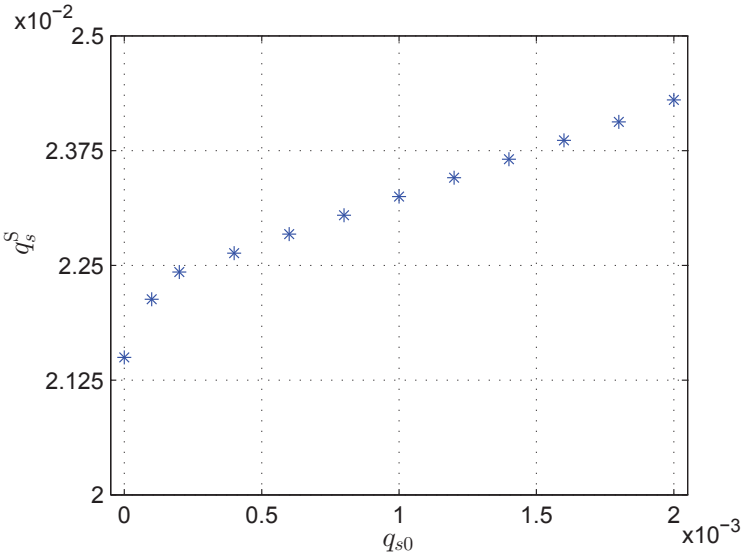

(b)

Figure 6.8: Imperfection sensitivity graphs. (a) Normalized peak load p_u ($= P/P_o^{\mathrm{C}}$) versus the initial out-of-straightness coordinate q_{s0}, (b) distribution of q_s^{S} versus q_{s0}.

6.2.1 Variation in stiffened plate length

In this section, initially, the parametric study is conducted by varying the global slenderness ratio L/r with changing the strut length L. Note that r is the section radius of gyration which is equal to $\sqrt{I/A}$, where I is the total second moment of area about the neutral axis of bending parallel to the main plate and A is the total cross-section area of the effective portion of the stiffened plate shown in Chapter 3. The other geometric properties of the effective portion stiffened plate are kept constant and are given in Table 6.1. The expression for the global buckling critical load P_o^{C} is given by Equation (3.36). The critical load for local buckling P_l^{C} is evaluated using the plate critical buckling stress formula given in Equation (2.26), where for the stiffener $t \equiv t_s$ and $b \equiv h_1$, and multiplying it by the total cross-sectional area A.

Plate breadth b	120 mm
Plate thickness t_p	2.4 mm
Stiffener depth(top) h_1	38 mm
Stiffener depth(bottom) h_2	1.2 mm
Stiffener thickness t_s	1.2 mm

Table 6.1: Geometric properties of stiffened plate.

Hitherto, the full set of equilibrium equations were solved when global buckling was critical (*i.e.* $P_o^{\mathrm{C}} < P_l^{\mathrm{C}}$). It is clear that varying the strut length L only affects the global critical load P_o^{C}, whereas varying the stiffener height h_1 affects both the global and the local critical loads, P_o^{C} and P_l^{C}, respectively.

The length L_l is determined when $P_l^{\mathrm{C}} < P_o^{\mathrm{C}}$ and interactive buckling does not occur sufficiently quickly (defined below). Therefore, the stiffened plate with $L < L_l$ exhibits effectively pure local buckling. The length L_o is determined when $P_o^{\mathrm{C}} < P_l^{\mathrm{C}}$ and

thus the stiffened plate with $L > L_o$ exhibits effectively pure global buckling and interactive buckling, again, does not occur sufficiently quickly. A critical length L_{c} is also determined for the condition where $P_o^{\mathrm{C}} = P_l^{\mathrm{C}}$. With such a condition, the secondary instability will be triggered simultaneously with the primary one. The current work considers a mid-span deflection value of $L/125$ as a limiting value for the global lateral deflection for both pinned and rigid cases; hence cases where $q_s > 0.008$ at the peak load, where $q_s = q_s^{\mathrm{u}}$ [1], are considered to have effectively negligible mode interaction. The stiffened plate length, where, $q_s^{\mathrm{u}} = 0.008$, is determined and denoted as L_o. Hence, interactive buckling, where local buckling is critical, occurs in the length range: $L_l < L < L_{\mathrm{c}}$. However, where global buckling is critical, interactive buckling occurs when the length lies in the range: $L_{\mathrm{c}} < L < L_o$; both cases are illustrated diagrammatically in Figure 6.9. For the range $L_{\mathrm{c}} < L < L_o$, the load

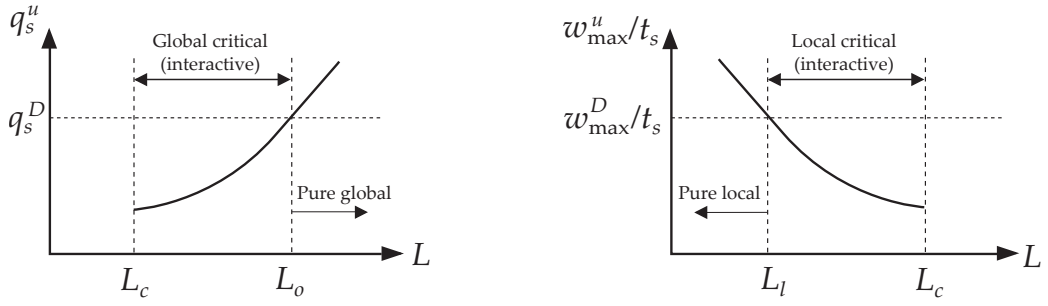

Figure 6.9: Interactive buckling regions while varying the stiffened plate length L. The length $L = L_c$ is defined when $P_o^{\mathrm{C}} = P_l^{\mathrm{C}}$, whereas stiffened plates with $L > L_o$ and $L < L_l$ are assumed to exhibit pure global buckling and pure local buckling respectively. The values q_s^{D} and $w_{\max}^{\mathrm{D}}$ define the limiting global and local mode amplitudes for pure global and local buckling respectively.

carrying capacity p_u for the perfect case is determined by the global critical load P_o^{C} and the post-buckling behaviour is then studied. Whereas, for the range where local

[1] Since the studied model in this section relatively represents the perfect case, the notation q_s^{S} is used in the proceeding results.

buckling is critical, a similar criterion is utilized for the maximum local out-of-plane deflection $w_{\max}$ at the peak load. In this range, the load carrying capacity p_u is determined as the peak load only. The study is conducted for both cases where the main plate–stiffener connection is pinned and rigid.

6.2.2 Variation in stiffener height

In this study, a similar method is used to vary the local slenderness λ_l, which is equal to h_1/t_s. Thus, the stiffener height h_1 is varied and hence the stiffener thickness t_s and the panel length L are kept constant as given in Table 3.1. Similarly, the critical stiffener height $h_{\rm c}$ is determined when $P_o^{\rm C} = P_l^{\rm C}$. By increasing h_1, the local critical load $P_l^{\rm C}$ decreases and the global critical load $P_o^{\rm C}$ increases. This is due to the increase in the second moment of area I about the bending axis parallel to the main plate. It is considered that the stiffener height $h_1 > h_l$, effectively pure local buckling occurs and therefore the interactive region where local buckling is critical is in the stiffener height range: $h_{\rm c} < h_1 < h_l$. However, decreasing h_1 implies that $P_l^{\rm C}$ increases and $P_o^{\rm C}$ decreases and therefore global buckling can become critical. It is also considered that the stiffener height $h_1 < h_o$ exhibits effectively pure global buckling and therefore the interactive region where global buckling is critical is in the stiffener height range: $h_o < h_1 < h_{\rm c}$. Figure 6.10 shows these features diagrammatically. It is worth noting that the limiting value for the stiffener local out-of-plane deflection is identified where a kink (significant slope change) is observed in the equilibrium path for both the pinned or rigid cases separately.

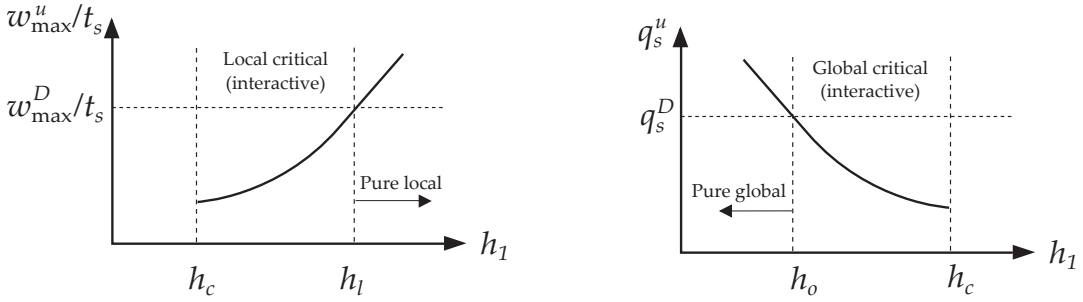

(a) (b)

Figure 6.10: Interactive buckling regions while varying the stiffener height h_1. The stiffener height $h_1 = h_c$ is defined when $P_o^{\mathrm{C}} = P_l^{\mathrm{C}}$, whereas stiffened plates with $h_1 > h_l$ and $h_1 < h_o$ are assumed to exhibit pure local buckling and pure global buckling respectively. The values q_s^{D} and $w_{\max}^{\mathrm{D}}$ define the limiting global and local mode amplitude for pure global and local buckling respectively.

6.2.3 Buckling strength curve

It is well-known that the failure mechanism primarily occurs due to structural instability and plasticity in slender and stocky structural members, respectively. The normalized global slenderness $\bar{\lambda}_o$ can be obtained from (Trahair *et al.*, 2008):

$$\bar{\lambda}_o = \sqrt{\frac{\sigma_Y}{\sigma_o^{\mathrm{C}}}}, \tag{6.2}$$

and the normalized local slenderness $\bar{\lambda}_l$ is calculated from:

$$\bar{\lambda}_l = \sqrt{\frac{\sigma_Y}{\sigma_{l,s}^{\mathrm{C}}}}, \tag{6.3}$$

where σ_Y and σ_o^{C} are the yield and the global buckling stresses, respectively. Currently, σ_Y is taken as 355 N/mm^2. In addition, $\sigma_{l,s}^{\mathrm{C}}$ is the critical stress of the stiffener which is derived from Equation (2.26), and therefore the normalized local slenderness is given by:

$$\bar{\lambda}_l = \frac{h_1}{t_s}\sqrt{\frac{12(1-\nu^2)}{k_p\pi^2}\left(\frac{\sigma_Y}{E}\right)}. \tag{6.4}$$

The global and local critical stresses, normalized with respect to σ_Y, hence, $\bar{\sigma}_o = \sigma_o^{\mathrm{C}}/\sigma_Y$ and $\bar{\sigma}_l = \sigma_{l,s}^{\mathrm{C}}/\sigma_Y$ respectively, are then obtained for the elastic buckling curve, thus:

$$\bar{\sigma}_o = (\bar{\lambda}_o)^{-2}, \qquad \bar{\sigma}_l = (\bar{\lambda}_l)^{-2}. \tag{6.5}$$

The idealized buckling design curves are therefore plotted in terms of the nondimensional stress and slenderness, as shown in Figure 6.11. It is clear that for $\bar{\lambda}_x > 1$,

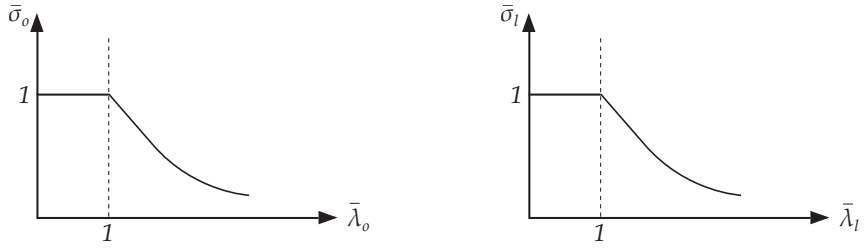

(a) (b)

Figure 6.11: The idealized strength curve in terms of normalized quantities for (a) global buckling stress versus global slenderness and (b) local buckling stress versus the local slenderness.

where $x = \{o, l\}$, columns are relatively slender and elastic buckling dominates; but for $\bar{\lambda}_x < 1$, columns are stocky and plasticity dominates. With imperfections, however, the situation is less distinct. Nevertheless, for $\bar{\lambda}_x \gg 1$, the elastic buckling load is approximately the ultimate load and plasticity effects are indeed negligible. In the following section, numerical examples are presented for an example set of stiffened plate lengths L as well as stiffener heights h_1; the corresponding normalized slendernesses are calculated using Equations (6.2) and (6.4) respectively.

6.2.4 Numerical results and discussion

Pinned main plate–stiffener connection

In this section, numerical continuations are performed in Auto for the stiffened plate with a pinned joint between the stiffener and the main plate (*i.e.* $c_p = 0$). It is observed in Figure 6.12 that, for the particular section properties given in Table 6.1, panel lengths between $L_l = 800$ mm and $L_o = 3500$ mm are the most vulnerable to interactive buckling, whereas with $L < L_l$ and $L > L_o$ are vulnerable to pure local buckling and pure global buckling respectively. The critical strut length L_c is found to be approximately 1235 mm by both the theoretical calculation and the numerical solution.

Figure 6.13 shows the results in terms of the classic curve that was presented by van der Neut (1969), see Figure 2.10. This shows P_u/P_l^{C} versus $P_o^{\mathrm{C}}/P_l^{\mathrm{C}}$ for varying L. It is observed that for $L > L_o$, the stiffened plate exhibits pure global buckling that is weakly stable, after the critical bifurcation point. For $L_c < L < L_o$, the strut exhibits a weakly stable equilibrium path after the critical bifurcation point, followed by an unstable interactive post-buckling path after the secondary bifurcation point. For $L \approx L_c$, the global and the local buckling modes are triggered practically simultaneously and the stiffened plate exhibits an unstable interactive post-buckling path. For $L_l < L < L_c$, the strut exhibits a stable equilibrium path after the critical bifurcation point, followed by an unstable interactive post-buckling path after the secondary bifurcation point. Finally for $L < L_l$, the strut exhibits pure local buckling of the main plate that is strongly stable. Note that for $L_l < L < L_o$, all equilibrium paths exhibit cellular buckling behaviour during mode interaction.

With the section properties given in Table 3.1 and L being fixed, the numerical continuations are carried out for varying the stiffener height h_1. Figure 6.14 corresponds

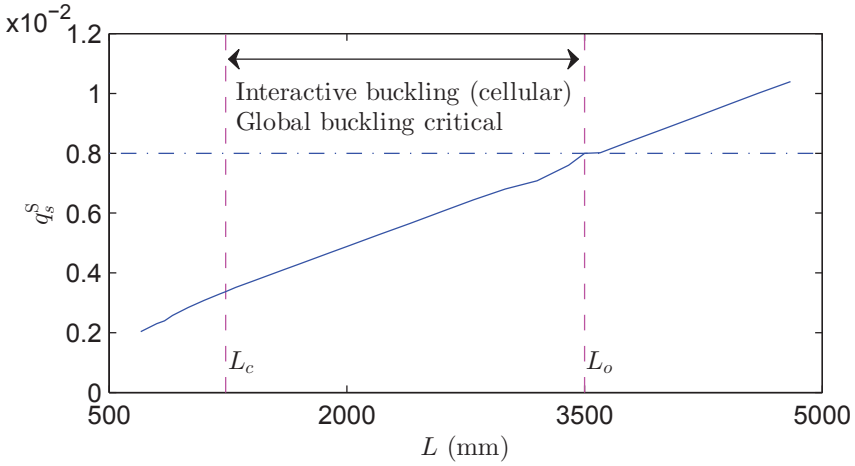

(a)

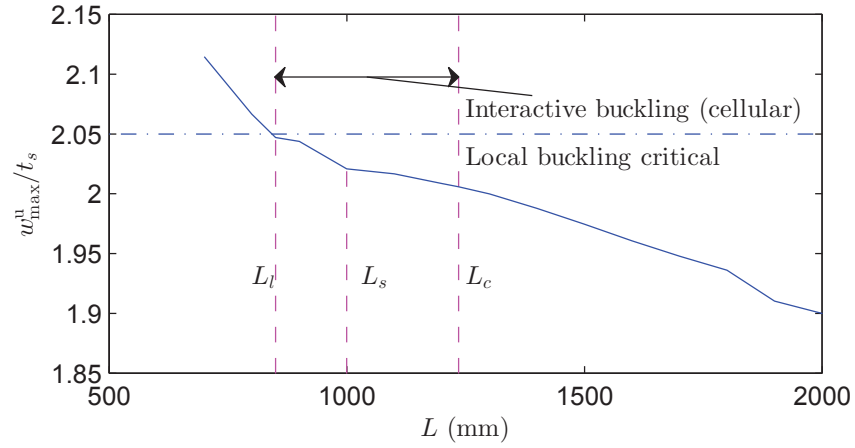

(b)

Figure 6.12: Pinned case, varying length L. Graphs show (a) the normalized lateral displacement at the secondary bifurcation point q_s^{S} $(= q_s^u)$ and (b) the normalized maximum local out-of-plane displacement $w_{\max}^u/t_s$ at the peak load p_u, versus the strut length L, for the cases where global and local buckling are critical, respectively. The vertical dashed line with label L_c represents the critical stiffened plate length where $P_o^{\mathrm{C}} = P_l^{\mathrm{C}}$. The horizontal dot-dashed lines represent the amount of displacement, above which interactive buckling is assumed to be insignificant $(q_s^{\mathrm{D}}, w_{\max}^{\mathrm{D}})$; the interactive region is therefore $L_l < L < L_o$. The vertical dashed line L_s represents the strut length which p_u begins to deviate from P_l^{C} significantly.

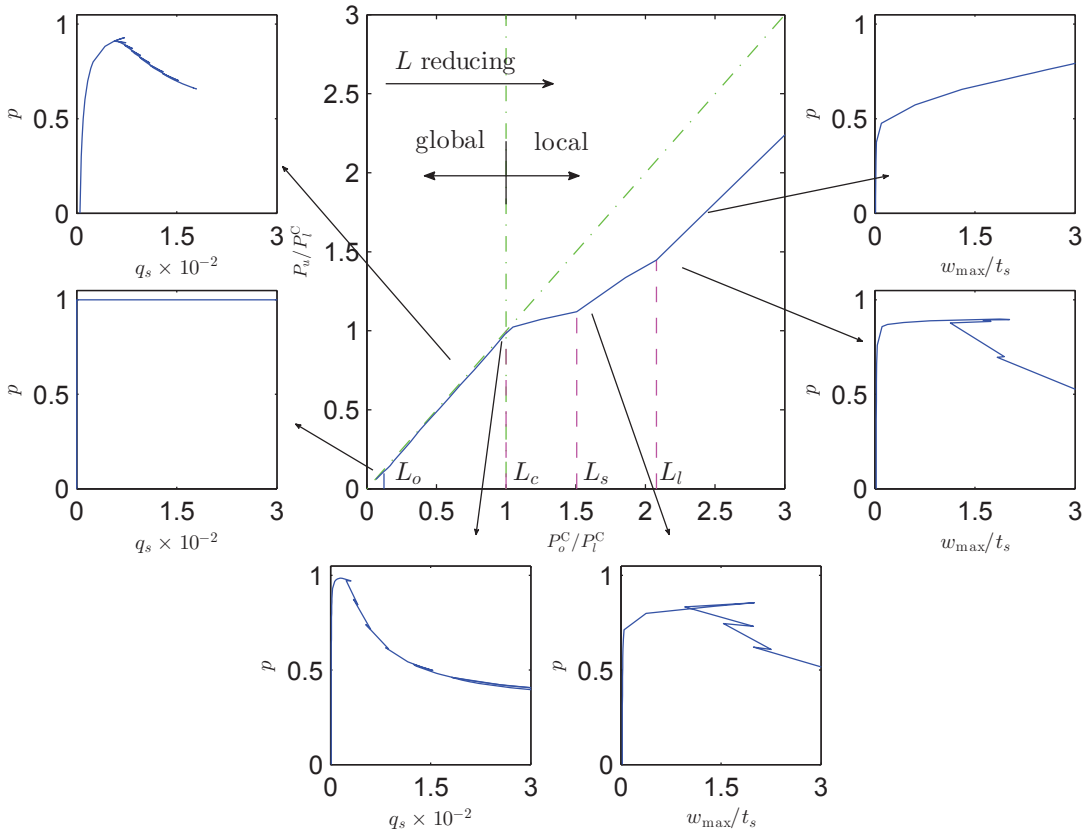

Figure 6.13: Pinned case, varying length L. The central graph shows the normalized ultimate load P_u/P_l^{C} versus the normalized global critical load $P_o^{\mathrm{C}}/P_l^{\mathrm{C}}$. The solid line represents the actual numerical solutions whereas the dashed lines representing L_l, L_c, L_s and L_o correspond directly to Figure 6.12. The surrounding graphs show examples of the equilibrium paths corresponding to the different parts of the central graph, separated by the dot-dashed lines.

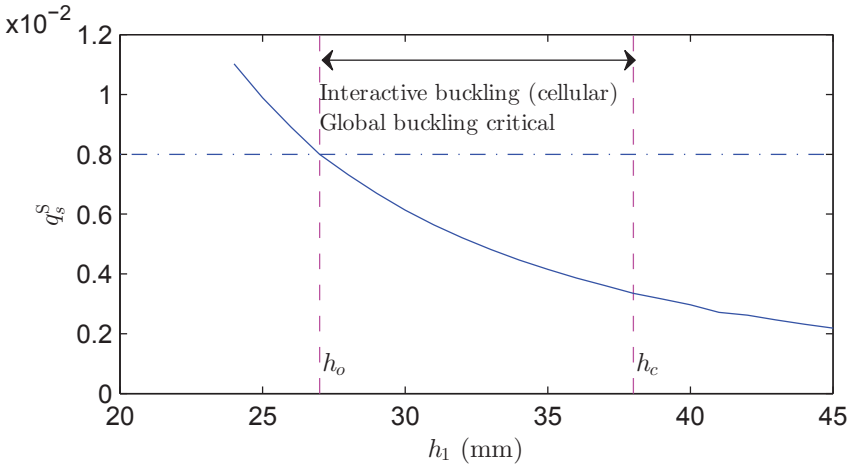

(a)

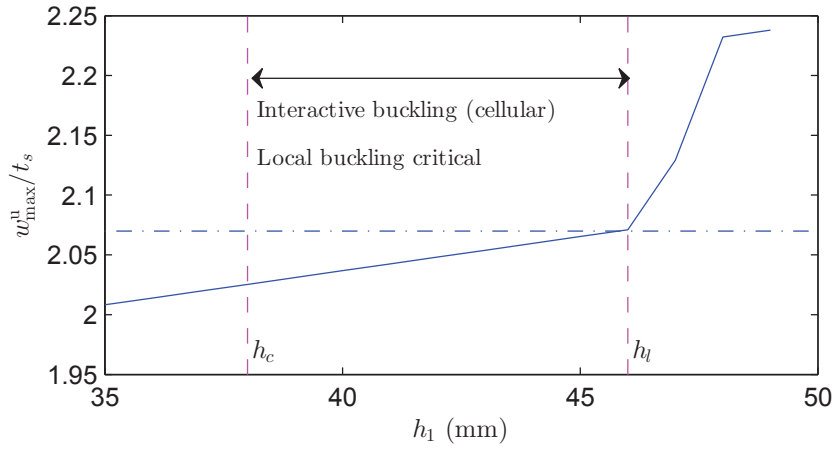

(b)

Figure 6.14: Pinned case, varying stiffener height h_1. Graphs show (a) the normalized lateral displacement at the secondary bifurcation point q_s^{S} $(= q_s^u)$ and (b) the normalized maximum local out-of-plane displacement $w_{\max}^u/t_s$ at the peak load p_u, versus the stiffener height h_1, for the cases where global and local buckling are critical, respectively. The vertical dashed line with label h_c represents the critical stiffened plate length where $P_o^{\mathrm{C}} = P_l^{\mathrm{C}}$. The horizontal dot-dashed line represents the amount of displacement, above which interactive buckling is assumed to be insignificant (q_s^{D}, $w_{\max}^{\mathrm{D}}$); the interactive region is therefore $h_o < h_1 < h_l$.

to Figure 6.12, for varying h_1. It is observed in Figure 6.14 that the stiffened plates with stiffener height between $h_o = 27$ mm and $h_l = 46$ mm are most vulnerable to interactive buckling, whereas stiffeners with $h_1 > h_l$ and $h_1 < h_o$ are vulnerable to pure local buckling and pure global buckling respectively. The critical stiffener height h_c is found to be approximately 38 mm by both theoretical calculation and the numerical solution.

Figure 6.15 shows a plot of P_u/P_l^{C} versus $P_o^{\mathrm{C}}/P_l^{\mathrm{C}}$ for varying h_1, and examples of the actual equilibrium paths for different ranges of h_1. It is observed that for $h_1 < h_o$, the strut exhibits pure global buckling that is weakly stable, after the critical bifurcation point. For $h_o < h_1 < h_c$, the strut exhibits a weakly stable equilibrium path after the critical bifurcation point, followed by an unstable interactive post-buckling path after the secondary bifurcation point. For $h_1 \approx h_c$, the global and the local buckling modes are triggered practically simultaneously and the strut exhibits an unstable interactive post-buckling path. For $h_c < h_1 < h_l$, the strut exhibits a stable equilibrium path after the critical bifurcation point, followed by an unstable interactive post-buckling path after the secondary bifurcation point. Finally for $h_1 > h_l$, the strut exhibits pure local buckling. Again, all equilibrium paths exhibit cellular buckling behaviour within the interactive region.

Rigid main plate–stiffener connection

In this section, numerical continuations are presented for the stiffened plate with a rigid joint between the main plate and the stiffener ($c_p \to \infty$). Initially, the stiffened plate length L is varied with the section properties given in Table 6.1. Figures 6.16 and 6.17 correspond to Figures 6.12 and 6.13, for the rigid main plate–stiffener junction, respectively. According to the graphs in Figure 6.16, it can be observed that a stiffened plate with a length between $L_c = 720$ mm and $L_o = 2100$ mm are most vulnerable

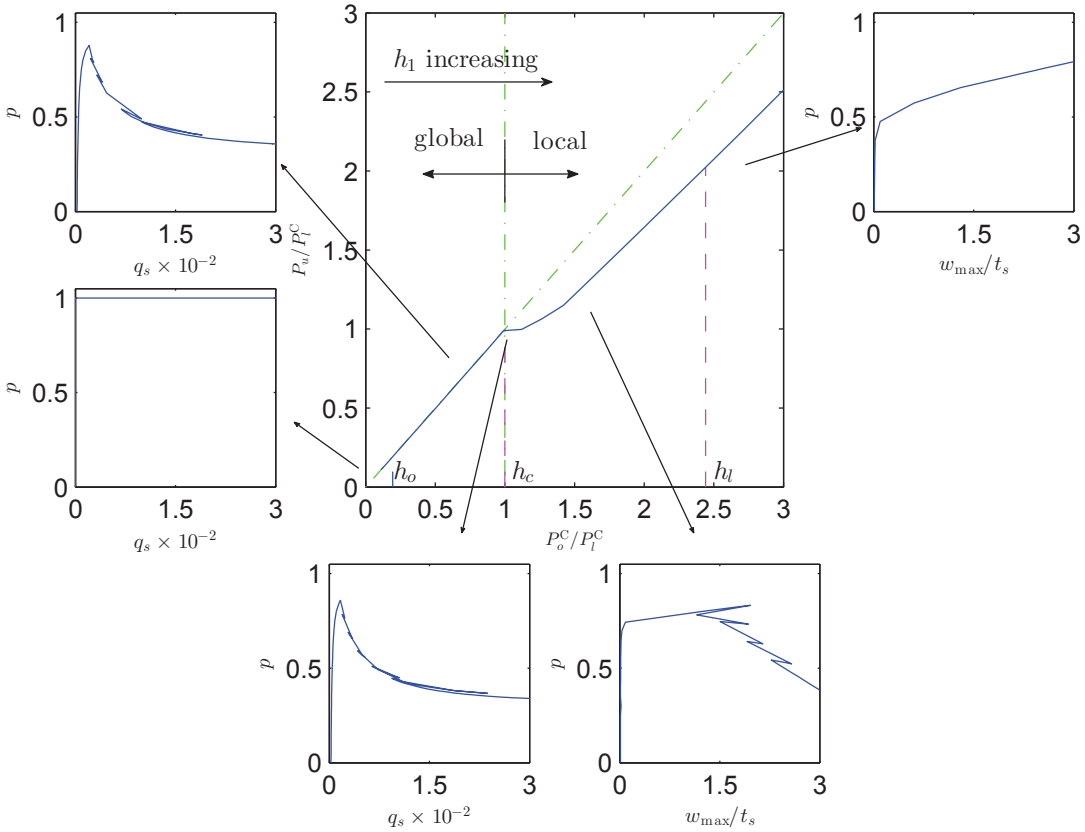

Figure 6.15: Pinned case, varying stiffener height h_1. The central graph shows the normalized ultimate load P_u/P_l^{C} versus the normalized global critical load $P_o^{\mathrm{C}}/P_l^{\mathrm{C}}$. The solid line represents the actual numerical solutions whereas the dashed lines representing h_l, h_c and h_o correspond directly to Figure 6.14. The surrounding graphs show examples of the equilibrium paths corresponding to the different parts of the central graph, separated by the dot-dashed lines.

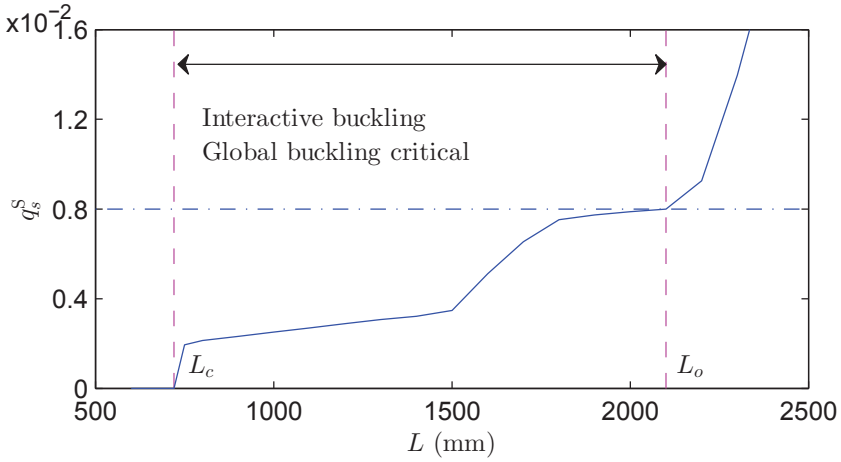

(a)

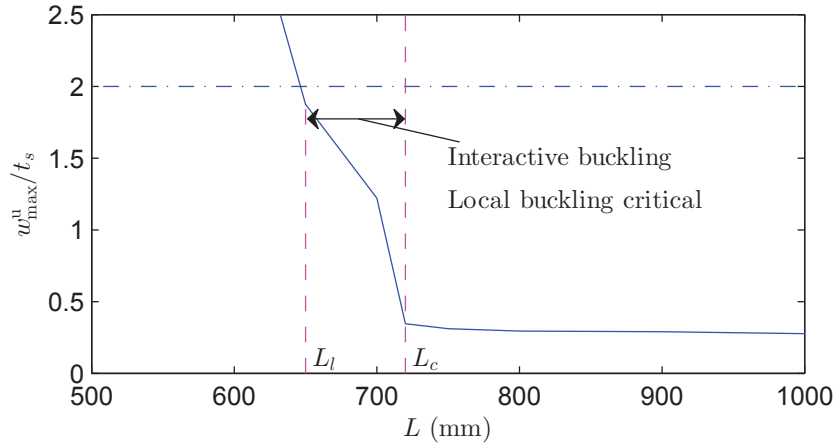

(b)

Figure 6.16: Rigid case, varying length L. Graphs show (a) the normalized lateral displacement at the secondary bifurcation point q_s^{S} $(= q_s^u)$ and (b) the normalized maximum local out-of-plane displacement $w_{\max}^u/t_s$ at the peak load p_u, versus the strut length L, for the cases where global and local buckling are critical, respectively. The vertical dashed line with label L_c represents the critical stiffened plate length where $P_o^{\mathrm{C}} = P_l^{\mathrm{C}}$. The horizontal dot-dashed lines represent the amount of displacement, above which interactive buckling is assumed to be insignificant $(q_s^{\mathrm{D}}, w_{\max}^{\mathrm{D}})$; the interactive region is therefore $L_l < L < L_o$.

to interactive buckling where global buckling is critical, whereas struts with $L > L_o$ are vulnerable to pure global buckling. On the other hand, a stiffened plate with a length between $L_l = 650$ mm and $L_c = 720$ mm are most vulnerable to interactive buckling where local buckling is critical, whereas struts with $L < L_l$ are vulnerable to pure local buckling.

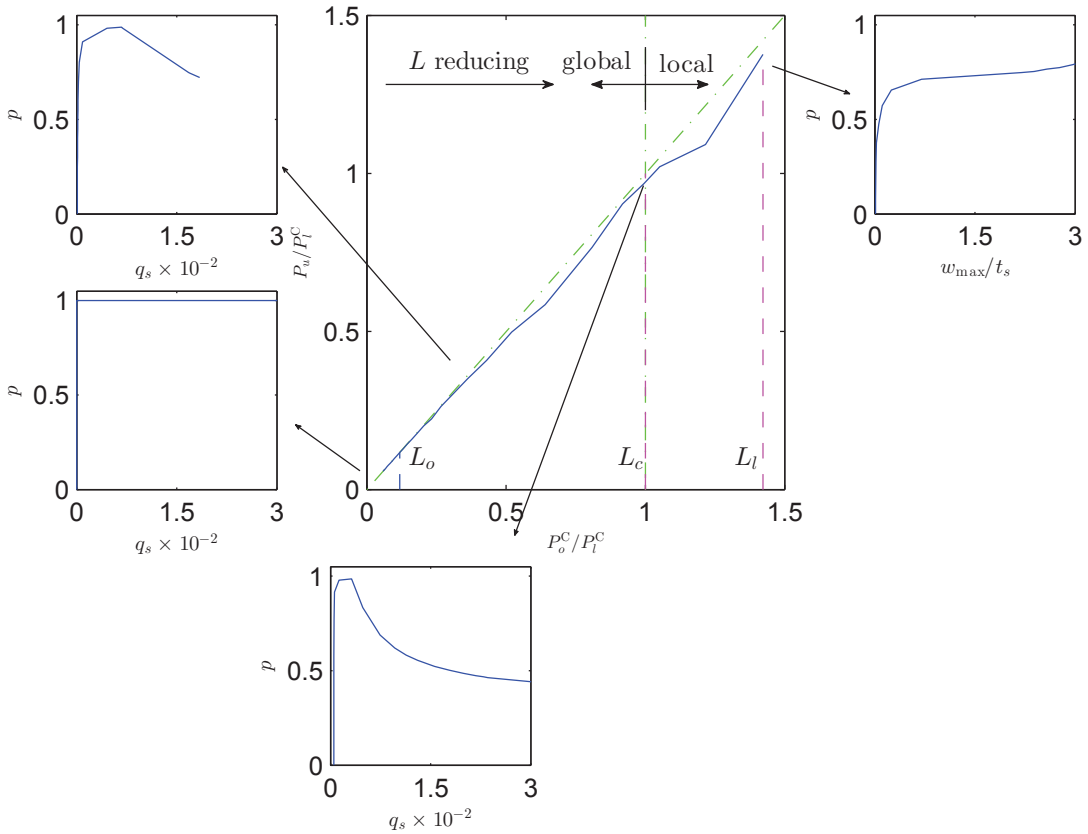

Figure 6.17: Rigid case, varying length L. The central graph shows the normalized ultimate load P_u/P_l^{C} versus the normalized global critical load $P_o^{\mathrm{C}}/P_l^{\mathrm{C}}$. The solid line represents the actual numerical solutions whereas the dashed lines representing L_l, L_c and L_o correspond directly to Figure 6.16. The surrounding graphs show examples of the equilibrium paths corresponding to the different parts of the central graph, separated by the dot-dashed lines.

The stiffener height h_1 is also varied for the stiffened plate with the geometric properties in Table 6.1 with the length L being fixed at the critical value, for the fully rigid main plate–stiffener connection. It is observed in Figure 6.18 that the stiffened plate with the stiffener heights between $h_o = 26$ mm and $h_l = 39$ mm are most vulnerable to interactive buckling, whereas the stiffener with $h_1 > h_l$ and $h_1 < h_o$ are vulnerable to pure local buckling and pure global buckling respectively. The critical stiffener height h_c has the same value as the one in the pinned case. Figure 6.19 shows a very similar trend as shown in Figure 6.15.

6.2.5 Interactive buckling zone

The region where interactive buckling is significant is summarized in Tables 6.2 and

	$\min(L_l, L_s)$ (mm)	L_c (mm)	L_o (mm)
Pinned	800	1235	3500
Rigid	650	720	2100

Table 6.2: Summary of values for L_l, L_s, L_c and L_o, for struts with the properties given in Table 6.1, for both the pinned and the fully rigid main plate–stiffener connection. Note that the stiffener height $h_1 = 38$ mm in both the pinned and the rigid joint cases.

6.3 in terms of the stiffened plate length L and the stiffener height h_1 respectively,

	$\min(h_l, h_s)$ (mm)	h_c (mm)	h_o (mm)	L (mm)
Pinned	46	38	27	1235
Rigid	39	38	26	720

Table 6.3: Summary of values for h_l, h_s, h_c and h_o, for struts with the properties given in Table 6.1, for both the pinned and the rigid joint cases.

for both the pinned and the rigid main plate–stiffener connection. In the interactive

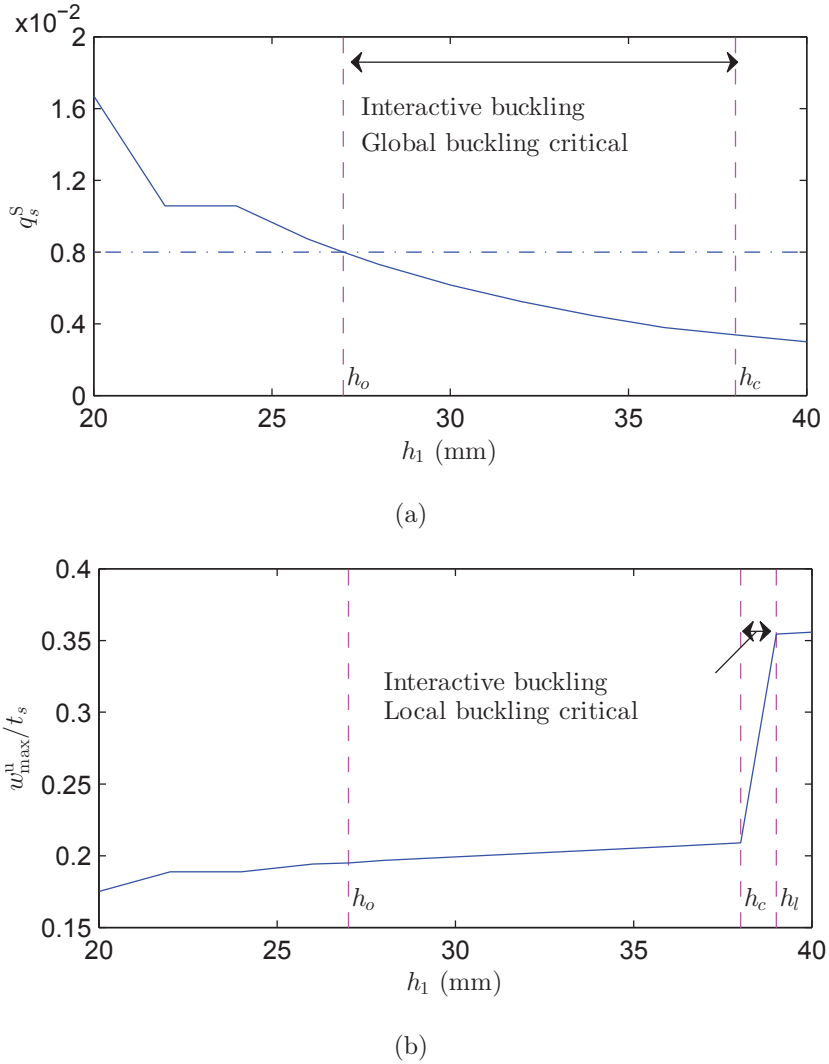

Figure 6.18: Rigid case, varying stiffener height h_1. Graphs show (a) the normalized lateral displacement at the secondary bifurcation point q_s^{S} $(= q_s^u)$ and (b) the normalized maximum local out-of-plane displacement $w_{\max}^u/t_s$ at the peak load p_u, versus the stiffener height h_1, for the cases where global and local buckling are critical, respectively. The vertical dashed line with label h_c represents the critical stiffened plate length where $P_o^{\mathrm{C}} = P_l^{\mathrm{C}}$. The horizontal dot-dashed line represents the amount of displacement, above which interactive buckling is assumed to be insignificant (q_s^{D}, $w_{\max}^{\mathrm{D}}$); the interactive region is therefore $h_o < h_1 < h_l$.

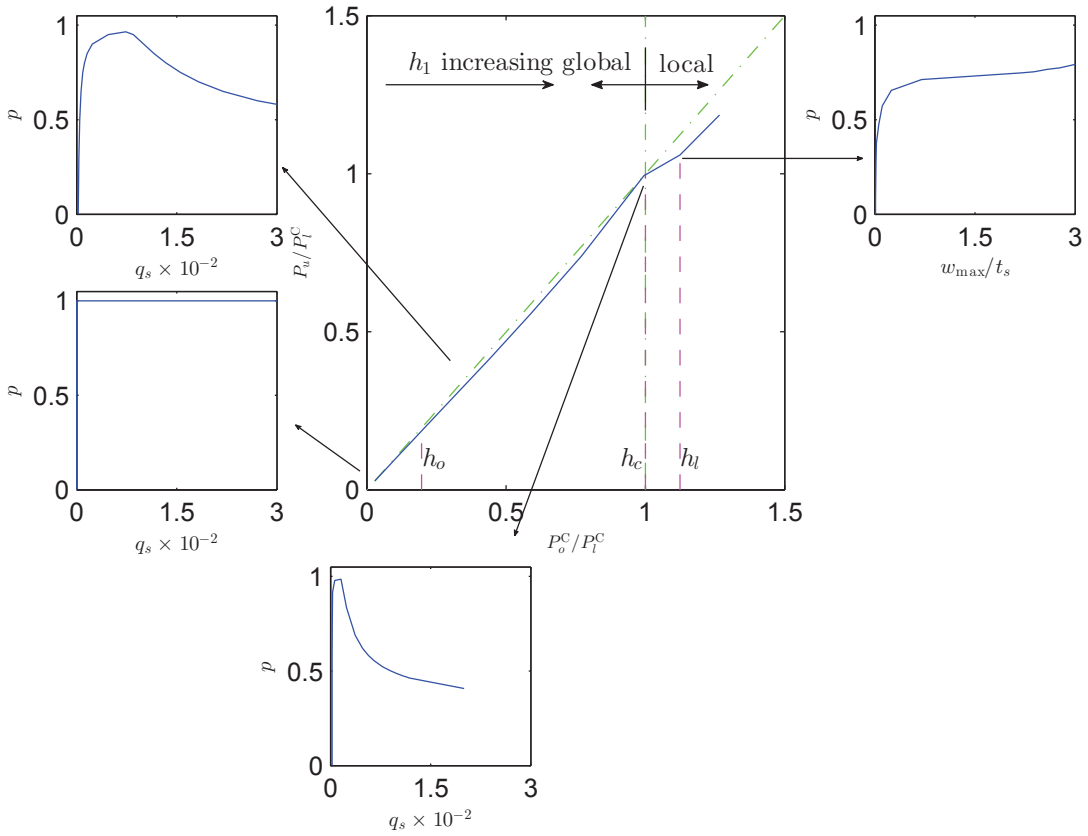

Figure 6.19: Rigid case, varying stiffener height h_1. The graph shows the normalized ultimate load P_u/P_l^{C} versus the normalized global critical load $P_o^{\mathrm{C}}/P_l^{\mathrm{C}}$. The solid line represents the actual numerical solutions whereas the dashed lines representing h_l, h_c and h_o. The surrounding graphs show examples of the equilibrium paths corresponding to the different parts of the central graph, separated by the dot-dashed lines.

zone, the post-buckling behaviour is highly unstable after the secondary instability is triggered. It is clear that by increasing the rigidity of the connection between the main plate and the stiffener, the vulnerability to interactive buckling is reduced, in terms of both the stiffened plate length L and the stiffener height h_1. Tables 6.4 and 6.5 summarize the values of the global and the local normalized slendernesses,

	$\bar{\lambda}_l$	$\bar{\lambda}_c$	$\bar{\lambda}_o$
Pinned	2.088	2.09	5.62
Rigid	1.22	1.23	3.39

Table 6.4: Summary of values for $\bar{\lambda}_l$, $\bar{\lambda}_c$, and $\bar{\lambda}_o$, for struts with the properties given in Table 6.2, for both the pinned and the rigid joint cases.

	$\bar{\lambda}_l$	$\bar{\lambda}_c$	$\bar{\lambda}_o$
Pinned	2.52	2.09	3.19
Rigid	1.25	1.23	2.06

Table 6.5: Summary of values for $\bar{\lambda}_l$, $\bar{\lambda}_c$, and $\bar{\lambda}_o$, for struts with the properties given in Table 6.3, for both the pinned and the rigid joint cases.

$\bar{\lambda}_o$ and $\bar{\lambda}_l$, the values of which are calculated using Equations (6.2) and (6.4), directly corresponding to the values of the stiffened plate lengths and the stiffener height given in Table 6.2 and Table 6.3, respectively.

Note that the global and the local normalized slendernesses, for each critical stiffened plate length L_c and the critical stiffener height h_c, are equal, and are therefore denoted using a single piece of notation $\bar{\lambda}_c$.

When L is varied, the normalized global slenderness only changes and therefore $\bar{\lambda}_c \approx \bar{\lambda}_l$ as seen in Table 6.4. However, as h_1 is varied the normalized local slenderness $\bar{\lambda}_l$ changes together with the normalized global slenderness. Therefore, since the critical length L_c is different for the pinned and the rigid cases (see Table 6.3), $\bar{\lambda}_c$ differs from

both $\bar{\lambda}_o$ and $\bar{\lambda}_l$, as seen in Table 6.5. Figure 6.20(a–b) shows the idealized strength curves (see Figure 6.11) corresponding to the values of global and the local normalized slendernesses given in Tables 6.4 and 6.5, respectively. With imperfections, of course, the reduction from the idealized strength curve is likely to be the greatest where $\bar{\lambda} = \bar{\lambda}_c$.

6.3 Concluding remarks

Imperfection sensitivity and parametric studies were performed for an example set of material and geometric properties of a series of thin-walled stiffened plates for two limiting cases where the main plate was assumed to provide a pinned and rigid connection to the stiffener.

Initially, imperfection sensitivity studies were conducted for the cases with the presence of the global and local imperfections only. The model identified the highly imperfection sensitive nature of the struts that are susceptible to cellular buckling. Significant reduction in the load-carrying capacity was observed for the struts with a small initial global and local imperfections. It was also found that the local imperfection that had a localized (modulated) profile was always seemed to be the worst case in terms of the load-carrying capacity, as was the case for axially loaded sandwich struts (Wadee, 2000). The study on different forms of global and local imperfections indicates the need for caution in numerical assessments during the design process for actual thin-walled stiffened plates that undergo interactive buckling behaviour.

The investigation also focused on changing the global and the local slendernesses by varying the panel length and the stiffener height. A deflection based criterion was defined such that an interactive buckling dominated region, where the interaction between global and local buckling dominates, may be determined. For pinned

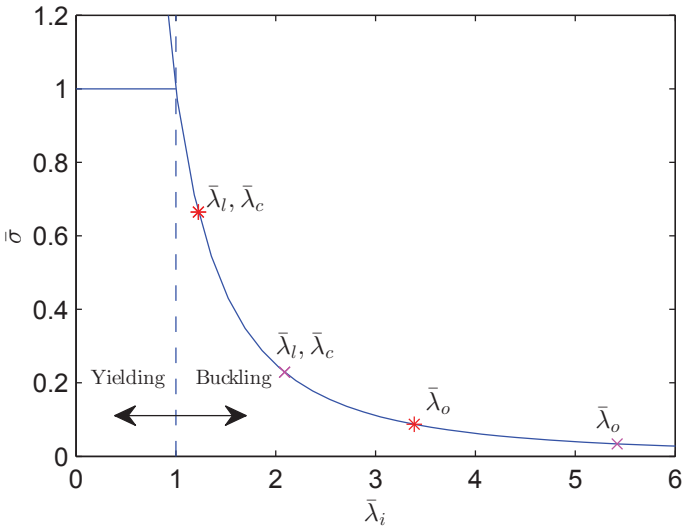

(a)

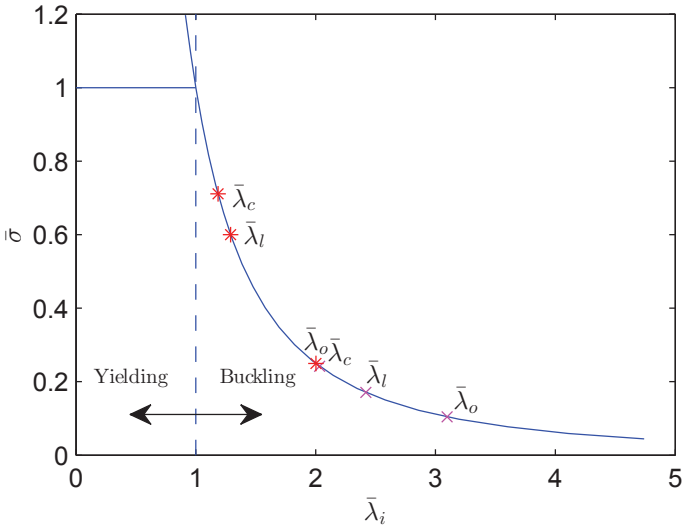

(b)

Figure 6.20: The idealized strength curves with the symbols representing the global and the local normalized slendernesses given in (a) Table 6.4 and (b) Table 6.5. Symbols ($*$) and ($\times$) represent the cases where the main plate–stiffener joint is assumed to be rigid and pinned respectively. Note the higher slenderness values for the pinned cases.

main plate–stiffener connections, all examples (including where the global mode or the local mode was critical) within the interactive region exhibit unstable cellular buckling. For a fully rigid main plate–stiffener connection, examples for the cases where global buckling was critical, exhibit unstable post-buckling responses without the observation of the cellular behaviour, as found in Chapter 4.

Chapter 7

General conclusions

This thesis has presented a series of analytical models with increasing complexity that account for the interactive buckling phenomena in axially-loaded thin-walled stringer-stiffened plates with a varying rigidity of the main plate–stiffener connection. Using the calculus of variations, the analytical models have been developed based on elasticity theory and total potential energy principles. The models focused on the nonlinear interaction between the global (Euler) buckling mode and the local buckling mode of the stiffener as well as the main plate.

The highly unstable post-buckling behaviour followed by a sequence of snap-backs has been highlighted, outlining sequential destabilization and restabilization. This phenomenon captured the vulnerability to cellular buckling behaviour for stiffened plates with rotationally weak main plate–stiffener connections. Imperfection sensitivity and parametric studies were conducted highlighting some important behaviour that needs particular attention in the context of structural design.

The research study, initially, focused on a perfect case, adapted to investigate the effect of varying the rigidity of the main plate–stiffener connection, by introducing

a rotational spring that restricted the relative rotation between the main plate and the stiffener. Distinct features were captured by the numerical examples for the case where global buckling was critical. In that case, the stiffened plate first buckled globally at the primary bifurcation point and then followed the weakly stable post-buckling path until a secondary bifurcation point, where interactive buckling of the stiffener was triggered. For the pinned case, cellular buckling was found with a characteristic sequence of snap-backs in the mechanical response; each snap-back corresponded to the new formation of a peak or trough in the local buckling mode profile. The buckling mode of the stiffener changed from localized to periodic with a progressively reducing wavelength. Although, the effect of the snap-backs reduced by increasing the rigidity of the main plate–stiffener connection, the mode interaction persisted and the local buckling profile still changed wavelength.

The model was then extended to include the local deflection of the main plate. In addition, two types of geometric imperfections were included into the equilibrium equation: an initial out-of-straightness (global imperfection) and an initial out-of-plane displacement of the stiffener as well as the main plate (local imperfection). Significant reductions in the load-carrying capacity were observed for the structure with a small initial global imperfection or both global and local imperfection components.

The developed analytical models were compared to published experiments (Fok *et al.*, 1976) and a finite element (FE) model formulated in Abaqus (2011). In the FE models, 4-noded shell elements (S4R) were used and Riks analyses were performed to generate the post-buckling response, with the introduced imperfection obtained from the linear eigenvalue analysis. The comparison between the analytical model and the corresponding results from both the FE model and the experimental results were found to be excellent. Indeed, the comparisons were seen to be the best where the main plate buckles in sympathy with the stiffener and where the rigidity of the joint connecting the stiffener to the main plate was high. It was also found that the static

FE model formulated in Abaqus, compared very well to the analytical model in the neighbourhood of the secondary instability. The FE model, however, seemed to have problems by not allowing the local buckling wavelength to change. In particular, it was unable to track any cellular buckling, even though it is clearly seen in experiments of closely related structural components (Becque, 2008; Becque & Rasmussen, 2009a; Wadee & Gardner, 2012; Wadee & Bai, 2014).

Imperfection sensitivity studies were carried out for the cases with a global imperfection only and a local imperfection only by varying the local imperfection amplitude A_0 and the global imperfection amplitude q_{s0}, respectively. The results revealed the highly imperfection sensitive nature of the stiffened plate. Moreover, two forms of the local imperfection, namely a periodic and a modulated imperfection were examined. In order to carry out meaningful comparisons, the initial imperfection end-shortening $\mathcal{E}_0$ was introduced; essentially a measure of the imperfection size that avoided using simply the amplitude. By keeping $\mathcal{E}_0$ constant, it was found that the modulated localized imperfections always resulted in a more severe reduction in the load-carrying capacity. It was also found that the worst case form for larger imperfections (larger $\mathcal{E}_0$) was always associated with a larger number of waves (larger β), which is a consequence of the steadily reducing wavelength in the nonlinear response of the perfect system. However, as $\mathcal{E}_0$ was increased, the degree of localization (α) reduced for the systems which showed cellular buckling.

Moreover, parametric studies were conducted for two limiting cases where the main plate–stiffener connection rigidity was assumed to provide a pinned or a rigid support. The global and local slendernesses were varied by changing the stiffened plate length and the stiffener height respectively. The results were presented in a similar way to the classic curve described by van der Neut (1969). The parametric regions most vulnerable to interactive buckling were determined for both limiting cases. Since distinct global buckling and local buckling of the stiffener are well understood, the focus was on

investigating the post-buckling behaviour for the struts within the interactive region. For the pinned main plate–stiffener connection, the interaction between the global and the local modes always resulted in highly unstable cellular buckling behaviour. The parametric study provided a methodology for investigating such structures. It allowed full investigation of the effect of changing section properties on the buckling and post-buckling behaviours. The analytical model identified the potentially dangerous region where the strut is most vulnerable to the highly unstable interactive and cellular post-buckling behaviour, which would have to be treated with great caution in design considerations.

7.1 Further work

Hitherto, a thin-walled simply-supported stiffened panel with uniformly spaced longitudinal blade stiffeners were considered. The analytical model has been developed to investigate the interaction between the global (Euler) buckling and the local buckling of the stringer-stiffened plate.

The analytical model can be adapted for a stiffened plate with lipped stiffeners as shown in Figure 7.1(a). This type of stiffener would introduce the possibility of distortional buckling. Similar to the current research study, the relative rigidity of the connection between the stiffener and the lip can be provided by a rotational spring with stiffness c_l at the stiffener–lip junction, as shown in Figure 7.1(c). Hence, the shape of the local buckling mode along the width of the lip can be estimated by a nonlinear function that is again a summation of both polynomial and trigonometric terms. Appendix C presents an outline formulation that may be used as a starting point for modelling this. Since lipped sections are known to suffer from distortional buckling, the interaction between the global and the distortional buckling mode may also be considered in the equilibrium equation.

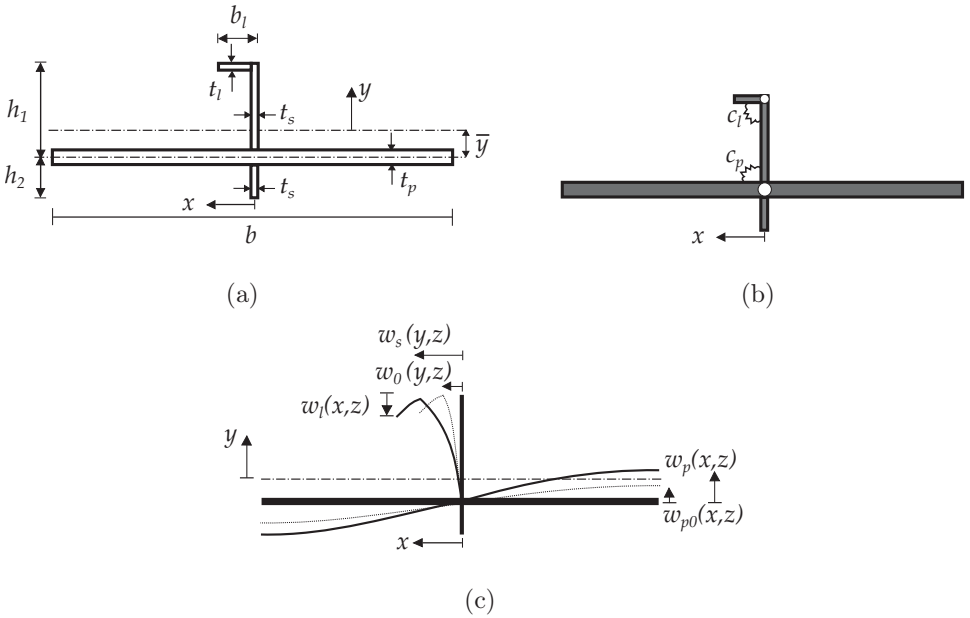

Figure 7.1: (a) Lipped stiffened plate cross-section geometry. (b) Modelling the joint rigidity of the main plate–stiffener and lip–stiffener connections with rotational spring of stiffnesses c_p and c_l respectively. (c) Local out-of-plane deflection of the stiffener $w_s(y,z)$ with initial imperfection $w_0(y,z)$, local out-of-plane deflection of the main plate $w_p(x,z)$ with initial imperfection $w_{p0}(x,z)$ and local out-of-plane deflection of the lip $w_l(x,z)$.

In the literature (Hunt *et al.*, 2000; Wadee & Edmunds, 2005), the Maxwell load (P^{M}) has been calculated for snaking problems, which is known to be a realistic lower bound strength for the system. Presently, however, it is more complex to determine such a quantity because the system axial load P does not oscillate about a fixed load P^{M} as the deformation increases, unlike the diagram shown in Figure 2.13. This is primarily owing to the fact that, unlike other systems that exhibit cellular buckling, such as cylindrical shells and confined layered structures (Hunt *et al.*, 2000), in the current case there are in fact two effective loading sources as the mode interaction takes hold: the axial load P, which generally decreases, and the sinusoidally varying (in z) tilt generalized coordinate q_t, which represents the axial component of the

global buckling mode and generally increases. The notion of determining the "body force", as discussed in Hunt and Wadee (1998), could be used as a way to calculate the effective Maxwell load, but this has been left for future work.

As mentioned earlier, the Abaqus/Riks method in the current FE model has difficulty in capturing the wavelength change of the local buckling mode pattern in the post-buckling response. A possible way to overcome this problem might be to perform Dynamic/Explicit analysis within Abaqus, instead of static Riks analysis. It has been found in the literature that Abaqus/Explicit, which solves equations of motion as opposed to static ones, is potentially capable of tracing sharp snap-backs in the post-buckling response (Degenhardt *et al.*, 2001). Therefore, further investigations would be required to focus on treating the problem as a dynamical system within Abaqus such that snap-backs may be replicated more readily. Issues such as determining the inertial matrix would need addressing, but are likely to be tractable. Nevertheless the model developed in the present thesis has provided a fresh insight into the behaviour of a very common structural element by identifying the potential occurrence of the phenomenon of cellular buckling, a highly dangerous form of instability. This should sound a note of caution to structural analysts and designers in that subtle, yet hazardous, phenomena may be being missed by standard analysis techniques and software. Analytical approaches still provide a powerful, rigorous but still practical methods for understanding complex instability problems.

Appendix A

Expressions for the direct strain for an imperfect stiffener

Consider a simply-supported and axially loaded stiffened plate, as shown in Figure 3.2(b). The local out-of-plane deflection of the stiffener $w_s(y, z)$ with the initial imperfection $w_0(y, z)$ was introduced in Figure 4.3. After buckling, the deflected shape of the stiffened plate can be sketched diagrammatically as shown in Figure A.1. The expression for the direct strains arising from the local out-of-plane displacement

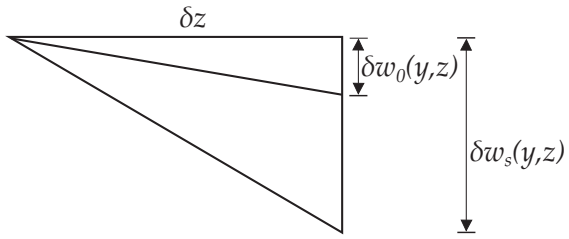

Figure A.1: Outline the out-of-plane deflection of a stiffener $w_s(y, z)$ with the initial imperfection $w_0(y, z)$ in a specimen with length δz along the stiffened plate.

component in the middle surface of the stiffener is:

$$\begin{aligned}\varepsilon_{z,l} &= \frac{\left(\delta w^2 + \delta z^2\right)^{1/2} - \left(\delta w_{s0}^2 + \delta z^2\right)^{1/2}}{\left(\delta w_{s0}^2 + \delta z^2\right)^{1/2}}, \\ &= \frac{\left(\delta w^2 + \delta z^2\right)^{1/2}}{\left(\delta w_{s0}^2 + \delta z^2\right)^{1/2}} - 1,\end{aligned} \tag{A.1}$$

dividing the numerator and the denominator of the fraction by δz^2, the expression for $\varepsilon_{z,l}$ becomes:

$$\begin{aligned}\varepsilon_{z,l} &= \frac{\left(w'^2 + 1\right)^{1/2}}{\left(w_{s0}'^2 + 1\right)^{1/2}} - 1, \\ &= \left(w'^2 + 1\right)^{1/2} \left(w_{s0}'^2 + 1\right)^{-1/2} - 1, \\ &\approx \left(1 + \frac{1}{2} w'^2\right) \left(1 - \frac{1}{2} w_{s0}'^2\right) - 1, \\ &\approx \frac{1}{2} w'^2 + \frac{1}{2} w_{s0}'^2 - \frac{1}{4} w'^2 w_{s0}'^2,\end{aligned} \tag{A.2}$$

by neglecting the higher order term from the final expression, the relationship for $\varepsilon_{z,l}$ is thus:

$$\varepsilon_{z,l} = \frac{1}{2} w'^2 + \frac{1}{2} w_{s0}'^2. \tag{A.3}$$

Appendix B

Expressions for definite integrals

The full expressions of the definite integrals for the stiffener and the main plate were obtained in MAPLE, thus:

Expressions for the definite integrals of the stiffener

$$\{f^2\}_y = h_1 \left[\frac{1}{3} + S_4^2\left(\frac{2\pi^6}{945} - \frac{3}{2}\right) + S_4\left(\frac{2}{\pi} - \frac{7\pi^3}{180}\right)\right]. \tag{B.1}$$

$$\{f''^2\}_y = \frac{\pi^4}{h_1^3} S_4^2\left(\frac{\pi^2}{3} - \frac{3}{2}\right). \tag{B.2}$$

$$\{ff''\}_y = \frac{\pi}{h_1} S_4\left[S_4\left(\frac{3\pi}{2} - \frac{\pi^5}{45}\right) - 1 + \frac{\pi^2}{6}\right]. \tag{B.3}$$

$$\{f'^2\}_y = \frac{1}{h_1}\left[1 + S_4^2\left(\frac{\pi^6}{45} - \frac{3\pi^2}{2}\right)\right]. \tag{B.4}$$

$$\{f^4\}_y = h_1\left[\frac{1}{5} + S_4^4\left(16\pi^4 - \frac{6717\pi^2}{8} + \frac{2901517}{432} + \frac{8\pi^{12}}{1216215} + \frac{2\pi^6}{315}\right) + S_4^3\left(\frac{7207}{6\pi}\right.\right.$$
$$\left.\left. -\frac{449\pi}{4} - \frac{47\pi^3}{60} - \frac{103\pi^9}{498960}\right) + S_4^2\left(\frac{93}{2\pi^2} - 7 + \frac{23\pi^6}{7560}\right) + S_4\left(\frac{4}{\pi} - \frac{24}{\pi^3} - \frac{\pi^3}{35}\right)\right]. \tag{B.5}$$

$$\{Yf^2\}_y = h_1\left[\frac{1}{4} + S_4^2\left(\frac{11}{12} - \frac{16}{\pi^2} + \frac{29\pi^6}{30240}\right) + S_4\left(\frac{2}{\pi} - \frac{8}{\pi^3} - \frac{\pi^3}{45}\right)\right]. \tag{B.6}$$

$$\{yf^2\}_y = h_1\left\{\frac{h_1}{4} - \frac{\bar{y}}{3} + S_4^2\left[h_1\left(\frac{29\pi^6}{30240} + \frac{11}{12} - \frac{16}{\pi^2}\right) + \bar{y}\left(\frac{3}{2} - \frac{2\pi^6}{945}\right)\right]\right.$$
$$\left. +S_4\left[h_1\left(\frac{2}{\pi} - \frac{\pi^3}{45} - \frac{8}{\pi^3}\right) + \bar{y}\left(\frac{7\pi^3}{180} - \frac{2}{\pi}\right)\right]\right\}. \tag{B.7}$$

$$\{f^2f'^2\}_y = \frac{1}{h_1}\left[\frac{1}{3} + S_4^4\left(\frac{603833\pi^2}{864} - \frac{1385\pi^4}{16} + \frac{47\pi^6}{30} + \frac{\pi^8}{945} + \frac{2\pi^{12}}{93555}\right) + S_4^3\left(\frac{745\pi}{6}\right.\right.$$
$$\left.\left. -\frac{275\pi^3}{24} - \frac{41\pi^9}{90720} - \frac{3\pi^5}{40}\right) + S_4^2\left(\frac{7}{4} + \frac{\pi^6}{252} - \frac{\pi^2}{2}\right) + S_4\left(\frac{7\pi^3}{180} - \frac{2}{\pi}+\right)\right]. \tag{B.8}$$

Expressions for the definite integrals for the main plate

$$\{g^2\}_x = b\left[\frac{1}{2} + J_p^2\left(\frac{31}{480} - \frac{2}{\pi^3}\right) + J_p\left(\frac{8}{\pi^3} - \frac{1}{4}\right)\right]. \tag{B.9}$$

$$\{g''^2\}_x = \frac{1}{b^3}\left[\frac{\pi^4}{2} + J_p^2\left(4 - 2\pi + \frac{\pi^4}{32}\right) + J_p\left(8\pi - \pi^4\right)\right]. \tag{B.10}$$

$$\{gg''\}_x = \frac{1}{b}\left[J_p^2\left(\frac{2}{\pi} - \frac{\pi^2}{32} - \frac{1}{3}\right) + J_p\left(\frac{\pi^2}{4} - \frac{8}{\pi}\right) - \frac{\pi^2}{2}\right]. \tag{B.11}$$

$$\{g'^2\}_x = \frac{1}{b}\left[\frac{\pi^2}{2} + J_p^2\left(\frac{\pi^2}{32} - \frac{2}{\pi} + \frac{1}{3}\right) + J_p\left(\frac{8}{\pi} - \frac{\pi^2}{4}\right)\right]. \tag{B.12}$$

$$\begin{aligned}\{g^4\}_x = b\Bigg[\frac{3}{8} + J_p^4\left(\frac{9}{32\pi^4} + \frac{144}{\pi^5} - \frac{5}{27\pi^3} - \frac{1440}{\pi^7} + \frac{6001}{645120}\right) + J_p^3\left(\frac{20}{9\pi^3} - \frac{576}{\pi^5}\right.\\ \left.+\frac{5760}{\pi^7} - \frac{9}{4\pi^4} - \frac{47}{640}\right) + J_p^2\left(\frac{9}{2\pi^4} - \frac{80}{9\pi^3} + \frac{77}{320}\right) + J_p\left(\frac{320}{27\pi^3} - \frac{3}{8}\right)\Bigg].\end{aligned} \tag{B.13}$$

$$\begin{aligned}\{g^2 g'^2\}_x = \frac{1}{b}\Bigg[\frac{\pi^2}{8} + J_p^4\left(\frac{5}{64\pi^2} - \frac{13}{216\pi} - \frac{144}{\pi^5} + \frac{14}{\pi^3} + \frac{17}{1120} + \frac{47\pi^2}{30720}\right) + J_p^3\left(\frac{13}{18\pi}\right.\\ \left.-\frac{5}{8\pi^2} - \frac{56}{\pi^3} + \frac{576}{\pi^5} - \frac{1}{12} - \frac{31\pi^2}{1920}\right) + J_p^2\left(\frac{5}{4\pi^2} - \frac{26}{9\pi} + \frac{1}{6} + \frac{61\pi^2}{960}\right)\\ +J_p\left(\frac{104}{27\pi} - \frac{\pi^2}{8}\right)\Bigg].\end{aligned} \tag{B.14}$$

Appendix C

Initial analytical model for a lipped stiffened plate

The analytical model can be adapted for a stiffened plate with lipped stiffeners as shown in Figure 7.1(a). This type of stiffener would introduce the possibility of distortional buckling. The relative rigidity of the connection between the stiffener and the lip can be provided by a rotational spring with stiffness c_l at the stiffener–lip junction, as shown in Figure 7.1(c). Hence, the shape of the local buckling mode along the width of the lip can be estimated by a nonlinear function that is again a summation of both polynomial and trigonometric terms. The general form of approximate deflection shape for a lipped stiffened plate can be expressed by the following equation:

$$w_l(x, z) = L(x)w_l(z), \tag{C.1}$$

where:

$$L(x) = -\left[L_0 + L_1 X_l + L_2 X_l^2 + L_3 X_l^3 + L_4 \sin(\pi X_l)\right], \tag{C.2}$$

and $X_l(x) = x/b_l$. For $L(x)$, the coefficients L_0, L_1, L_2, L_3 and L_4 are determined by applying appopriate boundary conditions for the lip. At the junction between the

stiffener and the lip, $x = 0$ and $y = h_1 - \bar{y}$, the conditions are:

$$w_l(x,z) = 0, \quad D_l \frac{\partial^2}{\partial x^2} w_l(x,z) = c_l \frac{\partial}{\partial x} w_l(x,z), \tag{C.3}$$

whereas at the lip tip, $x = b_l$, the conditions are:

$$w_l(x,z) = w_l(z), \quad \frac{\partial^2}{\partial x^2} w_l(x,z) = 0, \quad \frac{\partial^3}{\partial x^3} w_l(x,z) = 0, \tag{C.4}$$

where $D_l = Et_l^3/[12(1-\nu^2)]$ is the lip flexural rigidity. The function for the deflected shape $w_l(x,z)$ can be deduced from the above conditions and written thus:

$$w_l(x,z) = -\left\{ X_l + J_l \frac{\pi^3}{6} \left[3X_l^2 - X_l^3 - 2X_l + \frac{6}{\pi^3} \sin(\pi X_l) \right] \right\} w_l(z), \tag{C.5}$$

where:

$$J_l = \left\{ \pi \left[\frac{D_l \pi^2}{c_l b_l} + \frac{\pi^2}{3} - 1 \right] \right\}^{-1}. \tag{C.6}$$

Moreover, although the general form of the local deflection of the stiffener is the same as the expression in Equation (3.5), by adding the lip, the boundary conditions at the junction between the stiffener and the lip, $y = h_1 - \bar{y}$ are:

$$w_s(y,z) = w(z), \quad D_s \frac{\partial^2}{\partial y^2} w_s(y,z) = M_l, \quad D_s \frac{\partial^3}{\partial y^3} w_s(y,z) = Q_l, \tag{C.7}$$

where Q_l and M_l are the shear force and the bending moment at the lip and the stiffener junction, respectively. The boundary conditions for the stiffener at the junction between the stiffener and the main plate are the same as the ones in Equation (3.6). The function for the deflected shape $w_s(y,z)$ can be deduced from the above conditions and written thus:

$$\begin{aligned} w_s(y,z) = \Bigg\{ Y - S_4 \frac{\pi^3}{6} \left[2Y - 3Y^2 + Y^3 - \frac{6}{\pi^3} \sin(\pi Y) \right] + \lambda_l \left(\frac{1}{3} Q_l h_1^3 - \frac{1}{2} M_l h_1^2 \right) Y \\ - \lambda_l \left(\frac{1}{2} Q_l h_1^3 - \frac{1}{2} M_l h_1^2 \right) Y^2 + \lambda_l \left(\frac{1}{6} Q_l h_1^3 \right) Y^3 \Bigg\} w(z), \end{aligned} \tag{C.8}$$

where:

$$S_4 = \frac{6c_p h_1 + Q_l h_1^3 \lambda_l \left(6D_s + 2c_p h_1\right) - 3M_l h_1^2 \lambda_l \left(2D_s + c_p h_1\right)}{6D_s \pi^3 + 2c_p h_1 \pi^3 - 6c_p h_1 \pi}. \tag{C.9}$$

Similarly, according to the sympathetic local deflection of the lip, the relationship between the local deflection of the lip and the stiffener can be assumed, $w_l(z) = \lambda_l w(z)$. Therefore, by adding the moment equilibrium relationships at the lip–stiffener junction, an explicit relationship can be derived for the relating parameter λ_l, thus:

$$\lambda_l = \left(\frac{b_l}{h_1}\right)\left[\frac{6 + S_4\pi^3 - 6S_4\pi}{6 - 2S_4\pi^3 + 6S_4\pi + b_l Q_l h_1^2 - 3b_l M_l h_1}\right]. \tag{C.10}$$

References

Abaqus. 2011. *Version 6.10.* Providence, USA: Dassault Systèmes.

Allen, H. G. 1969. *Analysis and design of structural sandwich panels.* Oxford: Pergamon.

Allen, H. G., & Bulson, P. S. 1980. *Background to buckling.* London: McGraw-Hill.

Bazant, Z. P., & Cedolin, L. 1991. *Stability of structures: Elastic, inelastic, fracture, and damage theories.* Mineola, New York: Dover Publications.

Becque, J. 2008. *The interaction of local and overall buckling of cold-formed stainless steel columns.* Ph.D. thesis, School of Civil Engineering, University of Sydney, Sydney, Australia.

Becque, J., & Rasmussen, K. J. R. 2009a. Experimental investigation of the interaction of local and overall buckling of stainless steel I-columns. *ASCE J. Struct. Eng*, **135**(11), 1340–1348.

Becque, J., & Rasmussen, K. J. R. 2009b. Numerical investigation of the interaction of local and overall buckling of stainless steel I-columns. *ASCE J. Struct. Eng*, **135**(11), 1349–1356.

Bonello, M. A., Chryssanthopoulos, M. K., & Dowling, P. J. 1993. Ultimate strength

design of stiffened plates under axial compression and bending. *Marine Struct.*, **6**, 533–552.

British Standard Institute. EN1993, 2001. *Eurocode 3: Design of steel structures–Part 1-3: General rules–supplemetary rules for cold formed members and sheeting.* Brussels, Belgium: Comité Européen de Normalisation (CEN).

Budd, C. J., Hunt, G. W., & Kuske, R. 2001. Asymptotics of cellular buckling close to the maxwell load. *Proc. R. Soc. A*, **457**, 2935–2964.

Budiansky, B. (ed). 1976. *Buckling of structures.* Berlin Heidelberg: Springer. IUTAM symposium.

Bulson, P. S. 1970. *The stability of flat plates.* London, UK: Chatto & Windus.

Burke, J., & Knobloch, E. 2007. Homoclinic snaking: Structure and stability. *Chaos*, **17**(3), 037102.

Butler, R., Lillico, M., Hunt, G. W., & McDonald, N. J. 2000. Experiment on interactive buckling in optimized stiffened panels. *Structural and Multidisciplinary Optimization*, **23**(1), 40–48.

Carrera, E., Zappino, E., & Petrolo, M. 2012. Analysis of thin-walled structures with longitudinal and transversal stiffeners. *Trans. ASME J. Appl. Mech*, **80**, 011006–1–011006–12.

Casafont, M., Marimon, F., Pastor, M., & Ferrer, M. 2011. Linear buckling analysis of thin-walled members combining the generalised beam theory and the finite element method. *Computers and Structures*, **89**(21-22), 1982–2000.

Champneys, A. R., Hunt, G. W., & Thompson, J. M. T. (eds). 1999. *Localization and solitary waves in solid mechanics.* Advanced Series in Nonlinear Dynamics, vol. 12. World Scientific.

Chapman, S. J., & Kozyreff, G. 2009. Exponential asymptotics of localised patterns and snaking bifurcation diagrams. *Physica D*, **238**(3), 319–354.

Chilver, A. H. 1967. Coupled modes of elastic buckling. *J. Mech. Phys. Solids*, **15**, 15–28.

Choi, B. H., Hwang, M., T., Yoon, & Yoo, C. H. 2009. Experimental study of inelastic buckling strength and stiffness requirements for longitudinally stiffened panels. *Engineering Structures*, **31**(5), 1141–1153.

Coan, J. M. 1951. Large deflection theory for plates with small initial curvature loaded in edge compression. *Trans. ASME*, 73–143.

Cox, H. L. 1934. *Buckling of thin plates in compression*. Tech. rept. Air Ministry. Aeronautical Research Committee. Reports and Memoranda.

Crisfield, M. A. 1997. *Non-linear finite element analysis of solids and structures: Advanced topics*. 1st edn. New York, USA: John Wiley & Sons, Inc.

Croll, J. G., & Walker, A. C. 1972. *Elements of structural stability*. London: Macmillan.

Da Silva, L. S., & Hunt, G. W. 1990. Interactive buckling in sandwich structures with core orthotropy. *Mech. Struct. & Mach.*, **18**(3), 353–372.

Danielson, D. A., Kihl, D. P., & Hodges, D. H. 1990. Tripping of thin-walled plating stiffeners in axial compression. *Thin-Walled Struct.*, **10**, 121–142.

Dankowicz, H., Schilder, F., , & Saghafi, M. 2011. Continuation of connecting orbits with lin's method using COCO. *ENOC2011*, **29**, 24–29.

Davies, J. M., & Leach, P. 1994. First-order generalised beam theory. *J. Constr. Steel Res.*, **31**(2-3), 187–220.

Davies, J. M., Leach, P., & Heinz, D. 1994. Second-order generalised beam theory. *J. Constr. Steel Res.*, **31**(2-3), 221–241.

Degenhardt, R., Klein, H., Kling, A., Temmen, H., & Zimmermann, R. 2001. Buckling and post-buckling analysis of shells under quasi-static and dynamic loads. *Proceedings: Workshop 'Schwarzer Rumpf' (CFRP for Future Aircraft Structures), Braunschweig*.

Dhooge, A., Govaerts, W., & Kuznetsov, Yu. A. 2003. MatCont: A Matlab package for numerical bifurcation analysis of ODEs. *ACM TOMS*, **29**, 141–164.

Doedel, E. J., & Oldeman, B. E. 2011. *Auto-07p: Continuation and bifurcation software for ordinary differential equations*. Montreal, Canada: Concordia University.

Durban, D., Simmonds, J.G., Givoli, D., & Libai, A. 2001. *Advances in the mechanics of plates and shells: The avinoam libai anniversary volume*. Solid mechanics and its applications. Kluwer Academic.

Euler, L. 1744. *Methodus inveniendi lineas curvas maximi minimive proprietate gaudentes*. Appendix: De curvis elasticis. Lausanne and Geneva.

Fok, W. C., Rhodes, J., & Walker, A. C. 1976. Local buckling of outstands in stiffened plates. *Aero. Quart.*, **27**, 277–291.

Fok, W. C., Walker, A. C., & Rhodes, J. 1977. Buckling of locally imperfect stiffeners in plates. *ASCE J. Eng. Mech. Div.*, **103**(5), 895–911.

Forray, M. J. 1968. *Variational calculus in science and engineering*. New York, USA: McGraw-Hill.

Fox, C. 1987. *An introduction to the calculus of variations*. Dover Books on Mathematics. Mineola, New York: Dover Publications.

Galerkin, B. G. 1933. *Thin elastic plates.* Gostrojisdat, Leningrad; (In Russian).

Gardner, L., & Nethercot, D. A. 2004a. Experiments on stainless steel hollow sections-part 2: member behaviour of columns and beams. *J. Constr. Steel Res.*, **60**(9), 1319–1332.

Gardner, L., & Nethercot, D. A. 2004b. Numerical modeling of stainless steel structural components–a consistent approach. *ASCE J. Struct. Eng.*, **130**(10), 1586–1601.

Gell, G., & Thompsson, H. 2013. Application of first-order generalised beam theory on open thin-walled members, MSc Thesis. *Chalmers Univercity of Technology.*

Ghavami, K. 1994. Experimental study of stiffened plates in compression up to collapse. *J. Constr. Steel Res.*, **28**(2), 197–221.

Ghavami, K. G., & Khedmati, M. R. 2006. Numerical and experimental investigation on the compression behaviour of stiffened plates. *J. Constr. Steel Res.*, **62**(11), 1087–1100.

Goltermann, P., & Møllmann, H. 1989. Interactive buckling in thin walled beams—II. applications. *Int. J. Solids Struct.*, **25**(7), 729–749.

Goodier, J. N. 1946. Cylindrical buckling of sandwich plates. *Trans. ASME J. Appl. Mech*, **13**(4), A253–A260.

Graves Smith, T. R., & Sridharan, S. 1978. A finite strip method for the post-locally buckled analysis of plate structures. *Int. J. Mech. Sci.*, **20**, 833–842.

Grondin, G. Y., Elwi, A. E., & Cheng, J. 1999. Buckling of stiffened steel plates – a parametric study. *J. Constr. Steel Res.*, **50**(2), 151–175.

Hancock, G. J. 1978. Local, distortional and lateral buckling of i-beams. *ASCE J. Struct. Eng*, **104**(11), 1787–1798.

Hancock, G. J. 1981. Interaction buckling in I-section columns. *ASCE J. Struct. Eng*, **107**(1), 165–179.

Hencky, H. 1921. *Der spannungszustand in rechteckigen platten (the state of stress in rectangular plates)*. R. Oldenbourg.

Huber, M. T. 1929. *Probleme der static technish wichtiger orthotroper platten (static problems of the technically important orthotropic plates)*. Warsawa: Gebetner & Wolff.

Hunt, G. W., & Wadee, M. A. 1998. Localization and mode interaction in sandwich structures. *Proc. R. Soc. A*, **454**(1972), 1197–1216.

Hunt, G. W., & Wadee, M. K. 1991. Comparative lagrangian formulations for localized buckling. *Proc. R. Soc. Lond.*, **A**(434), 48–502.

Hunt, G. W., Williams, K. A. J., & Cowell, R. G. 1986. Hidden symmetry concepts in the elastic buckling of axially-loaded cylinders. *Int. J. Solids Struct.*, **22**(12), 1501–1515.

Hunt, G. W., Da Silva, L. S., & Manzocchi, G. M. E. 1988. Interactive buckling in sandwich structures. *Proc. R. Soc. A*, **417**(1852), 155–177.

Hunt, G. W., Lord, G. J., & Champneys, A. R. 1999. Homoclinic and heteroclinic orbits underlying the post-buckling of axially-compressed cylindrical shells. *Comput. Meth. Appl. Mech. Eng.*, **170**, 239–251.

Hunt, G. W., Peletier, M. A., Champneys, A. R., Woods, P. D., Wadee, M. A., Budd, C. J., & Lord, G. J. 2000. Cellular buckling in long structures. *Nonlinear Dyn.*, **21**(1), 3–29.

Hunt, G. W., Lord, G. J., & Peletier, M. A. 2003. Cylindrical shell buckling: A characterization of localization and periodicity. *Discrete Contin. Dyn. Syst.-Ser. B*, **3**(4), 505–518.

Hutchinson, J. W., & Koiter, W. T. 1970. Postbuckling theory. *Trans. ASME J. Appl. Mech.*, **23**(7), 1353–1366.

Koiter, W. T. 1945. *On the stability of elastic equilibrium.* Ph.D. thesis, Technische Hogeschool, Delft (Technological University of Delft), Delft, The Netherlands. English translation issued as NASA, Tech. Trans., F 10, 833, 1967.

Koiter, W. T. 1963. Elastic stability and post-buckling behaviour. *Proc. Symp. Nonlinear Problems*, 257–275.

Koiter, W. T. 1969. The nonlinear buckling problem of a complete spherical shell under uniform external pressure. *Proc. Kon. Nederl. Acad. Wet.*, **72**, 40–123. Amsterdam.

Koiter, W. T., & Pignataro, M. 1976. *A general theory for the interaction between local and overall buckling of stiffened panels.* Tech. rept. WTHD 83. Delft University of Technology, Delft, The Netherlands.

Li, Z., & Schafer, B.W. 2010. Buckling analysis of cold-formed steel members with general boundary conditions using CUFSM: conventional and constrained finite strip methods. *Pages 17–31 of: 20th Int. Spec. Conf. Cold-Formed Steel Struct.*

Lillico, M., Butler, R., Hunt, G. W., Watson, A., & Kennedy, D. 2003. Post-buckling of stiffened panels using strut, strip, and finite element methods. *AIAA Journal*, **41**(6), 1172–1179.

Lord, G. J., Champneys, A. R., & Hunt, G. W. 1997. Computation of localized post-buckling in long axially-compressed cylindrical shells. *Phil. Trans. R. Soc. Lond.*, A **355**(1732), 2137–2150.

Loughlan, J. (ed). 2004. *Thin-walled structures: Advances in research, design and manufacturing technology.* Taylor & Francis.

Lundquist, E. E., & Stowell, E. Z. 1942a. *Critical compressive stress for outstanding flanges.* Tech. rept. 734. Tech. Memo. NACA.

Lundquist, E. E., & Stowell, E. Z. 1942b. *Restraint provided a at rectangular plate by a sturdy stiffener along an edge of the plate.* Tech. rept. 735. Tech. Memo. NACA.

Marguerre, K. 1937. *The apparent width of the plate in compression.* Tech. rept. 833. Tech. Memo. NACA.

MATLAB. 2010. *version 7.10.0 (R2010a).* Natick, Massachusetts: The MathWorks Inc.

Menken, C. M., Groot, W. J., & Stallenberg, G. A. J. 1991. Interactive buckling of beams in bending. *Thin-Walled Struct.*, **12**, 415–434.

Møllmann, H., & Goltermann, P. 1989. Interactive buckling in thin walled beams—I. theory. *Int. J. Solids Struct.*, **25**(7), 715–728.

Murray, N. W. 1973. Buckling of stiffened panels loaded axially and in bending. *The Structural Engineer*, **51**(8), 285–300.

Murray, N. W. 1984. *Introduction to the theory of thin-walled structures.* Oxford Engineering Science Series. Clarendon Press.

Paik, J. K., Thayamballi, A. K., & Kim, Do Hyung. 1999. An analytical method for the ultimate compressive strength and effective plating of stiffened panels. *J. Constr. Steel Res.*, **49**(1), 43–68.

Pan, Y., & Louca, L. A. 1999. Experimental and numerical studies on the response of stiffened plates subjected to gas explosions. *J. Constr. Steel Res.*, **52**(2), 171–193.

Pignataro, M., Pasca, M., & Franchin, P. 2000. Post-buckling analysis of corrugated panels in the presence of multiple interacting modes. *Thin-Walled Struct.*, **36**(1), 47–66.

Plank, R. J., & Wittrick, W. H. 1974. Buckling under combined loading of thin, flat-walled structures by a complex fnite strip method. *Int. J. Num. Meth. Eng.*, **8**(2), 323–339.

Rhodes, J., & Harvey, J. M. 1971a. The post-buckling behaviour of thin flat plates in compression with the unloaded edges elastically restrained against rotation. *Int. J. Mech. Sci.*, **13**, 82–91.

Rhodes, J., & Harvey, J. M. 1971b. Effects of eccentricity of load or compression on the buckling and post-buckling behaviour of flat plates. *Int. J. Mech. Sci.*, **13**, 867–879.

Riks, E. 1972. Application of Newton's method to problem of elastic stability. *Trans. ASME J. Appl. Mech*, **39**(4), 1060–1065.

Ronalds, B. F. 1989. Torsional buckling and tripping strength of slender flat-bar stiffeners in steel plating. *Proc. Instn. Civ. Engrs.*, **87**(Dec.), 583–604.

Saito, D., & Wadee, M. A. 2009. Numerical studies of interactive buckling in pre-stressed steel stayed columns. *Eng. Struct.*, **31**(1), 1–15.

Sarawit, A. T., Kim, Y., Bakker, M. C. M., & Pekoz, T. 2003. The finite method for thin-walled members-applications. *Thin-Walled Struct.*, **41**, 191–206.

Schafer, B. W. 2002. Local, distortional, and Euler buckling of thin-walled columns. *ASCE J. Struct. Eng*, **128**(3), 289–299.

Schafer, B. W. 2008. Review: The direct strength method of cold-formed steel member design. *J. Constr. Steel Res.*, **64**(7-8), 766–778. International Colloquium on Stability and Ductility of Steel Structures 2006.

Schafer, B. W., & Peköz, T. 1999. Laterally braced cold-formed steel exural members with edge stiffened flanges. *ASCE J. Struct. Eng.*, **125**(2), 118–127.

Schardt, R. 1994. Generalized beam theory–an adequate method for coupled stability problems. *Thin-Walled Struct.*, **19**(2-4), 161–180.

Sewell, M. J. 1965. The static perturbation technique in buckling problems. *J. Mech. Phys. Solids*, **13**, 247–265.

Seydel, R. 1994. *Practical bifurcation and stability analysis: From equilibrium to chaos*. Interdisciplinary Applied Mathematics, vol. 5. New York, USA: Springer.

Sheikh, I. A., Grondin, G. Y., & Elwi, A. E. 2002. Stiffened steel plates under uniaxial compression. *J. Constr. Steel Res.*, **58**(5-8), 1061–1080.

Smith, D. W. 1976. Bridge failures. *ICE Proceedings*, **60**(3), 367–382.

Sridharan, S., & Peng, M. H. 1989. Performance of axially compressed stiffened plates. *Int. J. Solids Struct.*, **25**(8), 879–899.

Sridharan, S., & Peng, M. H. 1991. An optimization strategy for wide stiffened plates subjected to interaction of local and overall buckling. *Comput. Struct.*, **41**(2), 233–243.

Sridharan, S., & Zeggane, M. 2001. Stiffened plates and cylindrical shells under interactive buckling. *Finite Elements in Analysis and Design*, **38**(2), 155–178.

Supple, W. J. 1967. Coupled branching configurations in the elastic buckling of symmetric structural systems. *Int. J. Mech. Sci.*, **9**, 97–112.

Taylor, C., & Dawes, J. H. P. 2010. Snaking and isolas of localised states in bistable discrete lattices. *Phys. Lett. A*, **375**, 14–22.

Thompson, J. M. T. 1967. Towards a general statistical theory of imperfection-sensitivity in elastic post-buckling. *J. Mech. Phys. Solids.*, **15**, 413–417.

Thompson, J. M. T., & Hunt, G. W. 1973. *A general theory of elastic stability*. London: Wiley.

Thompson, J. M. T., & Hunt, G. W. 1984. *Elastic instability phenomena.* London: Wiley.

Thompson, J. M. T., & Lewis, G. M. 1972. On the optimum design of thin-walled compression members. *J. Mech. Phys. Solids.*, **20**, 101–109.

Thompson, J. M. T., & Supple, W. J. 1973. Erosion of optimum designs by compound branching phenomena. *J. Mech. Phys. Solids*, **21**, 135–144.

Thompson, J. M. T., Tulk, J. D., & Walker, A. C. 1976. An experimental study of imperfection-sensitivity in the interactive buckling of stiffened plates. *Pages 149–159 of: Buckling of structures.* International Union of Theoretical and Applied Mechanics. Berlin Heidelberg: Springer.

Timoshenko, S. P. 1915. *On large deflections of circular plates.* Tech. rept. 89. Mem. Inst. Ways Commun.

Timoshenko, S. P. 1921. On the correction for shear of the differential equation for transverse vibration of prismatic bars. *Phil. Mag.*, **41**, 744–746.

Timoshenko, S. P., & Gere, J. M. 1961. *Theory of elastic stability.* New York, USA: McGraw-Hill.

Timoshenko, S. P., & Woinowsky-Krieger, S. 1959. *Theory of plates and shells.* New York, USA: 2nd edn, McGraw-Hill.

Trahair, N. S., Bradford, M. A., Nethercot, D. A., & Gardner, L. 2008. *The behaviour and design of steel structures to EC3.* 4th edn. Taylor and Francis.

Tulk, J. D., & Walker, A. C. 1976. Model studies of the elastic buckling of a stiffened plate. *J. Strain Anal. Eng. Des.*, **11**(3), 137–143.

Tvergaard, V. 1973a. Imperfection sensitivity of a wide integrally stiffened panel under compression. *Int. J. Solids Struct.*, **9**, 177–192.

Tvergaard, V. 1973b. Influence of post-buckling behaviour on optimum design of stiffened panels. *Int. J. Solids Struct.*, **9**, 1519–1534.

Tvergaard, V., & Needleman, A. 1976. Mode interaction in an eccentrically stiffened elastic-plastic panel under compression. *Pages 160–171 of:* Budiansky, B. (ed), *Buckling of structures*. International Union of Theoretical and Applied Mechanics. Berlin Heidelberg: Springer.

van der Heijden, G. H. M., Champneys, A. R., & Thompson, J. M. T. 2002. Spatially complex localisation in twisted elastic rods constrained to a cylinder. *Int. J. Solids Struct.*, **39**, 1863–1883.

van der Neut, A. 1968. *The longitudinal stiffness of simply supported imperfect plate strips*. Internal report. Delft University of Technology, Delft University of Technology, Department of Aerospace Engineering, Report VTH-152.

van der Neut, A. 1969. The interaction of local buckling and column failure of thin-walled compression members. *Pages 389–399 of:* Hetényi, M., & Vincenti, W. G. (eds), *Applied mechanics*. International Union of Theoretical and Applied Mechanics. Berlin Heidelberg: Springer.

van der Neut, A. 1974. *Mode interaction with stiffened panels*. Tech. rept. VTH-180. Delft university of technology.

van der Neut, A. 1976. Mode interaction with stiffened panels. *Pages 117–132 of:* Budiansky, B. (ed), *Buckling of structures*. International Union of Theoretical and Applied Mechanics. Berlin Heidelberg: Springer.

Ventsel, E., & Krauthammer, T. 2001. *Thin plates and shells: Theory: Analysis, and applications*. CRC Press.

von Kármán, T., Sechler, E. E., & Donnell, L. H. 1932. The strength of thin plates in compression. *Trans. ASME J. Appl. Mech*, **54**(APM), 54–55.

Wadee, M. A. 1998. *Localized buckling in sadwich structures.* Ph.D. thesis, University of Bath, Bath, UK.

Wadee, M. A. 1999. Experimental evaluation of interactive buckle localization in compression sandwich panels. *J. Sandw. Struct. Mater.*, **1**(3), 230–254.

Wadee, M. A. 2000. Effects of periodic and localized imperfections on struts on nonlinear foundations and compression sandwich panels. *Int. J. Solids Struct.*, **37**(8), 1191–1209.

Wadee, M. A. 2007. Nonlinear mathematics in structural engineering. *Mathematics Today*, **43**, 104–108.

Wadee, M. A., & Bai, L. 2014. Cellular buckling in I-section struts. *Thin-Walled Struct.*, **81**, 89–100.

Wadee, M. A., & Edmunds, R. 2005. Kink band propagation in layered structures. *J. Mech. Phys. Solids*, **53**(9), 2017–2035.

Wadee, M. A., & Gardner, L. 2012. Cellular buckling from mode interaction in I-beams under uniform bending. *Proc. R. Soc. A*, **468**(2137), 245–268.

Wadee, M. A., & Hunt, G. W. 1998. Interactively induced localized buckling in sandwich structures with core orthotropy. *Trans. ASME J. Appl. Mech*, **65**(2), 523–528.

Wadee, M. A., & Simões Da Silva, L. A. P. 2005. Asymmetric secondary buckling in monosymmetric sandwich struts. *Trans. ASME J. Appl. Mech*, **72**(5), 683–690.

Wadee, M. A., Yiatros, S., & Theofanous, M. 2010. Comparative studies of localized buckling in sandwich struts with different core bending models. *Int. J. Non-Linear Mech.*, **45**(2), 111–120.

Wadee, M. K., Hunt, G. W., & Whiting, A. I. M. 1997. Asymptotic and Rayleigh–Ritz routes to localized buckling solutions in an elastic instability problem. *Proc. R. Soc. A*, **453**(1965), 2085–2107.

Webster, A. G., & Plimpton, S. J. 1955. *Partial differential equations of mathematical physics*. Mineola, New York: Dover Publications.

Williams, F. W., & Wittrick, W. H. 1971. Numerical results for the initial buckling of some stiffened panels in compression. *Aero. Quart.*, **23**, 24–40.

Woods, P. D., & Champneys, A. R. 1999. Heteroclinic tangles and homoclinic snaking in the unfolding of a degenerate reversible Hamiltonian–Hopf bifurcation. *Physica D*, **129**(3–4), 147–170.

Yamaki, N. 1959. Post-buckling behaviour of rectangular plates with small initial curvature loaded in edge compression. *Trans. ASME J. Appl. Mech*, **27**(2), 355–342.

Yamaki, N. 1984. *Elastic stability of circular cylindrical shells*. Applied Mathematics and Mechanics Series, vol. 27. New York, USA: Elsevier.